1973

Electronic-spectra Of Single-crystal Potassium-bromide Containing Thallous Ion Impurity

Sheila Anne Thorsley

ELECTRONIC SPECTRA OF SINGLE CRYSTAL POTASSIUM BROMIDE CONTAINING THALLOUS ION IMPURITY

by

Sheila Anne Thorsley

Department of Chemistry

Submitted in partial fulfillment

of the requirements for the degree of

Doctor of Philosophy

Faculty of Graduate Studies

The University of Western Ontario

London, Canada

May 1973

ABSTRACT

The optical absorption and emission of the A-band of single crystal potassium bromide containing thallous ion impurity has been investigated over the temperature range, 15 K - 296 K.

The experimental absorption line shapes have been studied systematically as one or more symmetric or asymmetric gaussian bands in order to characterize the shape in terms of the fewest parameters. The best empirical fit was found to be the sum of two asymmetric gaussian bands. Interpretation of the experimental results on the basis of the configuration coordinate model was found to be unsatisfactory. The data are best explained by the Jahn-Teller interaction of the T_{2g} vibrational modes of the lattice with the excited state of the A-band.

The emission line shapes were characterized by two symmetric gaussian bands. The experimental results can be interpreted on the basis of the co-existence of two types of minima on the adiabatic potential energy surface of the excited state of the A absorption band as a consequence of Jahn-Teller interaction with E_g vibrational modes.

ACKNOWLEDGEMENTS

The publication of a thesis is never the sole effort of the person indicated on the title page. It is, rather, the summation of the work of a great many people who through previous publication or through personal contact have stimulated the ideas expressed in the following pages. For the efforts of all these people, I am deeply grateful.

I am especially indebted to my supervisor, Dr. P.W.M. Jacobs, who first introduced me to the field of solid state chemistry and whose understanding and encouragement made this work possible.

The efforts of Dr. J. Ross Macdonald in analyzing some of the data are gratefully acknowledged.

I would also like to thank Drs. O.E. Facey and L.L. Coatsworth for many stimulating discussions and Mrs. Marilyn Geiger for typing the manuscript.

This work would not have been possible without the encouragement of my family. The assistance and undaunted faith of my husband, Dan, cannot be adequately acknowledged.

This research was supported by the National Research Council of Canada. The personal support of the National Research Council (1966-1970) is also greatly appreciated.

TABLE OF CONTENTS

CERTIFICATE OF EXAMINATION	ii
ABSTRACT	iii
ACKNOWLEDGEMENTS	iv
TABLE OF CONTENTS	v
LIST OF TABLES	ix
LIST OF FIGURES	x
CHAPTER I - INTRODUCTION	1
CHAPTER II - THEORY	
1. Introduction	
1-1 Energy Levels of Free Thallium Ion	6
1-2 Energy Levels of Thallium Ion in the Crystal	6
1-3 Assignment of Absorption Bands to transitions on Tl^+ Ion	6
2. Optical Transitions in Crystals	8
2-1 Transitions in the Free Atom	8
2-2 Modifications Due to Crystal Medium	13
3. Calculation of Spectral Line Shapes	14
3-1 Born-Oppenheimer Approximation	14
3-2 Shape Function	17

4. Configuration Coordinate Approximation

4-1 Introduction 19

4-2 Quantum Line Shape - Linear Coupling 21

4-3 Semi-classical Approximation 26

4-3a Linear Coupling 28

4-3b Quadratic Coupling 30

5. Summary 33

CHAPTER III - GENERAL EXPERIMENTAL TECHNIQUES

1. Crystal Growth

1-1 Liquid Phase Purification 36

1-2 Vacuum Purification 37

1-2a Purification Furnace 37

1-2b Purification Apparatus 39

1-2c Vacuum System 42

1-2d Purification of the Melt 42

1-3 Doping with TlBr 43

1-4 Crystal Growth 44

2. Cryostats 48

3. Vacuum Line 52

4. Temperature Control

4-1 Measurements above 77 K 52

4-2 Measurements below 77 K 54

5. Measurement of Optical Absorption 57

6. Emission Measurements 60

6-1 Excitation System 61

6-2 Modification of the Detection System 64

6-3 Initial Focusing 65

6-4 Calibration of the Optical System

6-4a Theory 65

6-4b Method 67

6-5 Experimental Procedure 70

CHAPTER IV - EXPERIMENTAL MEASUREMENTS AND DATA PROCESSING

1. Experimental Measurements

1-1 Crystal Samples 73

1-2 Temperature Selection 74

1-3 Absorption Measurements 74

1-4 Emission Measurements 77

2. Chart Reading

2-1 General 78

2-2 Absorption 79

2-3 Emission 79

3. Computer Processing

3-1 Preliminary Data Treatment 79

3-2 Spectral Sensitivity Correction for Emission Data 80

3-3 Least Squares Analysis - MROCOS 84

3-4 Least Squares Analysis - BMDX85 85

CHAPTER V - EXPERIMENTAL RESULTS

1. Introduction 87

2. Absorption

2-1 Introduction 87

2-2 One Symmetric Gaussian Band 88

2-3 One Asymmetric Gaussian Band 91

2-4 Two Symmetric Gaussian Bands 94

2-5 Two Asymmetric Gaussian Bands 98

2-6 Three Symmetric Gaussian Bands 102

2-7 Standard Deviation of Line Shape Models 105

3. Emission

3-1 Introduction 142

3-2 Characterization of Emission Line Shape 142

CHAPTER VI - DISCUSSION

1. Absorption

1-1 Introduction 155

1-2 Single Band Analysis 156

1-3 Two Band Analysis 162

1-4 Three Band Analysis 165

1-5 Conclusions 166

1-6 Jahn-Teller Effect 166

2. Emission 179

CHAPTER VII - SUMMARY 190

REFERENCES 193

VITA 199

LIST OF TABLES

Table	Description	Page
[III-1]	Spectral Sensitivity Correction Factor	71
[IV-1]	Temperatures of Absorption Measurements, $KBr:Tl^+$	75
[IV-2]	Temperatures of Emission Measurements, $KBr:Tl^+$	76
	A-Band Absorption $KBr:Tl^+$:	
[V-1]	One Symmetric Gaussian Band	89
[V-2]	One Asymmetric Gaussian Band	92
[V-3]	Two Symmetric Gaussian Bands	95
[V-4]	Two Asymmetric Gaussian Bands	99
[V-5]	Three Symmetric Gaussian Bands	103
	Emission $KBr:Tl^+$ - A-Band Excitation:	
[V-6]	Three Symmetric Gaussian Bands	143
	A-Band Absorption $KBr:Tl^+$:	
[VI-1]	Parameters Derived from the Temperature Dependence of H_{obs}	159
[VI-2]	Parameters Derived from the Temperature Dependence of m_2	159
[VI-3]	Parameters Derived from $\Delta E_{splitting}$	172
[VI-4]	Absorption Line Shape Parameters	172
	Emission $KBr:Tl^+$ - A-Band Excitation:	
[VI-5]	Parameters Derived from the Temperature Dependence of H_{obs}	180

LIST OF FIGURES

Figure	Description	Page
[I-1]	Absorption KBr:Tl^+ - 82 K	3
[II-1]	Energy Levels of Thallous Ion	7
[II-2]	Configuration Coordinate Model	22
[III-1]	Vacuum Line for Crystal Purification	38
[III-2]	Filtration Vessel	40
[III-3]	Crystal Growing Ampoule	41
[III-4]	Crystal Growing Furnace	45
[III-5]	Power Circuit for Crystal Growing Furnace	46
[III-6]	Variable Temperature Cryostat	49
[III-7]	Crystal Holder	50
[III-8]	Vacuum Line for Cryostat Evacuation	53
[III-9]	Liquid Helium Transfer	55
[III-10]	Optical System of Cary Spectrophotometer	59
[III-11]	Optical System for Emission Measurements	62
[III-12]	Experimental Arrangement for Determination of Spectral Sensitivity	68
[III-13]	Power Circuit for Standard Lamp	69
[III-14]	Calibration Curve	72
[IV-1]	A-Band Absorption KBr:Tl^+ - 296.0 K Correction of experimental data for background absorption	81

[IV-2] A-Band Absorption KBr:Tl^+ - 296.0 K
Effect of division by the photon energy on the absorption band shape 82

[IV-3] Emission KBr:Tl^+ - 83.0 K A-Band Excitation
Correction of experimental data for spectral sensitivity and calculation of emission line shape 83

[V-1] A-Band Absorption KBr:Tl^+ at Four Temperatures 106

A-Band Absorption KBr:Tl^+

One Symmetric Gaussian Band:

[V-2] Resolution - 296.0 K 107

[V-3] Error Plot - 296.0 K 107

[V-4] Resolution - 83.0 K 108

[V-5] Error Plot - 83.0 K 108

[V-6] Resolution - 15.0 K 109

[V-7] Error Plot - 15.0 K 109

[V-8] H_{obs} against $T^{1/2}$ 110

[V-9] E_m against T 111

[V-10] I_m against T 112

A-Band Absorption KBr:Tl^+

One Asymmetric Gaussian Band:

[V-11] Resolution - 296.0 K 113

[V-12] Error Plot - 296.0 K 113

[V-13] Resolution - 83.0 K 114

[V-14] Error Plot - 83.0 K 114

[V-15] Resolution - 15.0 K 115

[V-16] Error Plot - 15.0 K 115

[V-17] H_{obs} against $T^{1/2}$ 116

[V-18] E_m against T 117

[V-19] I_m against T 118

[V-20] b against T 119

A-Band Absorption KBr:Tl^+

Two Symmetric Gaussian Bands:

[V-21] Resolution - 296.0 K 120

[V-22] Error Plot - 296.0 K 120

[V-23] Resolution - 83.0 K 121

[V-24] Error Plot - 83.0 K 121

[V-25] Resolution - 15.0 K 122

[V-26] Error Plot - 15.0 K 122

[V-27] H_{obs} against $T^{1/2}$ 123

[V-28] E_m against T 124

[V-29] I_m against T 125

[V-30] $\Delta E_{splitting}$ against $T^{1/2}$ 126

A-Band Absorption KBr:Tl^+

Two Asymmetric Gaussian Bands:

[V-31] Resolution - 296.0 K 127

[V-32] Error Plot - 296.0 K 127

[V-33] Resolution - 83.0 K 128

[V-34] Error Plot - 83.0 K 128

[V-35] Resolution - 15.0 K 129

[V-36] Error Plot - 15.0 K 129

[V-37] H_{obs} against $T^{1/2}$ 130

[V-38] E_m against T 131

[V-39] I_m against T 132

[V-40] b against T 133

[V-41] $\Delta E_{splitting}$ against $T^{1/2}$ 134

A-Band Absorption KBr:Tl^+

Three Symmetric Gaussian Bands:

[V-42] Resolution - 296.0 K 135

[V-43] Error Plot - 296.0 K 135

[V-44] Resolution - 83.0 K 136

[V-45] Error Plot - 83.0 K 136

[V-46] H_{obs} against $T^{1/2}$ 137

[V-47] E_m against T 138

[V-48] I_m against T 139

[V-49] $\Delta E_{splitting}$ against $T^{1/2}$ 140

[V-50] A-Band Absorption KBr:Tl^+

Standard Deviation of Fit 141

[V-51] Emission KBr:Tl^+ - A-Band Excitation at Five

Temperatures 147

Emission KBr:Tl^+ - A-Band Excitation

[V-52] Resolution - 296.0 K 148

[V-53] Error Plot - 296.0 K 148

[V-54] Resolution - 83.0 K 149

[V-55] Error Plot - 83.0 K 149

[V-56] Resolution - 15.5 K 150

[V-57] Error Plot - 15.5 K 150

[V-58] H_{obs} against $T^{1/2}$ 151

[V-59] E_m against T 152

[V-60] I_m against T 153

[V-61] $\Delta E_{splitting}$ against T 154

A-Band Absorption KBr:Tl^+

[VI-1] One Asymmetric Gaussian Band m_2 against T 161

[VI-2] Two Asymmetric Gaussian Bands m_2 against T 164

[VI-3] Theoretical Line Shape 171

[VI-4] Comparison of Theoretical and Experimental Line Shapes - θ=0.2, T=296.0 K 173

[VI-5] Comparison of Theoretical and Experimental Line Shapes - θ=0.1, T=144.5 K 174

[VI-6] Comparison of Theoretical and Experimental Line Shapes - θ=0.06, T=83.0 K 175

Emission KBr:Tl^+ - A-Band Excitation

[VI-7] Profile Plot of (y+g) as a Function of x_3 183

[VI-8] Profile Plot of (y+g) as a Function of x_3 184

[VI-9] Contour Plot of Adiabatic Potential Energy Surface - A=2.4, g=0 186

[VI-10] Contour Plot of Adiabatic Potential Energy Surface - A=2.4, g=0.4 187

CHAPTER I

INTRODUCTION

Some materials which contain impurities show characteristic absorption and under the influence of suitable excitation they fluoresce. Such materials have been investigated extensively during the present century. However, the need for efficient phosphors for fluorescent lights, cathode ray tubes, scintillation counters etc. has attracted a major portion of the attention to systems of commercial importance. This is unfortunate, since these phosphors are complex and not amenable to detailed theoretical interpretation.

There is a group of phosphors which are both physically and chemically simple. These are the alkali halides containing impurity ions having the s^2 configuration. Large single crystals of these materials can be prepared and the octahedral symmetry of the alkali halide lattice simplifies the theoretical approach. Moreover, since these phosphors show many characteristics common to phosphors in general, detailed understanding of the processes involved should provide the basis of a model for more complex systems.

The presence of a small concentration of thallous ion in pure potassium bromide induces optical absorption bands on the long wavelength side of the fundamental absorption of the host lattice. These

bands are designated A, B, C and D in order of increasing energy. The absorption spectrum of KBr:Tl^+ at 82 K is shown in Figure [I-1].

The first investigation of the absorption of alkali halide phosphors was done by Hilsch [1] in 1927. A number of others at the Göttingen school [2-5] continued the study during the next few years.

In 1938, Seitz [6] presented the first detailed explanation of the properties of alkali halide phosphors containing thallium as impurity. His interpretation was based on the assumption that monovalent thallium ions, Tl^+, replaced alkali metal ions in the lattice and that the long wavelength absorption resulting from the introduction of the impurity could be attributed to the excitation of the thallium ions.

The first theoretical calculation of the electron-lattice interaction was given by Williams [7,8,9] for A-band absorption and emission in KCl:Tl^+. He calculated the adiabatic energy as a function of a single radial configuration coordinate, the distance from the thallium ion to the neighbouring chloride ion. The theory was modified [10] to include spin-orbit interaction.

Klick and co-workers [11,12,13] were able to derive configuration coordinate curves on the basis of experimentally obtained parameters. It was assumed that both ground and excited states were simple harmonic oscillators, that the symmetric displacement of neighbouring halide ions was the important mode of vibration and that the excited state could be treated classically. Only four parameters were required to characterize the adiabatic potential curves; the force constants for the ground and excited states, and the relative displacements of the minima of the parabolic curves with respect to both energy and the configuration

FIGURE [I-1]

ABSORPTION KBr:Tl^+ - 82 K

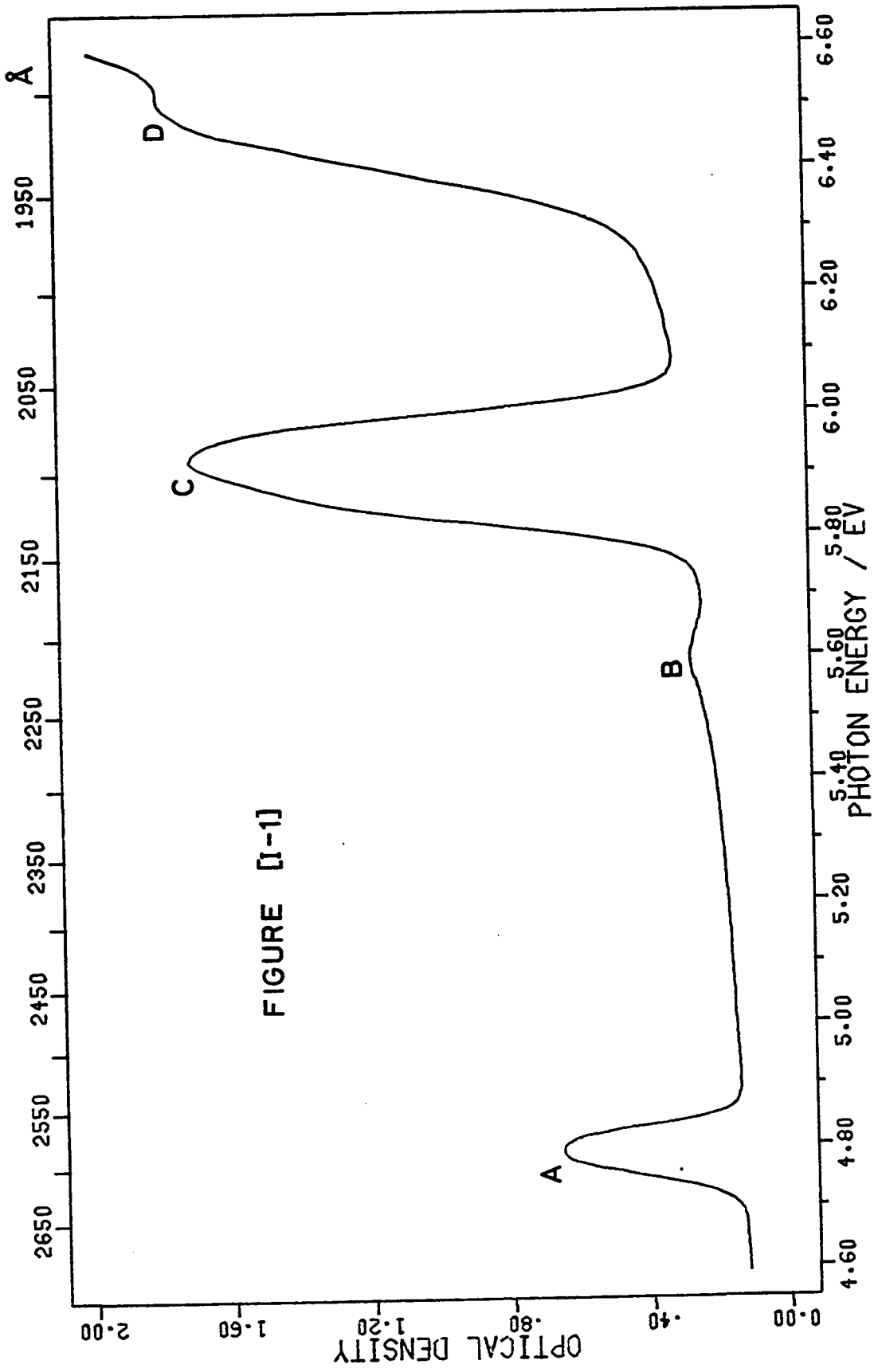
Å
2650
2550
2450
2350
2250
2150
2050
1950
A
B
C
D
OPTICAL DENSITY
0.00
.40
.80
1.20
1.60
2.00
4.60
4.80
5.00
5.20
5.40
5.60
5.80
6.00
6.20
6.40
6.60
PHOTON ENERGY / EV

FIGURE [I-1]

coordinate. A review of the configuration coordinate approach has been given by Klick and Schulman [14].

Experimental measurements on KI:Tl^+ [15] showed that the A and C bands were structured and it was found that even in systems where structure was not apparent, characterization in terms of a single configuration coordinate was inadequate [16]. Despite the limitations of the model, Edgerton and Teegarden [18] were able to propose a configuration coordinate diagram to explain the emission in KI:Tl^+.

Kamimura and Sugano [18] extended the one-dimensional configuration coordinate model to six dimensions by considering the interactions of the excited state with the E_g and T_{2g} vibrational modes of the lattice. Fukuda [19] presented extensive experimental data on the optical absorption of several ions with the s^2 configuration in a series of alkali halides. His calculations on the ratio of the dipole strength of the C band to that of the A band were consistent with Sugano's formula [20].

Toyozawa and Inoue [21] investigated the Jahn-Teller effect of the T_{2g} mode of vibration. They calculated absorption line shapes and were successful in explaining the structure in the A and C bands, certain asymmetric characteristics of the A band, and the temperature dependence of the separation energies of the fine structures of the bands. Based on the model of Toyozawa and Inoue, Cho [22] developed a general way of calculating numerically by Monte Carlo integration the absorption line shapes for unpolarized light due to singlet triplet transitions in the presence of various modes of lattice vibrations. Homna [23] used the moments of the absorption band shapes to calculate the numerical values of the vibronic coupling constants.

Excellent discussions on the entire field have been given by Williams [24], by Teegarden [25] and by Fowler [26].

Although considerable effort has been directed towards a study of the optical properties of Tl^+ in KCl [13,16,27-41], in KBr [32-36,42-46] and in KI [32,33,34,44-52], the exact nature of the interactions between the impurity ion and the host lattice particularly in emission is not fully understood. Our effort was concentrated on a detailed study of KBr:Tl^+. It was hoped that an intensive investigation of the temperature dependence of absorption and emission in the same sample would provide greater insight into the problem. The major emphasis was on the A-band since in KBr:Tl^+ this band is isolated from the B and C bands.

This thesis is divided into seven chapters. Chapter II contains a review of the theory which formed the basis of our approach to the analysis of the experimental results. Chapter III outlines the general experimental techniques used. The specific details of the experiments are given in Chapter IV and the results in Chapter V. In Chapter VI, the experimental results are discussed. Chapter VII is a summary of our findings.

CHAPTER II

THEORY

1. Introduction

1-1 Energy Levels of Free Thallium Ion

The ground state configuration of Tl^+ ion is s^2, $[Xe4f^{14}5d^{10}6s^2]$, and the first excited state has the configuration sp. The spectroscopic terms associated with these configurations are ^1S from s^2 and ^1P, ^3P from sp. The effect of spin-orbit interaction is to lift the degeneracy of the triplet state. The energy level scheme is shown in Figure [II-1].

1-2 Energy Levels of Thallium Ion in the Crystal

When TlBr is added to pure KBr, K^+ ions are replaced in the lattice by Tl^+ ions. As a result of the Madelung field [53], the free ion states are raised in energy, the ground state more than the excited states. In addition, the octahedral crystal field of the lattice splits the $^3P_2$ state of the free ion into two levels. The energy level diagram [6] for the low lying levels of thallous ion in the crystal is shown in Figure [II-1].

1-3 Assignment of Absorption Bands to Transitions on Tl^+ Ion

The strongest absorption band, C, corresponds to the completely allowed transition $^1A_{1g} \rightarrow {}^1T_{1u}$. The transition $^1A_{1g} \rightarrow {}^3T_{1u}$ is spin

FIGURE [II-1]

ASSIGNMENT OF ABSORPTION BANDS OF KBr:Tl^+ TO TRANSITIONS ON Tl^+ ION

A-band - $^1A_{1g} \rightarrow {}^3T_{1u}$

B-band - $^1A_{1g} \rightarrow {}^3T_{2u}$ or ^3E_u

C-band - $^1A_{1g} \rightarrow {}^1T_{1u}$

The energy scale refers to the free ion and the positions of the levels in the crystal are only approximate.

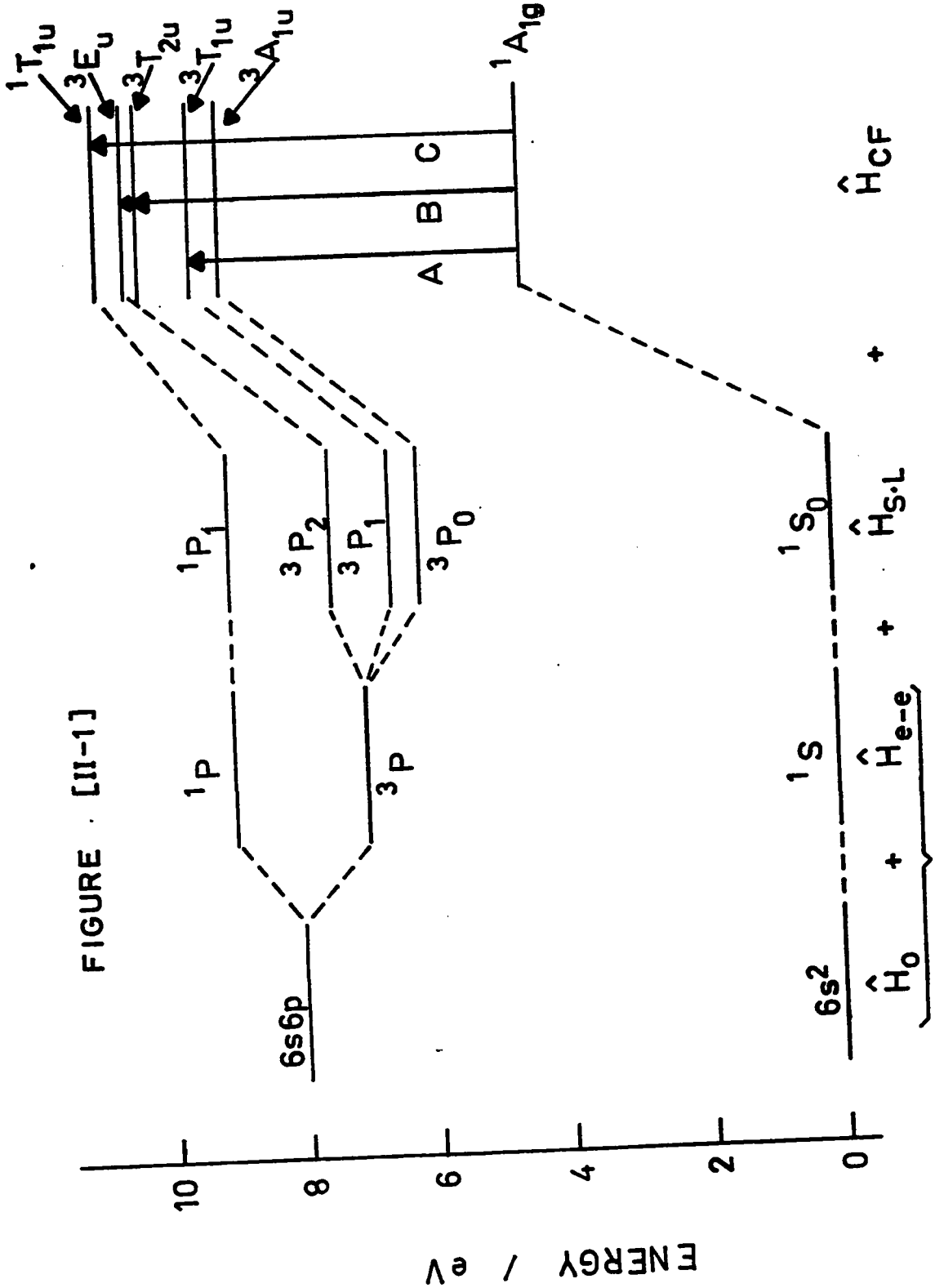
ENERGY / eV
10
8
6
4
2
0
$^1T_{1u}$
^3E_u
$^3T_{2u}$
$^3T_{1u}$
$^3A_{1u}$
$^1A_{1g}$
A
B
C
$\hat{H}_{CF}$
$^1P_1$
$^3P_2$
$^3P_1$
$^3P_0$
^1P
^3P
6s6p
$^1S_0$
$\hat{H}_{S\cdot L}$
^1S
$\hat{H}_{e-e}$
$6s^2$
$\hat{H}_o$
+

FIGURE [II-1]

forbidden but symmetry allowed in the crystal and occurs because of spin-orbit mixing of the singlet and triplet states. The A band results from this transition. The transitions $^1A_{1g} \rightarrow {}^3E_u$ or $^3T_{2u}$ are spin and symmetry forbidden but are weakly allowed in the crystal because of lattice vibrations. This causes the appearance of a weak absorption band, the B band. The transition $^1A_{1g} \rightarrow {}^3A_{1u}$ is completely forbidden. The D band is ascribed to a perturbed exciton [19].

Transitions to higher excited states will be obscured by the absorption edge of the crystal.

2. Optical Transitions in Crystals

Detailed treatment of the theory of optical transitions in crystals is given in several places [54,55,26]. Only a summary of the results will be given here.

2-1 Transitions in the Free Atom

For a system interacting with electromagnetic radiation, the total Hamiltonian can be written [56] as

$$\hat{H} = \hat{H}^0 + \hat{H}^1 \qquad \text{[II-1]}$$

where $\hat{H}^0$ is the time independent operator describing the unperturbed system and $\hat{H}^1$ is the perturbation due to the electromagnetic field. In the absence of the perturbation, the eigenfunction solutions to the equation

$$\hat{H}\Psi = i\hbar\partial\Psi/\partial t \qquad \text{[II-2]}$$

are

$$\Psi_j^o(t_o) = \psi_j^o \exp(-iE_j t_o/\hbar) \qquad \text{[II-3]}$$

The general solution is given by

$$\Psi(t_o) = \sum_j a_j \Psi_j^o(t_o) \qquad [II-4]$$

where $a_j^* a_j$ is the relative probability that the system is in the state j.

If the perturbation is present, equation [II-4] is no longer the solution of the wave equation [II-2]. However, the general solution can be written as

$$\Psi(t) = \sum_j a_j(t) \Psi_j^o(t) \qquad [II-5]$$

where the coefficients a_j are time dependent. The transition probability is given by the time derivative of $a_j^*(t) a_j(t)$.

The probability per unit time of a transition from an initial state n to a final state m is

$$w_{nm} = \frac{4\pi^2}{3\hbar} \frac{1}{4\pi\varepsilon_o} M_{mn}^2 \left[\rho(\nu) d\nu \right]_{\nu=\nu_{mn}} \delta(|E_m - E_n| - h\nu) \qquad [II-6]$$

where M_{mn} is the dipole moment matrix element

$$M_{mn} = \langle m | \sum_j -e \underset{\sim}{r}_j | n \rangle$$

and $[\rho(\nu)d\nu]_{\nu=\nu_{mn}}$ is the energy density of the radiation field evaluated at $\nu=\nu_{mn}$ i.e.

$$\rho(\nu)d\nu = N(h\nu_{mn}) = N(|E_m - E_n|)$$

where N is the number of photons per unit volume and $h\nu_{mn}$ is their energy. Then

$$w_{nm} = \frac{4\pi^2 e^2}{3\hbar} \frac{1}{4\pi\varepsilon_o} |E_m - E_n| \; N \; |\underset{\sim}{r}_{mn}|^2 \; \delta(|E_m - E_n| - h\nu) \qquad [II-7]$$

where

$$\underset{\sim}{r}_{mn} = \langle m | \sum_j \underset{\sim}{r}_j | n \rangle$$

If the light beam is polarized, $\frac{1}{3}|\underset{\sim}{r}_{mn}|^2$ is replaced by $|\underset{\sim}{\eta}\cdot\underset{\sim}{r}_{mn}|^2$ where $\underset{\sim}{\eta}$ is the unit polarization vector.

Equation [II-7] is valid only under the following conditions [26].

(a) N is small.

(b) Before the transition occurs, the probability that the system is in the state n is 1, i.e. $a_n^* a_n = 1$.

(c) Only electronic dipole transitions are included.

(d) The transition takes place between discrete states.

It should be noted here that

$$w_{mn} = w_{nm} \qquad \text{[II-8]}$$

There are other quantities which are related to the transition probability.

1. Absorption Cross Section

The absorption cross section, Σ_{nm} is defined as the transition probability divided by the photon flux and integrated over the delta function.

$$\Sigma_{nm} = \int \frac{w_{nm}}{Nc}\, d(h\nu)$$

$$= \frac{4\pi^2 e^2 h\nu_{mn}}{3\hbar c(4\pi\varepsilon_o)} |\underset{\sim}{r}_{mn}|^2 \qquad \text{[II-9]}$$

2. Oscillator strength

The oscillator strength f_{mn} is defined by

$$f_{mn} = \frac{4\pi m_o}{3\hbar} \nu_{mn} |\underset{\sim}{r}_{mn}|^2 \qquad \text{[II-10]}$$

3. Absorption Coefficient

The absorption coefficient, k, is the probability that a photon will be absorbed in traversing a unit length of material. If I_ν is the

intensity of incident radiation, and dx the distance travelled through the material

$$dI_\nu = -kI_\nu dx \qquad \text{[II-11]}$$

Then

$$k_{nm}(h\nu) = \frac{w_{nm} N_A}{Nc}$$

$$= \frac{4\pi^2 e^2 N_A (h\nu_{mn})}{3\hbar c (4\pi\varepsilon_o)} |\underset{\sim}{r}_{mn}|^2 \delta(|E_m - E_n| - h\nu) \qquad \text{[II-12]}$$

N_A is the number of absorbing atoms per unit volume.

The absorption coefficient depends linearly on the photon energy, $h\nu_{mn}$. The absorption line shape, I, is defined as absorption coefficient divided by photon energy. For an absorbing sample obeying the Beer-Lambert law,

$$I_\nu = I_{\nu o} \exp[-kd]$$

where $I_{\nu o}$ is the intensity of the beam incident upon a sample of thickness d and k is the absorption coefficient. Then

$$\log\left(\frac{I_{\nu o}}{I_\nu}\right) = \text{optical density} = \frac{kd}{2.303}$$

or

$$k = \frac{2.303 \text{ optical density}}{d}$$

Therefore, the absorption line shape can be defined in terms of experimentally measured quantities as

$$I = \frac{2.303 \times \text{optical density}}{\text{crystal thickness} \times E} \qquad \text{[II-13]}$$

where E is the photon energy, $h\nu$.

4. Einstein Coefficients

In the presence of a uniform electromagnetic field of frequency, ν, $B_{mn}dt$ is the probability that the field will induce a transition from state m to state n with the emission of radiation and $B_{nm}dt$ is the probability that the field will induce a transition from state n to state m by absorption of radiation in time dt.

$$B_{nm} = B_{mn} = \frac{2\pi e^2}{3\hbar^2} |\underset{\sim}{r}_{mn}|^2 \frac{1}{4\pi\varepsilon_o} \qquad \text{[II-14]}$$

$A_{mn}dt$ is the probability that a system in state m will undergo a spontaneous transition to the state n in time dt.

$$A_{mn} = \frac{4e^2 (h\nu_{mn})^3}{3c^3\hbar^4} \frac{|\underset{\sim}{r}_{mn}|^2}{4\pi\varepsilon_o} \qquad \text{[II-15]}$$

The probability of spontaneous emission is proportional to the cube of the photon energy, $h\nu_{mn}$. The emission line shape, I, is $A_{mn}/(h\nu_{mn})^3$. The emission line shape in terms of experimental quantities is

$$I = \frac{\text{measured intensity of emission}}{E^3} \qquad \text{[II-16]}$$

All the relationships defined above refer to pairs of non-degenerate levels m and n. For degenerate states, $|\underset{\sim}{r}_{mn}|^2$ must be replaced by

$$\frac{\sum_{p,q} |\underset{\sim}{r}_{p,q}|^2}{g_i}$$

where p,q label the degenerate states and g_i is the degeneracy of the initial state [57].

2-2 Modifications Due to Crystal Medium

For a localized centre embedded in a crystal, certain modifications must be made to the expressions for the transition probability and related quantities.

The transition probability, w_{mn}, is proportional to the square of the electric field at the absorbing centre. Therefore, w_{mn} must be multiplied by $(E_{eff}/E_o)^2$ where E_{eff} is the magnitude of the field effective in inducing the transition and E_o is the average field in the medium. For a compact centre the ratio is given by the classical Lorentz expression [55],

$$\frac{E_{eff}}{E_o} = 1 + \tfrac{1}{3}(n^2-1) \qquad \text{[II-17]}$$

where n is the index of refraction.

In a medium of permittivity, ε, the energy density of the radiation field is proportional to $1/\varepsilon$ and $\varepsilon=n^2\varepsilon_o$, where ε_o is the permittivity of free space. Therefore, w_{nm} is proportional to n^{-2}. Also, the velocity of electromagnetic radiation is c/n where c is the velocity in free space. Hence in a crystal

$$k_{nm} = \frac{4\pi^2 e^2 N_A}{3\hbar c(4\pi\varepsilon_o)} \left[\frac{1}{n}\left(\frac{E_{eff}}{E_o}\right)^2\right] (h\nu_{mn}) \; |\underset{\sim}{r}_{mn}|^2 \delta(|E_m - E_n| - h\nu) \qquad \text{[II-18]}$$

and

$$A_{mn} = \frac{4e^2}{3c^3\hbar^4(4\pi\varepsilon_o)} \left[n\left(\frac{E_{eff}}{E_o}\right)^2\right] (h\nu_{mn})^3 |\underset{\sim}{r}_{mn}|^2 \qquad \text{[II-19]}$$

3. Calculation of Spectral Line Shapes

In principle, the spectral line shapes can be calculated accurately from the equations given in the preceding section. However, serious problems are encountered in evaluating the matrix element $|\underset{\sim}{r}_{mn}|^2$ when the transition occurs in a solid. The main difficulty is in separating accurately the motion of the electrons from that of the lattice. The usual approach is to use the Born-Oppenheimer approximation which in essence assumes that the positions of the atoms do not change significantly during the time required for electronic excitation.

3-1 Born-Oppenheimer Approximation

In the Born-Oppenheimer approximation, the nuclear and electronic motions are separated by writing the state function $\Psi(\underset{\sim}{r},\underset{\sim}{R})$ as the product

$$\Psi_{n\eta}(\underset{\sim}{r},\underset{\sim}{R}) = \psi_{n\underset{\sim}{R}}(\underset{\sim}{r})\chi_{n\eta}(\underset{\sim}{R}) \qquad \text{[II-20]}$$

where n denotes a set of electronic quantum numbers and η a set of nuclear quantum numbers. ψ is the electronic wave function and depends parametrically on the nuclear configuration through the nuclear coordinates, $\underset{\sim}{R}$. χ is the wave function for nuclear motion and depends on the electronic state through n.

$\psi_{n\underset{\sim}{R}}(\underset{\sim}{r})$ satisfies the Schrödinger equation

$$[\hat{T}_e + U(\underset{\sim}{r},\underset{\sim}{R})]\psi_{n\underset{\sim}{R}}(\underset{\sim}{r}) = E_n(\underset{\sim}{R})\psi_{n\underset{\sim}{R}}(\underset{\sim}{r}) \qquad \text{[II-21]}$$

which describes the electronic states at adiabatically fixed nuclear coordinates. $U(\underset{\sim}{r},\underset{\sim}{R})$ contains all the potential energies arising from electron-electron, electron-nucleus and nucleus-nucleus interactions. As the atoms vibrate, U changes and so $\psi_{n\underset{\sim}{R}}(\underset{\sim}{r})$ and $E_n(\underset{\sim}{R})$ change continuously and adiabatically.

$\chi_{n\eta}(\underset{\sim}{R})$ satisfies the Schrödinger equation

$$[\hat{T}_N + E_n(\underset{\sim}{R})]\chi_{n\eta}(\underset{\sim}{R}) = E_{n\eta}\chi_{n\eta}(\underset{\sim}{R}) \qquad [II-22]$$

which describes the vibrational motion of the nuclei in a potential energy $E_n(\underset{\sim}{R})$ supplied by the average positions of the electrons. $E_n(\underset{\sim}{R})$ is generally referred to as the adiabatic potential. Expansion of $E_n(\underset{\sim}{R})$ about the equilibrium positions of the atoms and neglecting terms of third order and higher gives an adiabatic potential quadratic in R. Then equation [II-22] is the equation of a set of harmonic oscillators. For the ground state, n≡a,

$$E_a(\underset{\sim}{R}) = \sum_j \tfrac{1}{2}M_j\omega_{ja}^2Q_j^2 \qquad [II-23]$$

where Q_j is one of the normal coordinates and ω_{ja} is the angular frequency for the jth normal coordinate for vibrations of the nuclei in the ground electronic state. Equation [II-22] can be written as

$$\sum_j\left[\frac{-\hbar^2}{2M_j}\frac{\partial^2}{\partial Q_j^2} + \tfrac{1}{2}M_j\omega_{ja}^2Q_j^2\right]\chi_{a\alpha}(\underset{\sim}{R}) = E_{a\alpha}\chi_{a\alpha}(\underset{\sim}{R}) \qquad [II-24]$$

where α labels the vibrational state. The solutions to equation [II-24] are

$$\chi_{a\alpha}(\underset{\sim}{R}) = \prod_j \phi_{a\alpha j}(Q_j) \qquad [II-25]$$

where the normal mode state functions, $\phi_{a\alpha j}(Q_j)$, satisfy the equation

$$\left[\frac{-\hbar^2}{2M_j}\frac{\partial^2}{\partial Q_j^2} + \tfrac{1}{2}M_j\omega_{ja}^2Q_j^2\right]\phi_{a\alpha j}(Q_j) = \varepsilon_{a\alpha j}\phi_{a\alpha j}(Q_j) \qquad [II-26]$$

The solutions to equation [II-26] are the harmonic oscillator eigenfunctions and eigenvalues.

In order to discuss transitions from the ground state, a, to some excited state, b, it is necessary to obtain the vibrational wave functions for the excited state. To avoid complications in evaluating matrix elements, the adiabatic potential $E_b(\underset{\sim}{R})$ must be expanded in terms of the normal coordinates of the ground state. Then

$$E_b(\underset{\sim}{R}) = E_{ab} + \Sigma_j A_j Q_j + \Sigma_j B_j Q_j^2 + \Sigma_{i\neq j} C_{ij} Q_i Q_j \qquad [II-27]$$

where $B_j = \frac{1}{2} M_j \omega_{jb}^2$ and E_{ab} is equal to the energy difference $(E_b - E_a)$ evaluated when the positions of the nuclei are such that E_a is a minimum, (see Figure [II-2]). If all the C_{ij} are zero, the vibrational wave function for the excited state would be the product of harmonic oscillator functions differing from the ground state functions in their frequencies through B_j and referred to a different origin through A_j. In general the cross terms $C_{ij}Q_iQ_j$ will be small and for simplicity, it is assumed that $C_{ij}=0$ for all i,j. Then the excited state wave functions are

$$\chi_{b\beta}(\underset{\sim}{R}) = \Pi_j \phi_{b\beta j}(Q_j) \qquad [II-28]$$

where the $\phi_{b\beta j}(Q_j)$ satisfy the equation

$$\left[\frac{-\hbar^2}{2M_j} \frac{\partial^2}{\partial Q_j^2} + E_{abj} + A_j Q_j + M_j \omega_{jb}^2 Q_j^2 \right] \phi_{b\beta j}(Q_j) = \varepsilon_{b\beta j} \phi_{b\beta j}(Q_j) \qquad [II-29]$$

E_{abj} is the energy associated with the jth normal mode as a result of an adiabatic transition from the energy minimum in the ground state. The solutions of equation [II-29] are simple harmonic wave functions referred to the displaced origin.

3-2 Shape Function

The transition probability, w_{ab} (see Equation [II-7]), is proportional to $|\underset{\sim}{r}_{ab}|^2$ where

$$\underset{\sim}{r}_{ab} = \langle \psi_{b\underset{\sim}{R}} \chi_{b\beta} | \underset{\sim}{r} | \psi_{a\underset{\sim}{R}} \chi_{a\alpha} \rangle \qquad \text{[II-30]}$$

summed in some suitable way over α and β. The Born-Oppenheimer approximation has been used to write the vibronic wave function for the ground and excited states as products of electronic and vibrational wave functions

$$\Psi_{a\alpha}(\underset{\sim}{r},\underset{\sim}{R}) = \psi_{a\underset{\sim}{R}}(\underset{\sim}{r})\chi_{a\alpha}(\underset{\sim}{R}) \qquad \text{[II-20]}$$

and

$$\Psi_{b\beta}(\underset{\sim}{r},\underset{\sim}{R}) = \psi_{b\underset{\sim}{R}}(\underset{\sim}{r})\chi_{b\beta}(\underset{\sim}{R})$$

$\chi_{a\alpha}(\underset{\sim}{R})$ and $\chi_{b\beta}(\underset{\sim}{R})$ are the products of simple harmonic oscillator functions (see Equations [II-25] and [II-28]).

The electronic wave functions $\psi_{a\underset{\sim}{R}}(\underset{\sim}{r})$ and $\psi_{b\underset{\sim}{R}}(\underset{\sim}{r})$, can be obtained by solving equation [II-21] but in general this is difficult to do. It is usual, therefore to use the Condon Approximation [58] which assumes that the electronic dipole moment, M_{ab}, depends only on an average value of the nuclear coordinates, $\underset{\sim}{R}$. The matrix element may then be factored as

$$\underset{\sim}{r}_{ab} = \langle \psi_b | \underset{\sim}{r} | \psi_a \rangle \langle \chi_{b\beta} | \chi_{a\alpha} \rangle \qquad \text{[II-31]}$$

For the transition $a \rightarrow b$ in a crystal, the absorption coefficient (see Equation [II-18]) can be written as

$$k_{ab}(h\nu) = \frac{4\pi^2 e^2 N_A (h\nu)}{3\hbar c (4\pi\varepsilon_o)} \left[\frac{1}{n} \left(\frac{E_{eff}}{E_o} \right)^2 \right] I_{ab}(h\nu) \qquad \text{[II-32]}$$

where $I_{ab}(h\nu)$ is called the shape function and is calculated by taking a thermal average over initial states and a sum over final states. Then

$$I_{ab}(h\nu) = Av_{\alpha}\sum_{\beta}|\langle\Psi_{b\beta}|\underset{\sim}{r}|\Psi_{a\alpha}\rangle|^2\ \delta(|\varepsilon_{b\beta}-\varepsilon_{a\alpha}|-h\nu)$$

$$\simeq Av_{\alpha}\sum_{\beta}|\langle\psi_{b\underset{\sim}{R}}\chi_{b\beta}|\underset{\sim}{r}|\psi_{a\underset{\sim}{R}}\chi_{a\alpha}\rangle|^2\ \delta(|\varepsilon_{b\beta}-\varepsilon_{a\alpha}|-h\nu)$$

$$\simeq |\langle\psi_b|\underset{\sim}{r}|\psi_a\rangle|^2 Av_{\alpha}\sum_{\beta}|\langle\chi_{b\beta}|\chi_{a\alpha}\rangle|^2\ \delta(|\varepsilon_{b\beta}-\varepsilon_{a\alpha}|-h\nu) \qquad [II-33]$$

Thus the absorption line shape is determined essentially by the overlap integral $\langle\chi_{b\beta}|\chi_{a\alpha}\rangle$.

The emission probability (see Equation [II-19]) can be written as

$$A_{ba}(h\nu) = \frac{64\pi^2e^2\ (h\nu)^3}{3c^3h^4(4\pi\varepsilon_o)}\left[n\left(\frac{E_{eff}}{E_o}\right)^2\right]\int I_{ba}(h\nu)\ d(h\nu) \qquad [II-34]$$

where I_{ba} is of the same form as I_{ab} with the sum over α and the thermal average over β.

The shape functions, I_{ab} and I_{ba}, are proportional to the experimentally derived line shapes defined by equations [II-13] and [II-16].

4. Configuration Coordinate Approximation

4-1 Introduction

A frequently made simplification to the problem of calculating the line shapes is to assume that the ground and excited states can be represented in terms of a single normal coordinate, q.

The ground state adiabatic potential (see Equation [II-23]) is

$$E_a(q) = \tfrac{1}{2}M_a\omega_a^2 q^2 \qquad \text{[II-35]}$$

The vibrational state functions from the solution of equation [II-26] are

$$\phi_{a\alpha}(q) = \left[\frac{(M_a\omega_a/\hbar)^{1/2}}{\pi^{1/2}2^\alpha\alpha!}\right]^{1/2} \exp[-\tfrac{1}{2}\rho_a^2]\, H_\alpha(\rho_a) \qquad \text{[II-36]}$$

where $\rho_a=(M_a\omega_a/\hbar)^{1/2}q$ and $H_\alpha(\rho_a)$ is a Hermite polynomial. The ground state vibrational energies are

$$\varepsilon_{a\alpha} = (\alpha + \tfrac{1}{2})\hbar\omega_a \qquad \text{[II-37]}$$

For the excited state, the adiabatic potential (see Equation [II-27]) is

$$E_b = E_{ab} + Aq + \tfrac{1}{2}M_b\omega_b^2 q^2 \qquad \text{[II-38]}$$

If $M_b\omega_b^2=M_a\omega_a^2$, then E_b differs from E_a in the constant term E_{ab} and in the linear term Aq. Under these conditions, the adiabatic potentials E_a and E_b have the same shape. This is the linear coupling approximation. If $M_b\omega_b^2\neq M_a\omega_a^2$, then E_a and E_b have different shapes. This is called quadratic coupling.

The adiabatic potential for the excited state can also be written as

$$\begin{aligned} E_b &= E_o + \tfrac{1}{2}M_b\omega_b^2(q-q_o)^2 \\ &= E_o + \tfrac{1}{2}M_b\omega_b^2 q_o^2 - (M_b\omega_b q_o)q + \tfrac{1}{2}M_b\omega_b^2 q^2 \end{aligned} \qquad \text{[II-39]}$$

Comparing equations [II-39] and [II-38],

$$q_o = -A/(M_b\omega_b^2) \qquad \text{[II-40]}$$

and

$$E_o = E_{ab} - \tfrac{1}{2}M_b\omega_b^2 q_o^2 \qquad \text{[II-41]}$$

Equation [II-29] becomes

$$\left[\frac{-\hbar^2}{2M_b}\frac{\partial^2}{\partial q'^2} + \tfrac{1}{2}M_b\omega_b^2 q'^2\right]\phi_{b\beta}(q') = \varepsilon_{b\beta}\phi_{b\beta}(q') \qquad \text{[II-42]}$$

where $q' = q - q_o$

and $\varepsilon'_{b\beta} = \varepsilon_{b\beta} - E_o$

Before writing the solutions to equation [II-42], ρ' and E_o are defined in terms of the linear coupling constant, A. For a simple harmonic oscillator, the unit of length is $(\hbar/M\omega)^{1/2}$ and the unit of energy is $(\hbar\omega)$. Then, if

$$a = \frac{A}{\hbar\omega_b}\left(\frac{\hbar}{M_b\omega_b}\right)^{1/2}$$

$$q_o = \frac{-A}{M_b\omega_b^2} = -a\left(\frac{\hbar}{M_b\omega_b}\right)^{1/2}$$

and

$$\rho' = q'\left(\frac{M_b\omega_b}{\hbar}\right)^{1/2} = \rho_b + a$$

Also

$$E_o = E_{ab} - S\hbar\omega_b$$

where $S = \tfrac{1}{2}a^2$

S is called the Huang-Rhys parameter [59]. $(S-\frac{1}{2})$ is the average number of phonons created as the excited state relaxes after a Franck-Condon [58] transition.

The vibrational wave functions for the excited state are

$$\phi_{b\beta}(q') = \left[\frac{(M_b\omega_b/\hbar)^{\frac{1}{2}}}{\pi^{\frac{1}{2}}2^\beta\beta!}\right]^{\frac{1}{2}} \exp[-\tfrac{1}{2}(\rho_b+a)^2]\, H_\beta(\rho_b+a) \qquad [II-43]$$

and the corresponding electronic energies are

$$\varepsilon'_{b\beta} = (\beta + \tfrac{1}{2})\hbar\omega_b \qquad [II-44]$$

The excited state eigenfunctions and eigenvalues are referred to the origin (E_o, q_o), Figure [II-2].

4-2 Quantum Line Shape - Linear Coupling

The overlap integral (see Equation [II-33]) can be evaluated readily only if

$$\rho_b = \rho_a \equiv \rho \qquad [II-45]$$

which requires that

$$M_b\omega_b = M_a\omega_a \equiv M\omega$$

The two conditions [II-45] and $M_b\omega_b^2 = M_a\omega_a^2$ mean that both the reduced mass and the frequency must be the same in the ground state, a, and the excited state, b. Then

$$\langle\chi_{b\beta}|\chi_{a\alpha}\rangle = \frac{1}{\pi^{\frac{1}{2}}(\alpha!\beta!2^{\alpha+\beta})^{\frac{1}{2}}}\, I_{\alpha\beta} \qquad [II-46]$$

where

$$I_{\alpha\beta} = \int_{-\infty}^{\infty} \exp[-\tfrac{1}{2}(\rho+a)^2]\, H_\beta(\rho+a)\, \exp[-\tfrac{1}{2}\rho^2]\, H_\alpha(\rho)\, d\rho \qquad [II-47]$$

FIGURE [II-2]

CONFIGURATION COORDINATE MODEL

FIGURE [II-2]

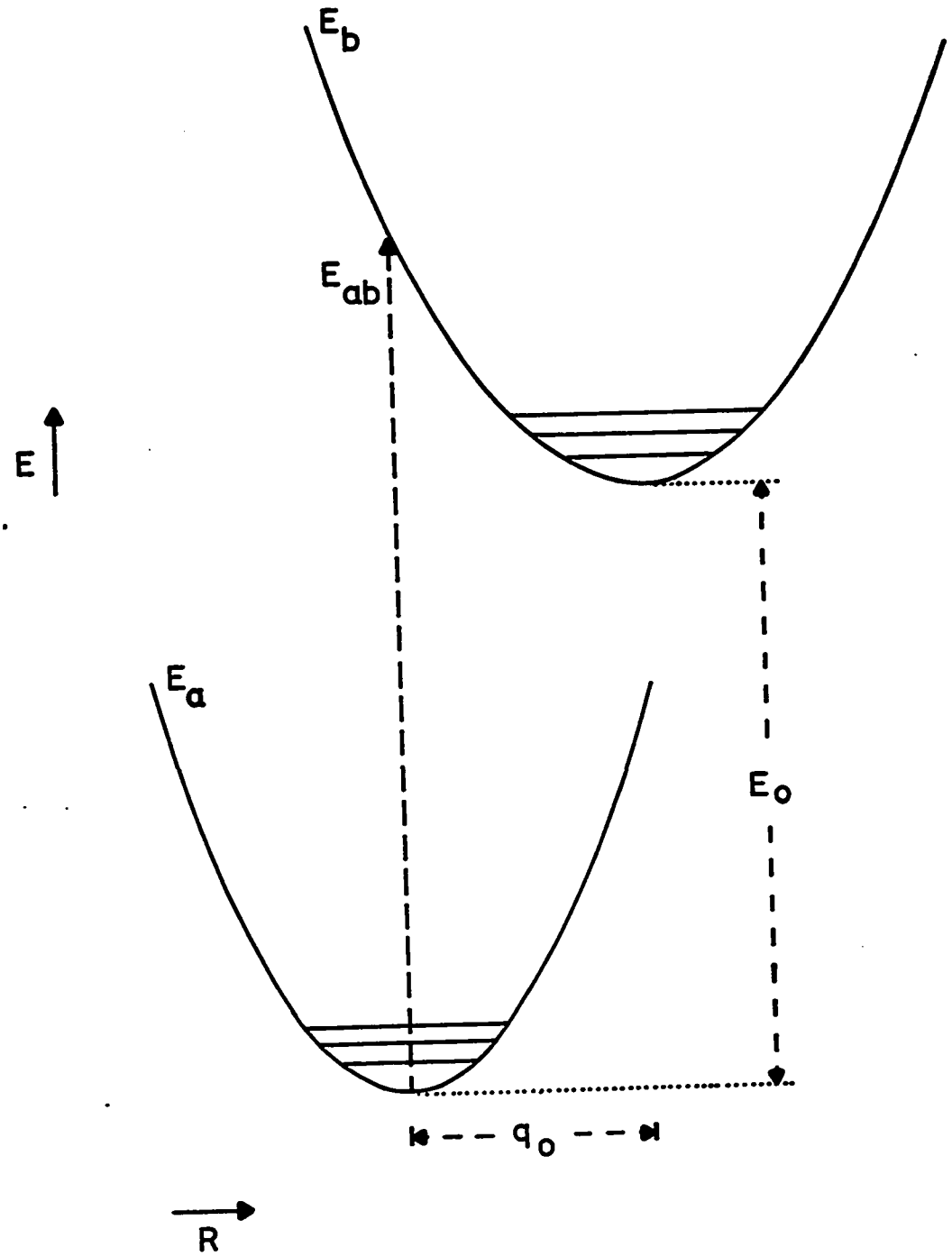

By using the generating function for the Hermite polynomials, equation [II-47] can be written as

$$I_{\alpha\beta} = \pi^{1/2}\exp[-\tfrac{1}{4}a^2]\sum_{\gamma=0}^{\infty}\frac{2^{\alpha}(a)^{\beta-\alpha}(-a^2/2)^{\gamma}\alpha!\beta!}{(\alpha-\gamma)!\gamma!(\beta-\alpha+\gamma)!} \qquad [II-48]$$

The overlap integral becomes

$$\langle\chi_{b\beta}|\chi_{a\alpha}\rangle = \exp[-\tfrac{1}{4}a^2]\left(\frac{\alpha!}{\beta!}\right)^{1/2}\sum_{\gamma=0}^{\infty}\frac{(-1)^{\gamma}(a^2/2)^{\gamma}\beta!(a/\sqrt{2})^{\beta-\alpha}}{\gamma!(\alpha-\gamma)!(\beta-\alpha+\gamma)!} \qquad [II-49]$$

$$= \exp[-\tfrac{1}{2}S]\left(\frac{\alpha!}{\beta!}\right)^{1/2} S^{\frac{1}{2}(\beta-\alpha)}\, L_{\alpha}^{\beta-\alpha}(S) \qquad [II-50]$$

where S is the Huang-Rhys parameter and L is the Laguerre polynomial.

The line shape is

$$I_{ab}(h\nu) = |\underset{\sim}{r}_{ab}|^2\, Av_{\alpha}^{\beta}\Sigma|\langle\chi_{b\beta}|\chi_{a\alpha}\rangle|^2\,\delta(|\varepsilon_{b\beta}-\varepsilon_{a\alpha}|-h\nu) \qquad [II-33]$$

$$= |\underset{\sim}{r}_{ab}|^2\sum_{\substack{\alpha=0\\ \beta=0}}^{\infty}\frac{\exp[-(\alpha+\tfrac{1}{2})\hbar\omega/kT]}{\sum_{\alpha'=0}^{\infty}\exp[-(\alpha'+\tfrac{1}{2})\hbar\omega/kT]}\exp[-S]\ X$$

$$\frac{\alpha!}{\beta!}S^{\beta-\alpha}\left\{L_{\alpha}^{\beta-\alpha}(S)\right\}^2\delta(|\varepsilon_{b\beta}-\varepsilon_{a\alpha}|-h\nu) \qquad [II-51]$$

The sums over α and β can be reduced to a single sum over p where

$$p = \beta-\alpha \qquad [II-52]$$

Then

$$I_{ab}(h\nu) = |\underset{\sim}{r}_{ab}|^2\sum_{p=-\infty}^{\infty}\exp[-S\coth(\hbar\omega/2kT)]\exp[p\hbar\omega/2kT]\ X$$

$$I_p[S\,\mathrm{csch}(\hbar\omega/2kT)]\,\delta(|\varepsilon_{b\beta}-\varepsilon_{a\alpha}|-h\nu) \qquad [II-53]$$

where I_p is a modified Bessel function [60].

In the limit T=0 K, $\alpha=0$ and $p=\beta-\alpha=\beta$. As $T \to 0$, $\mathrm{csch}(\hbar\omega/2kT) \to 0$ and the Bessel function can be written as [61]

$$I_p(z) = \frac{(\frac{1}{2}z)^p}{p!} \qquad \text{[II-54]}$$

where p is an integer greater than -1 and

$$z = S\ \mathrm{csch}(\hbar\omega/2kT) \qquad \text{[II-55]}$$

Then the shape function (see Equation [II-53]) at T=0 K reduces to

$$I_{ab}(h\nu) = \sum_{p=0}^{\infty} \frac{e^{-S} S^p}{p!} \delta(|\varepsilon_{b\beta}-\varepsilon_{a\alpha}|-h\nu)\ |\underset{\sim}{r}_{ab}|^2 \qquad \text{[II-56]}$$

The line shape consists of a series of evenly spaced delta functions with varying weights. The weighting factors increase with increasing p reaching a maximum near $p=\frac{1}{2}a^2$ and then decrease as p increases beyond this value [59,62]. Plots of line shape against p at T=0 K are given by Keil [63] for several values of the coupling constant, a. For large values of a, the curve defined by the envelope is very nearly gaussian.

For large arguments, the asymptotic expansion of the Bessel function is [64]

$$I_p(z) \approx \frac{e^z}{(2\pi z)^{\frac{1}{2}}} \left[1 + \sum_{n=1}^{\infty} \frac{(-1)^n (4p^2-1)(4p^2-3^2)\ldots(4p^2-[2n-1]^2)}{n!\,(8z)^n} \right] \qquad \text{[II-57]}$$

If $|p^2/2z| < 1$,

$$I_p(z) \approx \frac{1}{(2\pi z)^{\frac{1}{2}}} \exp\left(z - \frac{p^2}{2z}\right) \qquad \text{[II-58]}$$

where z is defined by equation [II-55].

At high temperatures

$$z \to S\left(\frac{2kT}{\hbar\omega}\right) \gg 1 \qquad \text{[II-59]}$$

and the expansion given by equation [II-58] is valid. Then in the high

temperature limit, the shape function is

$$I_{ab}(h\nu) = \frac{|\underset{\sim}{r}_{ab}|^2}{(2\pi z)^{\frac{1}{2}}} \sum_{p=-\infty}^{\infty} \exp\left(\frac{p\hbar\omega}{2kT} - \frac{p^2}{2z}\right) \delta(|\varepsilon_{b\beta}-\varepsilon_{a\alpha}|-h\nu) \qquad \text{[II-60]}$$

The spectrum consists of a series of lines at energies determined by the delta function and the intensity of the transition is determined by the exponential term. Experimentally the lines are unresolved and only the band envelope is measured. The characteristics of the band envelope can be investigated by omitting the delta function and treating p as a continuous variable. Then

$$I_{ab}(h\nu) \approx \frac{|\underset{\sim}{r}_{ab}|^2}{(2\pi z)^{\frac{1}{2}}} \exp\left(\frac{p\hbar\omega}{2kT} - \frac{p^2}{2z}\right) \qquad \text{[II-61]}$$

By differentiating with respect to p, the value of I_{ab} at the maximum can be found. Then

$$\frac{I_{ab}}{I_{ab}(\max)} = \exp\left[\frac{-(p-p_m)^2}{2z}\right] \qquad \text{[II-62]}$$

where p_m is the value of p at the maximum.

$$(\varepsilon_{b\beta}-\varepsilon_{a\alpha}) = E_o + (\beta-\alpha)\hbar\omega = E_o + p\hbar\omega \qquad \text{[II-63]}$$

But $(\varepsilon_{b\beta}-\varepsilon_{a\alpha})$ is equal to the photon energy, E. Then

$$E - E_m = (p - p_m)\hbar\omega \qquad \text{[II-64]}$$

where E_m is the energy corresponding to the maximum in I_{ab}.

Therefore,

$$\frac{I_{ab}}{I_{ab}(\max)} = \exp\left[\frac{-(E-E_m)^2}{2z(\hbar\omega)^2}\right] \qquad \text{[II-65]}$$

Thus for a single mode in the harmonic approximation and for the case of linear coupling, the line shape is accurately gaussian at high temperatures.

4-3 Semi-Classical Approximation

An alternative approach to the problem of calculating the line shape is to treat the ground and excited states as classical oscillators and to define an effective temperature so that the average energy in the initial state is that of a quantum mechanical oscillator.

$$I_{ab}(h\nu) = Av_{\alpha}\sum_{\beta}|\langle\Psi_{b\beta}|\underset{\sim}{r}|\Psi_{a\alpha}\rangle|^2\delta(|\varepsilon_{b\beta}-\varepsilon_{a\alpha}|-h\nu) \qquad [II-33]$$

where

$$Av_{\alpha} = \sum_{\alpha}\frac{\exp[-\varepsilon_{a\alpha}/kT]}{\sum_{\alpha'}\exp[-\varepsilon_{a\alpha'}/kT]} = \sum_{\alpha}\rho_{a\alpha} \qquad [II-66]$$

Using the Born-Oppenheimer approximation,

$$I_{ab}(h\nu) = \sum\sum_{\alpha\beta}\rho_{a\alpha}|\langle\psi_{b\underset{\sim}{R}}\chi_{b\beta}|\underset{\sim}{r}|\psi_{a\underset{\sim}{R}}\chi_{a\alpha}\rangle|^2\delta(|\varepsilon_{b\beta}-\varepsilon_{a\alpha}|-h\nu)$$

and using the Condon approximation,

$$I_{ab}(h\nu) = |\langle\psi_a|\underset{\sim}{r}|\psi_b\rangle|^2\sum\sum_{\alpha\beta}\rho_{a\alpha}|\langle\chi_{b\beta}|\chi_{a\alpha}\rangle|^2\delta(|\varepsilon_{b\beta}-\varepsilon_{a\alpha}|-h\nu)$$

$$= |\underset{\sim}{r}_{ab}|^2\sum\sum_{\alpha\beta}\rho_{a\alpha}|\langle\chi_{b\beta}|\chi_{a\alpha}\rangle|^2\delta(|\varepsilon_{b\beta}-\varepsilon_{a\alpha}|-h\nu) \qquad [II-67]$$

If the transition is to a state of large vibrational quantum number, then the excited state potential can be treated classically, i.e.

$$\varepsilon_{b\beta}(q) = E_b(q) \qquad [II-68]$$

The sum over β in equation [II-67] can now be done using closure.

$$\sum_{\beta} |\langle\chi_{b\beta}|\chi_{a\alpha}\rangle|^2 = \sum_{\beta}\langle\chi_{b\beta}|\chi_{a\alpha}\rangle^*\langle\chi_{b\beta}|\chi_{a\alpha}\rangle$$

$$= \sum_{\beta}\langle\chi_{a\alpha}|\chi_{b\beta}\rangle\langle\chi_{b\beta}|\chi_{a\alpha}\rangle$$

$$= \langle\chi_{a\alpha}|\chi_{a\alpha}\rangle \qquad \text{[II-69]}$$

since

$$\sum_{\beta} |\chi_{b\beta}\rangle\langle\chi_{b\beta}| = 1$$

$\langle\chi_{a\alpha}|\chi_{a\alpha}\rangle = 1$ if the wave functions are normalized. Then equation [II-67] reduces to

$$I_{ab}(h\nu) = |\underset{\sim}{r}_{ab}|^2 \sum_{\alpha}\rho_{a\alpha}\delta(|E_b(q)-\varepsilon_{a\alpha}|-h\nu) \qquad \text{[II-70]}$$

For sufficiently high temperatures, the ground state can also be treated classically, i.e.

$$\varepsilon_{a\alpha}(q) = E_a(q) \qquad \text{[II-71]}$$

Then

$$I_{ab}(h\nu) = |\underset{\sim}{r}_{ab}|^2 \sum_{\alpha}\rho_{a\alpha}\delta(|E_b(q)-E_a(q)|-h\nu)$$

$\rho_{a\alpha}$ becomes

$$\frac{\exp[-E_a(q)/kT]}{\int dq\, \exp[-E_a(q)/kT]} \equiv \rho_a$$

and

$\sum_{\alpha}\rho_{a\alpha}$ becomes $\int dq\rho_a$

Therefore

$$I_{ab}(h\nu) = |\underset{\sim}{r}_{ab}|^2 \int dq\, \frac{\exp[-E_a(q)/kT]}{\int dq\, \exp[-E_a(q)/kT]}\, \delta(|E_b(q)-E_a(q)|-h\nu) \qquad \text{[II-72]}$$

where the integrals are over the range $-\infty$ to $+\infty$.

$$E_a(q) = \tfrac{1}{2}K_a q^2 \qquad \text{[II-35]}$$

and

$$E_b(q) = E_o + \tfrac{1}{2}K_b(q-q_o)^2 \qquad \text{[II-39]}$$

Then

$$E = E_b(q)-E_a(q) = E_o + \tfrac{1}{2}K_b q_o^2 - K_b q_o q + \tfrac{1}{2}(K_b-K_a)q^2$$

$$= E_{ab} - K_b q_o q + \tfrac{1}{2}(K_b-K_a)q^2 \qquad \text{[II-73]}$$

4-3a Linear Coupling [65]

In the linear coupling case, $K_b=K_a\equiv K$ and

$$E = E_{ab} - K_b q_o q \qquad \text{[II-74]}$$

Then

$$I_{ab}(h\nu) = |\underset{\sim}{r}_{ab}|^2 \int_{-\infty}^{\infty} dq \, \frac{\exp[-Kq^2/2kT]}{\int_{-\infty}^{\infty} dq \, \exp[-Kq^2/2kT]} \, \delta(E_{ab}-Kq_o q-h\nu)$$

$$= |\underset{\sim}{r}_{ab}|^2 \left(\frac{K}{2\pi kT}\right)^{\frac{1}{2}} \int_{-\infty}^{\infty} dq \, \exp[-Kq^2/2kT]\,\delta(E_{ab}-Kq_o q-h\nu)$$

Using the delta function properties

$$\delta(-x) = \delta(x)$$

$$\delta(ax) = (1/|a|)\delta(x)$$

$$\int_{-\infty}^{\infty} f(x)\delta(x-b)dx = f(b)$$

$$I_{ab}(h\nu) = \frac{|\underset{\sim}{r}_{ab}|^2}{q_o} \left(\frac{1}{2\pi KkT}\right)^{\frac{1}{2}} \exp\left[\frac{-(E_{ab}-h\nu)^2}{2kTKq_o^2}\right] \qquad \text{[II-75]}$$

$I_{ab}(\max)$ can be evaluated by differentiating equation [II-75]. This leads to the results,

$$q_m = 0$$

and

$$E_m = E_{ab}, \text{ a constant.}$$

Then

$$\frac{I_{ab}}{I_{ab}(max)} = \exp\left[\frac{-(E-E_m)^2}{2kTKq_o^2}\right] \qquad [II-76]$$

Classically, the average energy of an oscillator is kT. Quantum mechanically, the average energy in the ground state is

$$\bar{\varepsilon}_a = (\bar{\alpha}+\tfrac{1}{2})\hbar\omega_a$$

where

$$\bar{\alpha} = (\exp[\hbar\omega_a/kT] - 1)^{-1}$$

Thus,

$$\bar{\varepsilon}_a = \tfrac{1}{2}\hbar\omega_a \coth(\hbar\omega_a/2kT)$$

The classical expression for the line shape can be used if the temperature, T, is replaced by an effective temperature, T^*, defined by

$$kT^* = \tfrac{1}{2}\hbar\omega_a \coth(\hbar\omega_a/2kT) = \bar{\varepsilon}_a \qquad [II-77]$$

At high temperatures, kT^* behaves like kT and at low temperatures $kT^* \rightarrow \tfrac{1}{2}\hbar\omega_a$. It is the introduction of the effective temperature which converts the classical expression to a semi-classical form [8].

Comparing equation [II-76] with the general expression for a gaussian curve

$$\frac{Y}{Y(max)} = \exp\left[\frac{-4\ln 2(E-E_m)^2}{H_{obs}^2}\right]$$

where H_{obs} is the full width at $\tfrac{1}{2}Y(max)$ and using equation [II-77] for T^* gives

$$H_{obs}^2 = (4\ln 2)Kq_o^2\hbar\omega_a \coth(\hbar\omega_a/2kT)$$

or

$$H_{obs} = H_o[\coth(\hbar\omega_a/2kT)]^{\frac{1}{2}} \qquad [II-78]$$

where $$H_o = [(4\ln 2)Kq_o^2\hbar\omega_a]^{\frac{1}{2}} \qquad [II-79]$$

The line shape derived in the semi-classical approximation is accurately gaussian. The position of the maximum is temperature independent and the temperature dependence of the half-width is given by equation [II-78].

With the use of equation [II-77], equation [II-76] becomes

$$\frac{I_{ab}}{I_{ab}(max)} = \exp\left[\frac{-(E-E_m)^2}{Kq_o^2(\hbar\omega)} \tanh(\hbar\omega/2kT)\right] \qquad [II-80]$$

The high temperature form of the quantum line shape (see Equation [II-65]) can be written, using equation [II-55], $S=\frac{1}{2}a^2$, and $q_o=-a(\hbar/M\omega)^{\frac{1}{2}}$, as

$$\frac{I_{ab}}{I_{ab}(max)} = \exp\left[\frac{-(E-E_m)^2}{Kq_o^2(\hbar\omega)} \sinh(\hbar\omega/2kT)\right] \qquad [II-81]$$

This equation is valid only for high temperatures, i.e. $(\hbar\omega/2kT)$ small. Under this condition

$$\sinh(\hbar\omega/2kT) \approx \tanh(\hbar\omega/2kT) \approx (2kT/\hbar\omega) \qquad [II-82]$$

and therefore the quantum line shape and semi-classical approximations give identical results in the high temperature limit.

4-3b Quadratic Coupling

For the quadratic coupling case, $K_b \neq K_a$, and $(E_b(q)-E_a(q))$ is given by equation [II-73]. Then equation [II-72] becomes

$$I_{ab}(h\nu) = |\underset{\sim}{r}_{ab}|^2 \int_{-\infty}^{\infty} dq \frac{\exp[-K_a q^2/2kT]}{\int_{-\infty}^{\infty} dq \exp[-K_a q^2/2kT]} \delta(E_{ab}-K_b q_o q+\tfrac{1}{2}(K_b-K_a)q^2-h\nu)$$

$$= |\underset{\sim}{r}_{ab}|^2 \left(\frac{K_a}{2\pi kT} \right)^{1/2} \int_{-\infty}^{\infty} dq \exp[-K_a q^2/2kT] \quad X$$

$$\delta(E_{ab} - K_b q_o q + \tfrac{1}{2}(K_b - K_a) q^2 - h\nu)$$

The integral can be evaluated using the following property of the delta function.

$$\delta((x-a)(x-b)) = (1/|a-b|)[\delta(x-a)+\delta(x-b)] \quad a \neq b$$

This gives the result

$$I_{ab}(h\nu) = |\underset{\sim}{r}_{ab}|^2 \left[\frac{C}{\pi} \right]^{1/2} \frac{1}{(K_b - K_a)} \left(\frac{1}{A(1+B/A^2)^{1/2}} \right) \exp(-CA^2\{1-[1+B/A^2]^{1/2}\}^2) \qquad \text{[II-83]}$$

where

$$A = \frac{K_b q_o}{(K_b - K_a)}$$

$$B = \frac{2(h\nu - E_{ab})}{(K_b - K_a)} \equiv \frac{2(E - E_{ab})}{(K_b - K_a)} \qquad \text{[II-84]}$$

$$C = \frac{K_a}{2kT^*}$$

It should be pointed out that

$$(1+B/A^2) = (1-q/A)^2$$

and therefore no imaginary quantities will be generated in taking the square root (see Equation [II-83]). Also, in the limit, $K_b = K_a$, the expression for $I_{ab}(h\nu)$ given by equation [II-83] reduces to that derived for linear coupling.

$I_{ab}(\max)$ can be evaluated by differentiating equation [II-83]. This leads to the results

$$q_m = \tfrac{1}{2}A\{1-(1-[2/CA^2])^{1/2}\} \qquad \text{[II-85]}$$

and

$$E_m = E_{ab} - \frac{(K_b - K_a)}{4}\left[A^2 - A^2(1-2/CA^2)^{1/2} + C^{-1}\right] \qquad \text{[II-86]}$$

Equations [II-85] and [II-86] are identical with those derived by Jacobs and Krishna Menon [66] by a different procedure. Then

$$\frac{I_{ab}}{I_{ab}^{(max)}} = \frac{(1+B_m/A^2)^{1/2}}{(1+B/A^2)^{1/2}} \exp\left[-CA^2\{[1-(1+B/A^2)^{1/2}]^2 - [1-(1+B_m/A^2)^{1/2}]^2\}\right] \qquad \text{[II-87]}$$

where

$$B_m = \frac{2(E_m - E_{ab})}{(K_b - K_a)}$$

The line shape is no longer accurately gaussian. Expansion of the exponential argument gives a power series in $(E-E_{ab})$ in which the lead term is quadratic. Since E_m is not equal to E_{ab}, the distribution about E_m will be asymmetric.

If $|1-(K_a/K_b)|$ is small compared to unity, then

$$q_m \approx \frac{q_o^2}{K_a[1-(K_a/K_b)]^2}\, kT^* \qquad \text{[II-88]}$$

and

$$E_m \approx E_{ab} - \frac{(K_b - K_a)}{K_a}\, kT^* \qquad \text{[II-89]}$$

so that E_m is expected to be a linear function of kT^*. This contrasts with the constant value of E_m $(=E_{ab})$ predicted for linear coupling.

For the line shape given by equation [II-87] the calculation of the full width at half-height is complicated. However, the second moment, m_2, which is closely related to H^2_{obs}, is

$$m_2 = \langle E^2 \rangle - \langle E \rangle^2$$

$$= \frac{K_b^2}{K_a} q_o^2 \, kT^* + \frac{\frac{1}{2}(K_b - K_a)^2}{K_a^2} (kT^*)^2 \qquad \text{[II-90]}$$

For the case of linear coupling, the line shape is symmetric gaussian and

$$m_2 = Kq_o^2 kT^* = \frac{H_{obs}^2}{8 \ln 2} \qquad \text{[II-91]}$$

Even if the distribution about E_m is asymmetric, the temperature dependence of H_{obs} for the case of quadratic coupling will be given by equation [II-78] to a good approximation.

5. Summary

Formally the absorption line shape can be calculated from

$$I_{ab}(h\nu) = Av_{\alpha}^{\beta} \Sigma |\langle \Psi_{b\beta} | \underset{\sim}{r} | \Psi_{a\alpha} \rangle|^2 \, \delta(|\varepsilon_{b\beta} - \varepsilon_{a\alpha}| - h\nu)$$

$$= |\langle \psi_b | \underset{\sim}{r} | \psi_a \rangle|^2 Av_{\alpha}^{\beta} \Sigma |\langle \chi_{b\beta} | \chi_{a\alpha} \rangle|^2 \, \delta(|\varepsilon_{b\beta} - \varepsilon_{a\alpha}| - h\nu) \qquad \text{[II-33]}$$

within the limits of the Born-Oppenheimer and Condon approximations. The emission line shape, I_{ba}, is of the same form as I_{ab} with the sum over α and the thermal average over β.

For a single mode, in the harmonic approximation, the line shape can be derived in either the linear coupling ($K_b = K_a$) or the quadratic coupling ($K_b \neq K_a$) case. For linear coupling the calculation can be done quantum mechanically or semi-classically. For quadratic coupling, the calculation is done semi-classically.

(a) Quantum Line Shape - Linear Coupling

At low temperatures

$$I_{ab}(h\nu) = \sum_{p=0}^{\infty} \frac{e^{-S} S^p}{p!} \delta(|\varepsilon_{b\beta}-\varepsilon_{a\alpha}|-h\nu) \; |\underset{\sim}{r}_{ab}|^2 \qquad \text{[II-56]}$$

which is approximately gaussian for large values of the coupling constant.

At high temperatures

$$I_{ab}(h\nu) = I_{ab}(h\nu)_{max} \exp\left[\frac{-(E-E_m)^2}{2z(\hbar\omega)^2}\right] \qquad \text{[II-65]}$$

which is accurately gaussian.

(b) Semi-classical Approximation - Linear Coupling

The line shape is given by

$$I_{ab}(h\nu) = I_{ab}(h\nu)_{max} \exp\left[\frac{-(E-E_m)^2}{2Kq_o^2 kT^*}\right] \qquad \text{[II-76]}$$

where

$$kT^* = \tfrac{1}{2}\hbar\omega[\coth(\hbar\omega/2kT)] \qquad \text{[II-77]}$$

The shape is accurately gaussian. E_m is independent of temperature and the temperature dependence of the half-width is given by

$$H_{obs} = H_o[\coth(\hbar\omega/2kT)]^{\frac{1}{2}} \qquad \text{[II-78]}$$

(c) Semi-classical Approximation - Quadratic Coupling

The line shape is given by

$$\frac{I_{ab}}{I_{ab}(max)} = \frac{(1+B_m/A^2)^{\frac{1}{2}}}{(1+B/A^2)^{\frac{1}{2}}} \exp[-CA^2([1-(1+B/A^2)^{\frac{1}{2}}]^2-[1-(1+B_m/A^2)^{\frac{1}{2}}]^2)] \qquad \text{[II-87]}$$

where

$$A = \frac{K_b q_o}{(K_b - K_a)}$$

$$B = \frac{2(E-E_{ab})}{(K_b-K_a)} \qquad B_m = \frac{2(E_m-E_{ab})}{(K_b-K_a)}$$

$$C = \frac{K_a}{2kT^*}$$

The shape is asymmetric gaussian and E_m depends on temperature.

$$E_m = E_{ab} - \frac{(K_b-K_a)}{4} \left[A^2 - A^2(1-2/CA^2)^{1/2} + C^{-1}\right] \qquad \text{[II-86]}$$

$$\approx E_{ab} - \frac{(K_b-K_a)}{K_a} kT^* \qquad \text{[II-89]}$$

The temperature dependence of the half-width is given to a good approximation by

$$H_{obs} = H_o[\coth(\hbar\omega/2kT)]^{1/2} \qquad \text{[II-78]}$$

CHAPTER III

GENERAL EXPERIMENTAL TECHNIQUES

1. Crystal Growth

1-1 Liquid Phase Extraction

The major residual impurities in reagent grade potassium bromide (KBr), which could interfere with the experiments planned for KBr:Tl^+ are heavy metal ions. An attempt was made therefore to increase the purity of the starting material by extraction of an aqueous solution with a solution of 8-hydroxyquinoline (oxine) in chloroform and subsequent recrystallization of the purified KBr.

Two kilograms of KBr (Fisher Certified Reagent) were dissolved in a minimum of conductivity water (~400 ml). The solution was extracted using a 1% w/w solution of oxine in chloroform, once with a 200 ml portion and three times with 100 ml portions. The KBr solution was then washed with pure chloroform, twice with 200 ml portions and once with a 100 ml portion. The solution was brought to boiling and evaporated down until KBr was beginning to precipitate. The hot solution was filtered through a large sinter and left to cool. The purified KBr was recrystallized from conductivity water and dried in an oven at 110 °C.

1-2 Vacuum Purification

Before crystal growth, the potassium bromide obtained from the extraction of reagent grade material with oxine was subjected to further purification using the equipment shown in Figures [III-1, III-2, III-3].

1-2a Purification Furnace

The purification furnace, PF, Figure [III-1], was constructed from a 22 in length of transite pipe 13.5 in O.D., circular end plates of ¼ in thick transite sheet, and a core of silica tubing 22 in long, 2.9 in O.D. surrounded by vermiculite. The furnace was mounted vertically in an external frame of dexion. The silica tube was covered with asbestos paper and wound in two halves with Chromel 'C' heating tape (0.125 in × 0.126 in; 0.361 Ω/ft) supplied by Hoskins Manufacturing Co. The top two inches were left bare. Each of the two 10 in halves was split into two sections. The outer 5 in sections were wound at 3.5 turns per inch and the central 5 in sections were wound at 1.7 turns per inch. The total resistance in each half of the furnace was 7 ohms. The two halves were connected in series and the current in each half could be controlled independently with powerstats.

The furnace temperature was regulated to ±1 K by a temperature controller obtained from the Thermovolt Instrument Co. It employed a Pt/Pt:13%Rh thermocouple as sensor and the photoelectrically activated relay drove a normally closed mercury switch that was used to initiate (and terminate) the heating cycle.

FIGURE [III-1]

VACUUM LINE FOR CRYSTAL PURIFICATION

P - oil pump

HD - mercury diffusion pump

T - liquid nitrogen traps

MG - McLeod gauge

N - nitrogen gas inlet

F - furnace for heating copper gauze

A - trap for the admission of bromine

DC - drying columns

SG - spiral gauge

M - mercury manometer

B - sulphuric acid bubbler

C - water trap

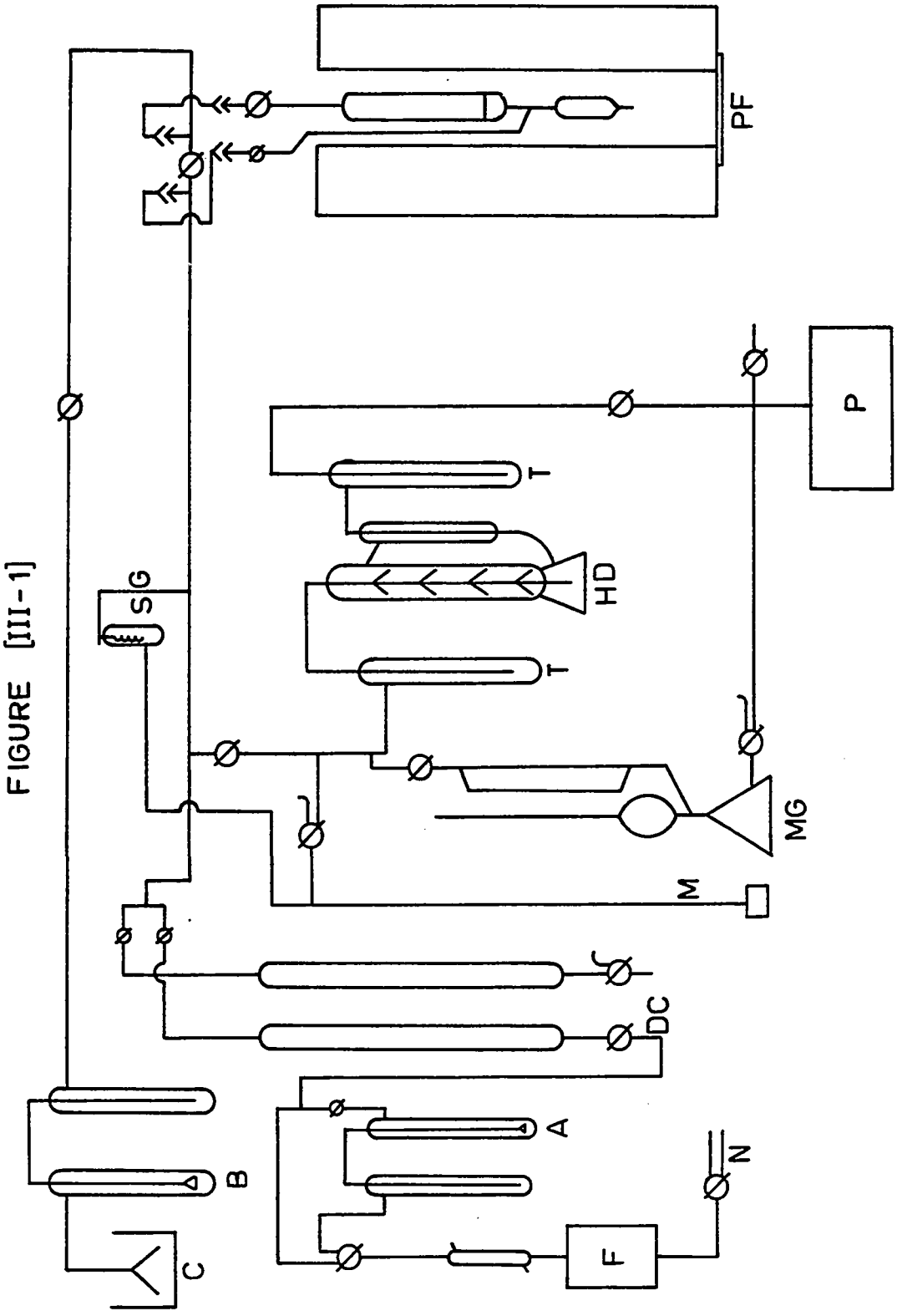

FIGURE [III-1]

1-2b Purification Apparatus

The filtration vessel is shown in Figure [III-2]. With the exception of the stopcocks and cones at the top, the apparatus was made from 'Spectrosil' silica. It consisted of a main chamber of a 160 mm length of 33 mm I.D. tubing joined at the lower end to a 40 mm length of 25 mm I.D. tubing and separated from it by a fine sintered glass disc. A side arm of 6 mm I.D. tubing joined the main section below the sinter and was held rigidly to it with silica bridges.

The silica crystal growing ampoule is shown in Figure [III-3]. It was 140 mm in overall length having a growing chamber ~76 mm long, 28 mm O.D. with the bottom tapering at an angle of 35-45° to end in a pip 12 mm long and 5 mm O.D. The ampoule was attached to the filtration vessel by a length of 8 mm I.D. tubing. Both the ampoule and filtration vessel were made to specification by Jencons Scientific.

The glassware was thoroughly cleaned before use. The filtration vessel was immersed in concentrated nitric acid for 20-30 minutes, rinsed in deionized water, then triply distilled water, drained well and left in an annealing oven overnight. The ampoule was cleaned with a stock mixture of 10% HF, 40% HNO_3, and 50% H_2O by weight for 15 minutes, rinsed with deionized water and left standing in deionized water overnight. The following day, it was given a final rinsing with triply distilled water, allowed to drain, and then blown onto the filtration vessel. After the ampoule had been attached, the filtration apparatus was rinsed with nitric acid, followed by deionized and triply distilled water and drained. The apparatus was then positioned in the purification furnace and dried under vacuum at 120 °C until the pressure in the system was less than 5×10^{-5} torr.

FIGURE [III-2]

FILTRATION VESSEL

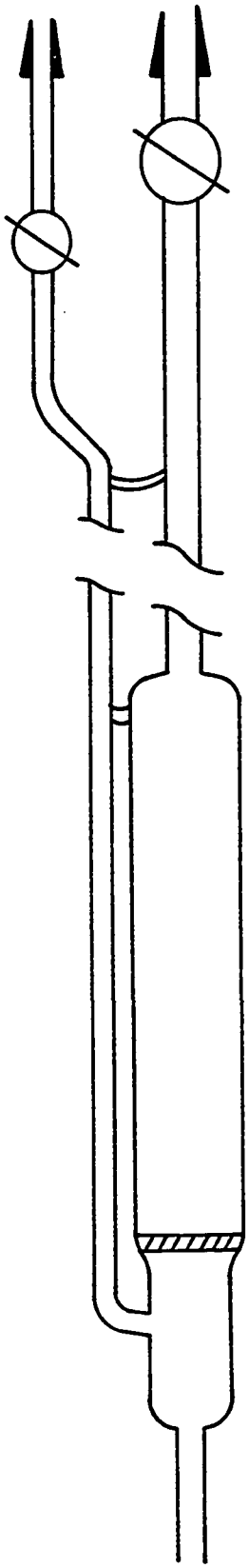

FIGURE [III-2]

FIGURE [III-3]

CRYSTAL GROWING AMPOULE

The ampoule was made entirely from silica.

FIGURE [III-3]

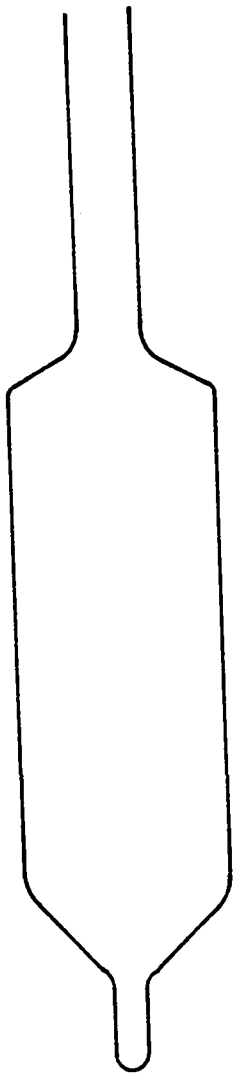

1-2c Vacuum System

The vacuum system, Figure [III-1], consisted of a Precision rotary oil pump, (P), a mercury diffusion pump, (HD), protected on each side by liquid nitrogen traps, (T), and a McLeod gauge, (MG). The main part of the system contained a nitrogen gas inlet, (N), a furnace, (F), in which copper gauze was heated to 500 °C, a trap, (A), fitted with a sinter for the admission of bromine, two drying columns, (DC), filled with a 3:1 mixture of anhydrous barium perchlorate and anhydrous magnesium perchlorate packed at each end with glass wool, a spiral gauge, (SG), with one side connected to a mercury manometer, (M), the filtration apparatus positioned in the purification furnace, a sulphuric acid trap, (B), followed by a water trap, (C). All taps and joints in the main section were greased with Kel-F, a fluorinated hydrocarbon supplied by Minnesota Mining and Manufacturing Co. The taps and joints in the pumping section were greased with Apiezon M grease since this section could be isolated from the main line.

1-2d Purification of the Melt

After cooling, the filtration apparatus was detached from the line and filled with 50 g of powdered, oxine extracted, potassium bromide using a long funnel to ensure that the salt entered the main chamber above the sinter. After removing any salt adhering to the stopcocks and wiping the outside with alcohol, the apparatus was sealed to the vacuum line with picein. The salt was heated to 120 °C under vacuum and left overnight. The temperature was raised in stages to 400 °C while maintaining a line pressure of 10^{-5} torr or less. At 400 °C the main line was isolated from the pumps and nitrogen which had been

purified over hot copper and dried was admitted until the pressure in the system was 1 atm. The nitrogen flow rate was reduced to 1-2 bubbles per second through the sulphuric acid bubbler, (B). When the temperature reached 550 °C, the nitrogen gas was forced down the narrow tube of the filtration apparatus and up through the KBr powder by closing tap 9. At 650 °C, HBr from a Matheson lecture bottle was admitted through one of the drying columns. The temperature was then raised to 770 °C to melt the KBr, (m.p. 730 °C), and HBr was passed through the melt for two hours at the rate of 1 bubble per second through the sulphuric acid bubbler. The melt was then treated for 30 minutes with a N_2/Br_2 gas mixture obtained by bubbling nitrogen gas through liquid bromine in trap A and passing the gas through a drying column. After the HBr, N_2/Br_2 gas treatment, the entire system was flushed with pure, dry nitrogen until there was no trace of bromine colour left. The molten salt was filtered into the crystal growing ampoule by creating a vacuum on the ampoule side of the sinter and then cooled to room temperature under an atmosphere of dry nitrogen.

1-3 Doping with TlBr

Two approaches were used for doping with TlBr. In the first, 0.03 mole % TlBr was added to the KBr before the purification of the KBr melt. Since the boiling point of TlBr (m.p. 480 °C) is 815 °C, the vapour pressure of thallous bromide is large at the temperature at which the purification of KBr was carried out, 740-750 °C, and much of the TlBr would be lost by evaporation. The appearance of a film of yellowish powder in the cool portion of the filtration apparatus supported this. In the second method, the TlBr was added after the

purification of the KBr was completed and the melt had cooled to room temperature, thereby eliminating the loss of TlBr which occurred in method one. A minor disadvantage is that the TlBr was not subjected to the treatment with HBr and Br_2. In either method, the crystal growing ampoule containing a mixture of nitrogen and hydrogen bromide in the approximate ratio of 3:1 at a total pressure of ~0.3 atm was sealed off at room temperature. This was calculated to give a pressure of 1 atm at the growing temperature. Both methods gave satisfactory results although the doping level was lower using the first method.

1-4 Crystal Growth

The crystals were grown using the Stockbarger technique. The furnace, Figure [III-4], consisted of a core of silica tubing surrounded by firebrick and mounted vertically in a box 20 in × 20 in × 22.5 in made from 0.25 in thick transite sheet bolted to a steel frame. The silica core consisted of two tubes; the one, (T_1), 22 in long 2.90 in O.D., was wound with heating tape and the other, (T_2), 10 in long 2.33 in O.D., was a sliding fit in the larger tube.

The top two inches of the furnace tube were left bare. The remaining 20 in were divided into two 10 in sections each wound with 7 ohms of Hoskins Chromel 'A' tape (0.188 in × 0.113 in; 0.239 Ω/ft). The total resistance of each half was split into two sections of ~2 ohms and ~5 ohms resistance, Figure [III-5], and an external variable resistance, (0-80 Ω), was connected in parallel with the 5 ohms furnace resistance. The two halves of the furnace were connected in series and the voltage supplied to each half was controlled by a powerstat.

The shorter inner tube supported a nickel baffle, (N). To permit

FIGURE [III-4]

CRYSTAL GROWING FURNACE

T_1 - silica tube

T_2 - silica tube

N - nickel baffle

D - silica disk

R - stainless steel rod

H - crystal growing ampoule holder

S - transite sheet

P - firebrick plug

FIGURE [III-4]

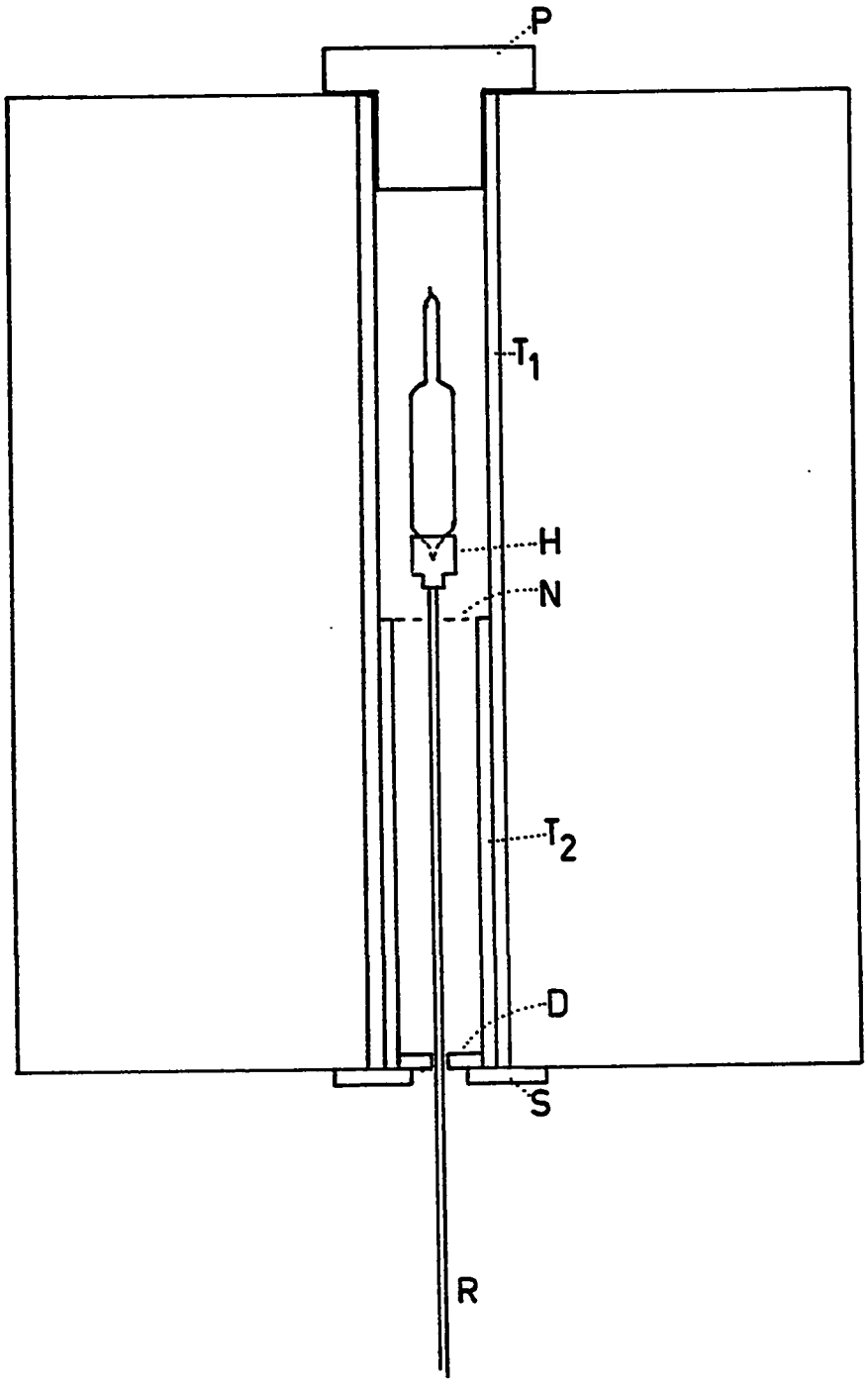

FIGURE [III-5]

POWER CIRCUIT

FOR

CRYSTAL GROWING FURNACE

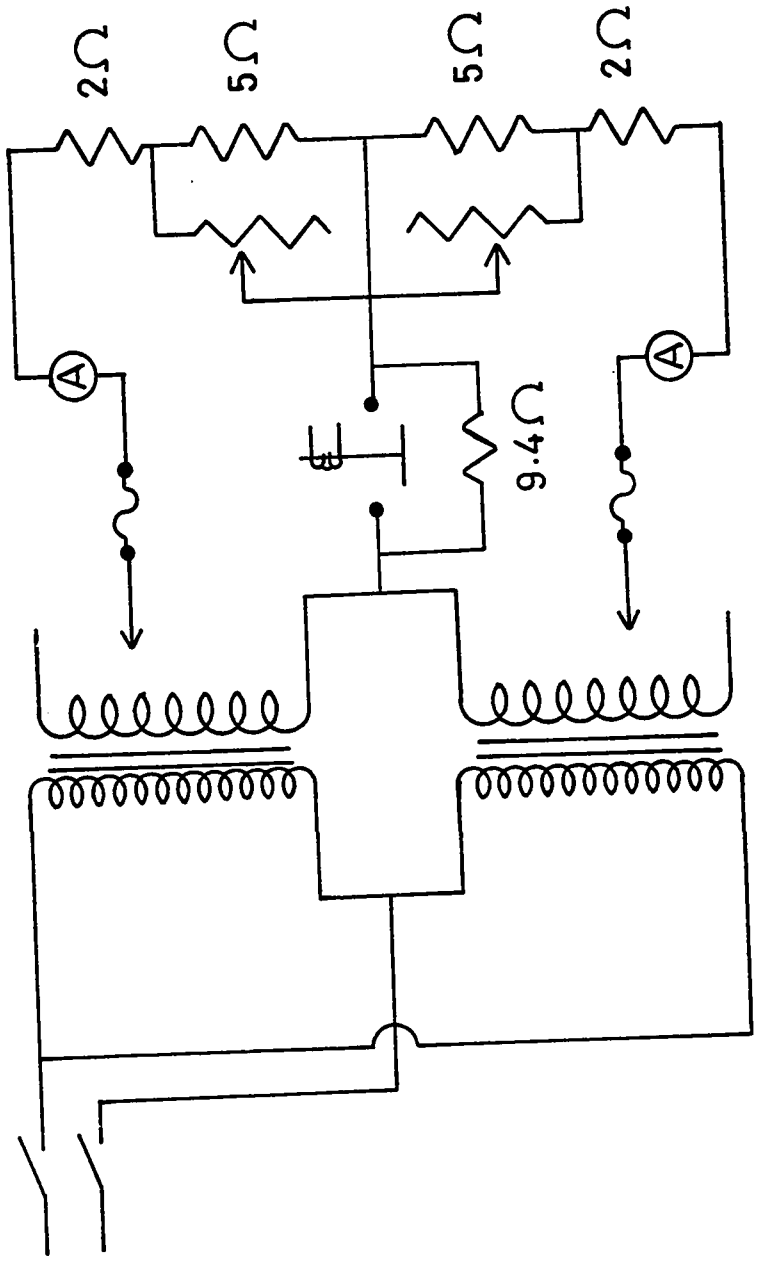

FIGURE [III-5]

visual inspection of the furnace, the bottom of the tube was fitted with a transparent silica disk, (D), drilled to accommodate the stainless steel rod, (R), used to support the crystal growing ampoule holder, (H), Figure [III-4]. The tubing and disk were held in place by a removable piece of transite sheet, (S), containing a central hole.

Two firebrick plugs, (P), were made to fit the top of the furnace. One was drilled out to allow for insertion of a thermocouple and the other was solid for use when the thermocouple was not in place. Temperature control was provided by a thermocouple sensor and Thermovolt controller as for the purification furnace.

The crystal growing ampoule was cemented vertically in a nickel holder tapered to fit the bottom of the ampoule and fitted with a stainless steel shaft so that the entire assembly could be lowered by means of an electrical motor. The ampoule was positioned centrally in the furnace with the bottom of the holder 3 cm above the baffle. By careful adjustment of voltages and resistances, a temperature gradient of 30 degrees per centimeter across the baffle was maintained. The temperature profile of the furnace was such that the melting point of pure KBr occurred just above the baffle. The crystal was lowered at a rate of ~4 mm per hour until the top of the crystal growing ampoule was just below the baffle. When growth was complete, the furnace temperature was lowered to 200 °C and the crystal allowed to cool slowly. Finally, the furnace was switched off and the ampoule removed when room temperature had been attained. A visual inspection of the ampoule showed a transparent, apparently single crystal, free from the sides of the ampoule, ~1.5 in long with a slight conical

depression at the top. Samples for optical measurements were cleaved from the central portion of the crystal.

2. Cryostats

In order that optical measurements could be made at different temperatures, two variable temperature cryostats of commercial design were used: a 'Select-A-Stat' research dewar manufactured by Sulfrian Cryogenics; and a 'Versa-Stat' dewar made by Cryogenics Associates Limited.

Both cryostats were similar in their basic design and consisted, Figure [III-6][67]of an upper canister, (N), used as a liquid nitrogen jacket, and a lower reservoir, (H), for liquid nitrogen or liquid helium. These were suspended in a jacket which could be evacuated and which was equipped with electrical ports, (E), for instrumentation, liquid feed throughs and vents, (F), and pressure relief valves. A demountable tailpiece provided access to the controlled temperature block, (B).

Cooling was achieved by using a heat exchanger. Liquid refrigerant siphoned from the bottom of the lower reservoir through 0.125 in O.D. thin walled tubing and evaporated. The cold gas passed through a coil wrapped around the block and was vented out the top of the cryostat through a micrometer needle valve, (M), which regulated the flow of gas.

A copper crystal holder, Figure [III-7], was fitted to the bottom of the controlled temperature block. A piece of 0.005 in thick pure indium foil was squeezed between the block and holder to ensure good thermal contact. Crystal samples were cleaved with a razor blade to a size approximately 6 mm × 10 mm × a thickness which depended upon the concentration of impurity. The crystal was mounted in the holder in

FIGURE [III-6]

VARIABLE TEMPERATURE CRYOSTAT

N - liquid nitrogen reservoir

H - liquid helium reservoir

E - electrical ports for instrumentation

F - liquid feed throughs

M - micrometer needle valve

B - controlled temperature block

FIGURE [III-6]

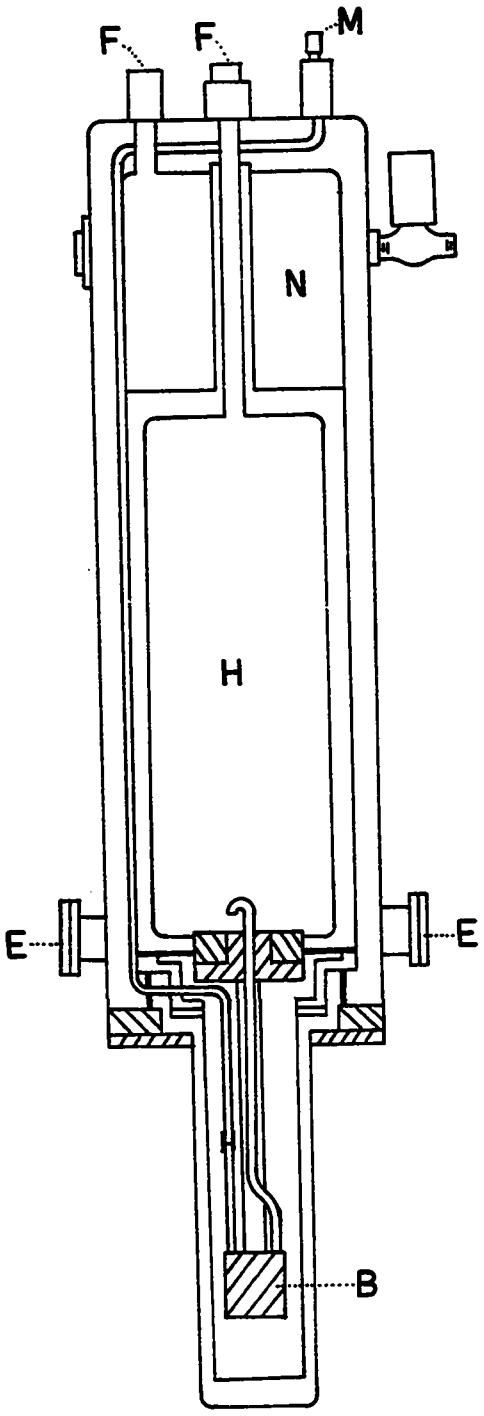

FIGURE [III-7]

CRYSTAL HOLDER

The crystal holder was made from pure copper.

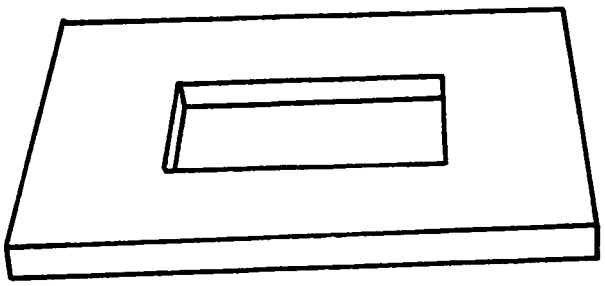

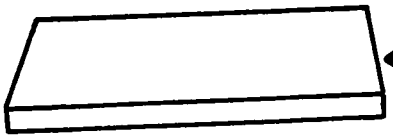

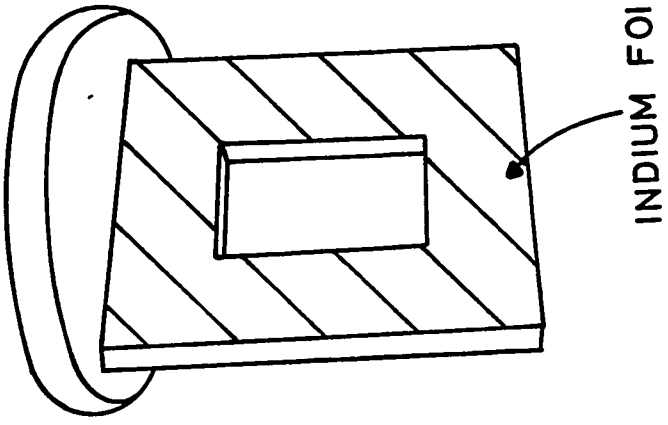

FIGURE [III-7]

the following manner. To enhance thermal contact, a piece of indium foil was pressed against the fixed plate of the holder and the crystal was placed against the foil. The second plate was attached using four screws tightened so that the crystal was mechanically secure without introducing unnecessary strain. Two radiation shields surrounded the crystal holder. The cryostat tailpiece was made with four windows spaced at ninety degrees, so that both absorption and emission measurements could be done without changing the crystal.

Temperature control was obtained by balancing the cooling available from liquid feed against continuous heat from a heater wound on the controlled temperature block. A regulated voltage was supplied by a powerstat and the current was measured with a milliameter. The temperature was monitored with a gold/0.03 atomic % iron vs. chromel thermocouple attached to the top of the crystal holder. The voltage across the thermocouple was measured using a potentiometer (H. Tinsley and Co. Ltd.). The null point was detected by a galvanometer (Guidline Instruments Ltd.) with a sensitivity of 500 mm/μA, nominal resistance 550 ohms. The voltages were converted to temperatures using the data given by Berman and Brock[68]. The thermocouple was calibrated at three temperatures; the melting point of ice, the sublimation point of dry ice and the boiling point of liquid nitrogen, to determine any correction factor.

3. Vacuum Line

The vacuum line used for pumping out the cryostats is shown in Figure [III-8]. With the exception of the flexible metal coupling, (C), the system was made of glass and was capable of attaining a pressure of $\sim 10^{-6}$ torr. A Precision rotary oil pump, (P), served as backing pump for the mercury diffusion pump, (HD), which was protected on either side by liquid nitrogen traps, (T_1 and T_2). The pressure was measured with a McLeod gauge, (MG). Connection to the cryostat was made via an Edwards High Vacuum flexible coupling, (C), and a glass ball joint, (BJ). This arrangement allowed the vacuum to be broken readily at the ball joint without the necessity of opening the entire vacuum system to air.

4. Temperature Control

4-1 Measurements above 77 K

The following procedure was used to make measurements between liquid nitrogen temperature and room temperature.

After mounting the sample in the crystal holder, the cryostat was reassembled, placed in either the absorption or emission sample compartment, and attached to the vacuum line. The external connections for the heater and thermocouple were made and the system was evacuated to a pressure of the order of 10^{-6} torr. A room temperature spectrum was recorded. The liquid nitrogen shield reservoir was then filled with liquid nitrogen and at the same time the heat exchanger was flushed with dry nitrogen gas to ensure that the system would remain ice free. The inner container was then filled with liquid nitrogen. The liquid nitrogen filling port was closed off and the micrometer regulated vent opened to force liquid nitrogen through the heat exchanger.

FIGURE [III-8]

VACUUM LINE FOR CRYOSTAT EVACUATION

p - oil pump

HD - mercury diffusion pump

T - liquid nitrogen traps

MG - McLeod gauge

C - flexible metal coupling

BJ - glass ball joint

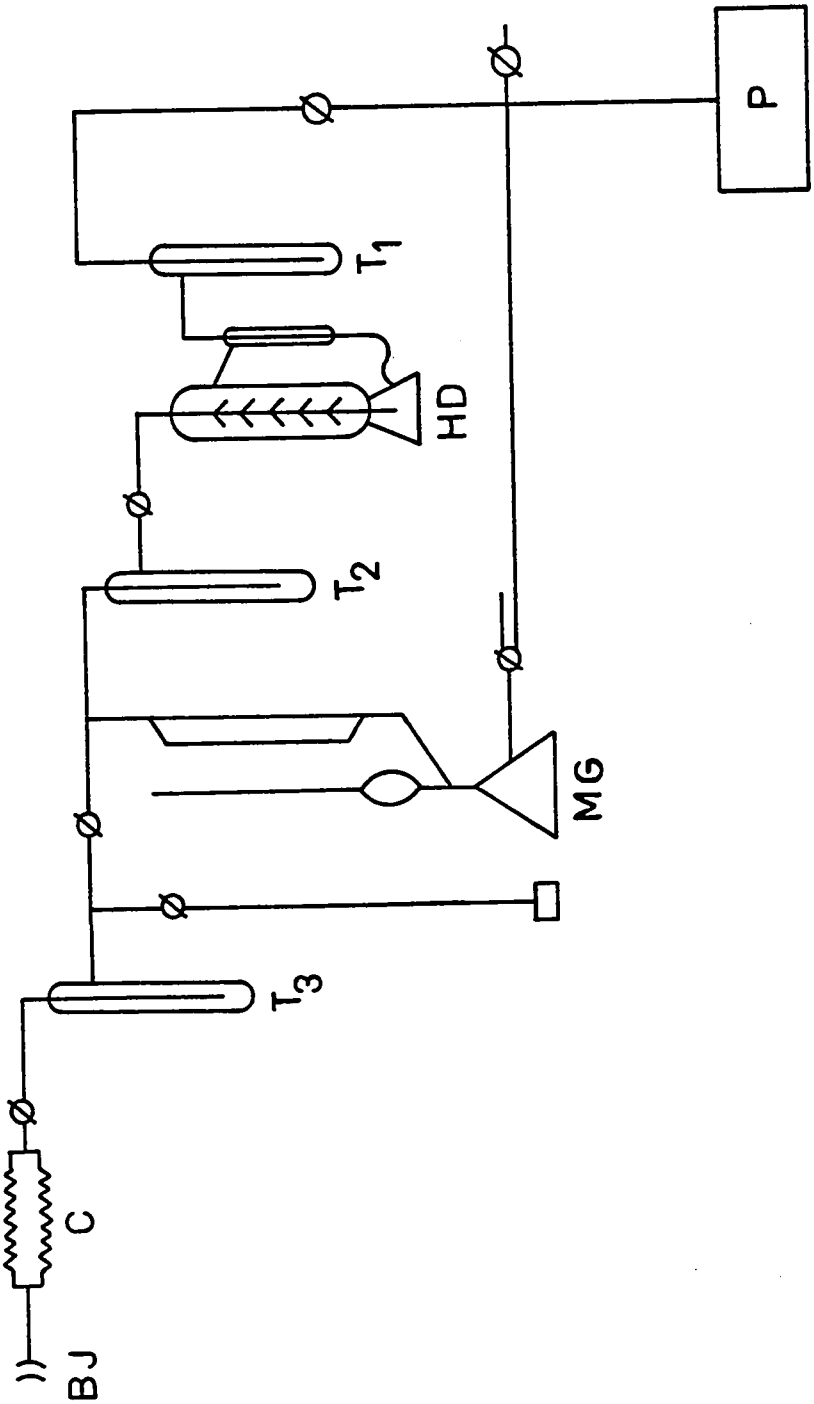

FIGURE [III-8]

The temperature was monitored until the minimum temperature was reached. This was 5-6 K above the boiling point of liquid nitrogen because of thermal radiation from the surroundings. After the block temperature stabilized, the liquid nitrogen reservoirs were topped up, all valves were closed and the system was left overnight.

The next day, the reservoirs were again topped up with liquid nitrogen and the block recooled to the minimum temperature attainable, by opening the micrometer valve, (M), Figure [III-9], fully.

A spectrum at this temperature could now be recorded. In order to obtain spectra at additional temperatures, the temperature was raised by reducing the flow of gas through the heat exchanger and by passing a constant AC current through the heater. By carefully balancing these two variables, the thermocouple voltage could be maintained to within 15 μV of a desired voltage which corresponded to a temperature variation of ±0.6 K. The series of spectra were taken in continuous sequence from 83 K to room temperature.

If a liquid helium run was to be done immediately, the block was recooled with liquid nitrogen. Otherwise, the cryostat was allowed to warm up on its own.

4-2 Measurements below 77 K

In order to achieve temperatures below 77 K a more complicated procedure was required.

After the cryostat was thoroughly precooled with liquid nitrogen, any liquid nitrogen which remained in the inner reservoir was pumped away. The heat exchanger and liquid helium chamber were purged with dry helium gas. Care was taken to avoid warming the controlled

FIGURE [III-9]

LIQUID HELIUM TRANSFER

V - valve

M - micrometer valve

G - pressure gauge

T - transfer tube

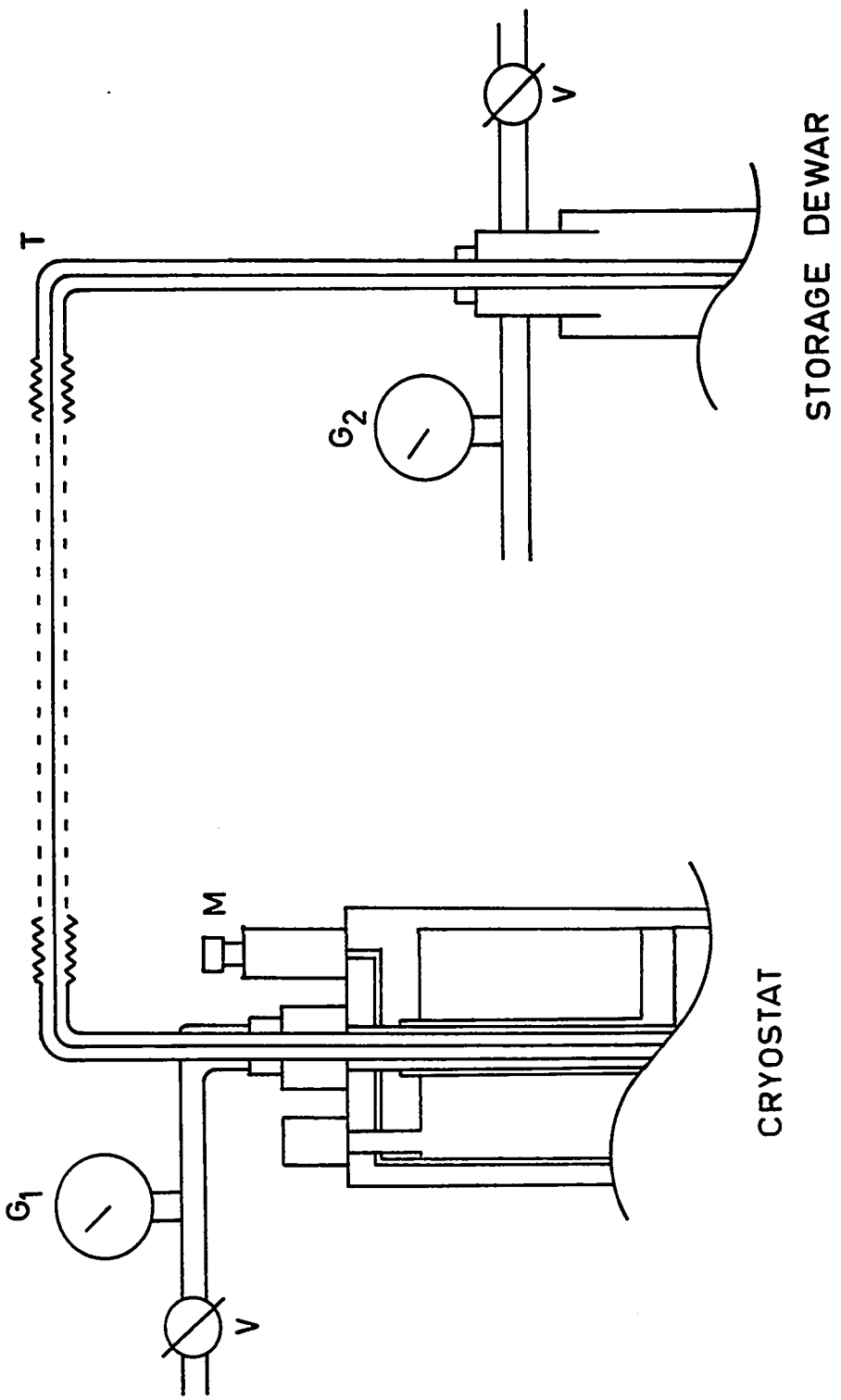

FIGURE [III-9]

temperature block too much since the amount of liquid helium required for cooling increased rapidly with increasing initial temperature of the block.

The liquid helium transfer tube, (T), consisted of a continuous thin-walled stainless steel tube 0.125 in in diameter sealed inside a U-shaped casing 0.375 in O.D., Figure [III-9]. The outer tubing of the cross piece was made of crimped stainless steel to give some flexibility to the system. The space between the tubes was evacuated. Before use, the transfer tube was flushed with dry helium gas.

The transfer tube was eased gently into both the storage dewar and the inner reservoir of the cryostat. The position of the storage dewar was altered to relieve any strain. While the transfer tube was lowered, the storage dewar was raised to keep the cross piece of the transfer tube horizontal. The transfer tube was lowered until its ends were ~1 cm from the bottom of each reservoir.

The cryostat was isolated from the vacuum line before the actual transfer was begun.

With the micrometer valve M (Figure [III-9]) on the cryostat closed, and valve V partially opened, the pressure in the storage dewar was raised with helium gas from a cylinder by 2.0-2.5 PSIG as indicated by gauge, G2. Under these conditions, the gauge, G1, on the cryostat vent will register 1.5-2.0 PSIG. For effective transfer a pressure difference of 5-8 oz across the system was maintained.

Fifteen minutes were allowed for cooling the reservoir itself before diverting part of the flow of cold gas through the heat exchanger by reducing the flow through V and opening M fully. The crystal holder

cooled slowly at first and then very rapidly reaching a minimum temperature of 15 K after approximately ten minutes.

In the range 15-49 K, the temperature of the crystal holder was controlled accurately by regulating the rate of flow of cold gas through the heat exchanger with the needle valve, M. In order to maintain the low temperatures it was necessary to transfer slowly so that there was no significant accumulation of liquid helium in the cryostat. If too much liquid helium was present, the rate of flow of cold gas could not be maintained and the temperature rose.

In order to stabilize at temperatures above 50 K, an accumulation of 300-400 ml of liquid helium in the cryostat was desirable. In this situation, the temperatures could be achieved readily by supplying a small quantity of heat until the desired temperature was reached. The heater could then be shut off and the temperature maintained by adjusting the micrometer valve. In the absence of liquid helium in the cryostat reservoir in this temperature region, a temperature variation of 1-2 K occurred during the time required to record a complete spectrum.

Measurements were taken at temperature intervals to 86 K providing an overlap region with results using liquid nitrogen. On completion of the run, the transfer tube was removed and the cryostat left to warm to room temperature.

5. Measurement of Optical Absorption

The instrument used for the measurement of optical absorption was a Cary Spectrophotometer, Model 14R, (Cary Instruments Ltd.) which is basically designed for the automatic recording of absorption spectra in the ultraviolet, visible and infrared regions. A schematic of the

optical system is shown in Figure [III-10][69].The spectrophotometer employs a double monochromator consisting of a 30° fused silica prism, (P), in series with an echelette grating, (G), each with its own collimating mirrors, (C), and slit system, (S). Interchangeable light sources for the instrument are a deuterium lamp, (D), a high intensity tungsten lamp, (T_1), for the visible region and a tungsten lamp, (T_2), for the near infrared region. Three detectors are provided; a RCA 1P28 photomultiplier, (A), for the ultraviolet and visible regions, a lead sulphide cell, (B_1), for infrared, and a special filter and lead sulphide cell, (B_2), also for infrared measurements.

The sample compartment was modified to accommodate the cryostats. The normal sample compartment cover was replaced by a plate having a light-tight collar which supported the cryostat vertically and which could be moved horizontally in one direction. The collar was designed so that the crystal was positioned centrally with respect to the height of the light beam and in the middle of the light path through the compartment. The entire cryostat could be moved across the light beam so that the absorbance in a transparent region of the sample could be minimized. A stop fitted with a micrometer head enabled precise relocation of the cryostat.

For absorption measurements the instrument was used in double beam mode and the response of the spectrophotometer was adjusted via the multipots to zero absorbance when both the sample and reference compartments were empty. Since the region of interest was the ultraviolet, the optical system was flushed with dry nitrogen gas to minimize interference from absorption by oxygen.

FIGURE [III-10]

OPTICAL SYSTEM

OF

CARY SPECTROPHOTOMETER

See text for explanation of symbols.

FIGURE [II-10]

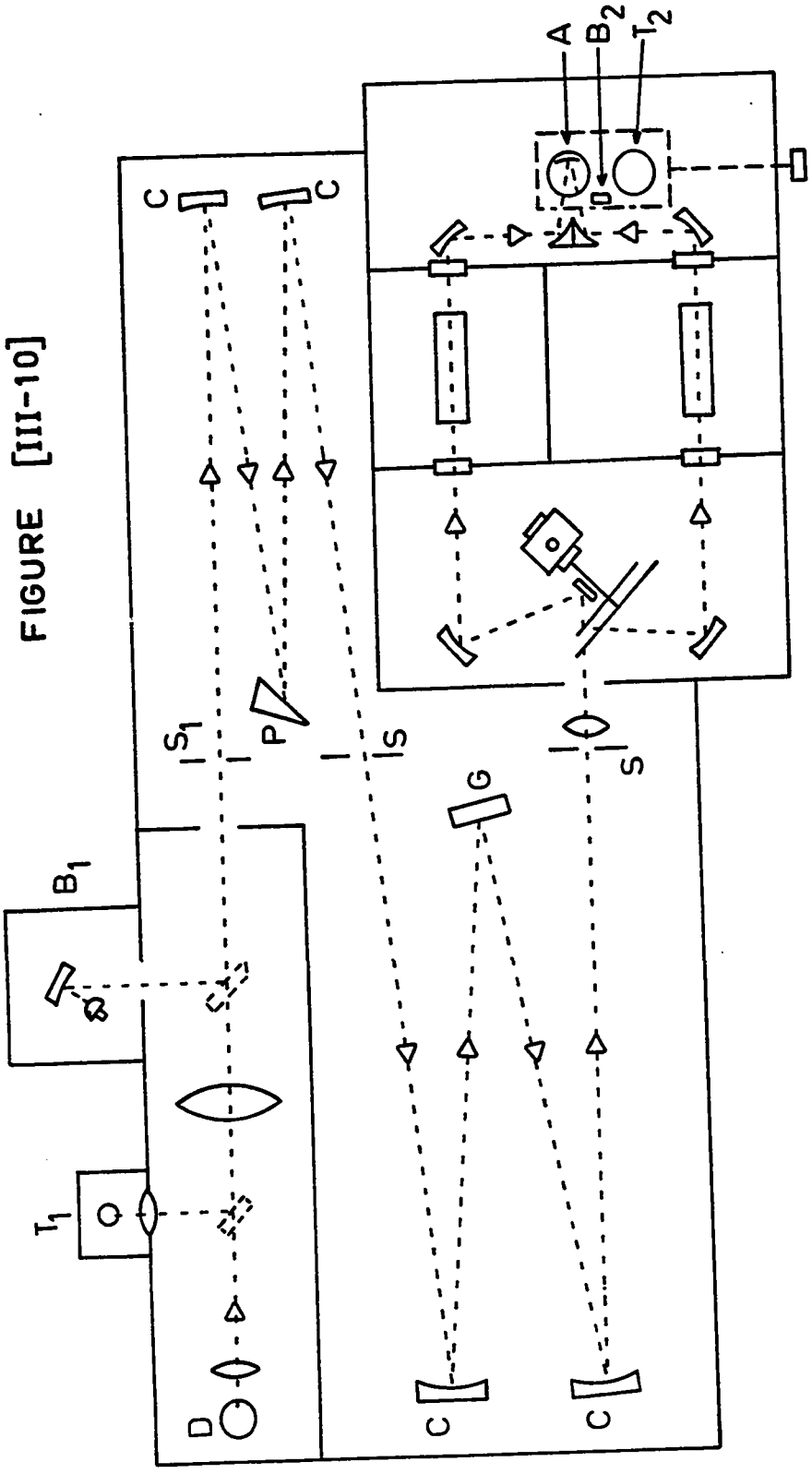

A warm up time of at least 30 minutes was allowed for the electronic components to stabilize. The voltage on the photomultiplier, the slit control setting and the scan speed were chosen for optimum signal to noise ratio within the restriction that the spectral band width passed by the spectrophotometer was narrow compared to the natural band width of the absorption band. This ensured that the recorded peak height was greater than 99.5 % of the true value [70].

All measurements were made on samples in an evacuated cryostat. The experimental results were recorded on the strip chart recorder as the wavelength region was scanned continuously.

6. Emission Measurements

An experimental luminescence system consists basically of a high intensity source from which a nearly monochromatic beam of radiation of suitable wavelength is selected. The exciting radiation is then focused on to the sample and the emission is observed at right angles to the excitation to avoid interference from it [71].

The available fluorescence accessory for the Cary was inadequate for the type of measurements to be made since the sample could not be cooled and the excitation wavelength in the ultraviolet was restricted to the two strong lines of a mercury arc.

An optical system for luminescence measurements was designed which would; (i) provide an independent and flexible means of exciting the sample

(ii) use the Cary spectrophotometer for analyzing the emitted light

(iii) cause minimum interference with the normal absorption operation of the instrument.

6-1 Excitation System

Since the wavelength region beyond 1.5 μ was not relevant to the work, the infrared detector, (B_1) Figure [III-10], situated at the back of the spectrophotometer was removed. This provided optical access to the entrance slit, (S_1), of the double monochromator.

The optical components were chosen for minimum loss of light intensity and maximum light gathering power. A properly evaporated aluminum film will give ~90% of the incident intensity on reflection, whereas a silica lens will provide only 50-60% transmission depending on its thickness [72].

In order to obtain the maximum efficiency in the light gathering power of the Cary, it was necessary to just fill the first collimating mirror, (C_1) Figure [III-11]. This was achieved by making the aperture ratio of the component which focuses the light emitted from the sample onto the slit the same as that of the mirror C_1, i.e. f/8. A 3 in diameter front surface aluminized concave spherical mirror, (CM), (John Unertil Optical Co.) with focal length of 10 in and effective diameter 2.5 in was chosen, Figure [III-11]. The mirror was placed 20 in from both the sample crystal and the entrance slit so that; (i) the image of the crystal on the entrance slit would not be magnified and (ii) the optics at the slit would be f/8.

A housing for this system was built from 3/4 in plywood and was equipped with a slide which would isolate it optically from the Cary. The inside of the compartment was painted a matt black to minimize light scattering. The optical components were mounted on a base plate of 1/2 in aluminum which had been sand blasted. Mounts for the mirrors

FIGURE [III-11]

OPTICAL SYSTEM

FOR

EMISSION MEASUREMENTS

See text for explanation of symbols.

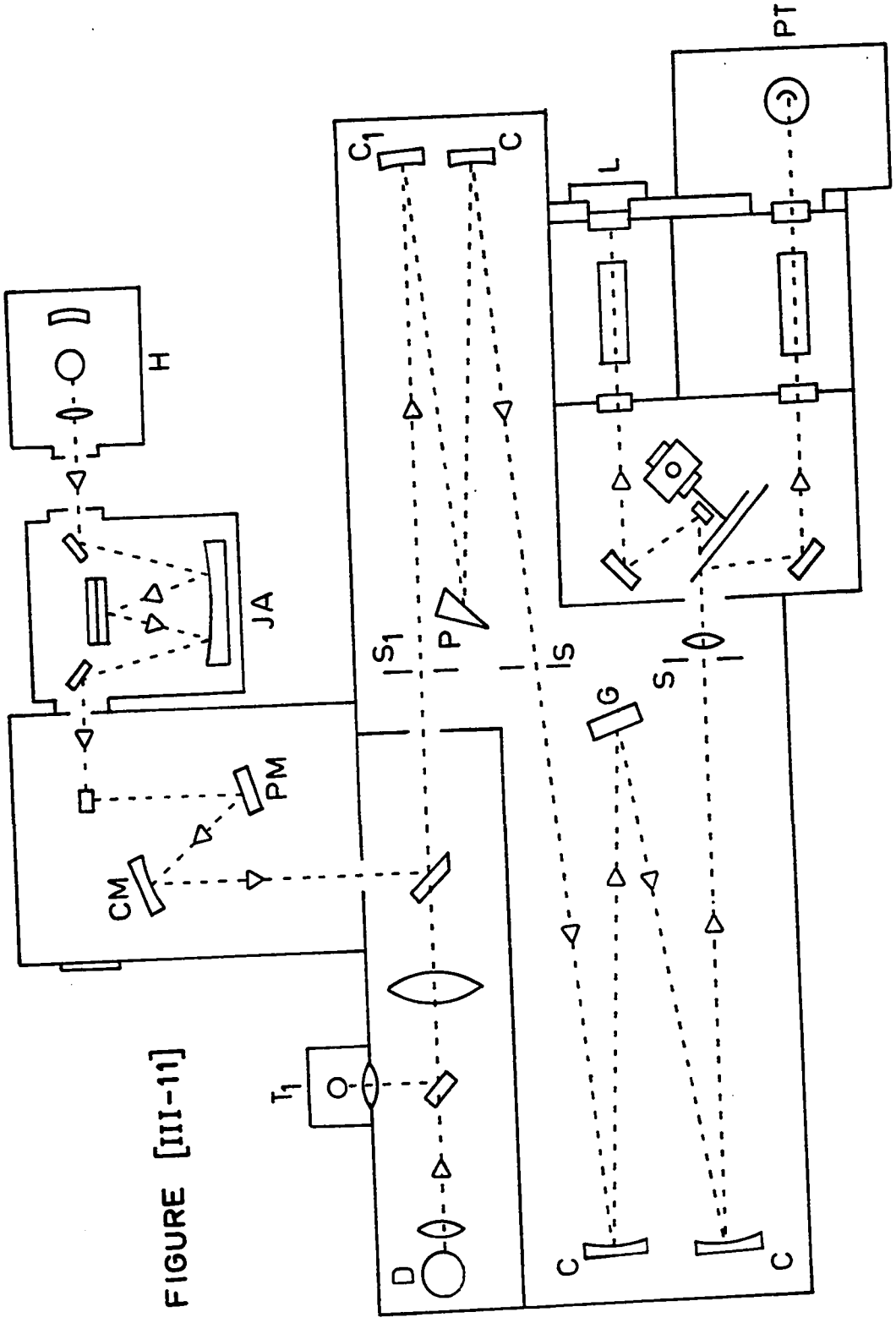

FIGURE [III-11]

were made from meccano parts and precision graduated mechanical microscope stages (Edmund Scientific Co.) to obtain facility for rotation, and X and Y movement necessary for critical focusing.

The sample itself was mounted in a variable temperature cryostat which in turn was supported vertically by a collar on plates which could be moved horizontally at right angles to each other. Mechanical stops fitted with micrometer heads enabled precise location of the cryostat.

A 200 watt mercury arc lamp, power supply and lamp housing, (H), Model M-701, was purchased from P.E.K. Labs Inc. The housing was equipped with an adjustable concave mirror for reflecting forward the light emitted backwards by the arc. The front opening was supplied with an iris diaphragm for use as a field stop. A silica lens of aperture ratio, f/3.5, (Thermal Syndicate Ltd.) was added between the arc lamp and the diaphragm to focus the source on to the entrance slit of a Jarrell-Ash quarter-meter grating monochromator, (JA), (Jarrell-Ash Co. Ltd.), Figure [III-11], which was used to select a suitable wavelength for excitation.

In addition to the P.E.K. 200 W Hg arc, a General Electric HA4 (100 W) Hg arc, and Osram Cadmium and Zinc 18 W lamps were acquired. An accurate wavelength calibration of both the Jarrell-Ash monochromator and Cary spectrophotometer was done using the G.E. HA4 Hg lamp and literature values for the wavelengths of the strong lines of a mercury arc [73].

Test measurements on a crystal of thallium doped potassium chloride[74] showed that the method of excitation was satisfactory, but that the

standard detector in the Cary spectrophotometer was inadequate for obtaining spectral traces accurate enough for mathematical analysis.

6-2 Modification of the Detection System

Because of the very low level of intensity of the emitted light, the standard RCA 1P28 photomultiplier had to be operated at maximum sensitivity in order to obtain a spectral trace. Under these conditions, the noise level in the detector was high and the signal to noise ratio was very unfavorable. A variable pen period control was obtained [75]. This accessory provided pen periods of 5, 10 and 20 seconds in addition to the standard pen period of 1 second. The signal to noise ratio could be increased by a factor equal to the square root of the increase in pen period[76].This modification gave some improvement but useful spectral data still could not be obtained. The entire Cary detector unit was then removed and a new system was designed, (PT) Figure [III-11].

The Cary signal recording system was modified to accept the output of an EMI 6255S thirteen stage photomultiplier whose anode to cathode voltage could be varied continuously from 0 volts to the specified limit of 1780 volts by a Harrison high stability D.C. power supply, Model 6110A. The photomultiplier was mounted in a refrigerator chamber purchased from Products for Research Inc. The dynode resistance chain was designed to give simple linear gain.

For the particular peak under investigation, spectral traces with good signal to noise ratios could now be obtained by adjusting the pen period and overall photomultiplier voltage.

6-3 Initial Focusing

Concave mirror, (CM), and plane mirror, (PM), Figure [III-11], were placed as closely as possible to their calculated positions. A ground glass screen took the place of the crystal sample. With the Cary monochromator set for 540 nm, and using the tungsten source, (T_2) Figure [III-10], the positions of the mirrors were refined until a non-magnified sharp image of the slit S_1 was formed on the screen. The image of the slit at CM was checked to ensure that it was not larger than the aperture of the mirror. To ensure that the light was not tilted out of horizontal, it was necessary that the mirrors be perpendicular to the centre of the beam.

6-4 Calibration of the Optical System

6-4a Theory [77]

An emission spectrum is in general a plot of luminescence intensity, measured in quanta per unit frequency interval, vs. frequency. If Q is the total number of quanta emitted per unit time in all frequencies, then $dQ/d\nu$ is a measure of the intensity at frequency ν. The true emission spectrum is obtained by plotting $dQ/d\nu$ against ν.

If the fluorescence of a sample is measured using a photomultiplier at constant sensitivity and a monochromator scanned at constant slit width, then the curve obtained is an apparent emission spectrum. In order to obtain a true spectrum, the experimental curve must be corrected for three frequency-dependent effects: (1) the change in the quantum efficiency of the photomultiplier; (2) the change in the band width of the monochromator arising from the frequency dependence of the linear dispersion; and (3) the transmission of the monochromator.

Thus, $A_\nu = (dQ/d\nu)(P_\nu B_\nu L_\nu) = (dQ/d\nu)(S_\nu)$ [III-1]

where A_ν is the observed photomultiplier output

P_ν is the relative quantum efficiency of the photomultiplier

B_ν is the relative band width at constant slit width

L_ν is the fraction of light transmitted by the monochromator.

$(dQ/d\nu)$ is the true emission spectrum and can be calculated from the observed spectrum by dividing the measured intensity at each point by the corresponding value of S_ν. S_ν is the spectral sensitivity factor for the optical system and is proportional to the output obtained if a source of constant spectral intensity is used to illuminate the entrance slit.

If a source of known spectral distribution is used to fill the collimator with light, and the photomultiplier response R_{s1} is measured as a function of frequency, then

$$S_\nu = R_{s1}/(dQ/d\nu)_{s1} \qquad \text{[III-2]}$$

where $(dQ/d\nu)_{s1}$ is the known spectral distribution of the standard source.

Calibration data for standard lamps are generally given in energy units per unit wavelength interval. To convert from energy to quanta it is necessary to multiply by the wavelength, λ, and to convert from unit wavelength interval to unit frequency interval it is necessary to multiply by λ^2. Thus

$$(dQ/d\nu)_{s1} \propto \lambda^3 (dE/d\lambda)_{s1}$$

and

$$S_\nu \propto R_{s1}/[\lambda^3 (dE/d\lambda)_{s1}] \qquad \text{[III-3]}$$

Because the terms of the above equation are in relative units only, it is appropriate to normalize S_ν at some convenient wavelength.

6-4b Method

A National Bureau of Standards 1000-watt Quartz Iodide Lamp [78] calibrated in the wavelength region 250-750 nm was used as the standard of spectral irradiance for the determination of the spectral sensitivity factor, S_ν, of the system.

The analyzing system for the recording of emission spectra was set up in the same configuration as when the original spectra were obtained, Figure [III-12]. A front surfaced aluminized plane mirror, (M), was placed at a 45° angle in the position normally occupied by the crystal. It should be noted that the optical arrangement is such that light originating at this mirror is focused on the slit of the monochromator. A rectangular stop, (A), 6 mm × 20 mm, was placed at the opening to the compartment in order to reduce the amount of reflected light entering the optical system without violating the condition that the entrance slit, (S_1), of the spectrophotometer be filled completely with radiant flux from the standard lamp. The lamp, (S_2), was mounted according to the instructions provided, [79], and positioned at a distance of 50 cm from the centre of the image of the entrance slit on the plane mirror, (M). The circuit, Figure [III-13], used to provide the stable 8.30 amp A.C. current required for lamp operation was similar to that described in Stair et al [78]. T_1 and T_2 are 20 A variable auto transformers and T_3 is a 20 A, 12.6 V centre tap filament transformer.

The output of the photomultiplier was recorded as a function of wavelength in the region 250-450 nm for different values of photomultiplier voltage. In addition, a Corning 7-54 filter, (F) Figure [III-12], whose transmission characteristics had been measured was placed between the

FIGURE [III-12]

EXPERIMENTAL ARRANGEMENT

FOR

DETERMINATION OF SPECTRAL SENSITIVITY

M - front surface aluminized mirror

A - aperture stop

S - standard lamp

F - filter (Corning #7-54)

S_1 - entrance slit of spectrophotometer

FIGURE [III-12]

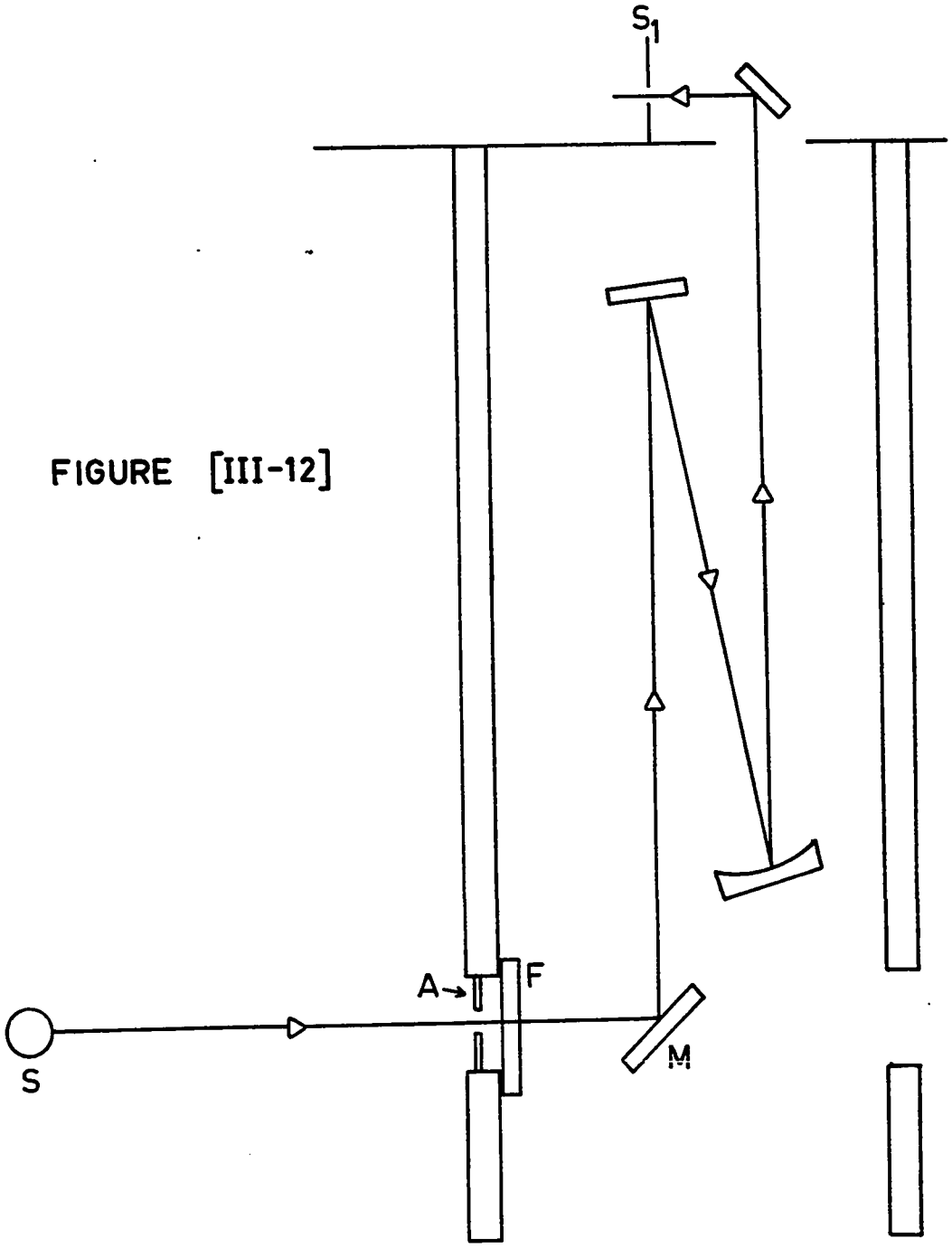

FIGURE [III-13]

POWER CIRCUIT

FOR

STANDARD LAMP

S - standard lamp

T - transformer

A - ammeter

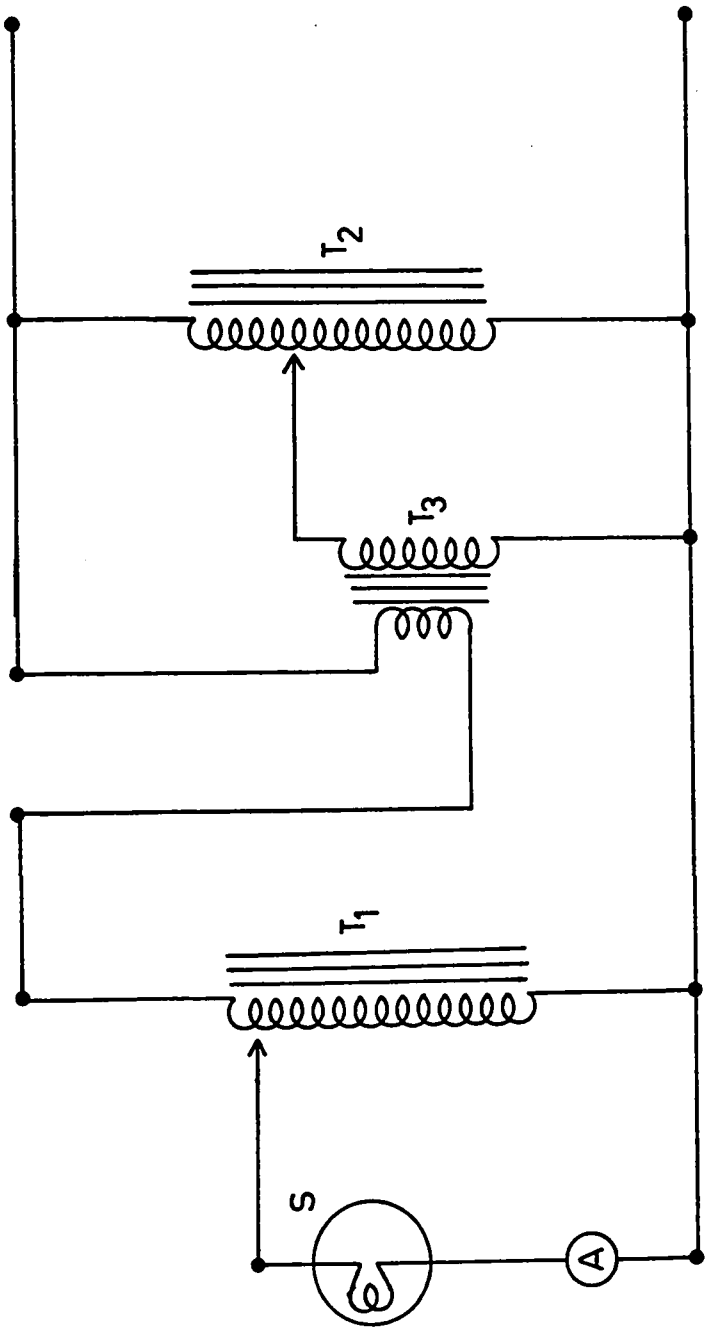

FIGURE [III-13]

aperture stop and the mirror. The photomultiplier response was measured again. It was found that the use of the filter to eliminate wavelengths longer than 450 nm reduced the stray light level considerably and gave more reliable and reproducible results.

The results are summarized in Table [III-1]. S_ν values normalized to 1.000 at 320 nm are plotted in Figure [III-14].

6-5 Experimental Procedure

Before an experiment was started, it was necessary to align the crystal properly. With the excitation source focused on the entrance slit, the Jarrell-Ash monochromator was set for ~540 nm. The cryostat could then be moved across the beam until the maximum amount of light passed through the side of the crystal. Then, with the Cary monochromator set at ~540 nm, an image of the slit, (S_1) Figure [III-11], was formed using a high intensity tungsten lamp at (L). The cryostat could then be moved so as to centre the image on the face of the crystal.

The Jarrell-Ash monochromator was reset to an appropriate excitation wavelength and the wavelength of maximum luminescence intensity was found. With the analyzing monochromator set at this wavelength, the crystal position was readjusted slightly to obtain the maximum signal possible. Results were recorded on the strip chart recorder while the wavelength region of interest was scanned continuously.

In general, best results were obtained with a voltage of 1000 V on the EMI photomultiplier and a pen period of 10 seconds. If the signal was particularly weak, the voltage on the photomultiplier could be increased at the expense of good signal to noise ratio.

TABLE [III-1]

SPECTRAL SENSITIVITY CORRECTION FACTOR

λ/nm	Calibrated Spectral Irradiance /W cm^{-2} nm^{-1}	Corning 7-54 filter % T	$\lambda(dE/d\lambda)$ /quanta cm^{-2} nm^{-1}	R_{s1}	S_ν /10^{-8}	S_ν normalized	$h\nu$ /eV
250	0.0171	54.6	2.334	0.003	2.056	0.948	4.958
60	0.0307	67.1	5.356	0.006	1.657	0.764	4.768
70	0.0531	73.75	10.057	0.010	1.297	0.598	4.591
80	0.0867	81.8	19.688	0.022	1.425	0.657	4.427
90	0.131	85.1	32.329	0.036	1.324	0.610	4.274
300	0.186	86.5	48.267	0.064	1.473	0.679	4.132
20	0.344	87.9	96.815	0.215	2.169	1.000	3.874
50	0.779	86.3	235.297	0.502	1.742	0.803	3.542
70	1.21	79.6	356.370	0.810	1.660	0.765	3.350
400	2.07	16.9	139.518	0.369	1.653	0.762	3.099
50	4.20	0.4	7.560	0.010	0.653	0.301	2.755

FIGURE [III-14]

CALIBRATION CURVE

Plot of spectral sensitivity factor against energy. The scale on the Y-axis indicates relative magnitude only.

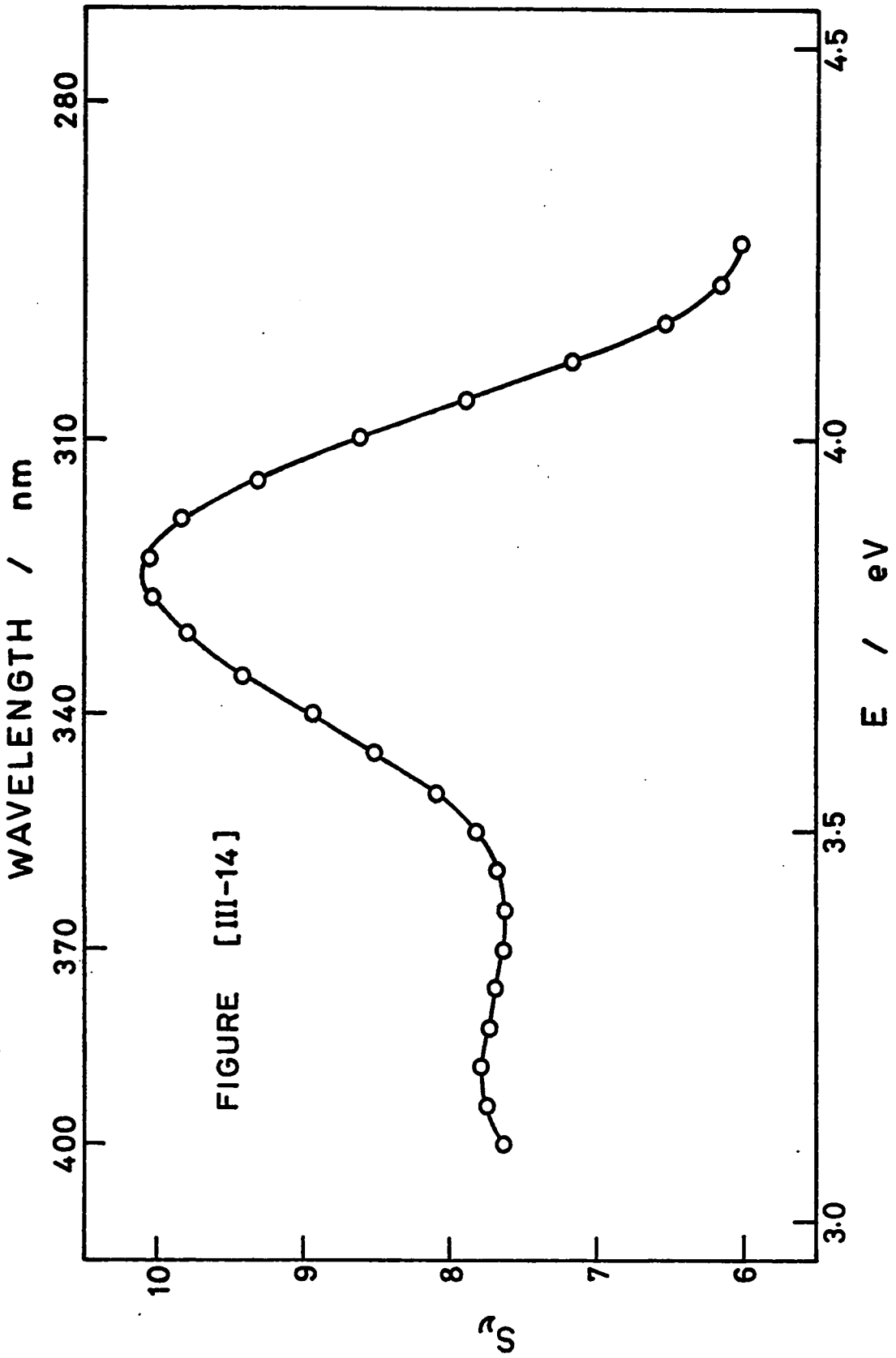

FIGURE [III-14]

CHAPTER IV

EXPERIMENTAL MEASUREMENTS AND DATA PROCESSING

1. Experimental Measurements

1-1 Crystal Samples

A crystal of oxine-extracted potassium bromide doped with thallous bromide, TlBr (Alpha Inorganics Inc.), was prepared according to method one described in Chapter III with a doping level of 0.03 mole % Tl^+ in the melt. Because of losses during purification, the actual concentration of Tl^+ in the crystal was considerably less.

A second crystal was grown using ultrapure KBr, ('Suprapur' - E. Merck Ag. Darmstat Germany), with a guaranteed assay of 99.997% purity. This crystal was doped with TlBr according to method two described previously and again a nominal Tl^+ concentration of 0.03 mole % in the melt was used. Essentially no TlBr was lost during preparation, and the actual impurity ion concentration could be assumed to be approximately the same as that in the melt.

Experimental measurements were made on the first crystal because the concentration of impurity was satisfactory for a study of the optical properties of the A-band. The impurity ion concentration in the second crystal was far too high and it was impossible to cleave the crystal thin enough so that the maximum optical density of the A-band

could be measured accurately. The actual piece of crystal used was 8 × 6 mm × 4.21 mm thick and its properties were such that both absorption and emission measurements could be made on the same sample.

1-2 Temperature Selection

Temperatures at which measurements were made were chosen to be spaced at approximately equal intervals on plots against $T^{\frac{1}{2}}$. A summary of the temperatures used is given for absorption in Table [IV-1] and for emission in Table [IV-2].

1-3 Absorption Measurements

With the sample in place, the position of the cryostat was adjusted until the absorption in the transparent region (~3000 Å) of the crystal was a minimum. Measurements were then obtained using a logarithmically wound slidewire on the recorder so that the optical density would be displayed linearly on the chart. Using this slidewire and the automatic scale change facility on the recorder, optical densities in the ranges 0-1 and 1-2 could be measured accurately. The range could be extended by the use of a neutral density filter. This is simply a pure nickel screen with conical sharp-edged holes which reduces the intensity of the reference beam in a wavelength independent manner [80]. The maximum optical density which could be measured with a good degree of accuracy was approximately 2.5. This upper limit was caused by limitations in the spectrophotometer due to residual stray light [81].

The wavelength region was scanned continuously from short to long wavelength at a rate of either 2.5 Å sec^{-1} or 0.5 Å sec^{-1}.

TABLE [IV-1]

TEMPERATURES OF ABSORPTION MEASUREMENTS, KBr:Tl^+

Run No.	T/K	$T^{1/2}/K^{1/2}$	Run No.	T/K	$T^{1/2}/K^{1/2}$
29	296.0	17.21	44	144.5	12.02
30	83.0	9.11	45	187.0	13.68
31	90.2	9.50	46	224.5	14.98
32	95.0	9.75	47	255.5	15.98
33	97.2	9.86			
34	105.0	10.25	101	15.0	3.87
35	133.2	11.54	102	20.2	4.49
36	170.3	13.05	103	25.0	5.00
37	209.2	14.46	104	31.5	5.61
			105	35.5	5.96
40	296.0	17.21	106	44.2	6.65
41	82.0	9.06	107	49.3	7.02
42	83.0	9.11	108	57.0	7.55
43	104.5	10.23			

TABLE [IV-2]

TEMPERATURES OF EMISSION MEASUREMENTS, KBr:Tl^+

Run No.	T/K	$T^{1/2}/K^{1/2}$	Run No.	T/K	$T^{1/2}/K^{1/2}$
1	296.0	17.21	130	84.0	9.17
2	83.0	9.11	131	84.0	9.17
3	92.0	9.59	132	15.5	3.94
4	83.0	9.11	133	19.3	4.39
5	88.2	9.39	134	24.8	4.98
6	93.0	9.65	135	31.4	5.60
7	98.2	9.91	136	31.0	5.57
8	107.2	10.35	136	25.0	5.00
9	113.4	10.65	137	28.5	5.39
10	133.8	11.57	138	42.5	6.52
11	170.2	13.05	139	49.5	7.04
12	170.2	13.05	140	49.0	7.00
13	209.0	14.46	141	57.0	7.55
14	252.2	15.88	142	64.1	8.01
15	296.0	17.21	143	73.0	8.54
			144	77.8	8.82
			145	87.3	9.34

The chart speed was such that 100 Å was displayed over $2\frac{2}{3}$ in at the faster scan speed and $13\frac{1}{3}$ in for the slower one. A wavelength mark was made automatically every 100 Å. For accurate reading over narrow bands, the slow scan speed was used.

1-4 Emission Measurements

The crystal was positioned for emission measurements as described in Chapter III, section 6-5. Several excitation sources were tried and a General Electric HA4 100 W mercury arc lamp with the glass envelope removed was found to be most suitable. The 2537 Å line was selected with a Jarrell-Ash quarter-meter monochromator equipped with 2 mm entrance and exit slits. This allowed a band pass of ~60 Å but since no other strong lines occur within ±30 Å of the 2537 Å line this resolution was sufficient to isolate the line of interest and at the same time provided maximum intensity in the exciting light. The voltage on the photomultiplier was set so that the maximum pen deflection was approximately 60% full scale at room temperature. This corresponded to a voltage of 1000 V. A linearly wound slidewire was used which in normal double beam operation would measure 0-100% transmittance. However, since only total emission intensity could be measured in the experiment, the slidewire acted as a linear voltage divider.

The wavelength region was scanned continuously from short to long wavelength at a rate of 2.5 Å sec^{-1}. The chart speed was the same as that used for absorption. Again a wavelength mark was recorded every 100 Å. The pen period was increased to 10 sec from 1 sec to reduce the response of the pen to noise. The slit on the Cary spectrophotometer was fixed at either 3 mm or 2.4 mm.

As the temperature was decreased, the emission intensity increased beyond the recording capabilities of the chart. In this situation, the slit width was reduced to 2.4 mm. With the photomultiplier voltage unaltered, the emission was measured at a convenient temperature using both slit widths so that a proper scaling factor could be obtained. The measured emission spectra were corrected for the spectral sensitivity of the detection system in the wavelength region 2900-4000 Å.

2. Chart Reading

2-1 General

Twelve inch chart paper was used for all experiments. It was ruled over eleven inches of the width every 0.1 in with major lines every inch. The labelled scale covered the range -0.05 to 1.05 so that optical density or transmittance could be read directly. The chart paper was ruled every $\frac{1}{3}$ in along its length.

When a chart was read, wavelength values were first marked at equal intervals starting at a 100 Å mark. The optical density/transmittance values were read to three decimal places either manually or using an analog to digital converter (Gerber Digital Data Reduction System Model GDDRS-3B-1, Gerber Scientific Instrument Company). These methods were found to give equivalent results. The manual method required subsequent keypunching of the data onto computer cards for processing. The analog to digital converter produced punched cards directly but required the addition of a code to take into account such things as scale changes and missing points.

2-2 Absorption

Experimental points were read every $\frac{1}{12}$ in corresponding to a wavelength interval of 3.125 Å at a scan speed of 2.5 Å sec^{-1}. If the slower scan speed was used, readings were taken every $\frac{5}{12}$ in so that the wavelength interval was unchanged. This gave approximately seventy-five points across the band.

In regions where a neutral density filter was required, the overlapping data was matched so that a complete spectrum was obtained. Neutral density filters with optical densities of 0.576 and 1.162 were used. Precautions were taken to ensure that the maximum optical density measurable by the machine (discussed previously) was not exceeded.

2-3 Emission

Experimental points were read every $\frac{1}{6}$ in corresponding to a wavelength interval of 6.25 Å at a scanning speed of 2.5 Å sec^{-1}. This gave approximately three hundred points across the band. In all cases the entire emission band was presented on the width of the chart paper so that none of the complications associated with scale change and neutral density filters were present.

3. Computer Processing

3-1 Preliminary Data Treatment

Raw experimental values were subjected to preliminary treatment before a least squares analysis was attempted.

In absorption, the background absorbance due to pure KBr was subtracted by means of a point by point calculation using the equation to a straight line to approximate the background absorption in the region of the A-band. The effect of this correction is shown in

Figure [IV-1] for the absorption at 296.0 K. The corrected optical density values were divided by the corresponding energy in electron volts [82] to give data proportional to the line shape, I. The effect on the absorption band shape resulting from this operation is illustrated in Figure [IV-2] where

$$D = \frac{OD}{(OD)_{\lambda_m}} - \frac{(OD/E)}{(OD/E)_{\lambda_m}}$$

and λ_m is the wavelength corresponding to the maximum optical density.

In emission, there was essentially no background correction since the background corresponded to no light on the detector. The emission data were divided by the cube of their energies [82]. The effect of this division is shown in Figure [IV-3].

The corrected experimental data were punched in a form compatible with the input requirements of the least squares programs.

3-2 Spectral Sensitivity Correction for Emission Data

The measured emission spectra were corrected for variation in the spectral response of the optical system in the wavelength region 2900 Å to 4000 Å. The spectral sensitivity values obtained from calibration with a standard lamp, Table [III-1], were fitted to a smooth curve using a cubic spline [83]. This fit is achieved by connecting each pair of adjacent points with a section of a third degree polynomial matching up each section so that the first and second derivatives are continuous at each point. A correction factor for each experimental point was calculated by interpolation. The corrected emission spectra were obtained by dividing the measured values by the appropriate factor (see Equation [III-1]). The effect of this correction is shown in Figure [IV-3].

FIGURE [IV-1]

A-BAND ABSORPTION KBr:Tl^+

RUN 29 - 296.0 K

O - raw experimental data

Δ - experimental data after subtraction of background absorption due to pure KBr.

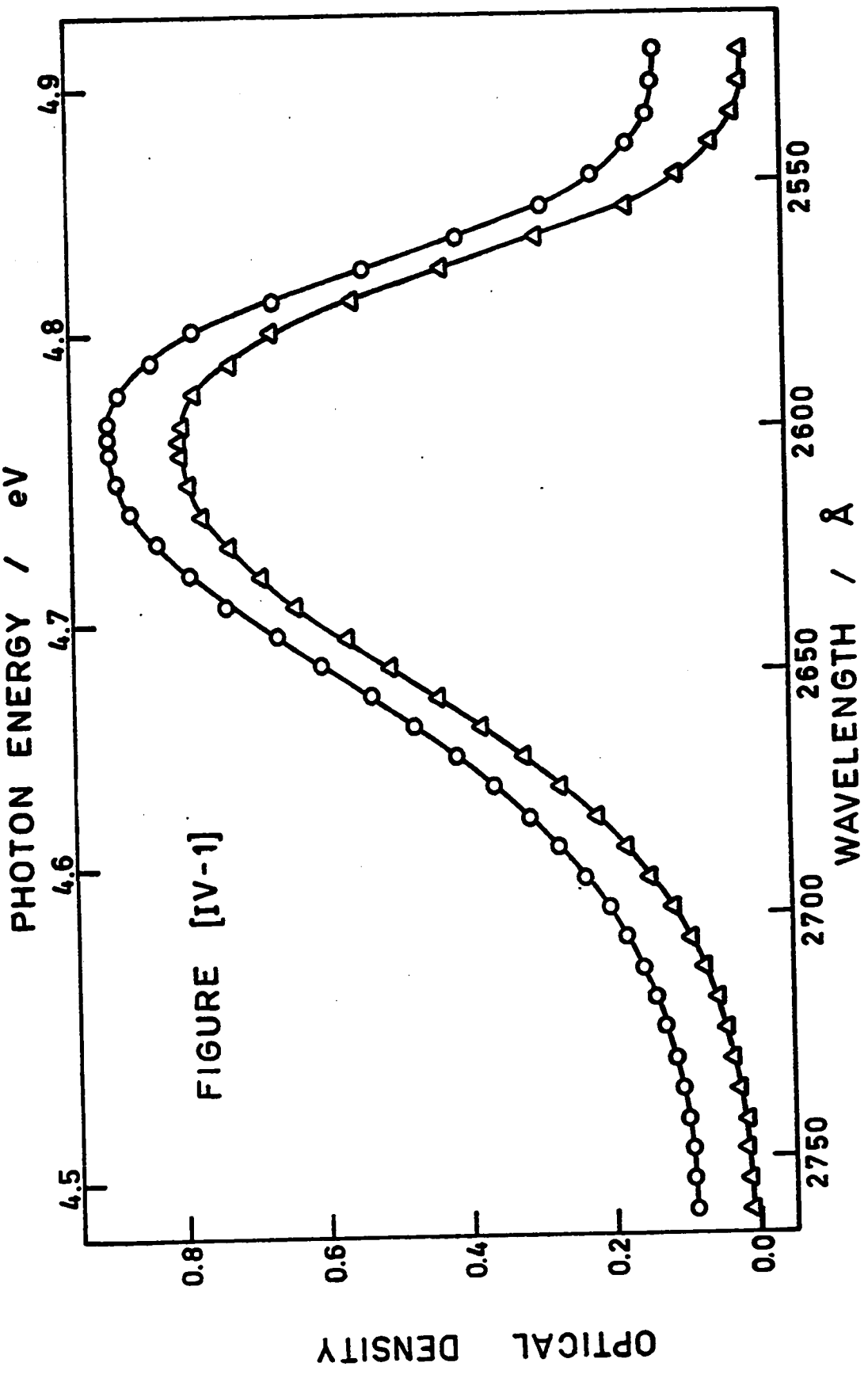
PHOTON ENERGY / eV
4.5
4.6
4.7
4.8
4.9
WAVELENGTH / Å
2750
2700
2650
2600
2550
OPTICAL DENSITY
0.0
0.2
0.4
0.6
0.8

FIGURE [IV-1]

FIGURE [IV-2]

A-BAND ABSORPTION KBr:Tl^+

RUN 29 - 296.0 K

EFFECT OF DIVISION BY THE PHOTON ENERGY

ON THE ABSORPTION BAND SHAPE

$$D = \frac{OD}{(OD)_{\lambda_m}} - \frac{(OD/E)}{(OD/E)_{\lambda_m}}$$

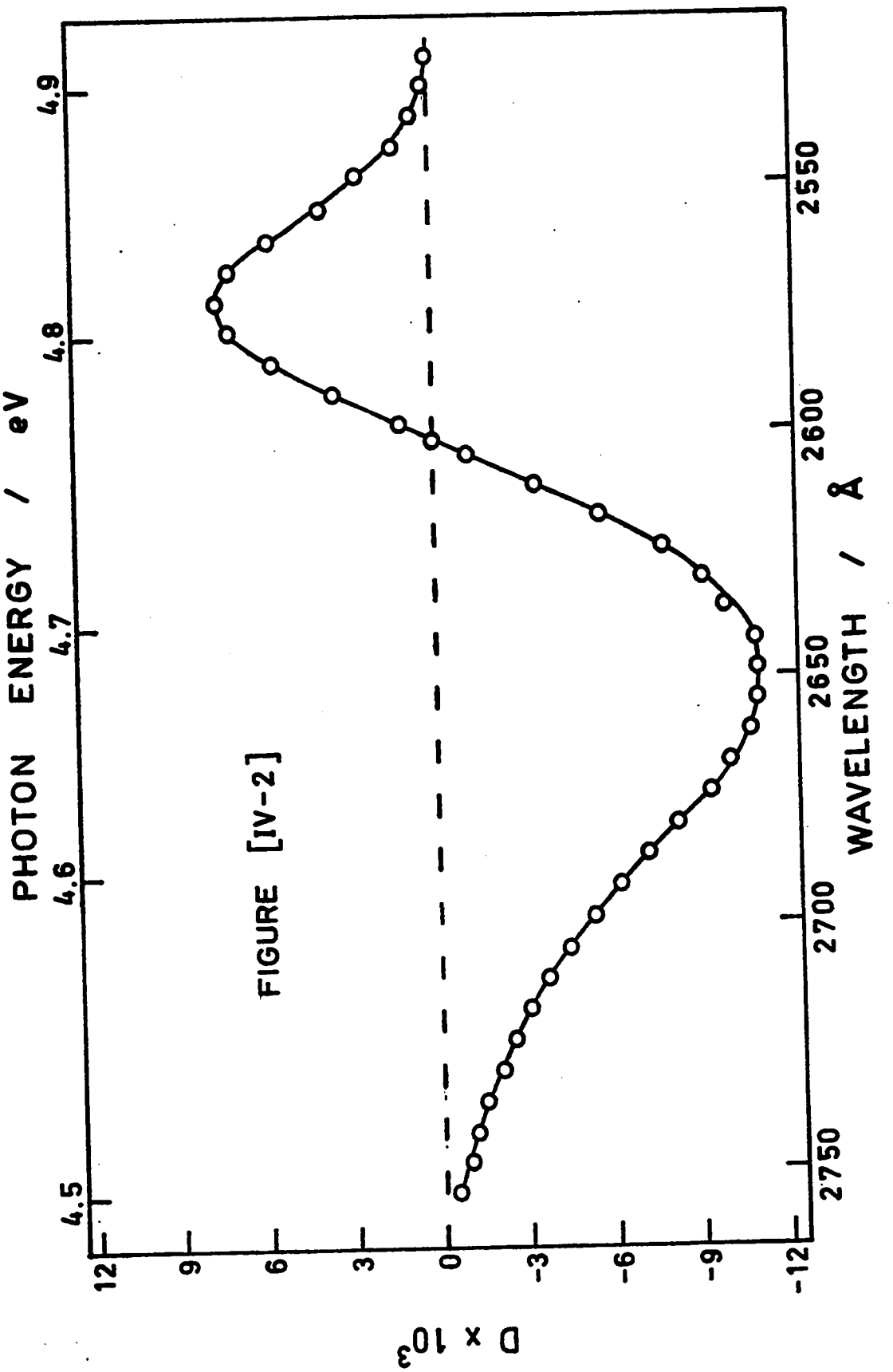
PHOTON ENERGY / eV
4.5
4.6
4.7
4.8
4.9
WAVELENGTH / Å
2750
2700
2650
2600
2550
D x 10³
12
9
6
3
0
-3
-6
-9
-12

FIGURE [IV-2]

FIGURE [IV-3]

EMISSION KBr:Tl^+

A-BAND EXCITATION

RUN 2 - 83.0 K

— — — — - raw experimental data

———— - experimental data after division by E^3

- - - - - - - - - experimental data after division by E^3 and corrected for spectral sensitivity

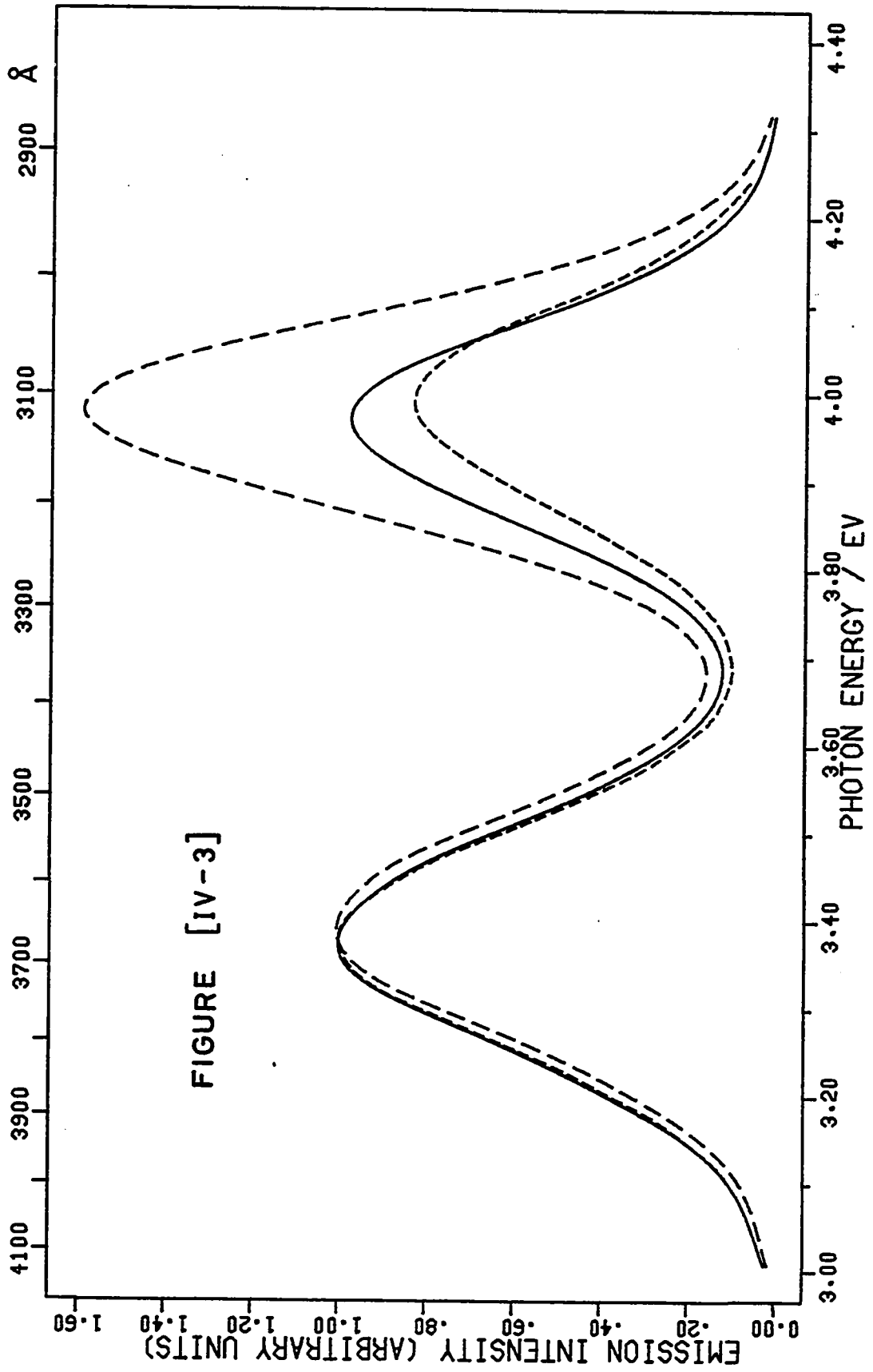
EMISSION INTENSITY (ARBITRARY UNITS)
0.00
.20
.40
.60
.80
1.00
1.20
1.40
1.60
PHOTON ENERGY / EV
3.00
3.20
3.40
3.60
3.80
4.00
4.20
4.40
Å
4100
3900
3700
3500
3300
3100
2900

FIGURE [IV-3]

3-3 Least Squares Analysis - MROCOS

A computer program, MROCOS (Mathematical Resolution Of Complex Overlapping Spectra), was obtained from Biggers et al [84]. It was specifically designed for resolving complex overlapping bands into individual bands and for mathematically comparing the sum of the individual bands with the experimental data. The individual bands could be fitted to a symmetric gaussian curve [85]. Initial estimates for parameters were required. These values were refined by a series of iterations to adjust the parameters to minimize the sum of the squares of deviations between the experimental and calculated data.

Modifications were made to adapt the program for use on an IBM 7040 computer. In addition, the program was altered to resolve overlapping bands in solids.

In absorption, the experimental line shape, I, defined by (see Equation [II- 13])

$$I = \frac{2.303 \times \text{optical density}}{\text{crystal thickness} \times E}$$

was the dependent variable and the energy in electron volts was the independent variable.

In emission, the line shape was defined by (see Equation [II-16]

$$I = \frac{\text{emitted intensity}}{\text{spectral sensitivity} \times E^3}$$

The emission line shape is a dimensionless quantity because absolute intensities were not determined.

The program provided best fit values for the parameters, the standard deviation for each parameter value, (σ_p), and the standard deviation of the fit, (σ).

3-4 Least Squares Analysis - BMDX85

BMDX85 is a non-linear least squares program obtained from the Health Sciences Computing Facility, UCLA [86]. It is a general program designed to fit data containing several dependent and independent variables to a functional form supplied by the user. The sum of the squares of deviations is minimized to obtain the best values of the parameters.

The program was used to resolve complex overlapping spectra for which there was one dependent and one independent variable. Two functional forms were used for this purpose.

One was a symmetric gaussian function described by the equation

$$I = \sum^{n} I_m \exp[-\ln 2(2[E-E_m]/H_{obs})^2] \qquad [IV-1]$$

where I is the observed intensity at energy E,

n is the number of individual gaussian bands,

and for each band, I_m is the maximum intensity at E_m and H_{obs} is the full width at $\frac{1}{2}I_m$.

The second functional form was the log-normal distribution function (asymmetric gaussian) [87]. It is described by the equation

$$I = \sum^{n} I_m \exp[-\ln 2(\ln[1+2b(E-E_m)/\Delta X_{1/2}]/b)^2] \qquad [IV-2]$$

where I, E, I_m, and E_m are as defined before. b is the skew parameter which takes into account the fact that the distributions on each side of E_m are not mirror images. $\Delta X_{1/2}$ is related to H_{obs} by

$$\Delta X_{1/2} = H_{obs} \times b/\sinh b$$

When b is zero, the log-normal distribution becomes identical with a symmetric gaussian.

3-4 Least Squares Analysis - BMDX85

BMDX85 is a non-linear least squares program obtained from the Health Sciences Computing Facility, UCLA [86]. It is a general program designed to fit data containing several dependent and independent variables to a functional form supplied by the user. The sum of the squares of deviations is minimized to obtain the best values of the parameters.

The program was used to resolve complex overlapping spectra for which there was one dependent and one independent variable. Two functional forms were used for this purpose.

One was a symmetric gaussian function described by the equation

$$I = \sum^{n} I_m \exp[-\ln 2(2[E-E_m]/H_{obs})^2] \qquad [IV-1]$$

where I is the observed intensity at energy E,

n is the number of individual gaussian bands,

and for each band, I_m is the maximum intensity at E_m and H_{obs} is the full width at $\frac{1}{2}I_m$.

The second functional form was the log-normal distribution function (asymmetric gaussian) [87]. It is described by the equation

$$I = \sum^{n} I_m \exp[-\ln 2(\ln[1+2b(E-E_m)/\Delta X_{1/2}]/b)^2] \qquad [IV-2]$$

where I, E, I_m, and E_m are as defined before. b is the skew parameter which takes into account the fact that the distributions on each side of E_m are not mirror images. $\Delta X_{1/2}$ is related to H_{obs} by

$$\Delta X_{1/2} = H_{obs} \times b/\sinh b$$

When b is zero, the log-normal distribution becomes identical with a symmetric gaussian.

In addition to the output information obtained in the MROCOS program, an asymptotic covariance matrix of the parameters is given.

All experimental results were analysed using either of these programs. For a symmetric gaussian, the two programs gave identical results. Analysis as asymmetric gaussian bands was done using BMDX85.

CHAPTER V

EXPERIMENTAL RESULTS

1. Introduction

Experimental measurements were made on a crystal of potassium bromide doped with thallous bromide, KBr:Tl^+.

After suitable corrections for background absorption and the spectral sensitivity of the spectrophotometer, the experimental line shapes were computer analyzed with non-linear least squares programs described previously.

2. Absorption

2-1 Introduction

The A-band absorption in KBr:Tl^+ is ascribed to the $^1S_o - {}^3P_1$ spin orbit allowed transition in the Tl^+ ion [6] and the maximum absorption occurs ~2600 Å (4.77 eV). As the temperature decreases, the position of the band maximum, E_m, shifts to higher energy, the maximum of the line shape, I_m, increases, the full width at one-half I_m, H_{obs}, decreases and the band itself appears to be more symmetric. These trends are illustrated in Figure [V-1] where the line shape, I, is plotted against energy at four representative temperatures. At no temperature in the range studied (296.0 K - 15.0 K) does the absorption band envelope give any indication of having more than one component.

The shape of the A-band was studied systematically. Models were chosen to be both consistent with the applicable theory and at the same time to characterize the shape in the fewest number of parameters. Consequently, the data were fitted using the following functions:

1. one symmetric gaussian curve (3 parameters);
2. one asymmetric gaussian curve (4 parameters);
3. sum of two symmetric gaussian curves (6 parameters);
4. sum of two asymmetric gaussian curves (8 parameters);
5. sum of three symmetric gaussian curves (9 parameters).

2-2 One Symmetric Gaussian Band

A symmetric gaussian band is characterized by its maximum intensity, (I_m), the position of this maximum, (E_m), and the full width of the band at one-half maximum intensity, (H_{obs}), (see Equation [IV-1]).

Parameter estimates for the least squares analysis were chosen from the charts. Best fit values for the parameters are summarized in Table [V-1]. The mean deviation in E_m was 0.001 eV (~0.02%), in I_m was 0.02 cm^{-1} eV^{-1} (~2%), and in H_{obs} was 0.001 eV (~1%).

Experimental data at 296.0 K, 83.0 K, and 15.0 K fitted as one symmetric gaussian band are shown in Figures [V-2,V-4,V-6]. The experimental values are plotted as points and the calculated best fit gaussian curve is plotted as a solid line. In addition, the error plots for each of the above data are given in Figures [V-3,V-5,V-7] respectively.

The temperature variation of the parameters (H_{obs},E_m, and I_m) is shown in Figures [V-8,V-9,V-10].

TABLE [V-1]

A-BAND ABSORPTION KBr:Tl^+ - ONE SYMMETRIC GAUSSIAN BAND

Run No.	T/K	E_m/eV	I_m/cm^{-1} eV^{-1}	H_{obs}/eV
29	296.0	4.744	0.93	0.164
30	83.0	4.789	1.92	0.083
31	90.2	4.787	1.82	0.088
32	95.0	4.785	1.75	0.090
33	97.2	4.785	1.75	0.092
34	105.0	4.783	1.66	0.095
35	133.2	4.777	1.48	0.108
36	170.3	4.769	1.28	0.123
37	209.3	4.761	1.14	0.136
40	296.0	4.743	0.93	0.162
41	82.0	4.789	1.94	0.082
42	83.0	4.788	1.93	0.083
43	104.5	4.785	1.72	0.093
44	144.5	4.776	1.47	0.109
45	187.0	4.768	1.26	0.125
46	244.5	4.759	1.13	0.140
47	255.5	4.753	1.04	0.149

Run No.	T/K	E_m/eV	I_m/cm^{-1} eV^{-1}	H_{obs}/eV
101	15.0	4.799	2.54	0.061
102	20.2	4.799	2.53	0.061
103	25.0	4.799	2.50	0.061
104	31.5	4.798	2.52	0.063
105	35.5	4.797	2.46	0.063
106	44.2	4.796	2.36	0.065
107	49.3	4.795	2.32	0.068
108	57.0	4.793	2.16	0.071
σ_p		0.001	0.02	0.001

(a) H_{obs} against $T^{1/2}$ (Figure [V-8])

The half-width varies linearly with $T^{1/2}$ at high temperatures and approaches a limiting value as T tends to zero. The solid line represents the calculated best fit to

$$H_{obs} = H_o[\coth(h\nu/2kT)]^{1/2} \qquad [II-78]$$

where H_o is the value of H_{obs} at T = 0 K.

(b) E_m against T (Figure [V-9])

The position of the band maximum shifts from 4.744 eV at 296.0 K to 4.799 eV at 15.0 K. The variation is linear at high temperature.

(c) I_m against T (Figure [V-10])

The band intensity increases smoothly as the temperature decreases.

2-3 <u>One Asymmetric Gaussian Band</u>

An asymmetric gaussian band can be characterized by the same three parameters describing a symmetric gaussian curve with the addition of a skew parameter, b, which arises from the fact that the sides of the band are no longer mirror images. This parameter becomes zero as the curve approaches a symmetric gaussian (see Equation [IV-2]).

Initial parameter estimates were the same as before with the addition of an arbitrarily chosen value for the skew parameter. Best fit values of the parameters are summarized in Table [V-2]. The mean deviation in E_m was 0.001 eV (~0.02%), in I_m was 0.02 cm^{-1} eV^{-1} (~2%), and in H_{obs} was 0.001 (~1%). The mean deviation in the skew parameter was 0.02. This could be as much as 50% of the value of b when this parameter was small. But when b is small its effect on the band shape is small (i.e. the band is almost symmetric).

TABLE [V-2]

A-BAND ABSORPTION KBr:Tl^+ - ONE ASYMMETRIC GAUSSIAN BAND

Run No.	T/K	E_m/eV	I_m/cm^{-1} eV^{-1}	H_{obs}/eV	b
29	296.0	4.757	0.95	0.160	-0.29
30	83.0	4.791	1.92	0.083	-0.08
31	90.2	4.790	1.82	0.088	-0.12
32	95.0	4.788	1.76	0.090	-0.13
33	97.2	4.789	1.75	0.091	-0.14
34	105.0	4.787	1.67	0.094	-0.16
35	133.2	4.783	1.48	0.107	-0.20
36	170.3	4.777	1.29	0.122	-0.21
37	209.3	4.770	1.15	0.135	-0.25
40	296.0	4.755	0.94	0.160	-0.28
41	82.0	4.791	1.94	0.082	-0.10
42	83.0	4.791	1.94	0.083	-0.09
43	104.5	4.788	1.73	0.092	-0.12
44	144.5	4.782	1.47	0.109	-0.18
45	187.0	4.776	1.27	0.124	-0.24
46	224.5	4.769	1.14	0.137	-0.25
47	255.5	4.764	1.04	0.147	-0.27

Run No.	T/K	E_m/eV	I_m/cm^{-1} eV^{-1}	H_{obs}/eV	b
101	15.0	4.797	2.54	0.061	+0.07
102	20.2	4.798	2.53	0.061	+0.07
103	25.0	4.797	2.50	0.061	+0.08
104	31.5	4.796	2.52	0.063	+0.06
105	35.5	4.796	2.46	0.063	+0.06
106	44.2	4.796	2.36	0.065	-0.02
107	49.3	4.795	2.32	0.068	+0.01
108	57.0	4.794	2.16	0.071	-0.02
σ_p		0.001	0.02	0.001	0.02

Experimental data at 296.0 K, 83.0 K and 15.0 K fitted as one asymmetric gaussian band are shown in Figures [V-11,V-13,V-15]. Their error plots are given in Figures [V-12,V-14,V-16].

The temperature variation of the parameters is shown in Figures [V-17,V-18,V-19,V-20].

(a) H_{obs} against $T^{\frac{1}{2}}$ (Figure [V-17])

The half-width variation with the square root of the temperature shows the same general features as for the symmetric gaussian curve. The best fit to equation [II-78] is again plotted as a solid line.

(b) E_m against T (Figure [V-18])

E_m shifts from 4.757 eV at 296.0 K to 4.797 eV at 15.0 K. Again, the variation is linear at high temperature.

(c) I_m against T (Figure [V-19])

I_m shows the same general shape as was observed in the symmetric gaussian case.

(d) b against T (Figure [V-20])

The plot of skew parameter against temperature shows that the absorption band is very asymmetric to the low energy side at high temperatures. The amount of asymmetry decreases with decreasing temperature, the band being essentially symmetric gaussian at 50 K. Below this temperature, the band is slightly asymmetric to the high energy side, the asymmetry increasing as T approaches 0 K.

2-4 Two Symmetric Gaussian Bands

The resolution of the absorption line shape envelope into two symmetric gaussian bands requires the use of six parameters. The calculated line shape is simply the algebraic sum of two separate

TABLE [V-3]

A-BAND ABSORPTION KBr:Tl^+ - TWO SYMMETRIC GAUSSIAN BANDS

Run No.	T/K	Band 1			Band 2		
		E_m/eV	I_m/cm^{-1} eV^{-1}	H_{obs}/eV	E_m/eV	I_m/cm^{-1} eV^{-1}	H_{obs}/eV
29	296.0	4.788	0.46	0.092	4.718	0.71	0.156
30	83.0	4.821	0.57	0.043	4.782	1.75	0.076
31	90.2	4.818	0.55	0.044	4.779	1.64	0.081
32	95.0	4.817	0.53	0.044	4.777	1.58	0.084
33	97.2	4.817	0.58	0.045	4.776	1.55	0.084
34	105.0	4.816	0.54	0.046	4.774	1.48	0.089
35	133.2	4.813	0.52	0.052	4.766	1.29	0.101
36	170.3	4.809	0.48	0.062	4.756	1.09	0.116
37	209.3	4.801	0.49	0.072	4.743	0.93	0.128
40	296.0	4.785	0.47	0.095	4.716	0.68	0.155
41	82.0	4.820	0.54	0.040	4.782	1.79	0.076
42	83.0	4.819	0.51	0.040	4.782	1.79	0.077

Run No.	T/K	Band 1			Band 2		
		E_m/eV	I_m/cm^{-1} eV^{-1}	H_{obs}/eV	E_m/eV	I_m/cm^{-1} eV^{-1}	H_{obs}/eV
43	104.5	4.818	0.49	0.043	4.777	1.57	0.086
44	144.5	4.813	0.49	0.052	4.766	1.30	0.103
45	187.0	4.807	0.50	0.063	4.753	1.06	0.118
46	224.5	4.801	0.47	0.072	4.742	0.92	0.131
47	255.5	4.795	0.48	0.081	4.731	0.81	0.141
101	15.0	4.808	2.14	0.051	4.778	1.17	0.037
102	20.2	4.808	2.08	0.051	4.778	1.21	0.038
103	25.0	4.805	2.23	0.057	4.776	0.78	0.034
104	31.5	4.811	1.93	0.048	4.779	1.55	0.040
105	35.5	4.809	1.95	0.051	4.777	1.31	0.041
106	44.2	4.819	1.06	0.040	4.786	2.04	0.053
107	49.3	4.815	1.35	0.046	4.781	1.78	0.051
108	57.0	4.818	0.96	0.048	4.782	1.79	0.059
σ_p		0.001	0.06	0.002	0.001	0.03	0.001

gaussian bands, each of which is defined by the three parameters E_m, I_m, and H_{obs}.

In order to obtain initial parameter values for computer processing, symmetric bands were estimated graphically and the parameters read directly from this sketch. The final values obtained for these parameters are given in Table [V-3]. The mean deviations are given in the last line of the table.

Experimental data at 296.0 K, 83.0 K and 15.0 K fitted as two symmetric gaussian bands are shown in Figures [V-21,V-23,V-25], along with their error plots in Figures [V-22,V-24,V-26].

The temperature variation of the parameters is shown in Figures [V-27,V-28,V-29].

(a) H_{obs} against $T^{1/2}$ (Figure [V-27])

From 83.0 K to 296.0 K the temperature variation of the half-width is linear with $T^{1/2}$ for both bands. For the high energy band below 83.0 K, the half-width increases to give a limiting value which is larger than the half-width at liquid nitrogen temperature. For the low energy band, the half-width continues to decrease and reaches a limiting value of 0.037 eV.

(b) E_m against T (Figure [V-28])

The change in the position of the band maximum with temperature is larger for the low energy component than for the high energy band. For both bands, E_m decreases linearly with T above 83.0 K. Below this temperature however, the band maximum for both bands decreases.

(c) I_m against T (Figure [V-29])

Above 83.0 K the intensity of the high energy band is approximately

constant. Below 83.0 K the intensity of this band increases sharply. The temperature dependence of the intensity for the low energy band is quite different. From 296.0 K to 83.0 K the intensity is greater than that of the high energy band and increases as T decreases. Below 83.0 K the band intensity increases and then decreases falling below the intensity of the high energy at approximately 30 K.

The separation energy of the two components of the absorption line shape, $\Delta E_{splitting} \equiv E_{12}$, is shown in Figure [V-30]. It varies linearly with $T^{1/2}$ at high temperature and approaches a limiting value as T approaches zero.

2-5 Two Asymmetric Gaussian Bands

Eight parameters are required to describe the absorption line shape envelope as the sum of two asymmetric gaussian bands. Each band is defined by E_m, I_m, H_{obs}, and b.

Converged values of the parameters obtained from the resolution as two symmetric gaussian bands along with arbitrarily chosen skew parameters were used as initial estimates. The final values are given in Table [V-4]. The mean deviations are given in the last line of the table.

Experimental data at 296.0 K, 83.0 K, and 15.0 K fitted as two asymmetric gaussian bands are shown in Figures [V-31,V-33,V-35], along with their error plots in Figures [V-32,V-34,V-36].

The temperature variation of the parameters is shown in Figures [V-37,V-38,V-39,V-40].

TABLE [V-4]

A-BAND ABSORPTION KBr:Tl^+ - TWO ASYMMETRIC GAUSSIAN BANDS

Run No.	T/K	Band 1				Band 2			
		E_m/eV	I_m/cm^{-1} eV^{-1}	H_{obs}/eV	b	E_m/eV	I_m/cm^{-1} eV^{-1}	H_{obs}/eV	b
29	296.0	4.806	0.25	0.072	-0.11	4.740	0.86	0.156	-0.19
30	83.0	4.815	1.35	0.047	+0.07	4.774	1.62	0.058	-0.21
31	90.2	4.819	0.91	0.048	+0.04	4.776	1.60	0.071	-0.12
32	95.0	4.818	0.87	0.048	+0.06	4.774	1.55	0.074	-0.13
33	97.2	4.818	0.58	0.047	-0.15	4.776	1.52	0.085	-0.12
34	105.2	4.819	0.48	0.044	-0.08	4.777	1.51	0.089	-0.06
35	133.2	4.817	0.77	0.054	+0.02	4.765	1.30	0.087	-0.19
36	170.3	4.815	0.67	0.062	+0.01	4.757	1.12	0.102	-0.21
37	209.3	4.813	0.41	0.065	+0.02	4.754	1.04	0.123	-0.19
40	296.0	4.802	0.50	0.084	-0.06	4.727	0.79	0.136	-0.28
41	82.0	4.815	1.41	0.045	+0.09	4.774	1.65	0.057	-0.23
42	83.0	4.810	1.58	0.049	+0.10	4.769	1.51	0.056	-0.25

Run No.	T/K	Band 1				Band 2			
		E_m/eV	I_m/cm^{-1} eV^{-1}	H_{obs}/eV	b	E_m/eV	I_m/cm^{-1} eV^{-1}	H_{obs}/eV	b
43	104.5	4.812	1.34	0.050	+0.10	4.767	1.43	0.062	-0.27
44	144.5	4.816	0.79	0.055	+0.06	4.764	1.29	0.088	-0.19
45	187.0	4.814	0.69	0.061	-0.00	4.755	1.10	0.103	-0.24
46	244.5	4.811	0.58	0.068	+0.00	4.747	0.99	0.116	-0.25
47	255.5	4.809	0.54	0.073	-0.04	4.740	0.91	0.125	-0.26
101	15.0	4.820	0.79	0.036	+0.19	4.790	2.34	0.053	+0.14
102	20.2	4.818	1.41	0.039	+0.16	4.787	2.19	0.044	+0.00
103	25.0	4.820	0.81	0.038	+0.25	4.790	2.31	0.052	+0.10
104	31.5	4.813	1.93	0.041	+0.15	4.781	1.99	0.038	-0.09
105	35.5	4.816	1.52	0.040	+0.16	4.784	2.11	0.044	-0.05
107	49.3	4.806	2.01	0.052	+0.03	4.773	1.22	0.041	-0.02
108	57.0	4.816	1.34	0.045	+0.08	4.780	1.77	0.052	-0.11
σ_p		0.001	0.09	0.001	0.02	0.002	0.04	0.003	0.02

(a) H_{obs} against $T^{1/2}$ (Figure [V-37])

The half-width values as a function of $T^{1/2}$ for the low energy band lie on a smooth curve. However, more scatter is observed for the high energy band and the functional relationship is therefore more uncertain.

(b) E_m against T (Figure [V-38])

For the high energy band, the shift of E_m with temperature is small [E_m = 4.802 eV at 296.0 K and E_m = 4.820 eV at 15.0 K]. The change in E_m is linear with T for high T, but there is essentially no change in E_m below 100 K. The shift of E_m with T is much larger for the low energy band [E_m = 4.727 eV at 296.0 K and E_m = 4.790 at 15.0 K]. The relationship between E_m and T for this band appears to be linear over the whole range of temperatures.

(c) I_m against T (Figure [V-39])

The intensity of the low energy band increases smoothly with decreasing temperature. The intensity values for the high energy band are not as well behaved. From 300 K to 120 K, I_m increases with increasing temperature. Below 120 K, the results are badly scattered but the intensity seems to increase rapidly from 100 K to 40 K and then to decrease sharply as T approaches 0 K.

(d) b against T (Figure [V-40])

The change in the skew parameter with T is not too clearly defined. At high temperatures for the low energy band, b is roughly constant ~-0.25. Below 80 K the value of this parameter increases having a zero value at ~25 K. As the temperature decreases below 25 K, b increases and is positive. The asymmetry of the high energy band is smaller than that of the low energy band, the skew parameter having a value in the

range ±0.1. b is negative at high T, positive at low T and has a zero value at ~160 K.

The temperature dependence of $\Delta E_{splitting} \equiv E_{12}$ is shown in Figure [V-41]. The relationship against $T^{1/2}$ is linear at high T and reaches a limiting value of 0.03 eV at T = 0 K.

2-6 Three Symmetric Gaussian Bands

The resolution of the absorption line shape envelope into three symmetric gaussian bands requires nine parameters, three for each band.

A graphical procedure similar to that used for the two band symmetric gaussian model was used to obtain initial estimates for the parameters. The results of the computer analysis are given in Table [V-5].

No results are shown below 82.0 K since the non-linear least squares program could not provide converged values for the parameters. Even below 100 K, the results are badly scattered. In some instances, the best resolution indicated two bands at the same energy. The errors in the parameters are much larger than those for any of the other models.

Experimental data at 296.0 K and 83.0 K fitted as three symmetric gaussian bands are shown in Figures [V-42,V-44] along with their error plots in Figures [V-43,V-45].

The temperature variation of the parameters is shown in Figures [V-46,V-47,V-48].

(a) H_{obs} against $T^{1/2}$ (Figure [V-46])

For all three bands, the variation of the half-width is linear with $T^{1/2}$ in the temperature range studied. In addition, there is some indication that the half-width of the highest energy band is beginning to approach a limiting value.

TABLE [V-5]

A-BAND ABSORPTION KBr:Tl^+ - THREE SYMMETRIC GAUSSIAN BANDS

Run No.	T/K	Band 1			Band 2			Band 3		
		E_m/eV	I_m/cm^{-1} eV^{-1}	H_{obs}/eV	E_m/eV	I_m/cm^{-1} eV^{-1}	H_{obs}/eV	E_m/eV	I_m/cm^{-1} eV^{-1}	H_{obs}/eV
29	296.0	4.802	0.39	0.075	4.744	0.60	0.117	4.684	0.33	0.160
30	83.0	4.816	1.15	0.051	4.776	1.33	0.059	4.752	0.27	0.076
31	90.2	4.819	0.62	0.045	4.779	1.57	0.078	4.749	0.068	0.105
32	95.0	4.817	0.58	0.045	4.777	1.55	0.081	4.729	0.044	0.104
34	105.0	4.818	0.57	0.046	4.782	0.98	0.076	4.758	0.61	0.091
35	133.2	4.816	0.60	0.053	4.772	1.05	0.086	4.737	0.34	0.108
36	170.3	4.813	0.54	0.061	4.763	0.89	0.096	4.722	0.31	0.121
37	209.3	4.809	0.48	0.066	4.758	0.74	0.101	4.711	0.36	0.133
40	296.0	4.798	0.41	0.081	4.738	0.61	0.120	4.677	0.27	0.164
41	82.0	4.816	0.93	0.046	4.776	0.93	0.057	4.777	0.73	0.086
42	83.0	4.817	0.85	0.046	4.777	1.42	0.065	4.778	0.26	0.105

Run No.	T/K	Band 1			Band 2			Band 3		
		E_m/eV	I_m/cm^{-1} eV^{-1}	H_{obs}/eV	E_m/eV	I_m/cm^{-1} eV^{-1}	H_{obs}/eV	E_m/eV	I_m/cm^{-1} eV^{-1}	H_{obs}/eV
43	104.5	4.817	0.78	0.049	4.773	1.12	0.070	4.769	0.37	0.107
44	144.5	4.815	0.53	0.052	4.769	1.22	0.095	4.722	0.11	0.124
45	187.0	4.812	0.54	0.060	4.762	0.88	0.097	4.718	0.31	0.126
46	244.5	4.807	0.47	0.067	4.753	0.78	0.108	4.704	0.28	0.141
47	255.5	4.805	0.45	0.071	4.748	0.41	0.111	4.692	0.29	0.149
σ_p		0.001	0.13	0.003	0.002	0.38	0.005	0.070	0.36	0.030

(b) E_m against T (Figure [V-47])

The position of the maximum for all three bands decreases linearly with temperature. The shift is largest for the lowest energy band and smallest for the highest energy band.

(c) I_m against T (Figure [V-48])

The results show a great deal of scatter especially at low temperatures. However, for the centre band, I_m appears to increase sharply as the temperature decreases. Only a slight increase is observed for the other two bands.

The separation energies E_{12}, [E_m(Band 1)-E_m(Band 2)], and E_{23}, [E_m(Band 2)-E_m(Band 3)], plotted against $T^{\frac{1}{2}}$ are shown in Figure [V-49]. Both E_{12} and E_{23} decrease with decreasing temperature, E_{23} decreasing the more rapidly. The results at temperatures where Band 2 and Band 3 are coincident, (E_{23}=0), do not appear to follow the trend at higher temperatures.

2-7 Standard Deviation for Line Shape Models

The standard deviation, σ, of the fit using the best values of the parameters in a least squares sense was calculated from the equation

$$\sigma^2 = \frac{\Sigma (I_{obs} - I_{calc})^2}{N - P}$$

where N is the number of data points used,

P is the number of parameters,

I_{obs} is the experimental value at a given energy,

and I_{calc} is the algebraic sum of the contributions of all bands at the same energy.

The standard deviation as a function of temperature for each of the models used is shown in Figure [V-50].

FIGURE [V-1]

A-BAND ABSORPTION KBr:Tl^+

— — — — 296.0 K

— — — — — 144.5 K

— — — — — — 83.0 K

--------- 15.0 K

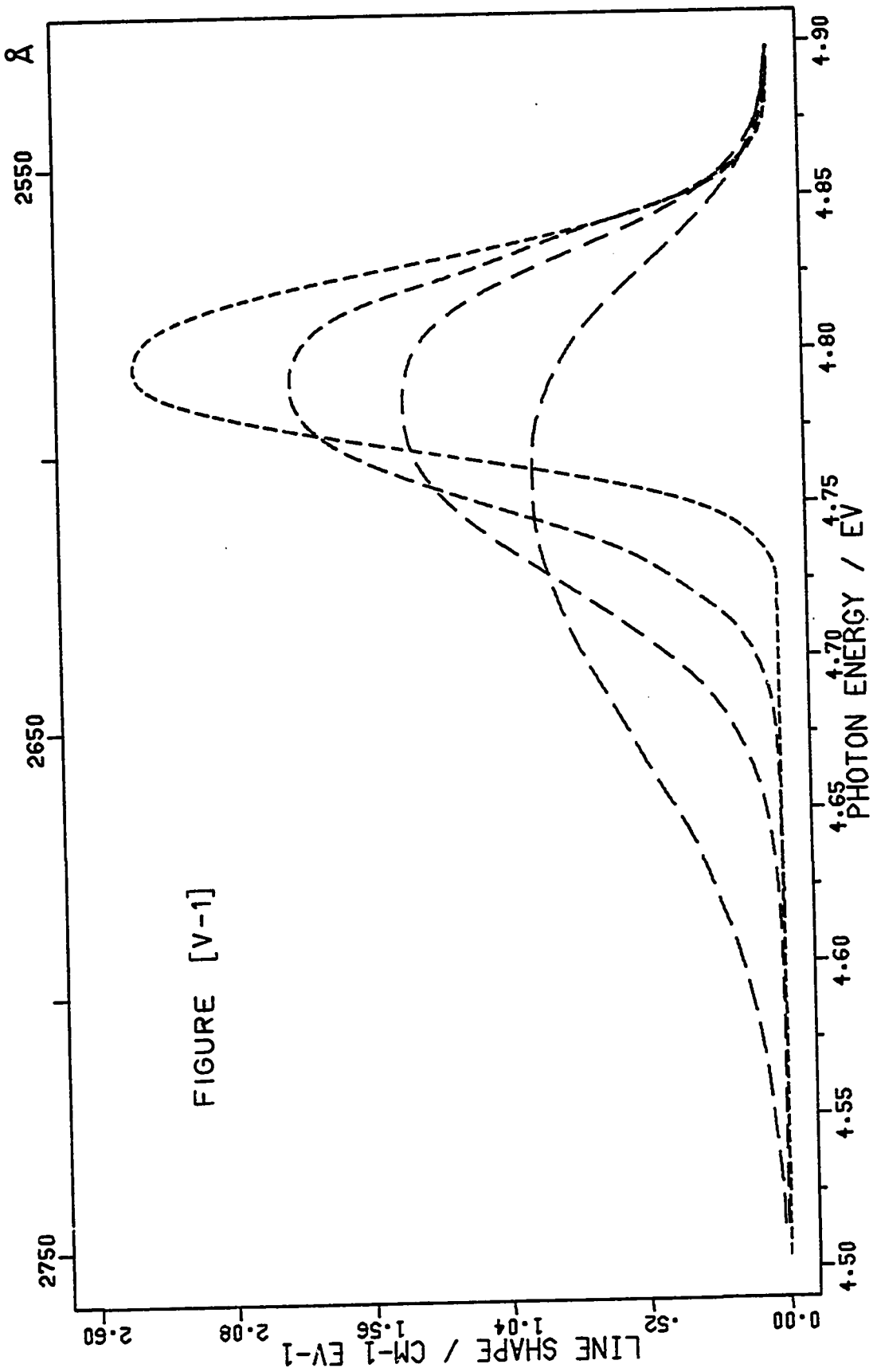
Å
2550
2650
2750
4.50
4.55
4.60
4.65
4.70
4.75
4.80
4.85
4.90
PHOTON ENERGY / EV
0.00
.52
1.04
1.56
2.08
2.60
LINE SHAPE / CM-1 EV-1

FIGURE [V-1]

A-BAND ABSORPTION KBr:Tl^+

1 SYMMETRIC GAUSSIAN BAND

RUN 29 - 296.0 K

FIGURE [V-2]

Δ - experimental points

The solid line is the calculated best fit.

FIGURE [V-3]

Plot of I(experimental) - I(calculated) for each experimental point.

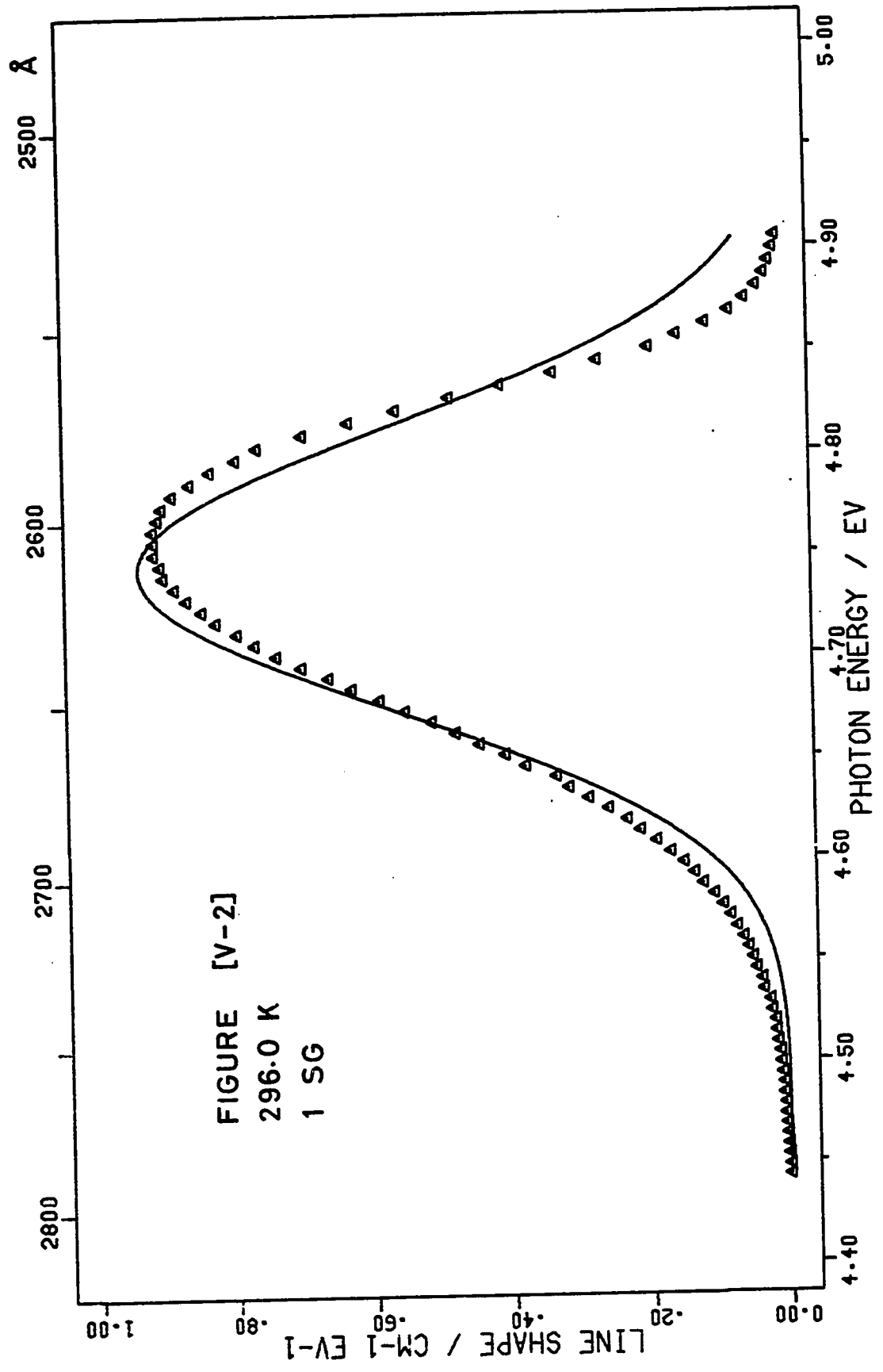
FIGURE [V-2]
296.0 K
1 SG
LINE SHAPE / CM-1 EV-1
PHOTON ENERGY / EV
Å
2500
2600
2700
2800
4.40
4.50
4.60
4.70
4.80
4.90
5.00
0.00
.20
.40
.60
.80
1.00

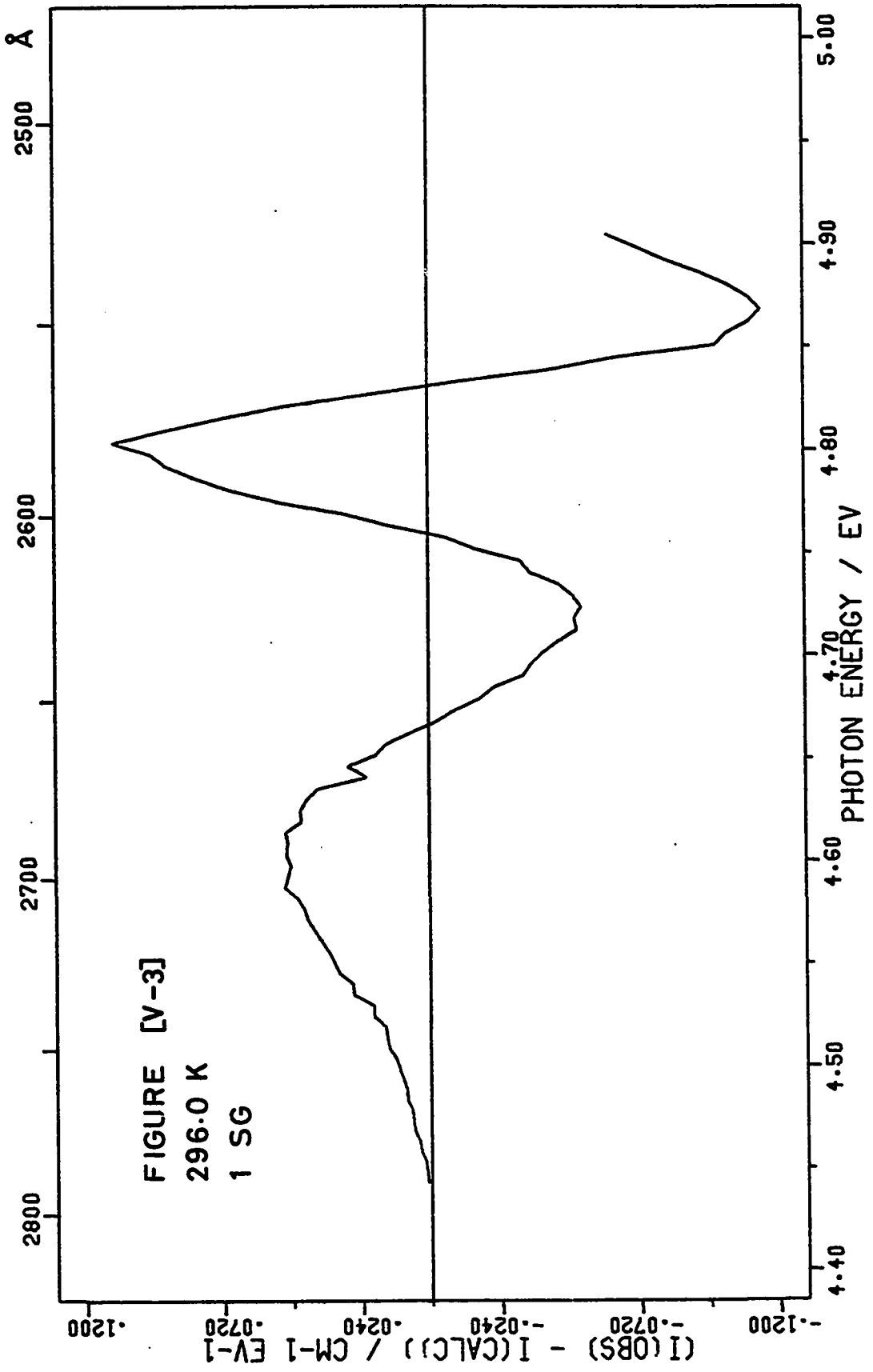
FIGURE [V-3]
296.0 K
1 SG
Å
2500
2600
2700
2800
5.00
4.90
4.80
4.70
4.60
4.50
4.40
PHOTON ENERGY / EV
(I(OBS) - I(CALC)) / CM-1 EV-1
-.1200
-.0720
-.0240
.0240
.0720
.1200

A-BAND ABSORPTION KBr:Tl^+

1 SYMMETRIC GAUSSIAN BAND

RUN 30 - 83.0 K

FIGURE [V-4]

Δ - experimental points

The solid line is the calculated best fit.

FIGURE [V-5]

Plot of I(experimental) - I(calculated)

for each experimental point.

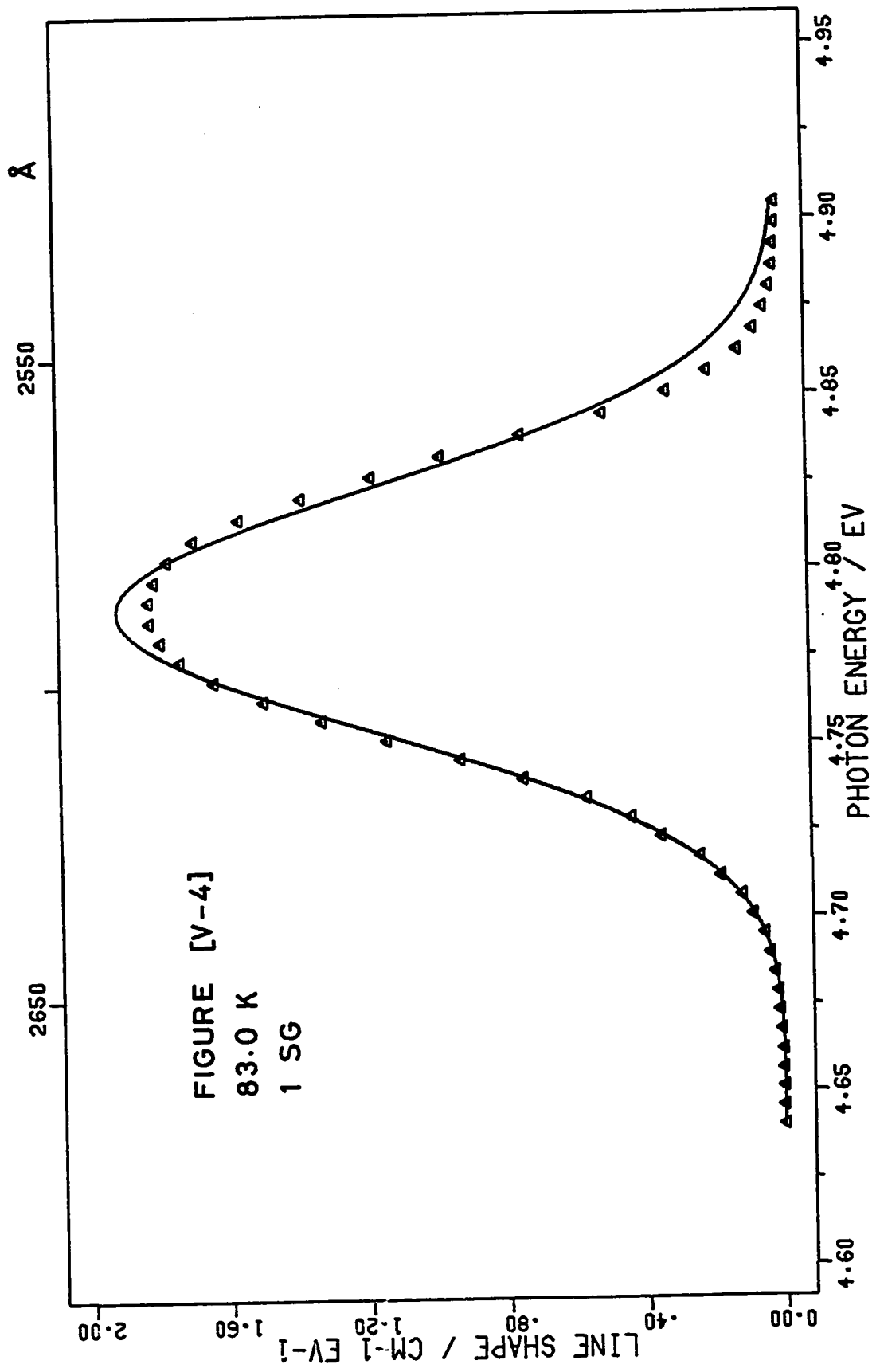
FIGURE [V-4]
83.0 K
1 SG
Å
2650
2550
LINE SHAPE / CM-1 EV-1
0.00
.40
.80
1.20
1.60
2.00
4.60
4.65
4.70
4.75
4.80
4.85
4.90
4.95
PHOTON ENERGY / EV

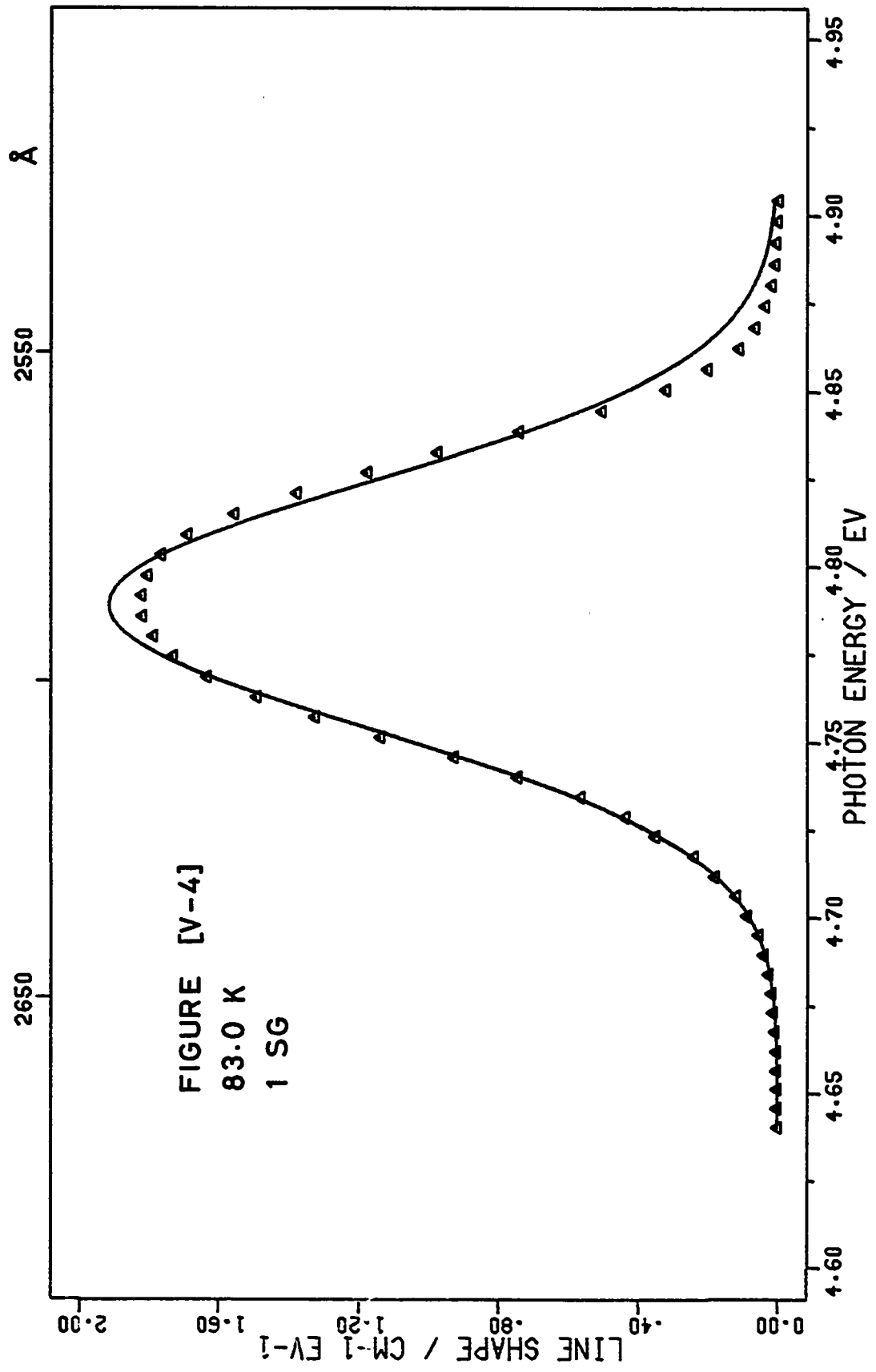
FIGURE [V-4]
83.0 K
1 SG
Å
2650
2550
LINE SHAPE / CM-1 EV-1
0.00
.40
.80
1.20
1.60
2.00
4.60
4.65
4.70
4.75
4.80
4.85
4.90
4.95
PHOTON ENERGY / EV

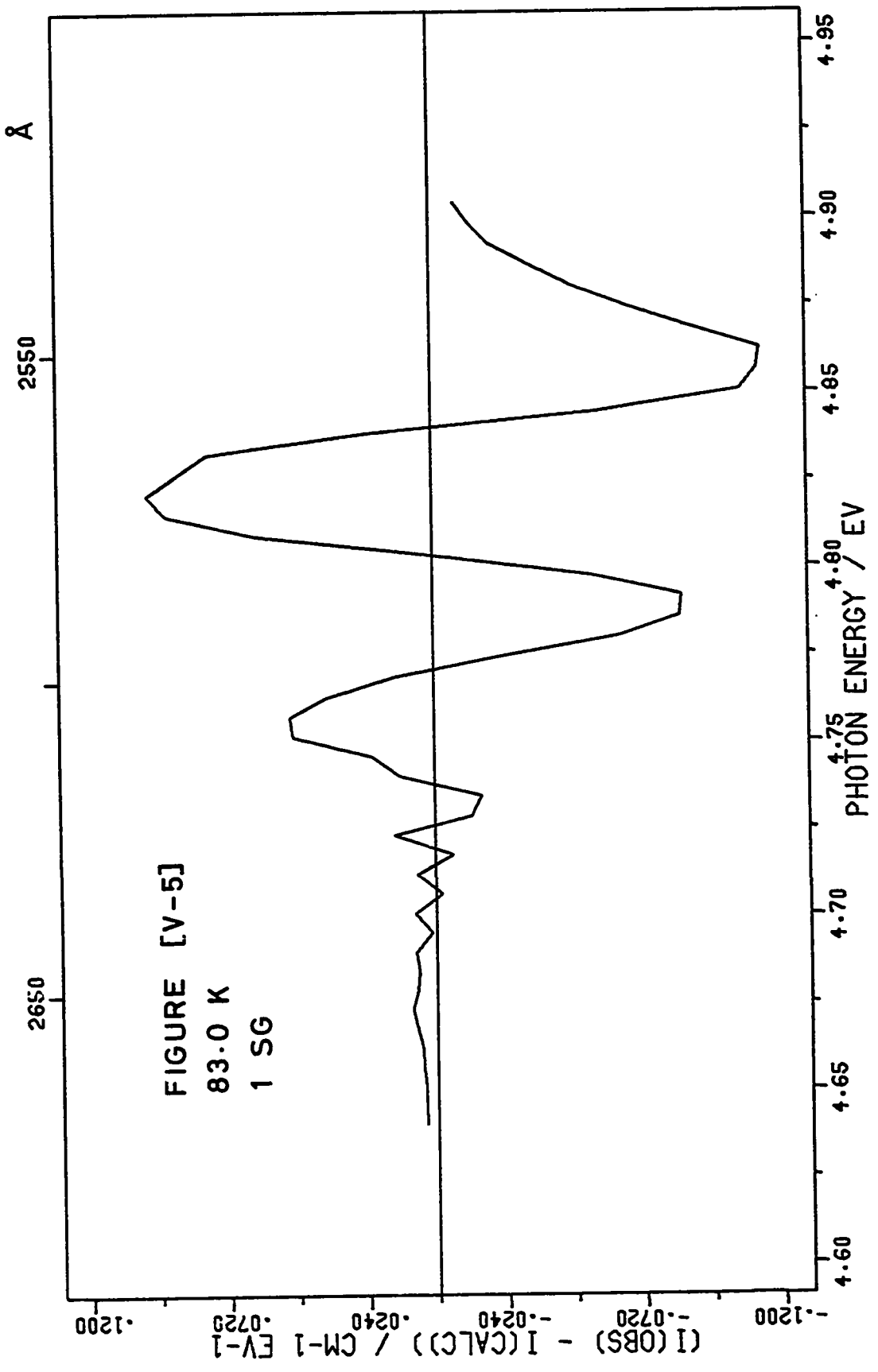
FIGURE [V-5]
83.0 K
1 SG
Å
2650
2550
4.60
4.65
4.70
4.75
4.80
4.85
4.90
4.95
PHOTON ENERGY / EV
(I(OBS) - I(CALC)) / CM-1 EV-1
-.1200
-.0720
-.0240
.0240
.0720
.1200

A-BAND ABSORPTION KBr:Tl^+

1 SYMMETRIC GAUSSIAN BAND

RUN 101 - 15.0 K

FIGURE [V-6]

Δ - experimental points

The solid line is the calculated best fit.

FIGURE [V-7]

Plot of I(experimental) - I(calculated) for each experimental point.

A-BAND ABSORPTION KBr:Tl^+

1 SYMMETRIC GAUSSIAN BAND

RUN 101 - 15.0 K

FIGURE [V-6]

Δ - experimental points

The solid line is the calculated best fit.

FIGURE [V-7]

Plot of I(experimental) - I(calculated) for each experimental point.

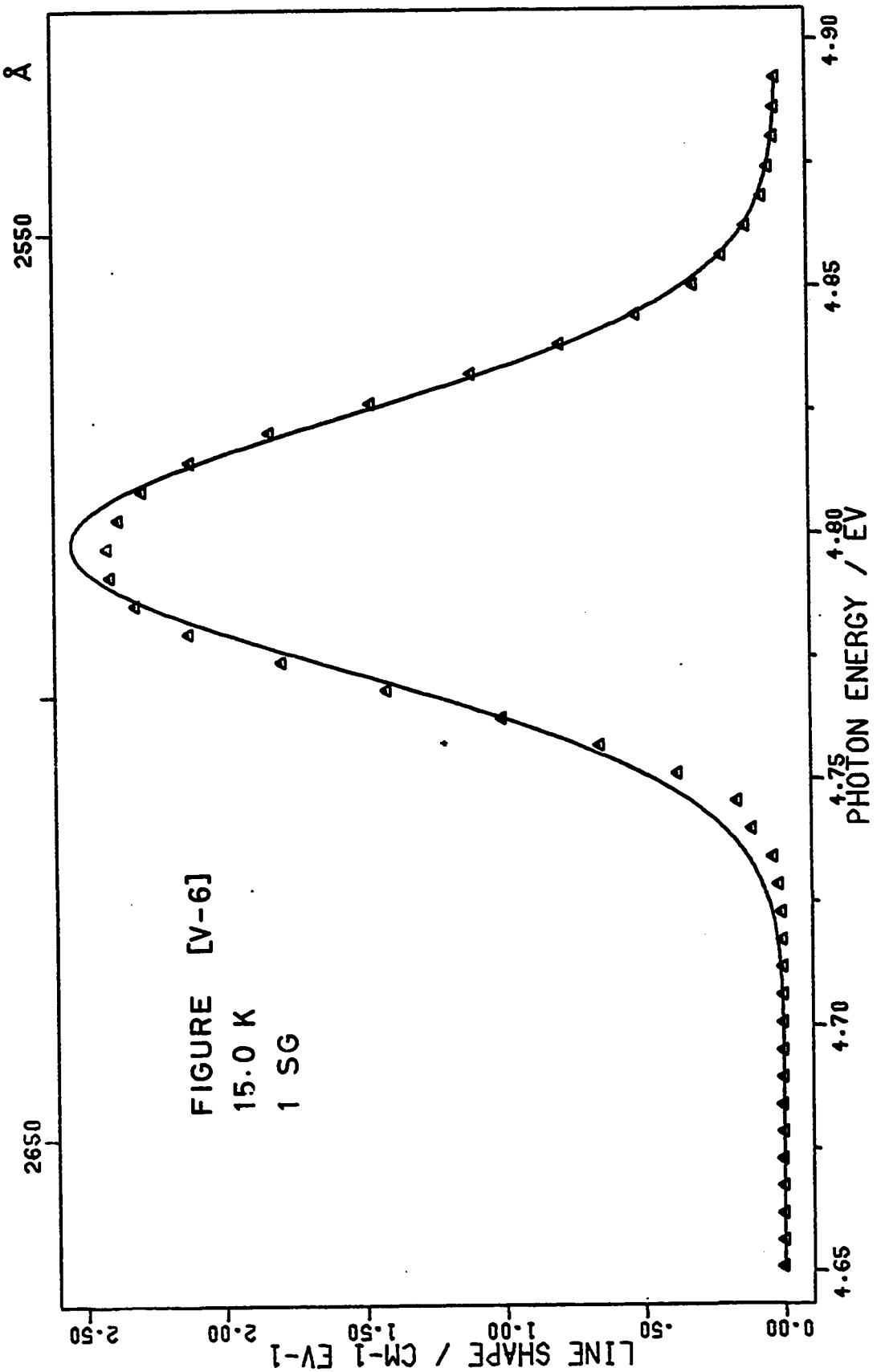
Å
2550
2650
4.65
4.70
4.75
4.80
4.85
4.90
PHOTON ENERGY / EV
0.00
.50
1.00
1.50
2.00
2.50
LINE SHAPE / CM-1 EV-1
FIGURE [V-6]
15.0 K
1 SG

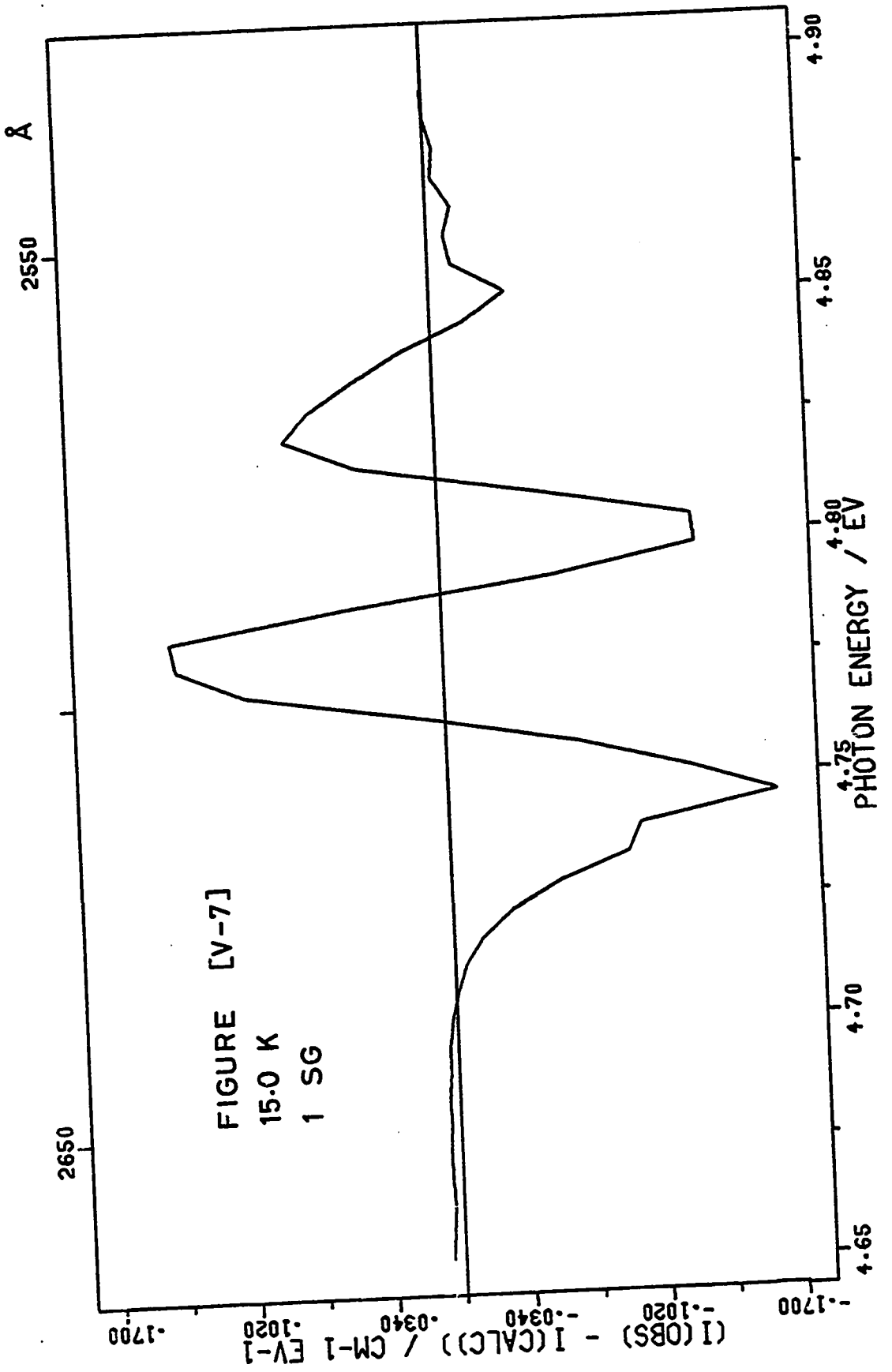
FIGURE [V-7]
15.0 K
1 SG
Å
2550
2650
4.65
4.70
4.75
4.80
4.85
4.90
PHOTON ENERGY / EV
(I(OBS) - I(CALC)) / CM-1 EV-1
-.1700
-.1020
-.0340
.0340
.1020
.1700

FIGURE [V-8]

A-BAND ABSORPTION KBr:Tl^+

1 SYMMETRIC GAUSSIAN BAND

H_{obs} against $T^{\frac{1}{2}}$

O - experimental parameter values

The solid line was calculated from equation [II-78].

$H_0 = 0.0572$ eV

$\nu = 1.62 \times 10^{12}$ sec^{-1}

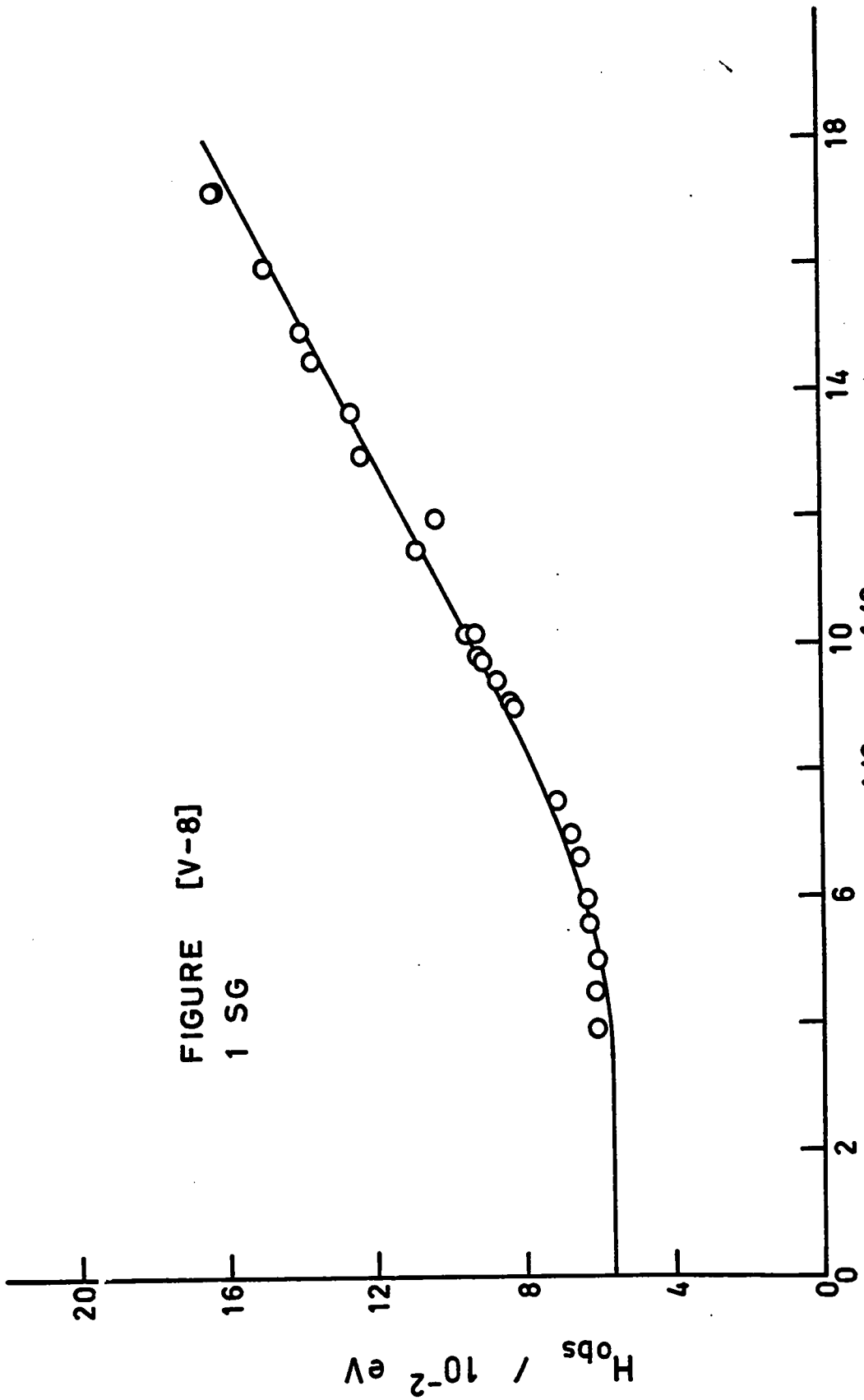

FIGURE [V-8]
1 SG

FIGURE [V-9]

A-BAND ABSORPTION KBr:Tl^+

1 SYMMETRIC GAUSSIAN BAND

E_m against T

O - experimental parameter values

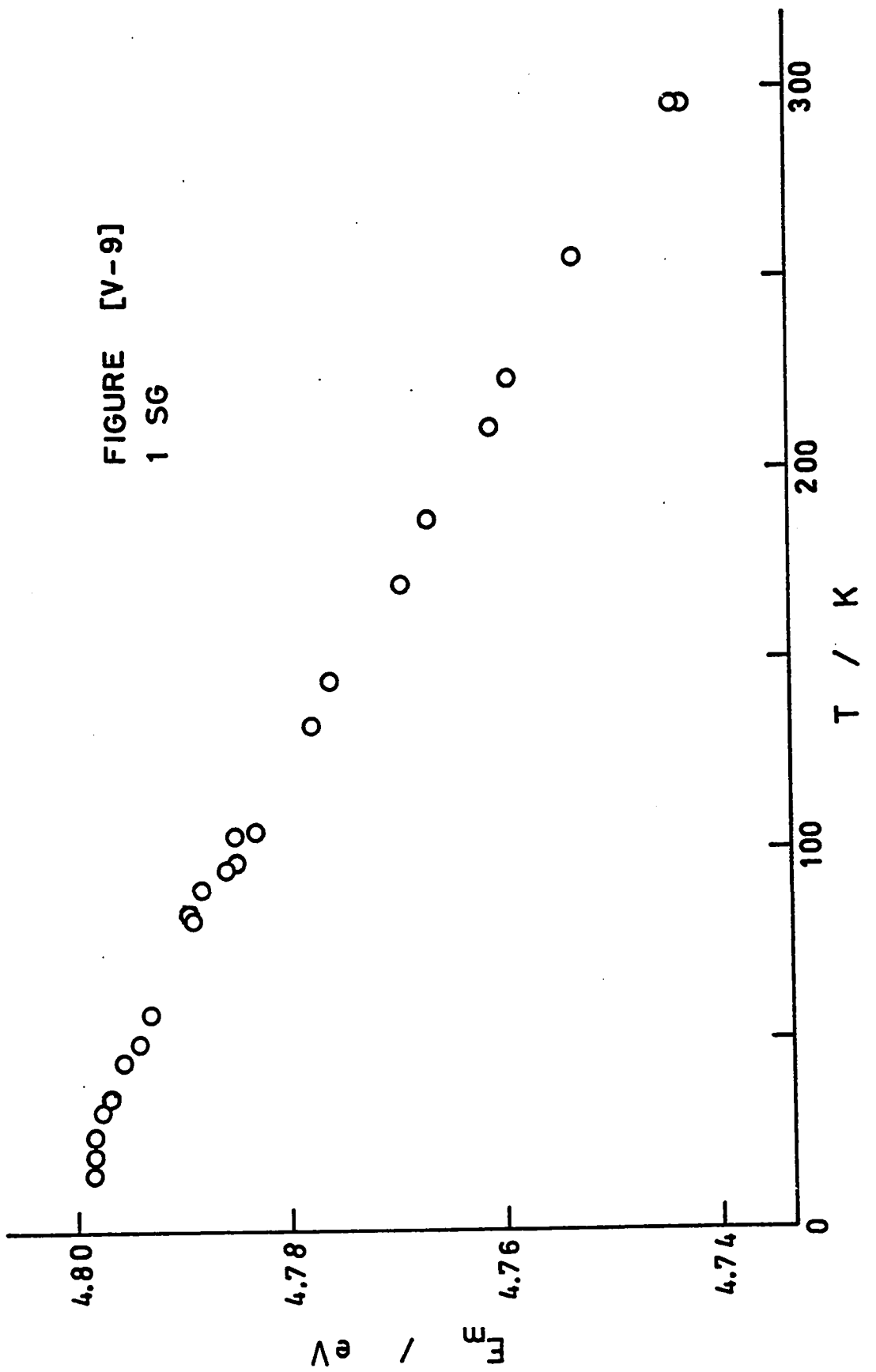

FIGURE [V-9]
1 SG

FIGURE [V-10]

A-BAND ABSORPTION KBr:Tl^+

1 SYMMETRIC GAUSSIAN BAND

I_m against T

O - experimental parameter values

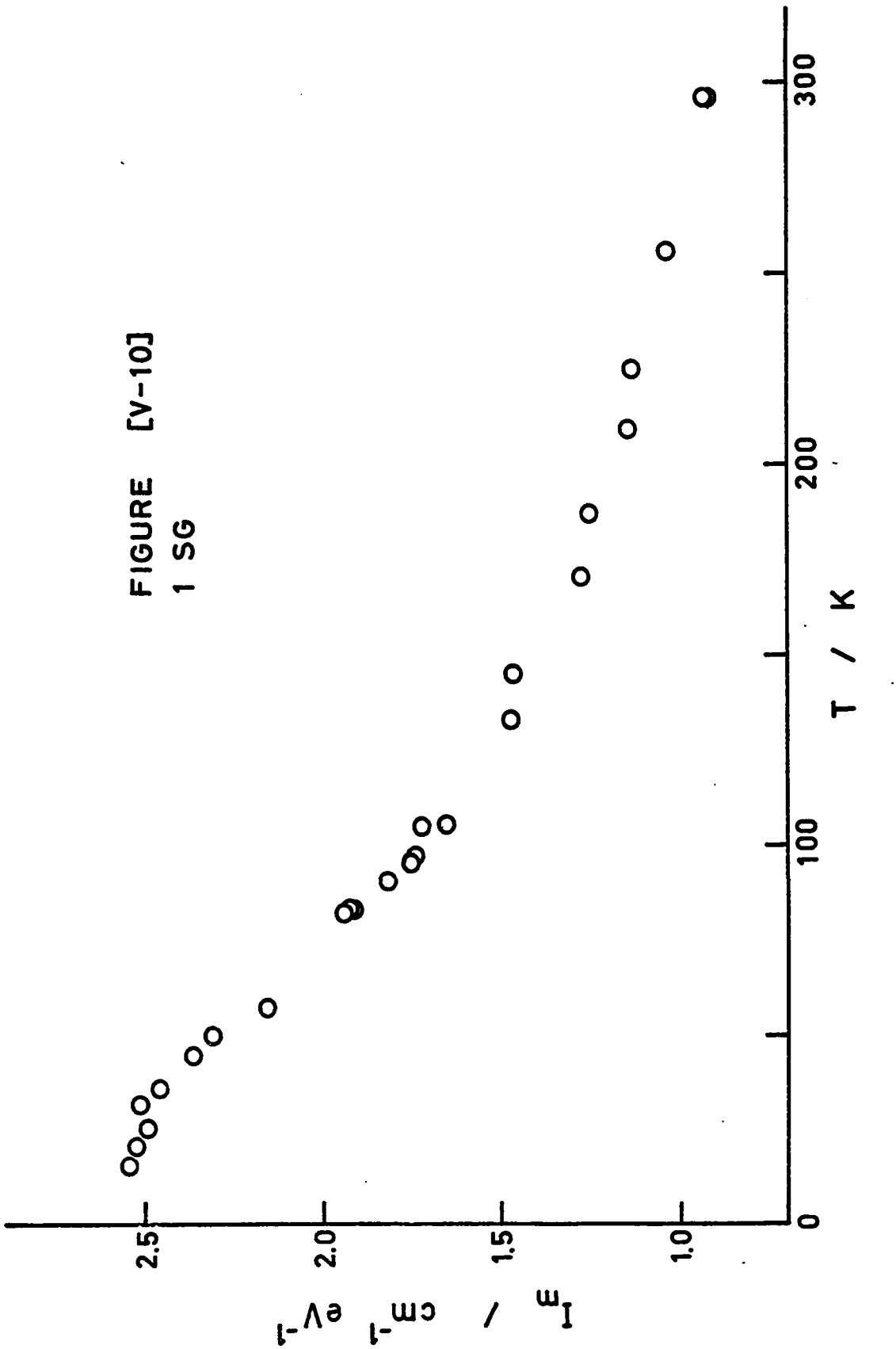
FIGURE [V-10]
1 SG
I_Σ / cm^{-1} eV^{-1}
2.5
2.0
1.5
1.0
0
100
200
300
T / K

A-BAND ABSORPTION KBr:Tl^+

1 ASYMMETRIC GAUSSIAN BAND

RUN 29 - 296.0 K

FIGURE [V-11]

Δ - experimental points

The solid line is the calculated best fit.

FIGURE [V-12]

Plot of I(experimental) - I(calculated) for each experimental point.

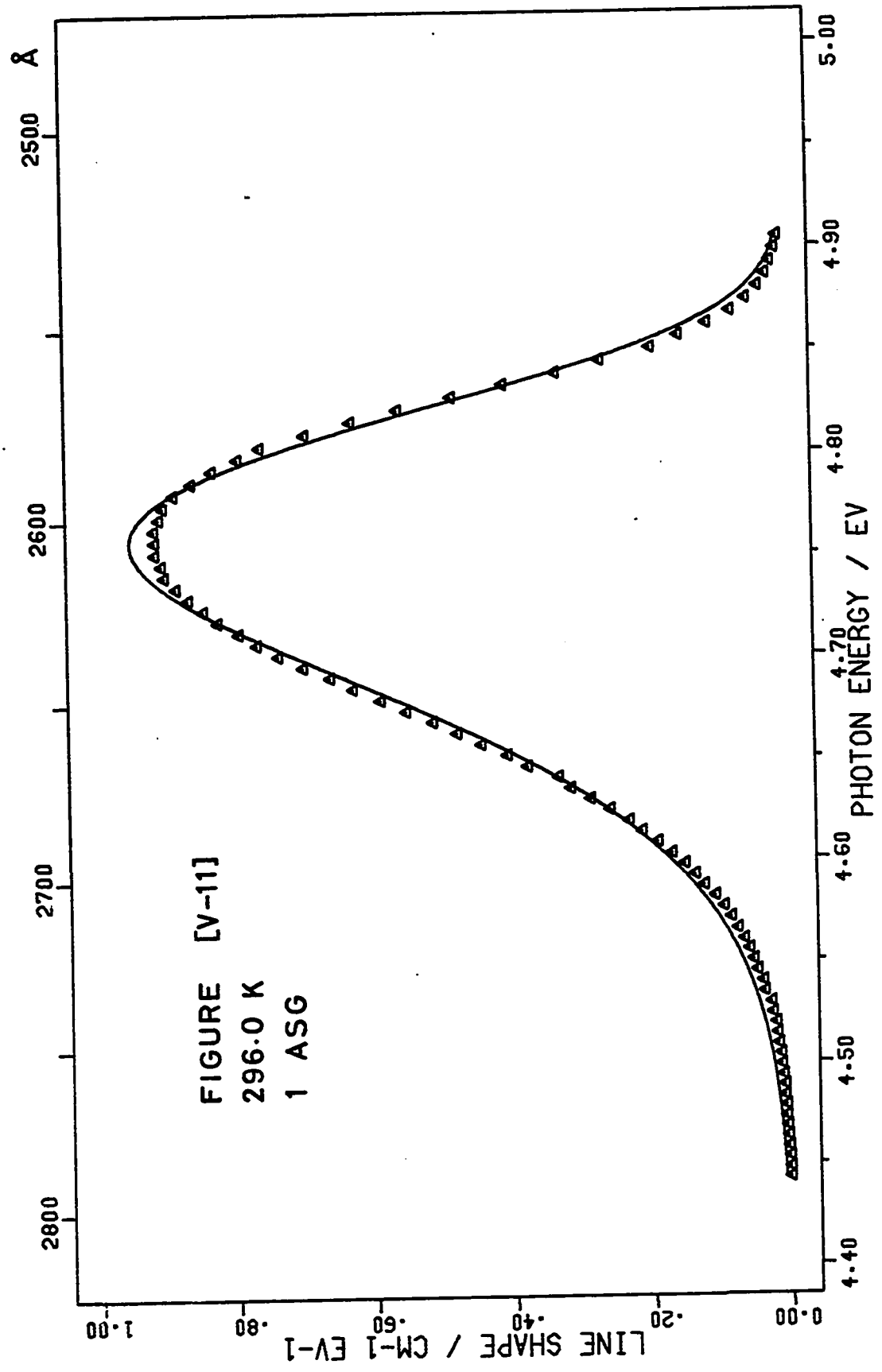
FIGURE [V-11]
296.0 K
1 ASG
LINE SHAPE / CM-1 EV-1
PHOTON ENERGY / EV
Å
0.00
.20
.40
.60
.80
1.00
4.40
4.50
4.60
4.70
4.80
4.90
5.00
2800
2700
2600
2500

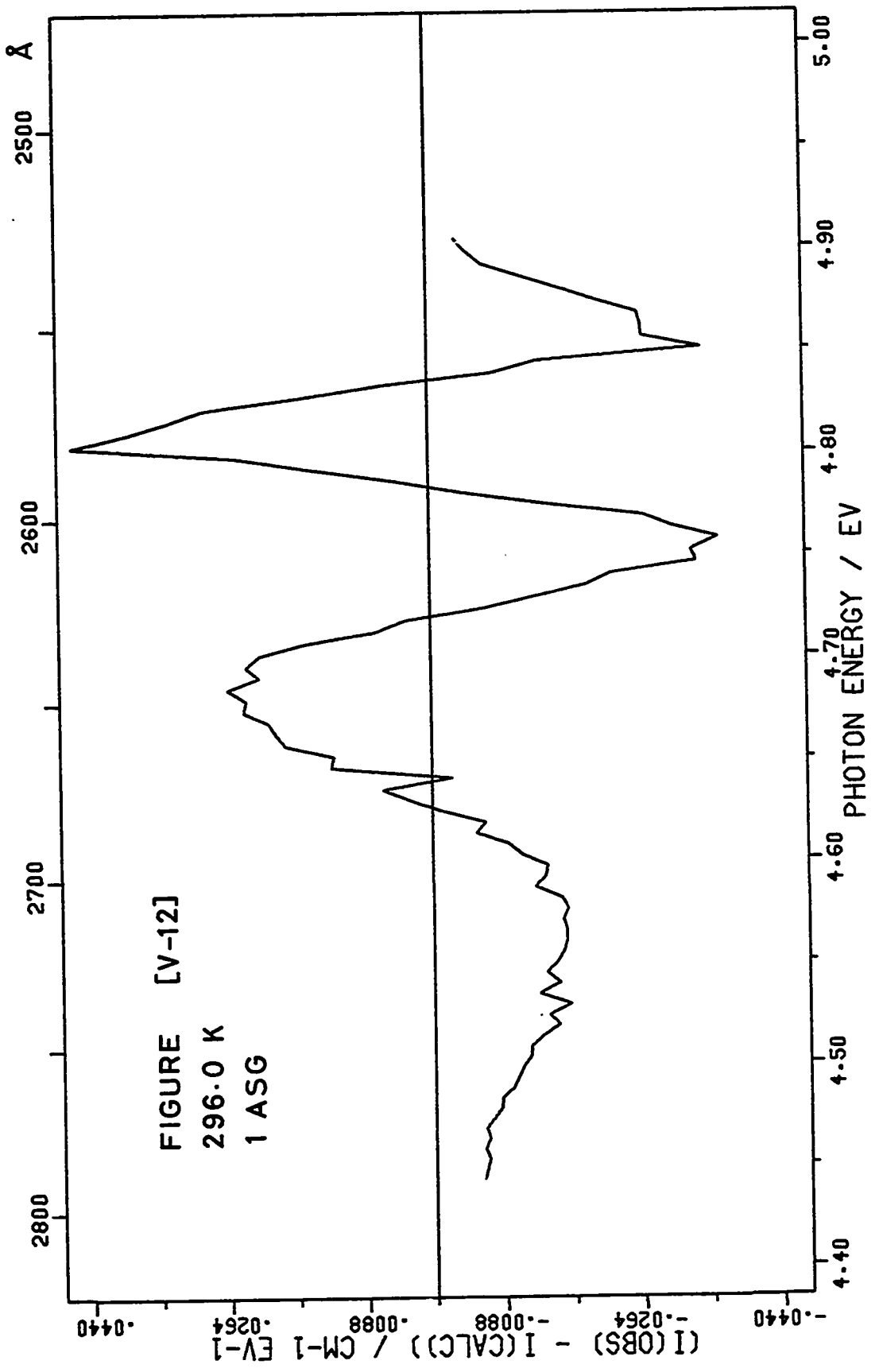
FIGURE [V-12]
296.0 K
1 ASG
Å
2500
2600
2700
2800
5.00
4.90
4.80
4.70
4.60
4.50
4.40
PHOTON ENERGY / EV
(I(OBS) - I(CALC)) / CM-1 EV-1
.0440
.0264
.0088
-.0088
-.0264
-.0440

A-BAND ABSORPTION KBr:Tl^+

1 ASYMMETRIC GAUSSIAN BAND

RUN 30 - 83.0 K

FIGURE [V-13]

Δ - experimental points

The solid line is the calculated best fit.

FIGURE [V-14]

Plot of I(experimental) - I(calculated) for each experimental point.

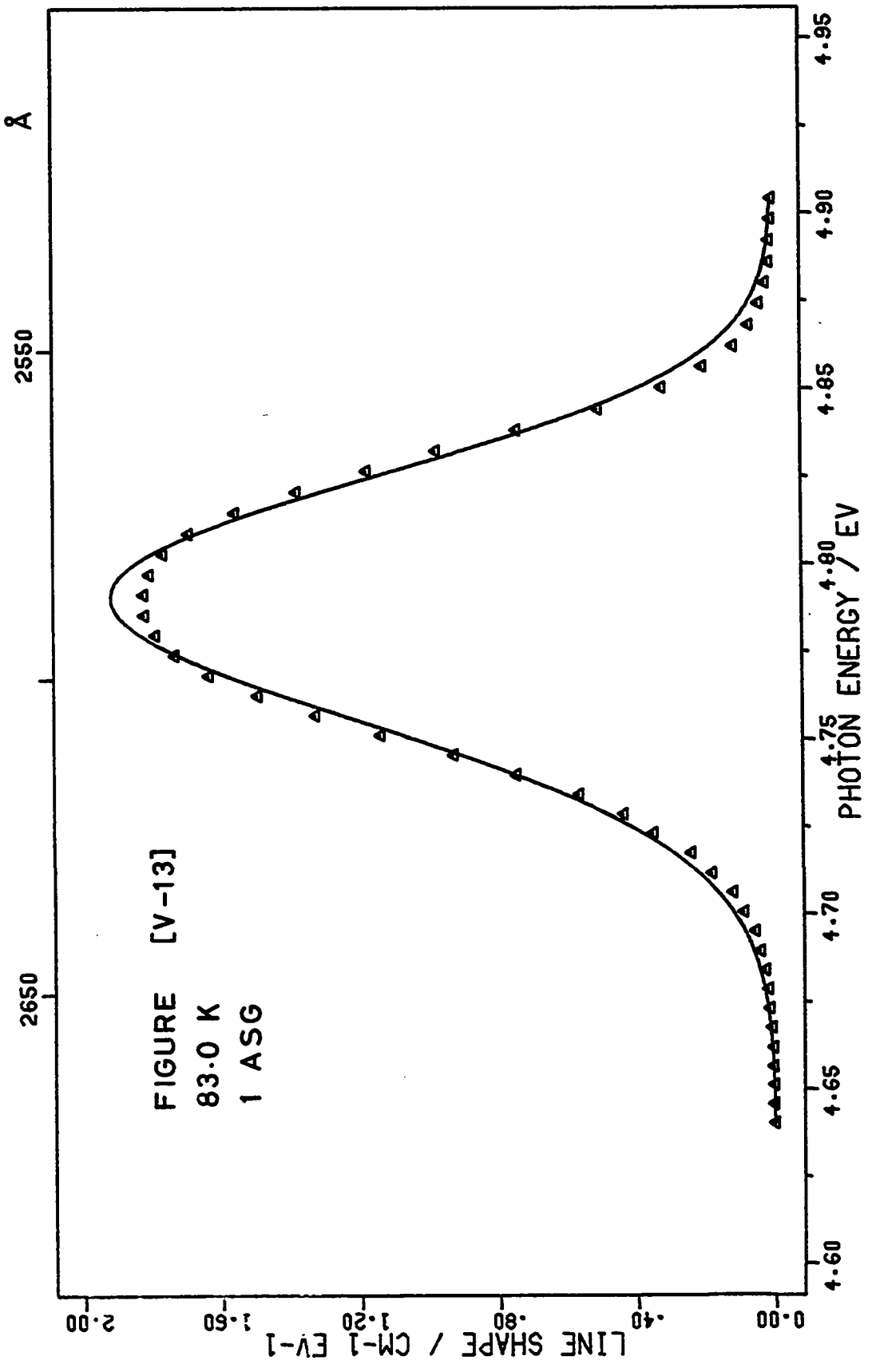
FIGURE [V-13]
83.0 K
1 ASG
Å
2650
2550
LINE SHAPE / CM-1 EV-1
0.00
.40
.80
1.20
1.60
2.00
4.60
4.65
4.70
4.75
4.80
4.85
4.90
4.95
PHOTON ENERGY / EV

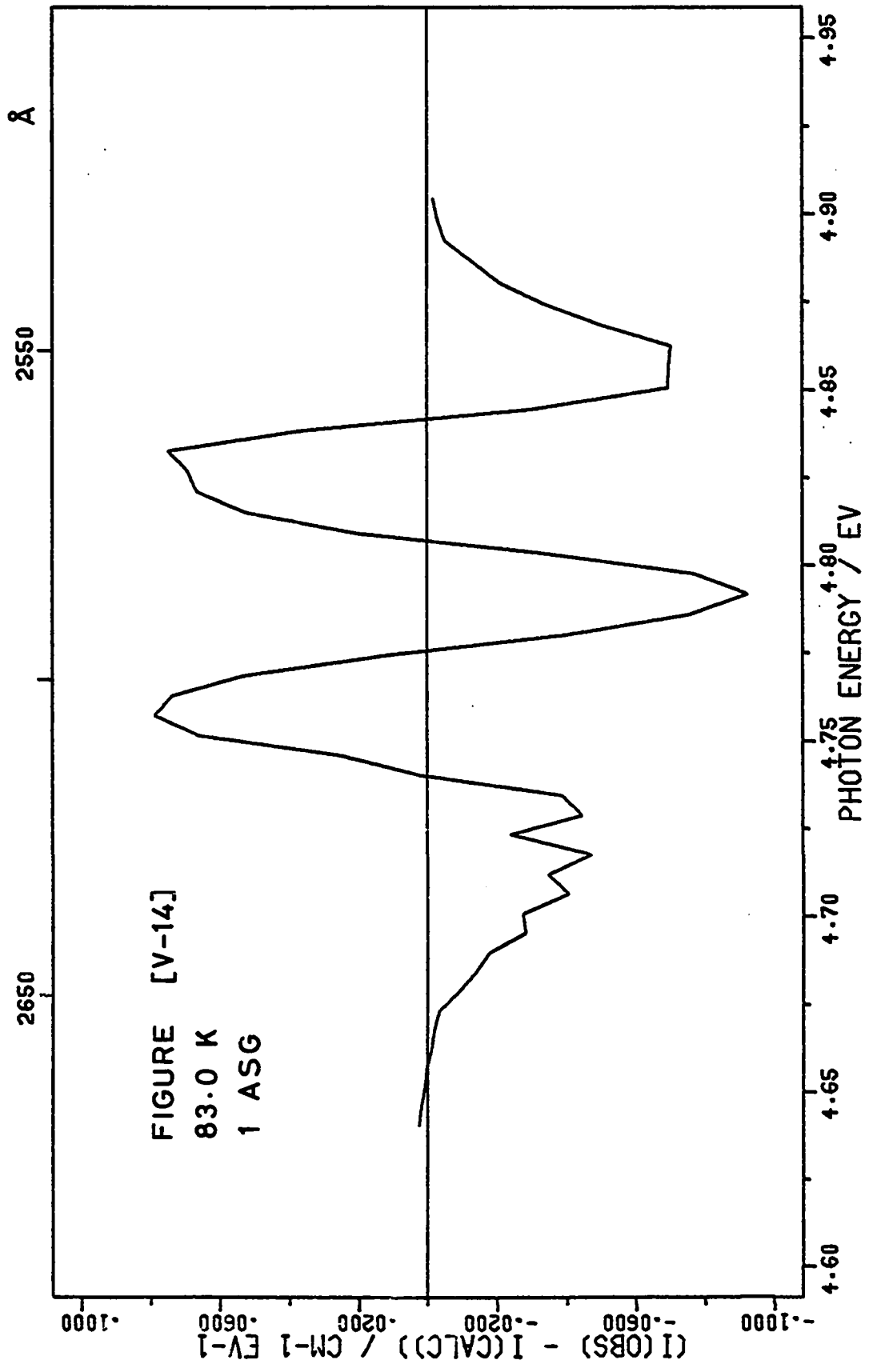
FIGURE [V-14]
83.0 K
1 ASG
Å
2650
2550
4.60
4.65
4.70
4.75
4.80
4.85
4.90
4.95
PHOTON ENERGY / EV
-.1000
-.0600
-.0200
.0200
.0600
.1000
(I(OBS) - I(CALC)) / CM-1 EV-1

A-BAND ABSORPTION KBr:Tl^+

1 ASYMMETRIC GAUSSIAN BAND

RUN 101 - 15.0 K

FIGURE [V-15]

Δ - experimental points

The solid line is the calculated best fit.

FIGURE [V-16]

Plot of I(experimental) - I(calculated) for each experimental point.

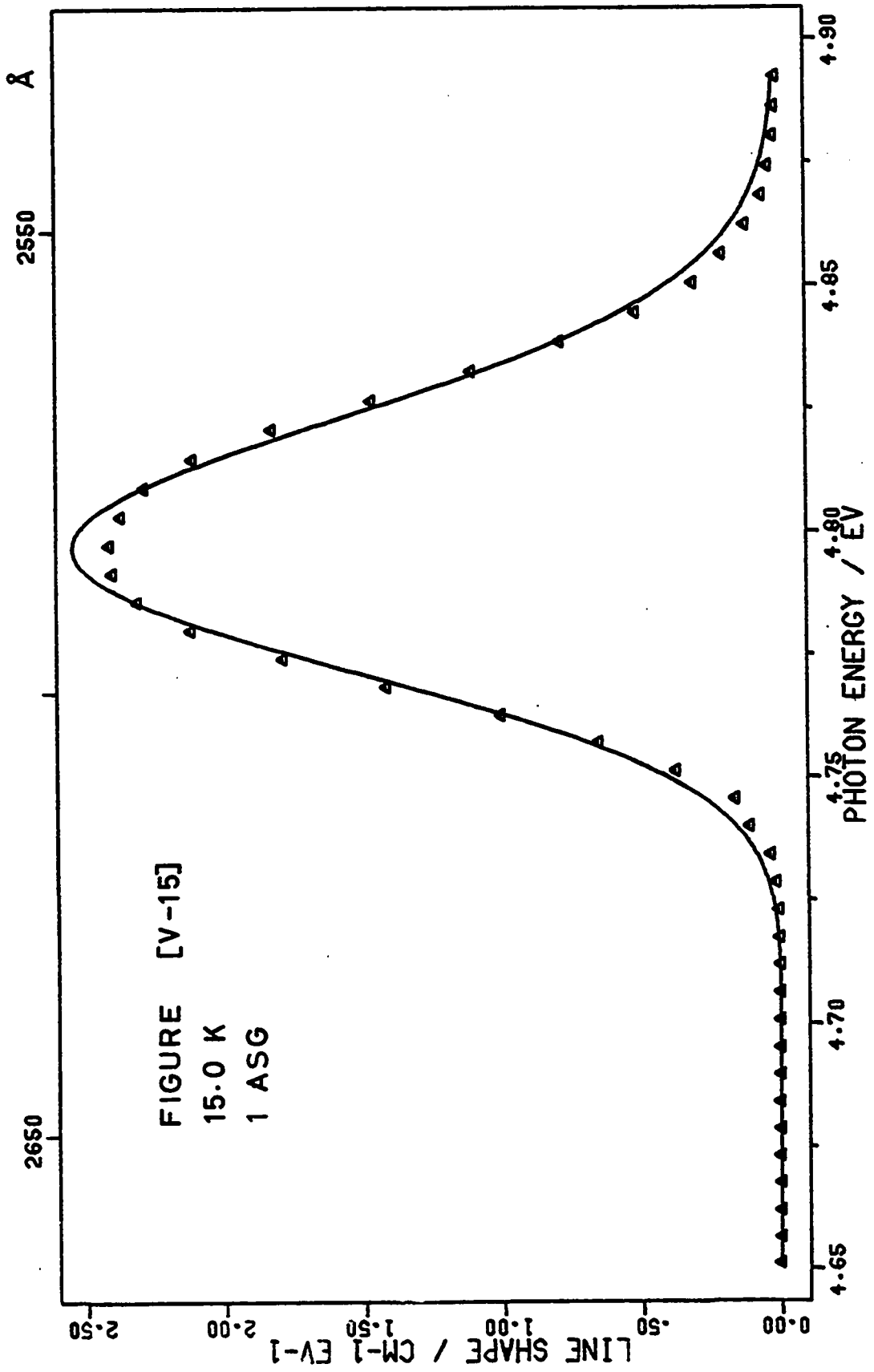
Å
2550
2650
4.65
4.70
4.75
4.80
4.85
4.90
PHOTON ENERGY / EV
0.00
.50
1.00
1.50
2.00
2.50
LINE SHAPE / CM-1 EV-1
FIGURE [V-15]
15.0 K
1 ASG

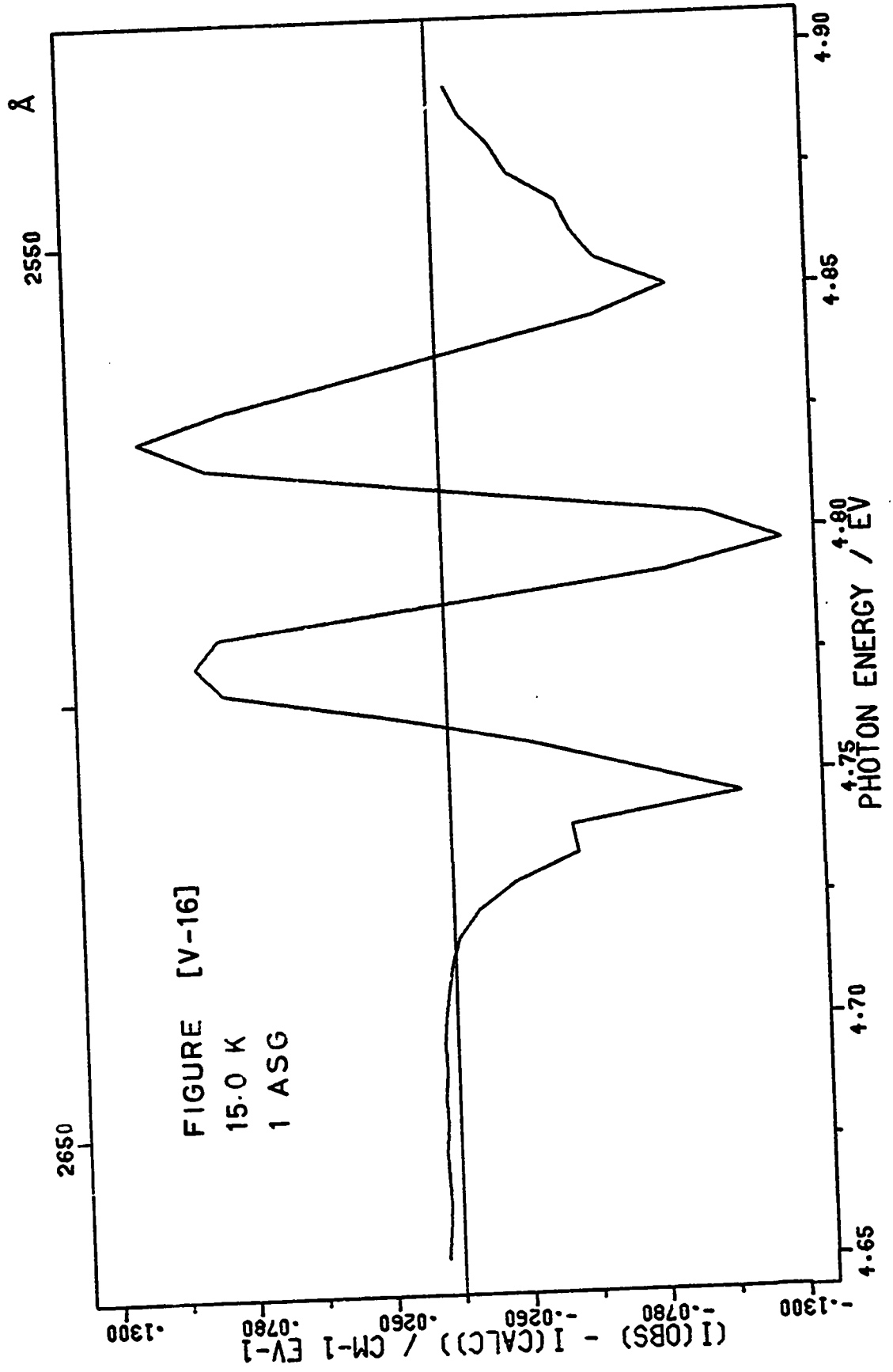
FIGURE [V-16]
15.0 K
1 ASG
2650
2550
Å
4.65
4.70
4.75
4.80
4.85
4.90
PHOTON ENERGY / EV
-.1300
-.0780
-.0260
.0260
.0780
.1300
(I(OBS) - I(CALC)) / CM-1 EV-1

FIGURE [V-17]

A-BAND ABSORPTION KBr:Tl^+

1 ASYMMETRIC GAUSSIAN BAND

H_{obs} against $T^{\frac{1}{2}}$

O - experimental parameter values

The solid line was calculated from equation [II-78].

$H_0 = 0.0577$ eV

$\nu = 1.68 \times 10^{12}$ sec^{-1}

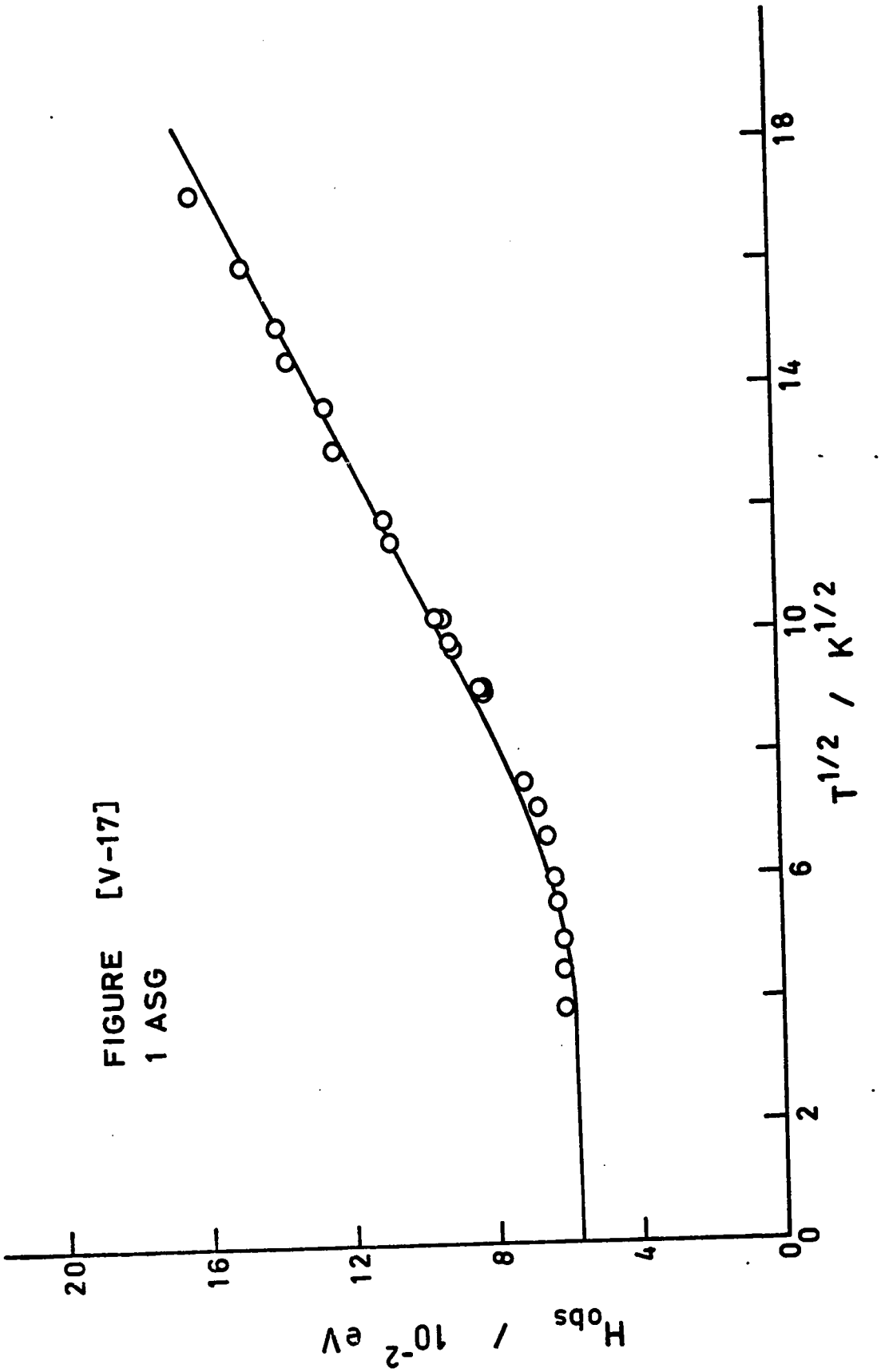

FIGURE [V-17]
1 ASG

FIGURE [V-18]

A-BAND ABSORPTION KBr:Tl^+

1 ASYMMETRIC GAUSSIAN BAND

E_m against T

O - experimental parameter values

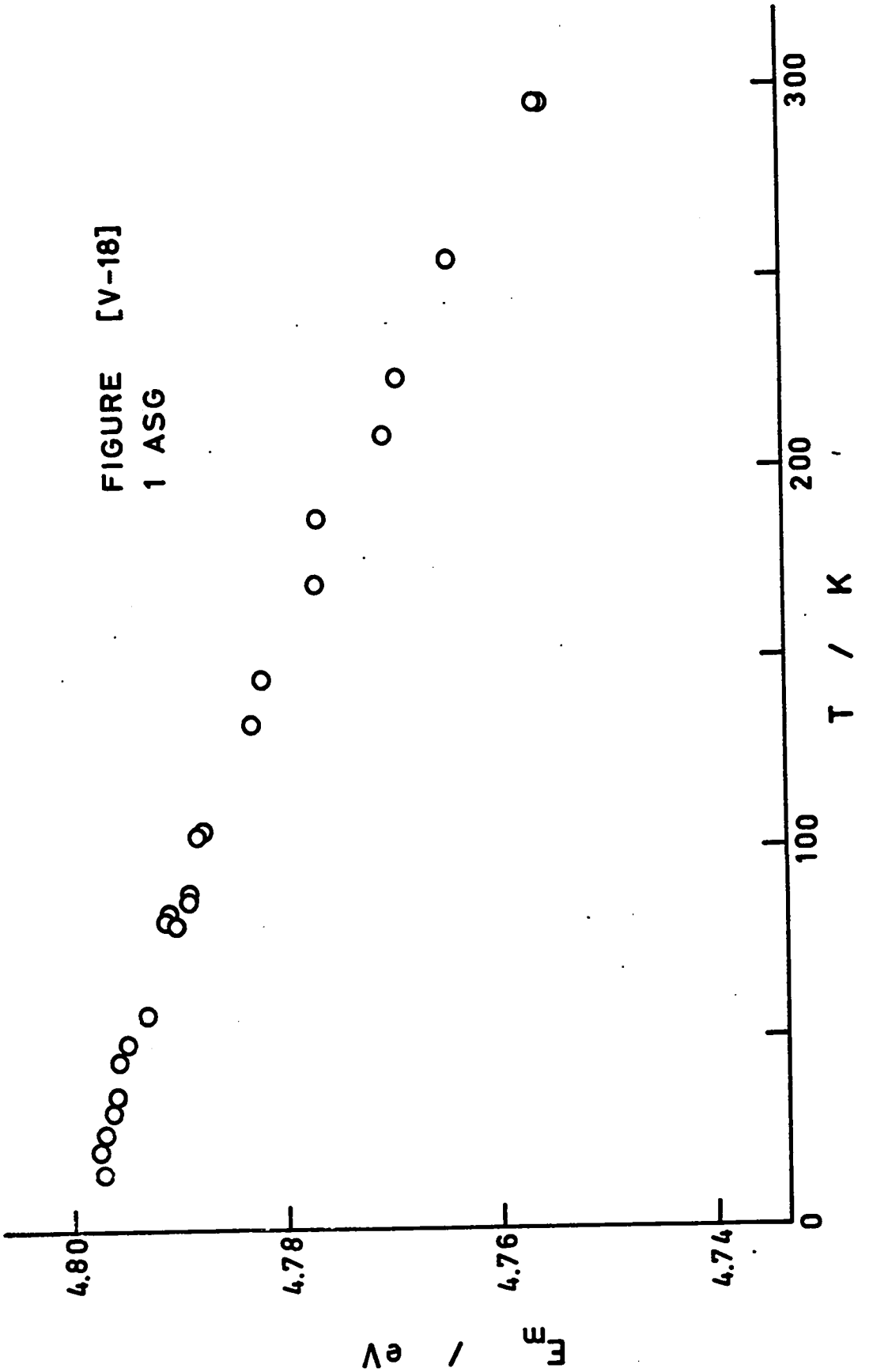

FIGURE [V-18]
1 ASG

FIGURE [V-19]

A-BAND ABSORPTION KBr:Tl^+

1 ASYMMETRIC GAUSSIAN BAND

I_m against T

O - experimental parameter values

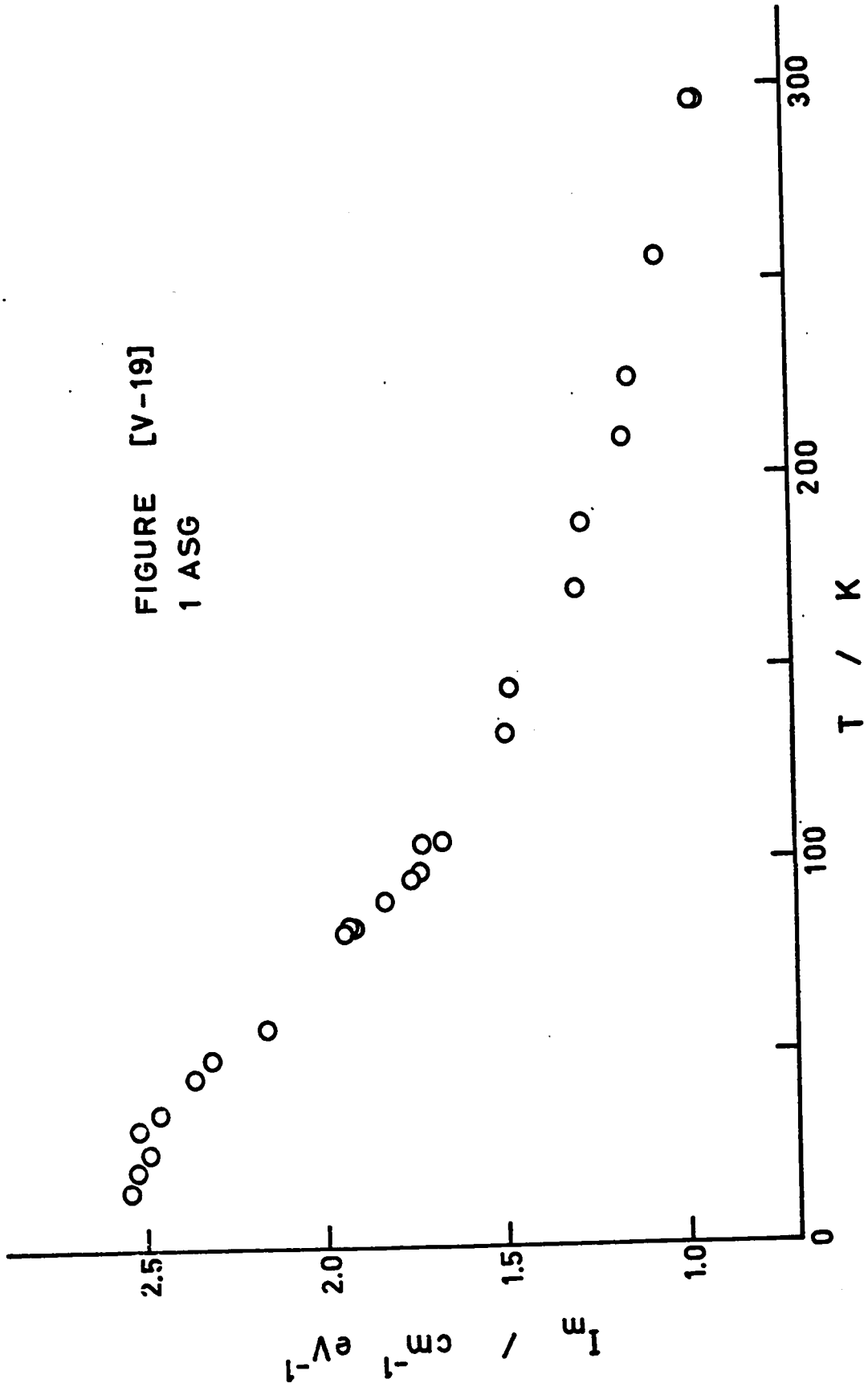
FIGURE [V-19]
1 ASG
I_m / cm^{-1} eV^{-1}
2.5
2.0
1.5
1.0
0
100
200
300
T / K

FIGURE [V-20]

A-BAND ABSORPTION KBr:Tl^+

1 ASYMMETRIC GAUSSIAN BAND

b against T

O - experimental parameter values

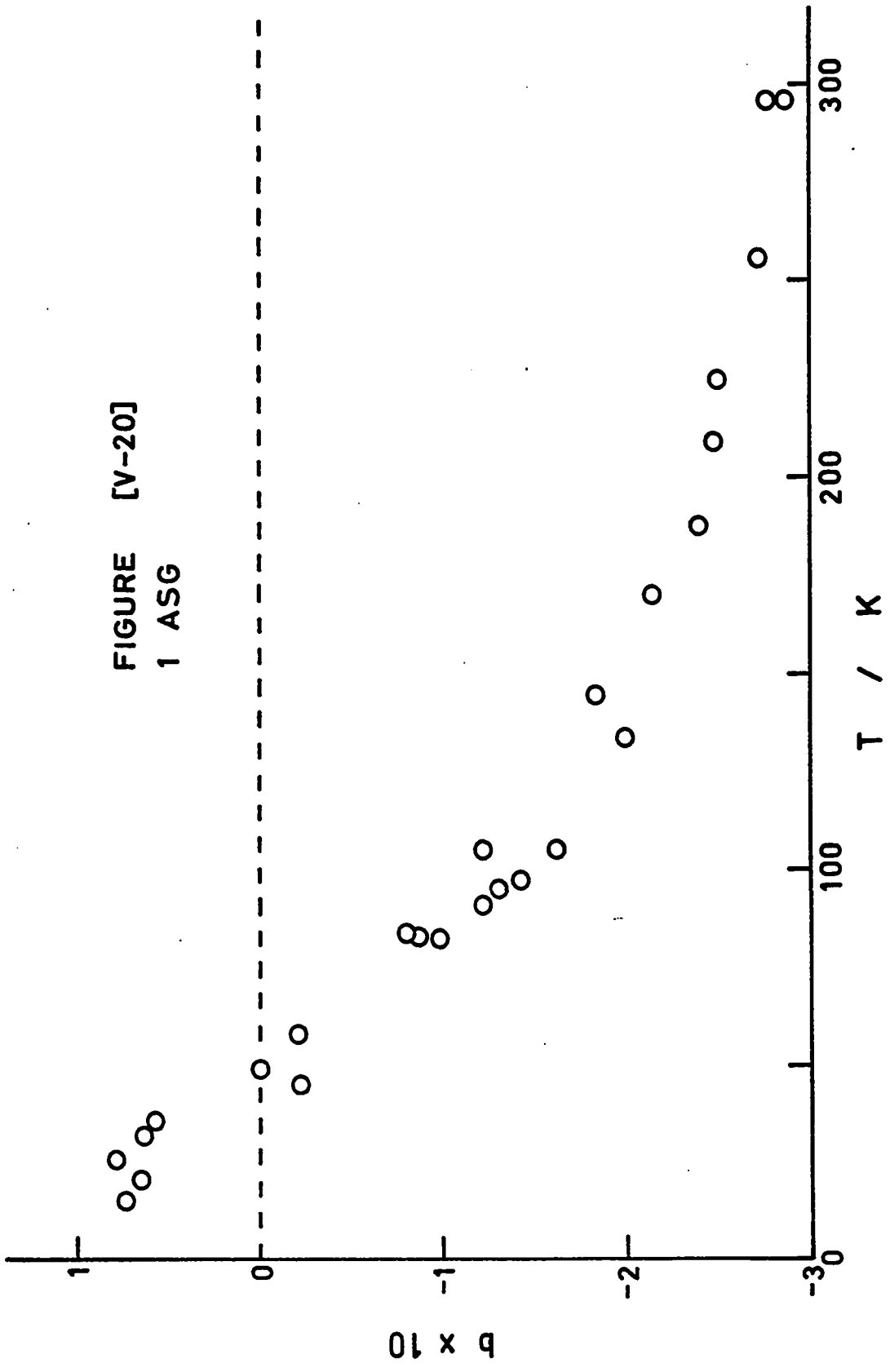

FIGURE [V-20]
1 ASG

A-BAND ABSORPTION KBr:Tl^+

2 SYMMETRIC GAUSSIAN BANDS

RUN 29 - 296.0 K

FIGURE [V-21]

Δ - experimental points

The solid lines are the calculated resolved bands and their sum.

FIGURE [V-22]

Plot of I(experimental) - I(calculated) for each experimental point.

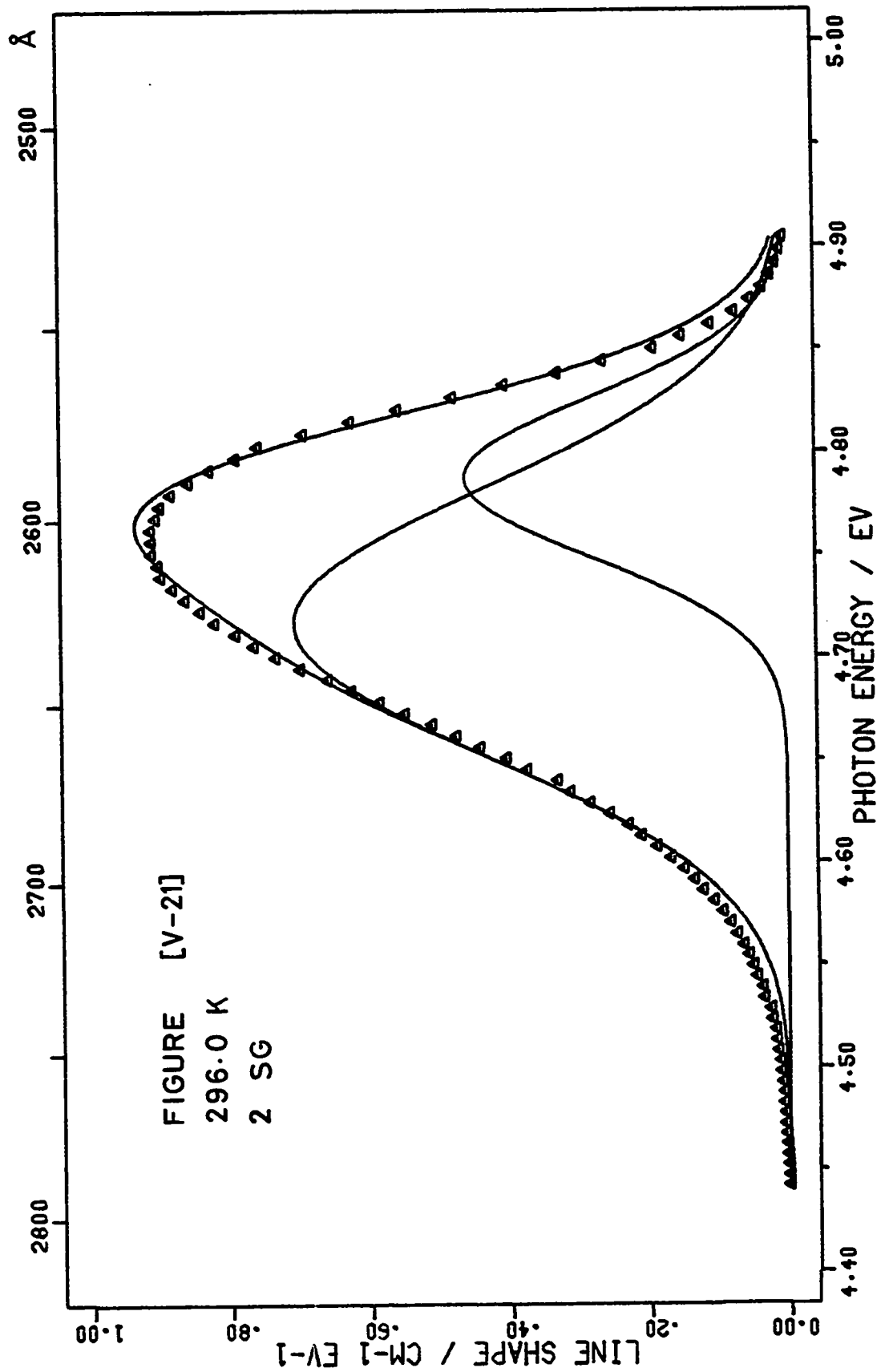
FIGURE [V-21]
296.0 K
2 SG
LINE SHAPE / CM-1 EV-1
PHOTON ENERGY / EV
Å
2800
2700
2600
2500
4.40
4.50
4.60
4.70
4.80
4.90
5.00
0.00
.20
.40
.60
.80
1.00

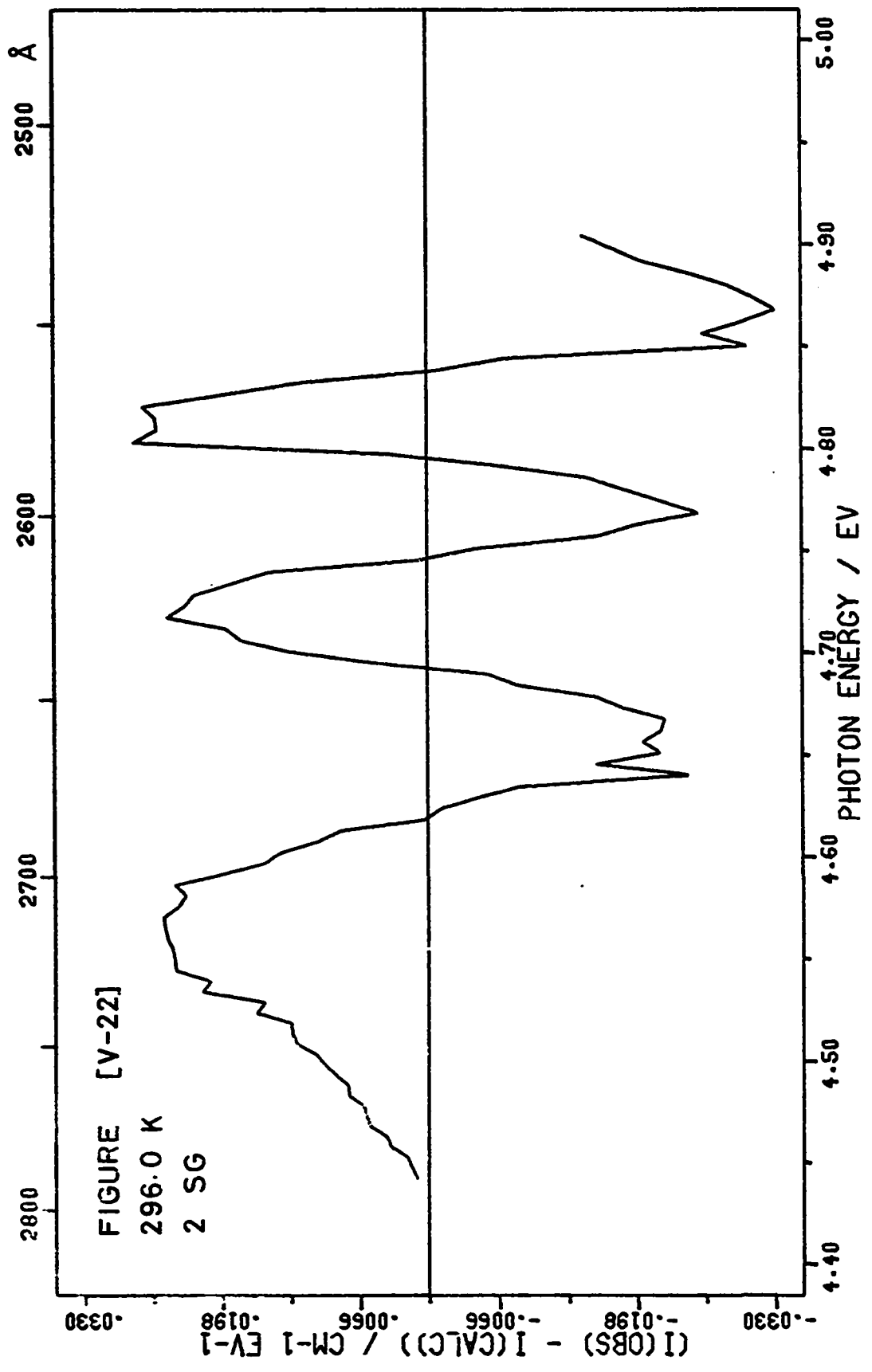
FIGURE [V-22]
296.0 K
2 SG
2800
2700
2600
2500 Å
4.40
4.50
4.60
4.70
4.80
4.90
5.00
PHOTON ENERGY / EV
-.0330
-.0198
-.0066
.0066
.0198
.0330
(I(OBS) - I(CALC)) / CM-1 EV-1

A-BAND ABSORPTION KBr:Tl^+

2 SYMMETRIC GAUSSIAN BANDS

RUN 30 - 83.0 K

FIGURE [V-23]

Δ - experimental points

The solid lines are the calculated resolved bands and their sum.

FIGURE [V-24]

Plot of I(experimental) - I(calculated) for each experimental point.

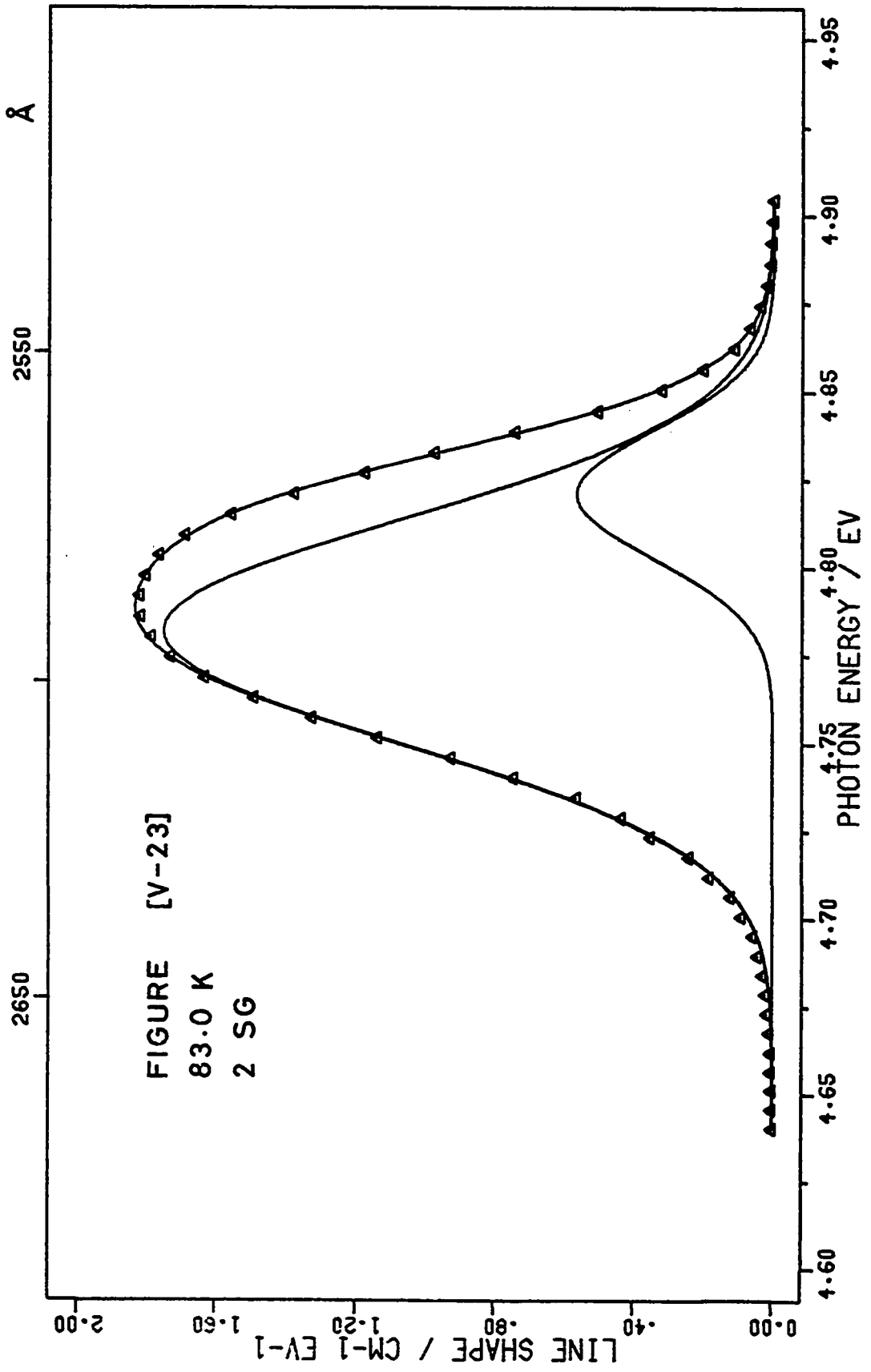
FIGURE [V-23]
83.0 K
2 SG
Å
2650
2550
LINE SHAPE / CM-1 EV-1
0.00
.40
.80
1.20
1.60
2.00
4.60
4.65
4.70
4.75
4.80
4.85
4.90
4.95
PHOTON ENERGY / EV

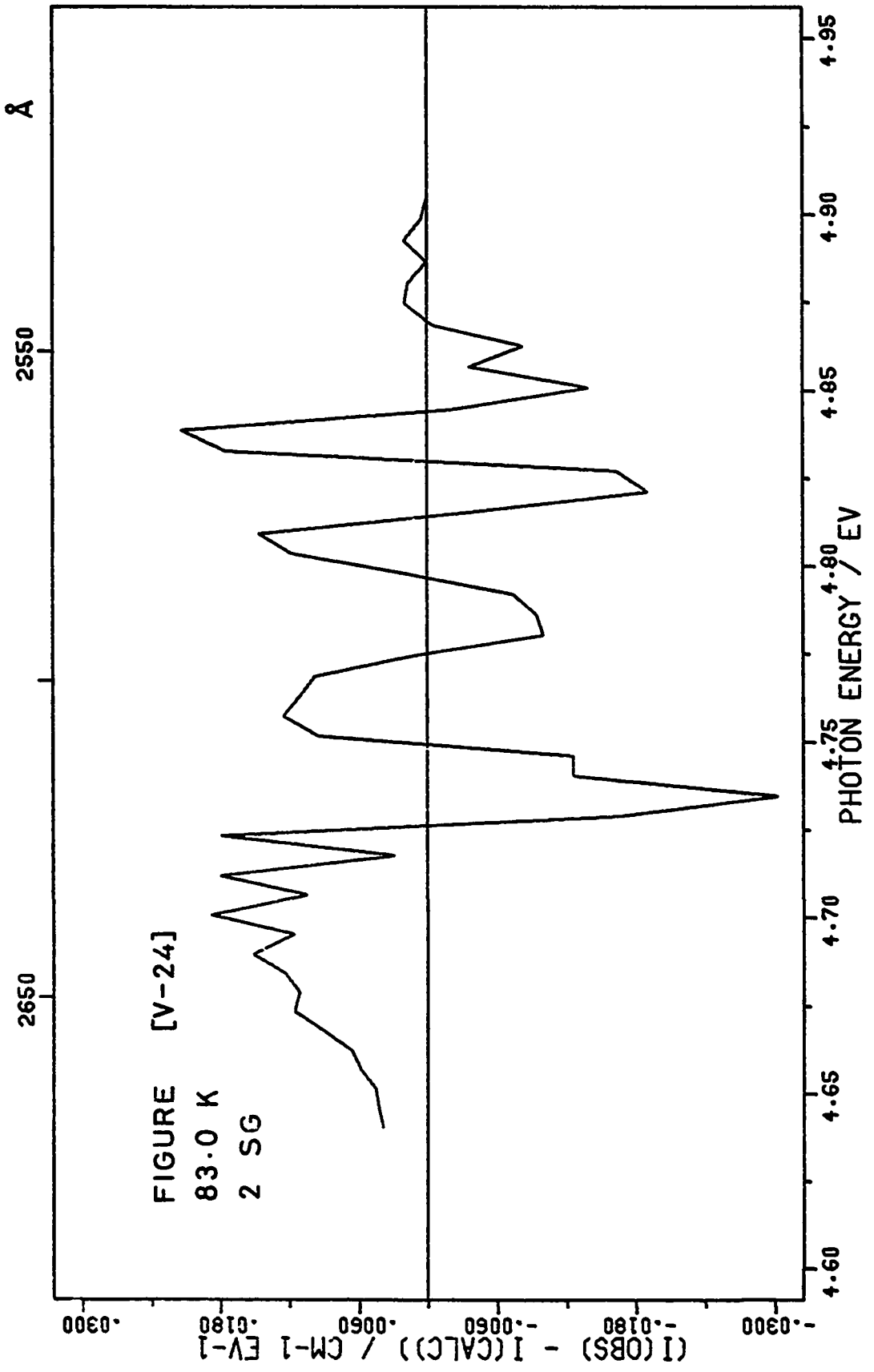
FIGURE [V-24]
83.0 K
2 SG
Å
2650
2550
4.60
4.65
4.70
4.75
4.80
4.85
4.90
4.95
PHOTON ENERGY / EV
(I(OBS) - I(CALC)) / CM-1 EV-1
-.0300
-.0180
-.0060
.0060
.0180
.0300

A-BAND ABSORPTION KBr:Tl^+

2 SYMMETRIC GAUSSIAN BANDS

RUN 101 - 15.0 K

FIGURE [V-25]

Δ - experimental points

The solid lines are the calculated resolved bands and their sum.

FIGURE [V-26]

Plot of I(experimental) - I(calculated) for each experimental point.

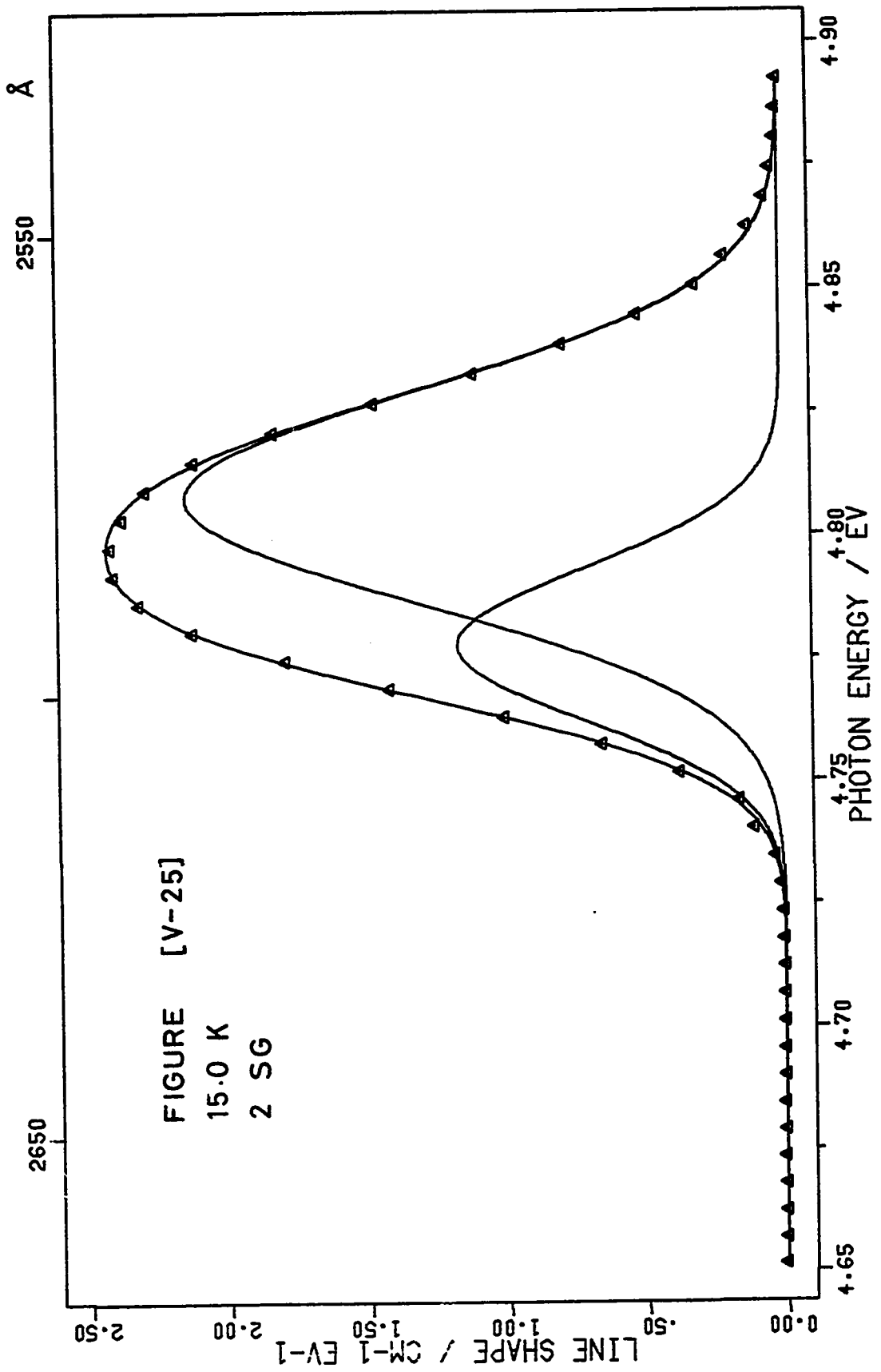
FIGURE [V-25]
15.0 K
2 SG
LINE SHAPE / CM-1 EV-1
PHOTON ENERGY / EV
Å
2650
2550
0.00
.50
1.00
1.50
2.00
2.50
4.65
4.70
4.75
4.80
4.85
4.90

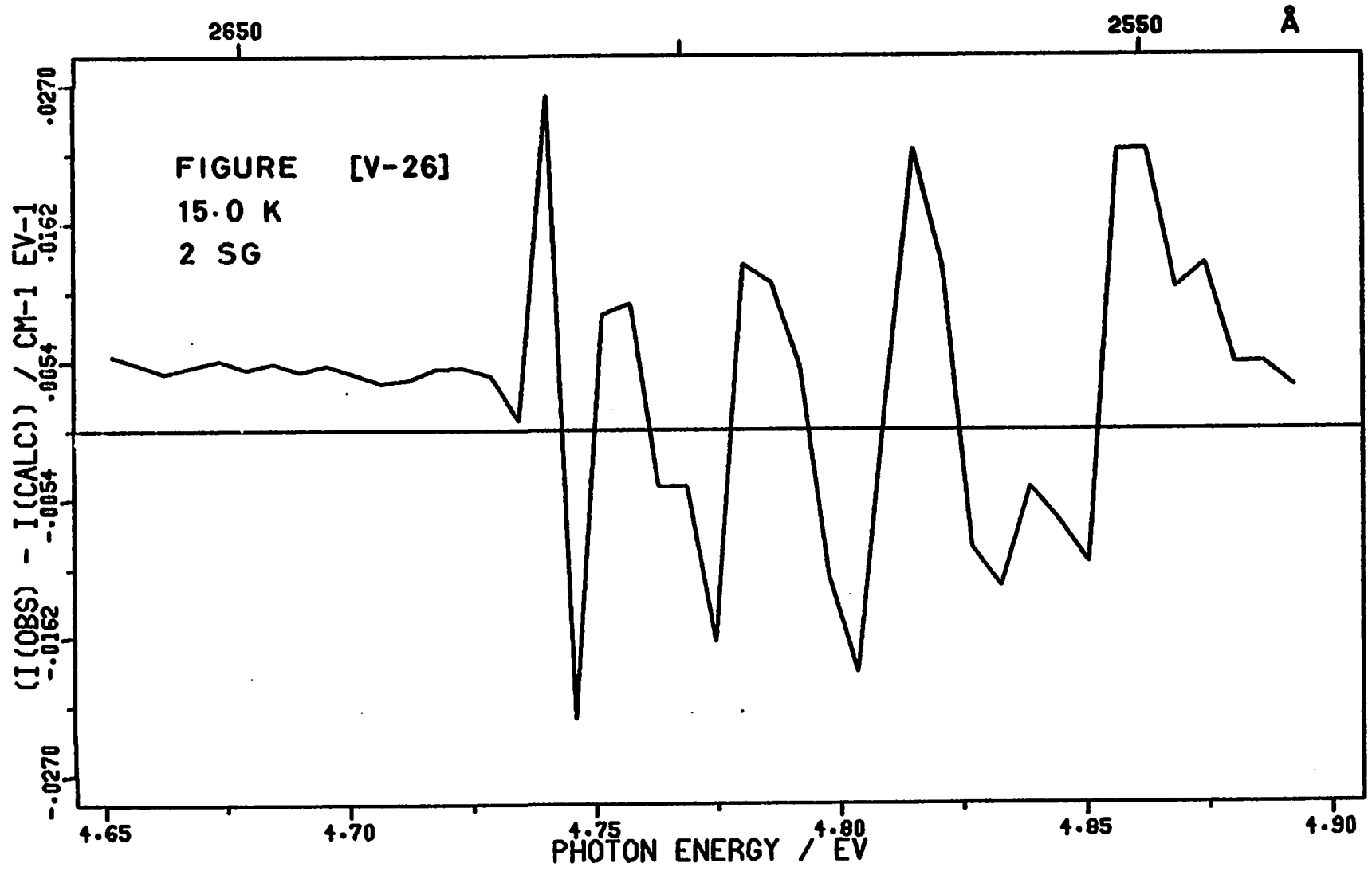
2650
2550
Å
FIGURE [V-26]
15.0 K
2 SG
(I(OBS) - I(CALC)) / CM-1 EV-1
.0270
.0162
.0054
-.0054
-.0162
-.0270
4.65
4.70
4.75
4.80
4.85
4.90
PHOTON ENERGY / EV

FIGURE [V-27]

A-BAND ABSORPTION KBr:Tl^+

2 SYMMETRIC GAUSSIAN BANDS

H_{obs} against $T^{\frac{1}{2}}$

■ - experimental parameter values Band 1

O - experimental parameter values Band 2

The solid lines were calculated from equation [II-78].

Band 1	Band 2
$H_0 = 0.044$ eV	$H_0 = 0.035$ eV
$\nu = 3.8 \times 10^{12}$ sec^{-1}	$\nu = 6.9 \times 10^{11}$ sec^{-1}

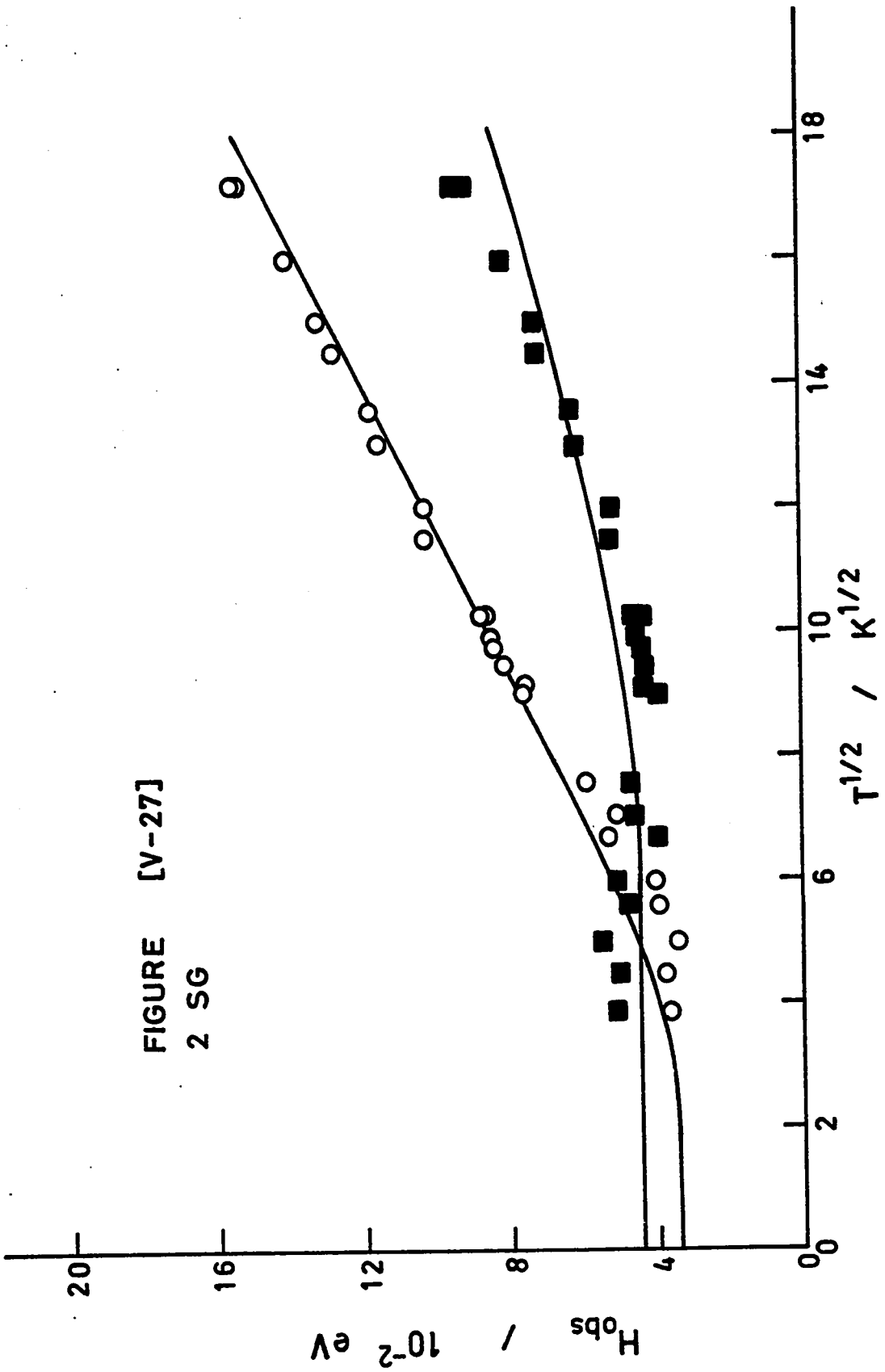

FIGURE [V-27]
2 SG

FIGURE [V-28]

A-BAND ABSORPTION KBr:Tl^+

2 SYMMETRIC GAUSSIAN BANDS

E_m against T

■ - experimental parameter values Band 1

○ - experimental parameter values Band 2

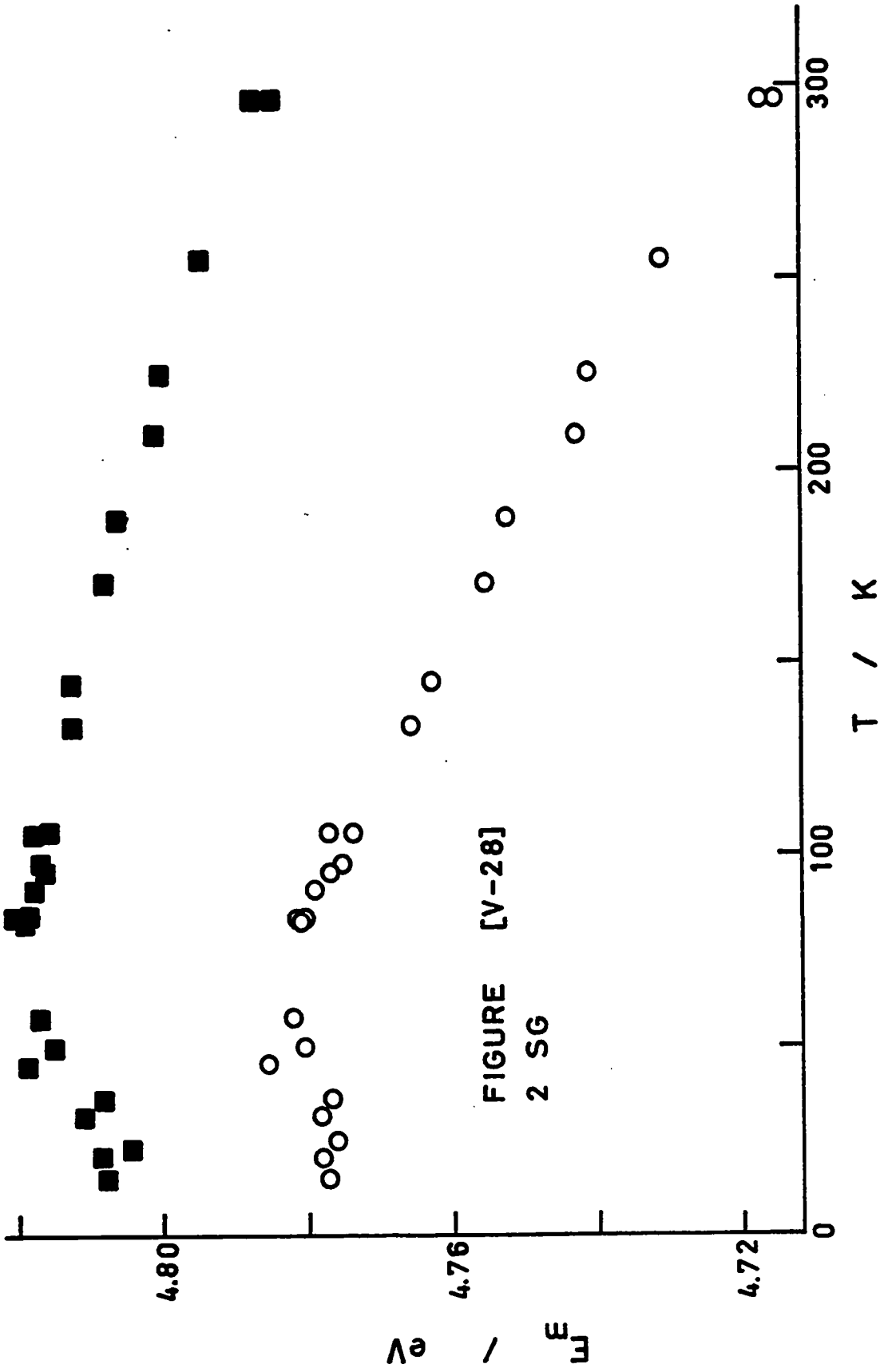

FIGURE [V-28]
2 SG

FIGURE [V-29]

A-BAND ABSORPTION KBr:Tl^+

2 SYMMETRIC GAUSSIAN BANDS

I_m against T

■ - experimental parameter values Band 1

○ - experimental parameter values Band 2

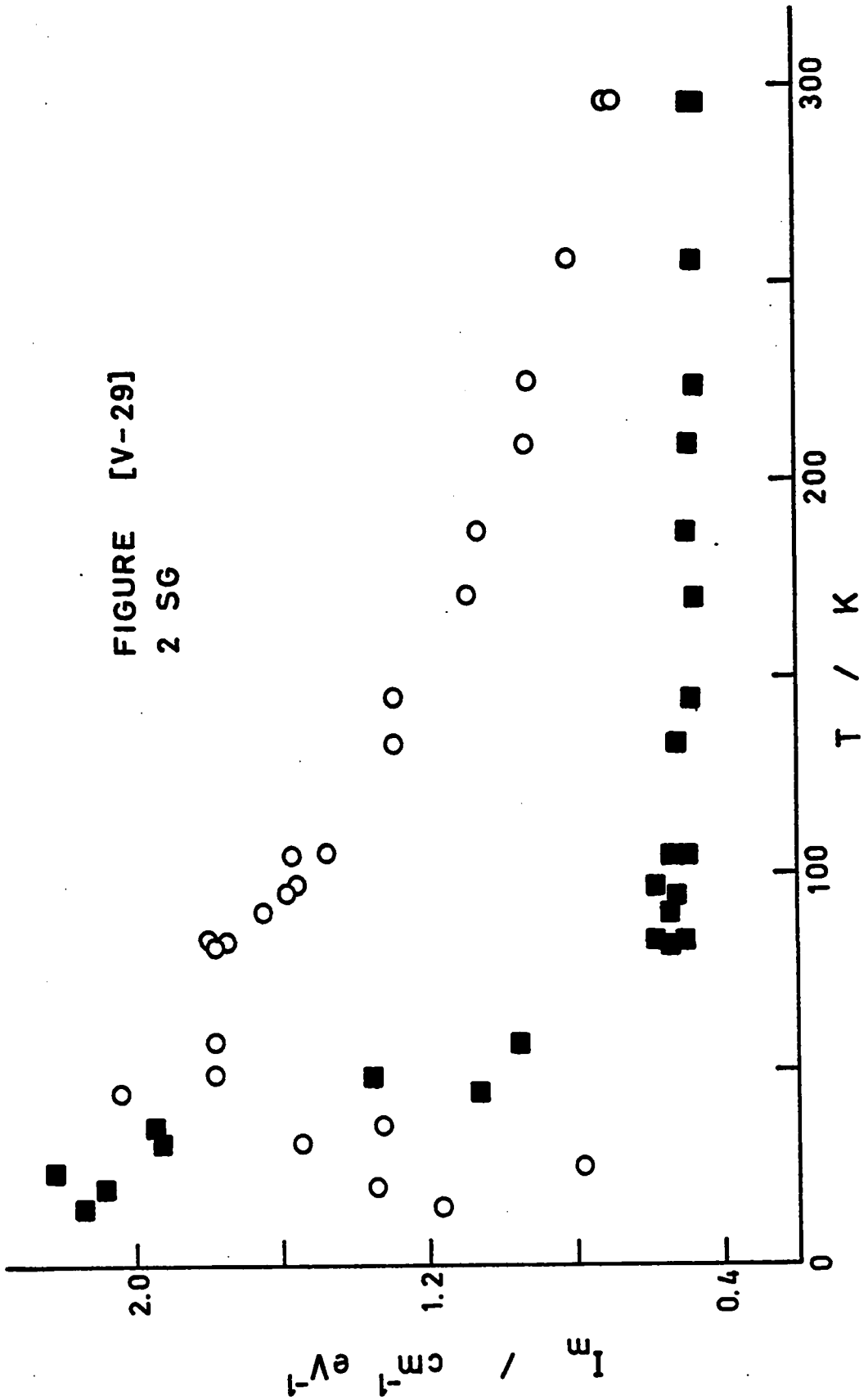
FIGURE [V-29]
2 SG
I_ε / cm^{-1} eV^{-1}
2.0
1.2
0.4
0
100
200
300
T / K

FIGURE [V-30]

A-BAND ABSORPTION KBr:Tl^+

2 SYMMETRIC GAUSSIAN BANDS

$\Delta E_{splitting}$ against $T^{1/2}$

O - experimental values

The solid line was calculated from equation [VI-27].

$\Delta E_o = 0.031$ eV

$\nu = 2.53 \times 10^{12}\ sec^{-1}$

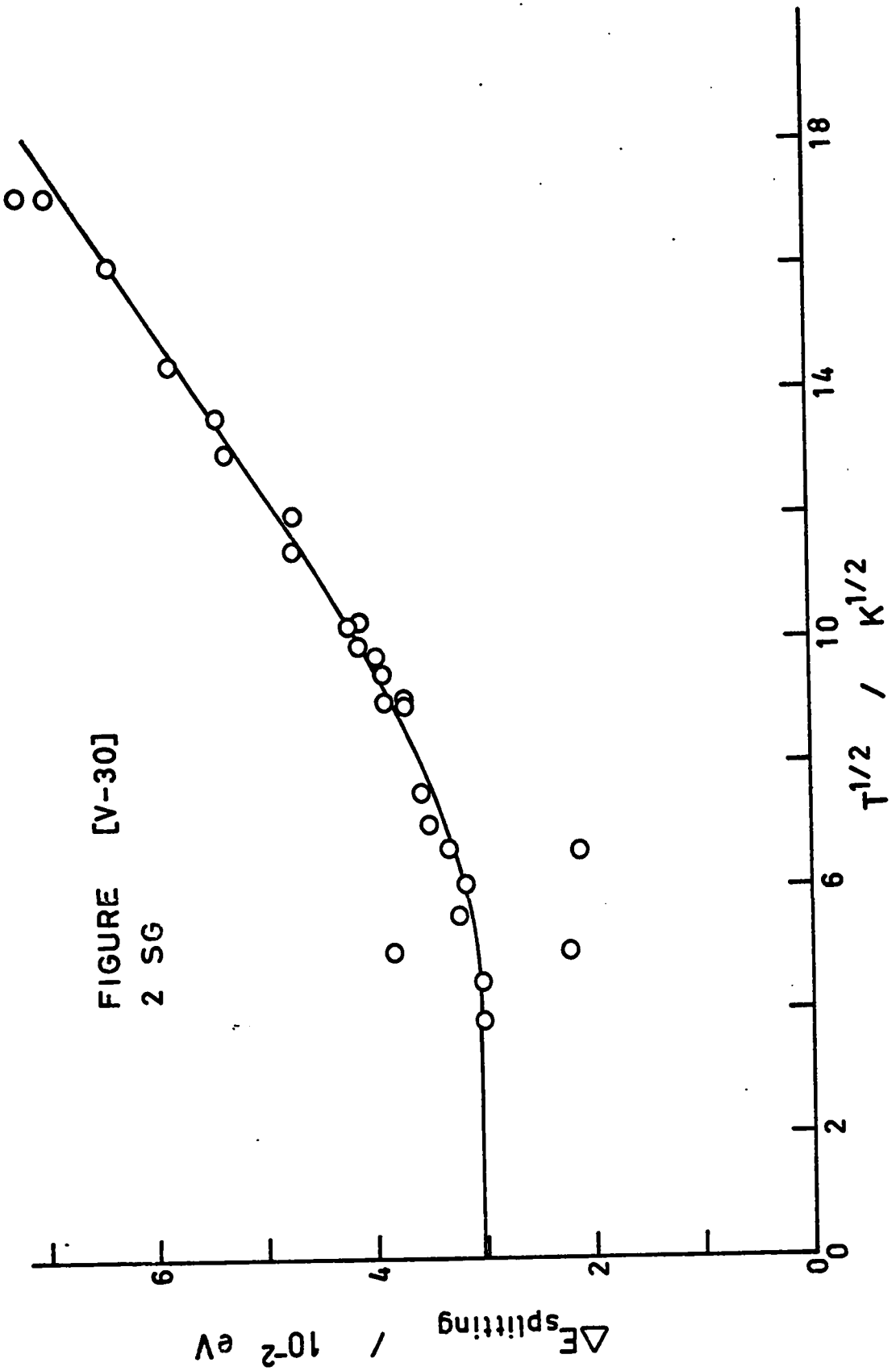

FIGURE [V-30]
2 SG

A-BAND ABSORPTION KBr:Tl^+

2 ASYMMETRIC GAUSSIAN BANDS

RUN 29 - 296.0 K

FIGURE [V-31]

Δ - experimental points

The solid lines are the calculated resolved bands and their sum.

FIGURE [V-32]

Plot of I(experimental) - I(calculated) for each experimental point.

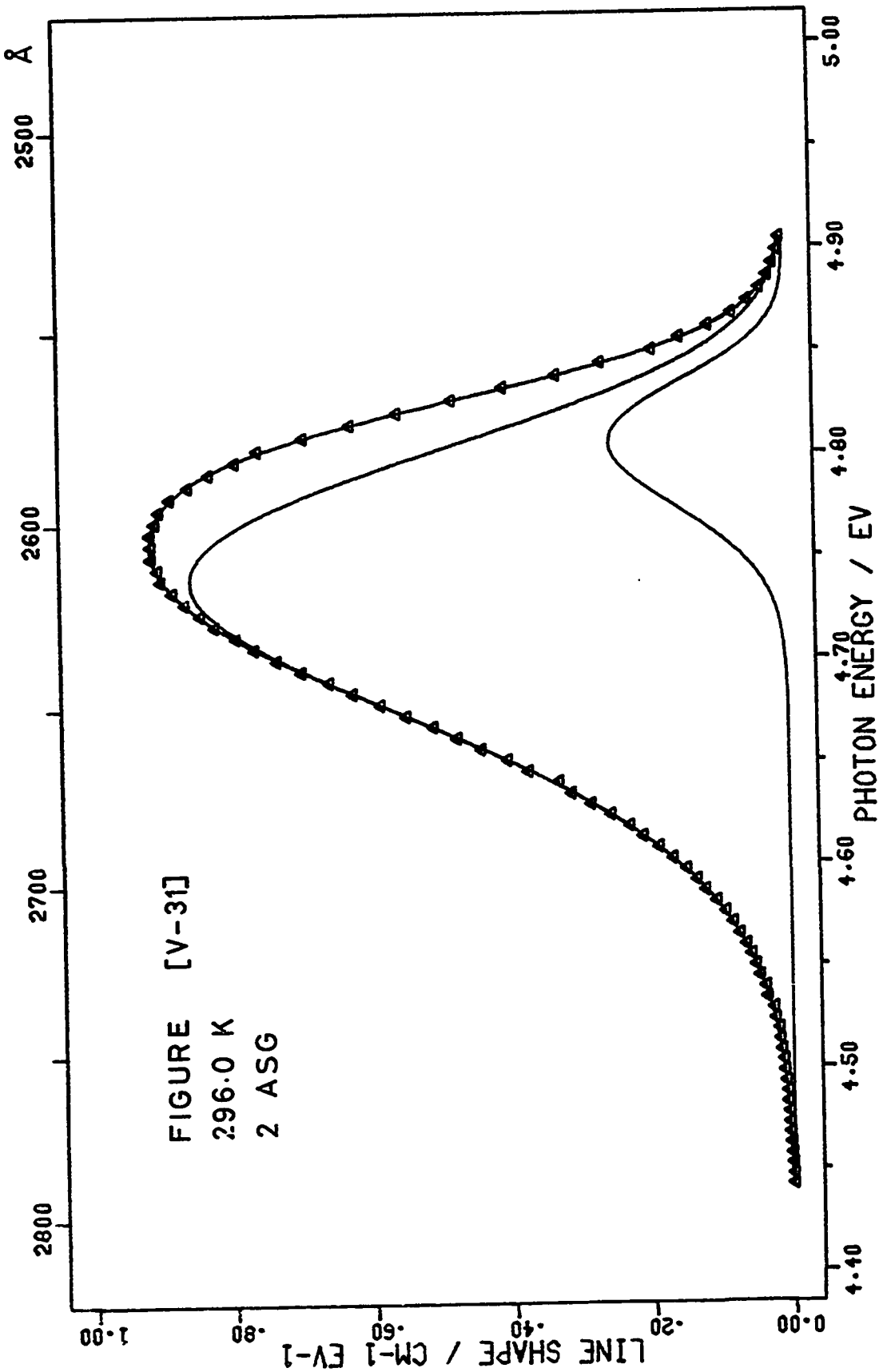
FIGURE [V-31]
296.0 K
2 ASG
LINE SHAPE / CM-1 EV-1
PHOTON ENERGY / EV
Å
2800
2700
2600
2500
4.40
4.50
4.60
4.70
4.80
4.90
5.00
0.00
.20
.40
.60
.80
1.00

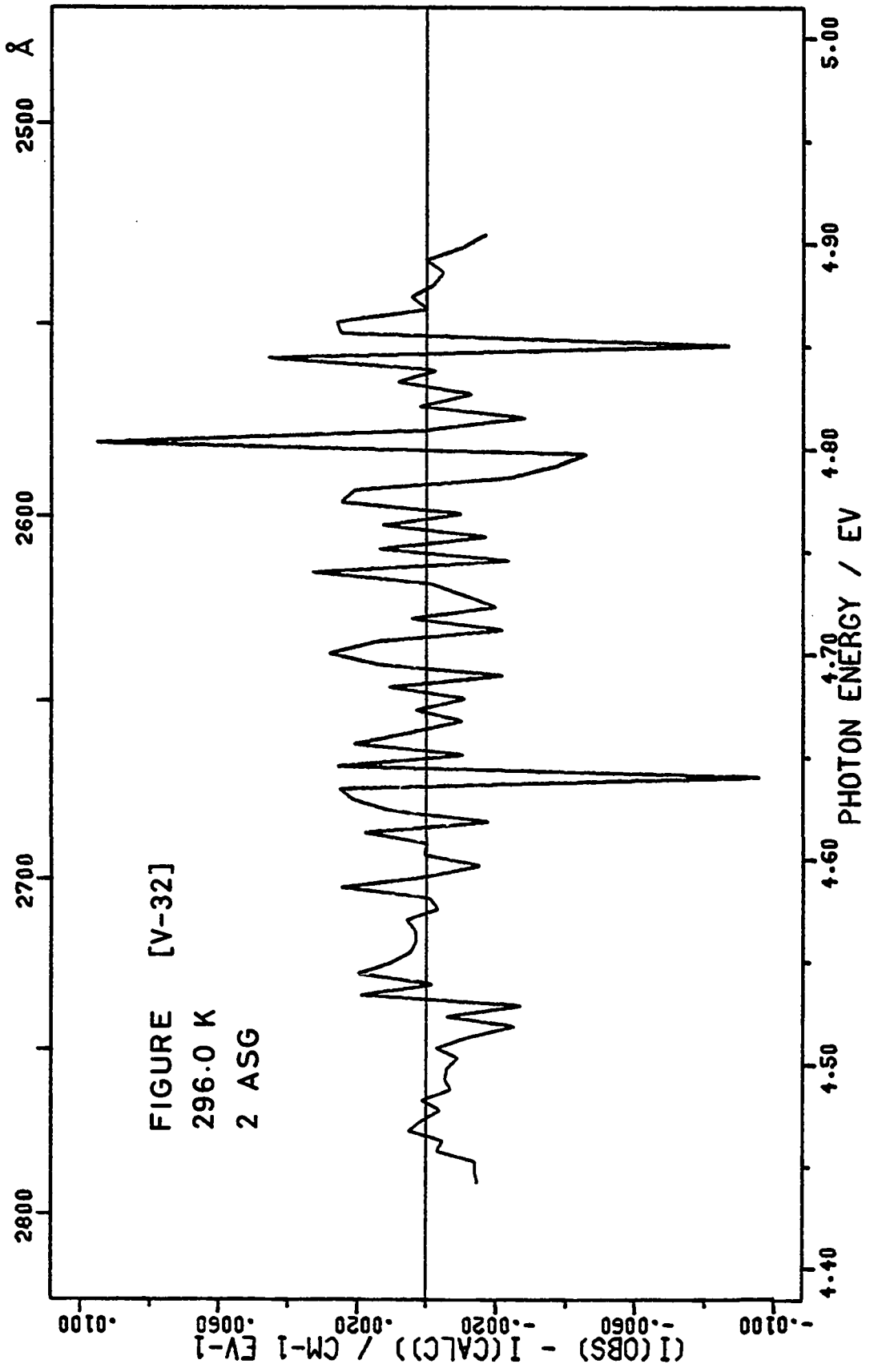
FIGURE [V-32]
296.0 K
2 ASG
2800
2700
2600
2500 Å
4.40
4.50
4.60
4.70
4.80
4.90
5.00
PHOTON ENERGY / EV
-.0100
-.0060
-.0020
.0020
.0060
.0100
(I(OBS) - I(CALC)) / CM-1 EV-1

A-BAND ABSORPTION KBr:Tl^+

2 ASYMMETRIC GAUSSIAN BANDS

RUN 30 - 83.0 K

FIGURE [V-33]

Δ - experimental points

The solid lines are the calculated resolved bands and their sum.

FIGURE [V-34]

Plot of I(experimental) - I(calculated) for each experimental point.

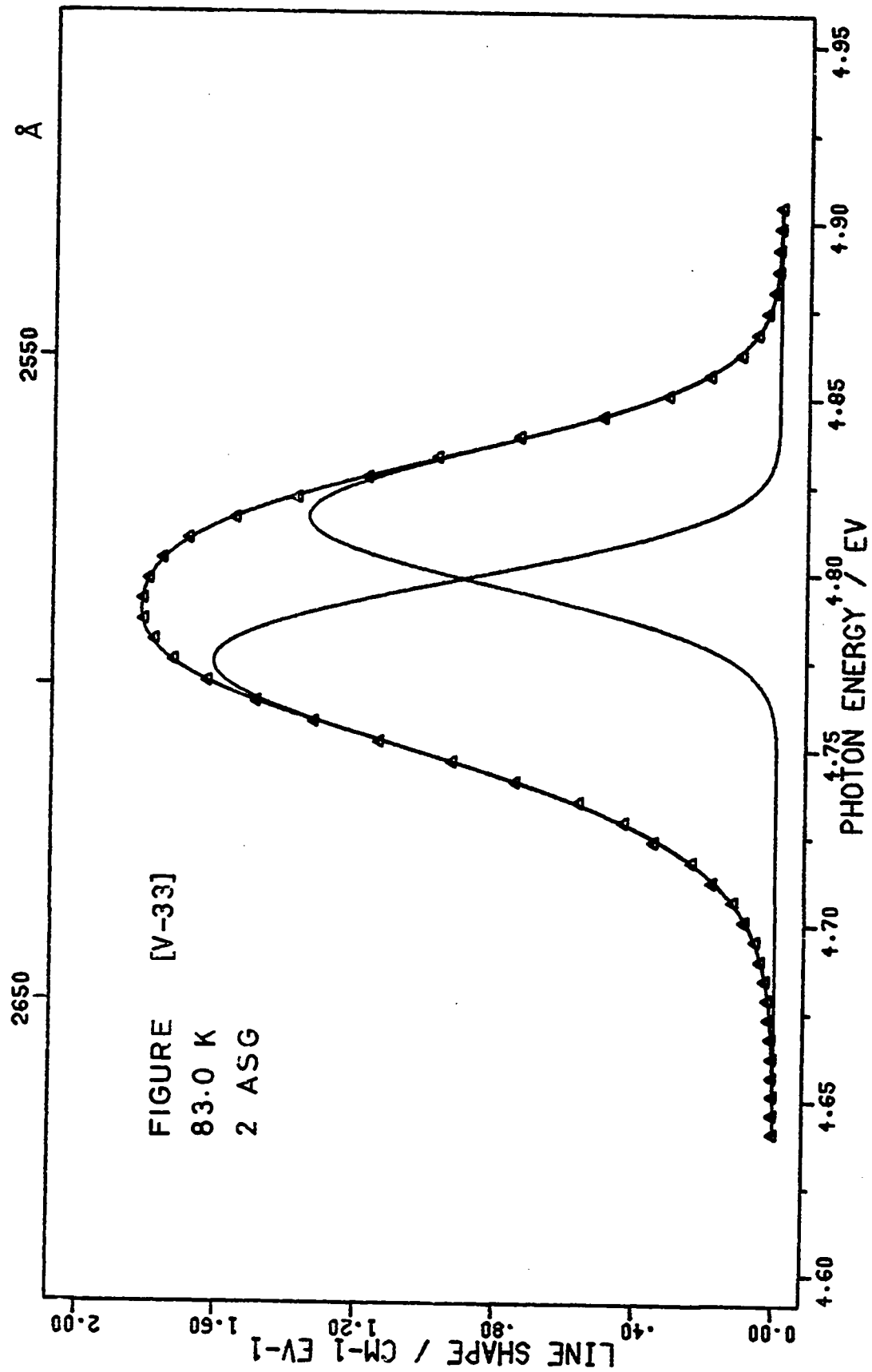
FIGURE [V-33]
83.0 K
2 ASG
Å
2650
2550
LINE SHAPE / CM-1 EV-1
0.00
.40
.80
1.20
1.60
2.00
4.60
4.65
4.70
4.75
4.80
4.85
4.90
4.95
PHOTON ENERGY / EV

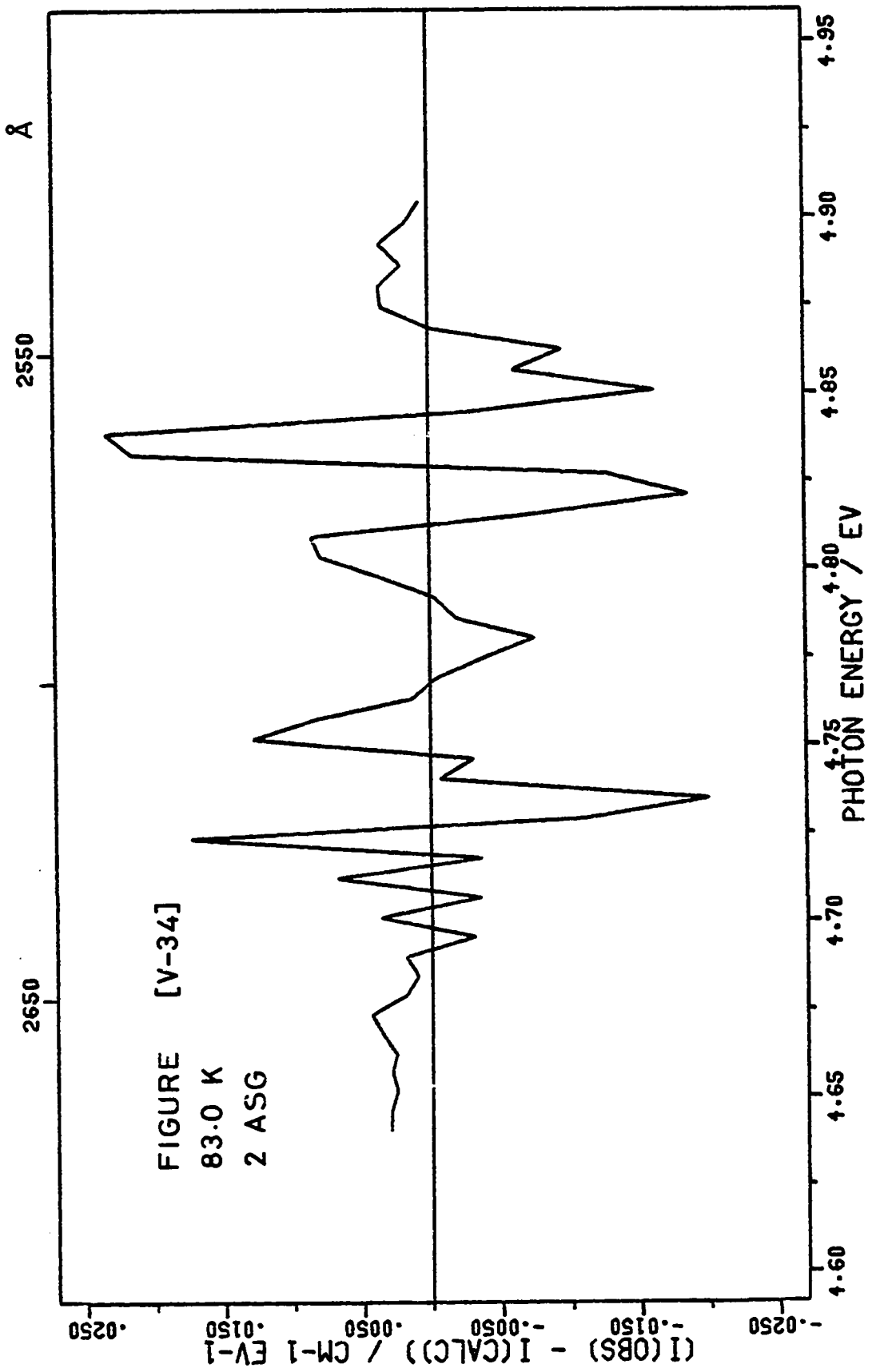
FIGURE [V-34]
83.0 K
2 ASG
Å
2550
2650
4.60
4.65
4.70
4.75
4.80
4.85
4.90
4.95
PHOTON ENERGY / EV
(I(OBS) - I(CALC)) / CM-1 EV-1
-.0250
-.0150
-.0050
.0050
.0150
.0250

A-BAND ABSORPTION KBr:Tl^+

2 ASYMMETRIC GAUSSIAN BANDS

RUN 101 - 15.0 K

FIGURE [V-35]

Δ - experimental points

The solid lines are the calculated resolved bands and their sum.

FIGURE [V-36]

Plot of I(experimental) - I(calculated) for each experimental point.

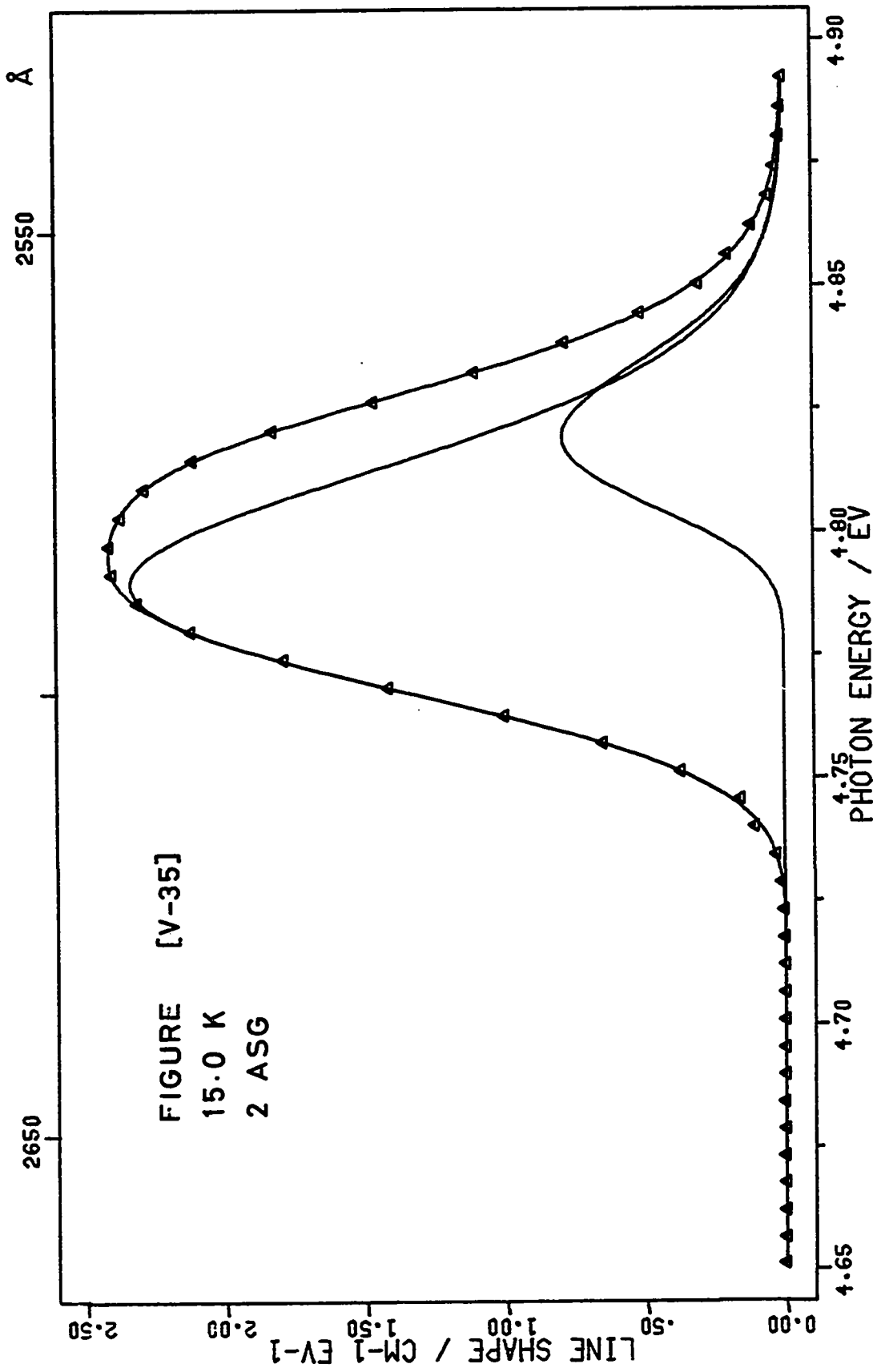
FIGURE [V-35]
15.0 K
2 ASG
Å
2650
2550
LINE SHAPE / CM-1 EV-1
0.00
.50
1.00
1.50
2.00
2.50
4.65
4.70
4.75
4.80
4.85
4.90
PHOTON ENERGY / EV

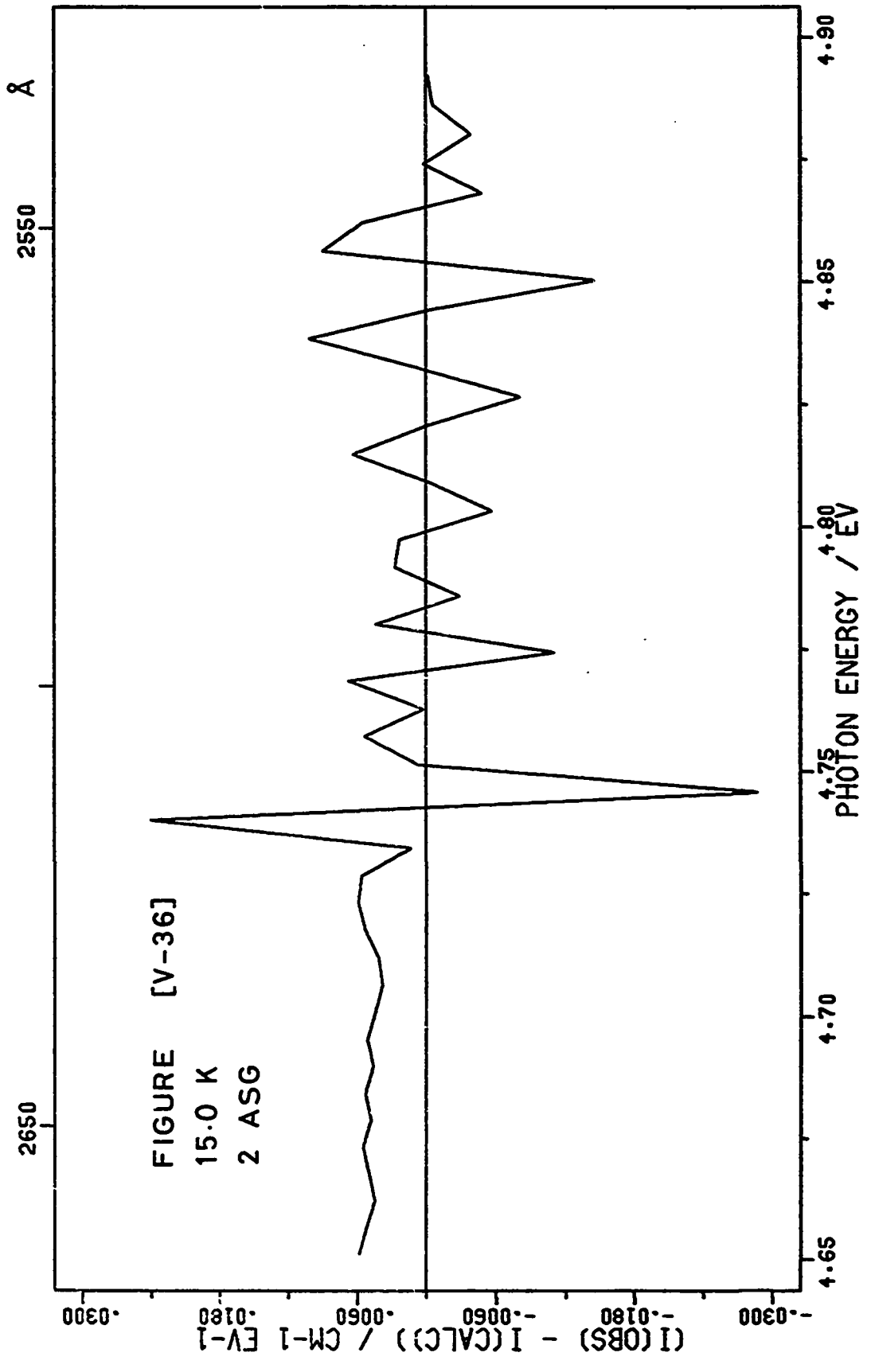
FIGURE [V-36]
15.0 K
2 ASG
Å
2650
2550
4.65
4.70
4.75
4.80
4.85
4.90
PHOTON ENERGY / EV
(I(OBS) - I(CALC)) / CM-1 EV-1
-.0300
-.0180
-.0060
.0060
.0180
.0300

FIGURE [V-37]

A-BAND ABSORPTION KBr:Tl^+

2 ASYMMETRIC GAUSSIAN BANDS

H_{obs} against $T^{\frac{1}{2}}$

■ - experimental parameter values Band 1

○ - experimental parameter values Band 2

The solid lines were calculated from equation [II-78].

Band 1	Band 2
$H_0 = 0.040$ eV	$H_0 = 0.039$ eV
$\nu = 3.4 \times 10^{12}$ sec^{-1}	$\nu = 1.1 \times 10^{12}$ sec^{-1}

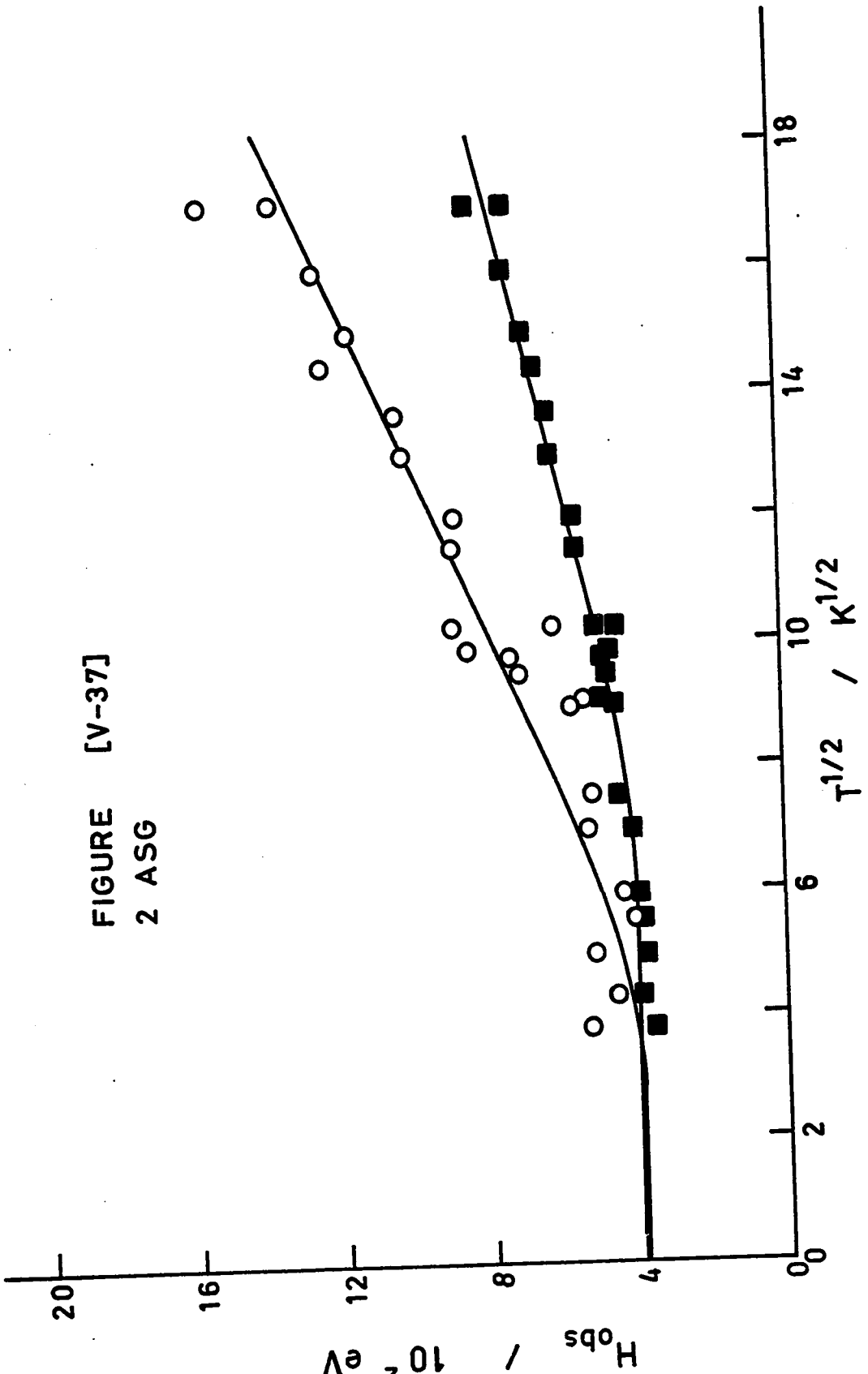

FIGURE [V-37]
2 ASG

FIGURE [V-38]

A-BAND ABSORPTION KBr:Tl^+

2 ASYMMETRIC GAUSSIAN BANDS

E_m against T

■ - experimental parameter values Band 1

O - experimental parameter values Band 2

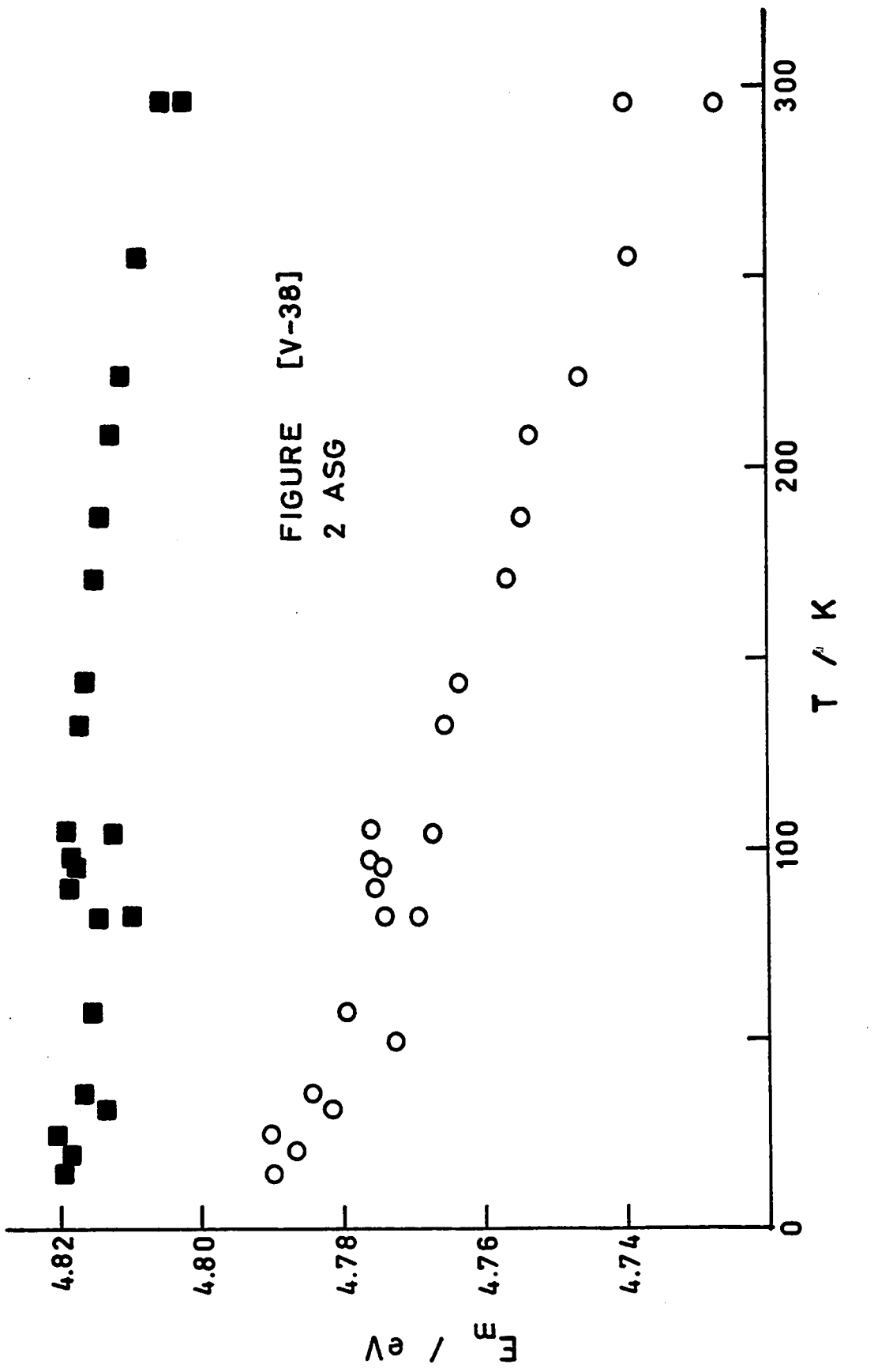

FIGURE 2 ASG [V-38]

FIGURE [V-39]

A-BAND ABSORPTION KBr:Tl^+

2 ASYMMETRIC GAUSSIAN BANDS

I_m against T

■ - experimental parameter values Band 1

○ - experimental parameter values Band 2

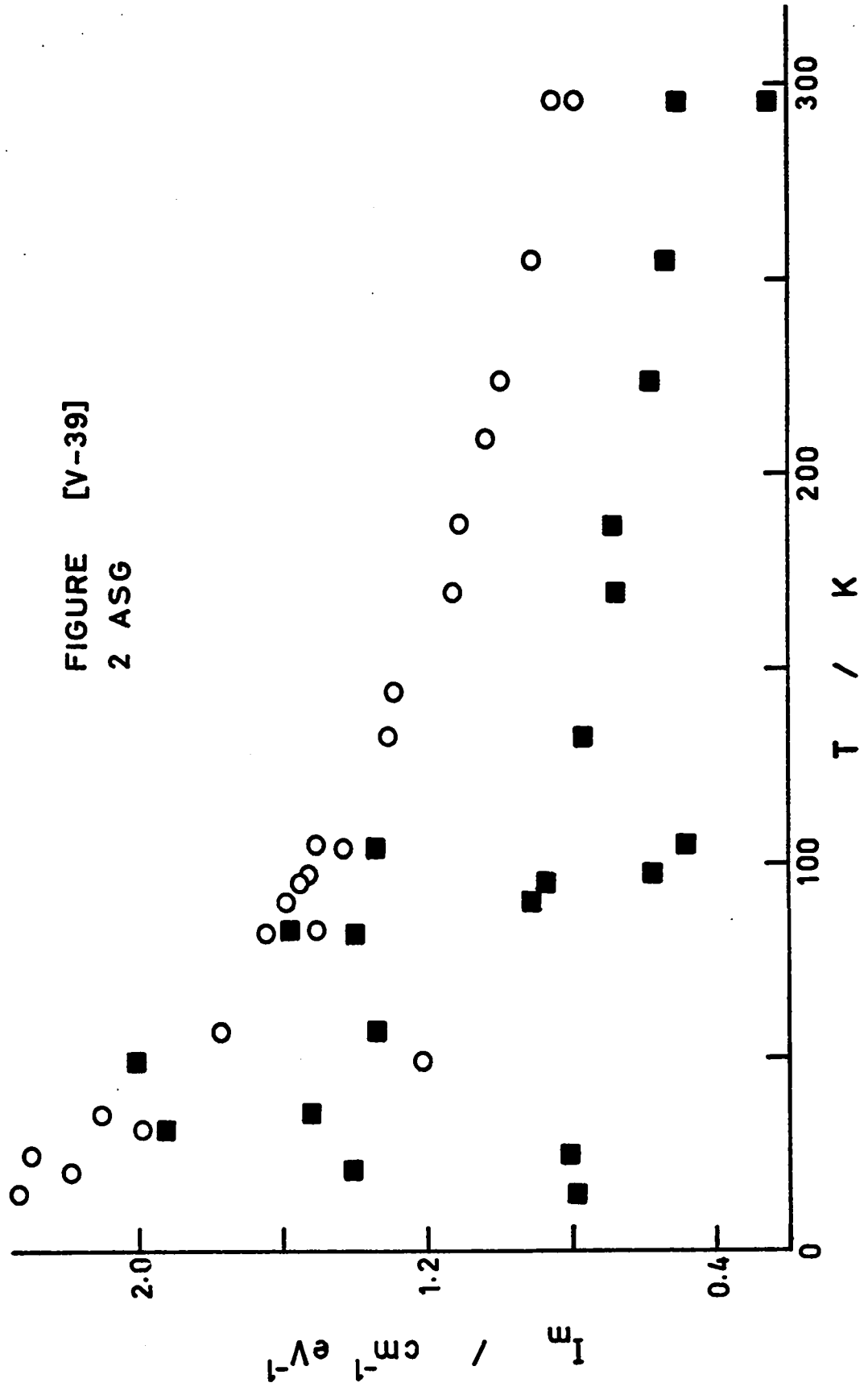
FIGURE [V-39]
2 ASG
I_m / cm^{-1} eV^{-1}
2.0
1.2
0.4
0
100
200
300
T / K

FIGURE [V-40]

A-BAND ABSORPTION KBr:Tl^+

2 ASYMMETRIC GAUSSIAN BANDS

b against T

■ - experimental parameter values Band 1

○ - experimental parameter values Band 2

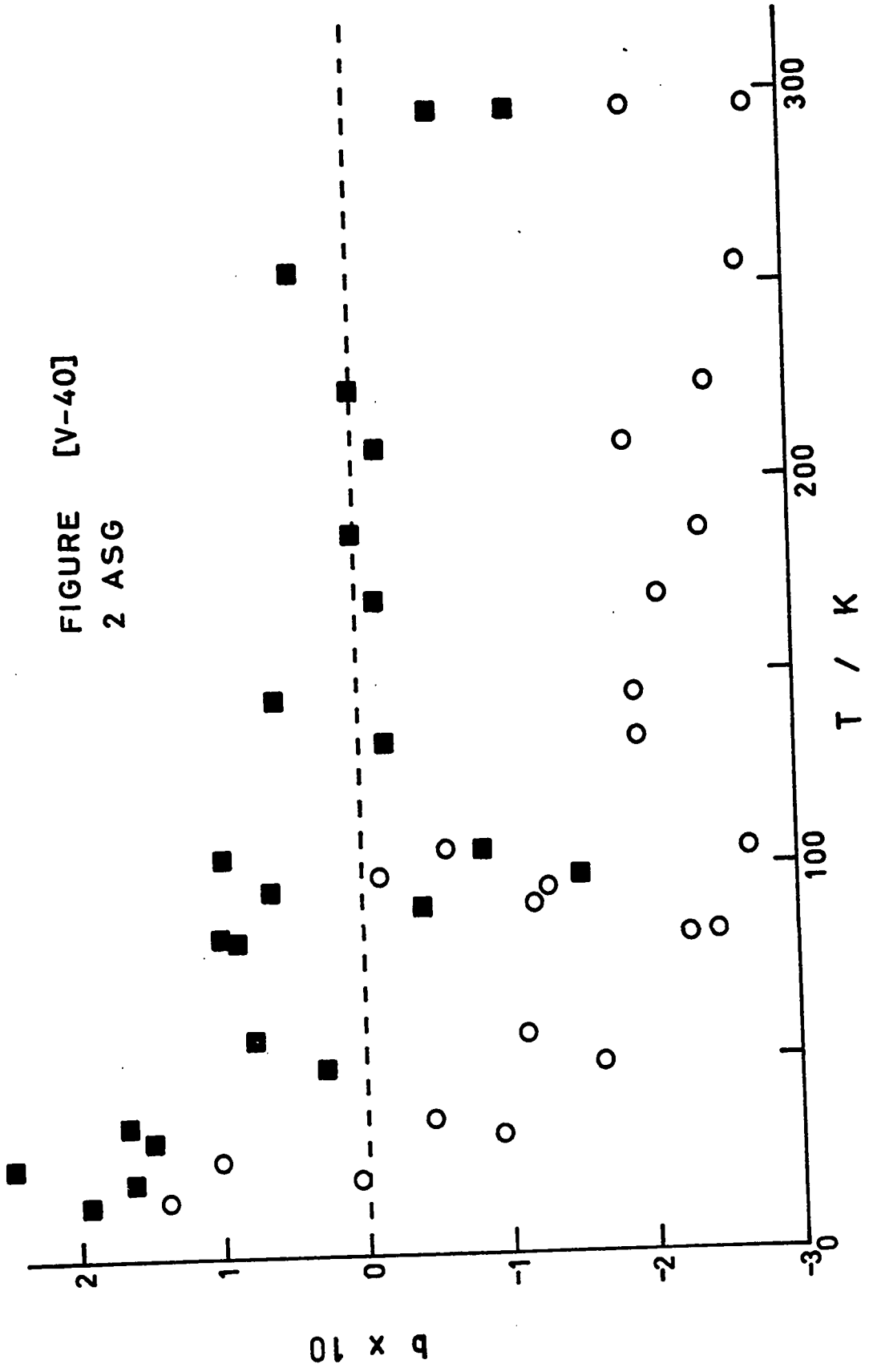

FIGURE [V-40]
2 ASG

FIGURE [V-41]

A-BAND ABSORPTION KBr:Tl^+

2 ASYMMETRIC GAUSSIAN BANDS

$\Delta E_{splitting}$ against $T^{\frac{1}{2}}$

O - experimental parameter values

The solid line was calculated from equation [VI-27].

$$\Delta E_o = 0.030 \text{ eV}$$

$$\nu = 2.19 \times 10^{12} \text{ sec}^{-1}$$

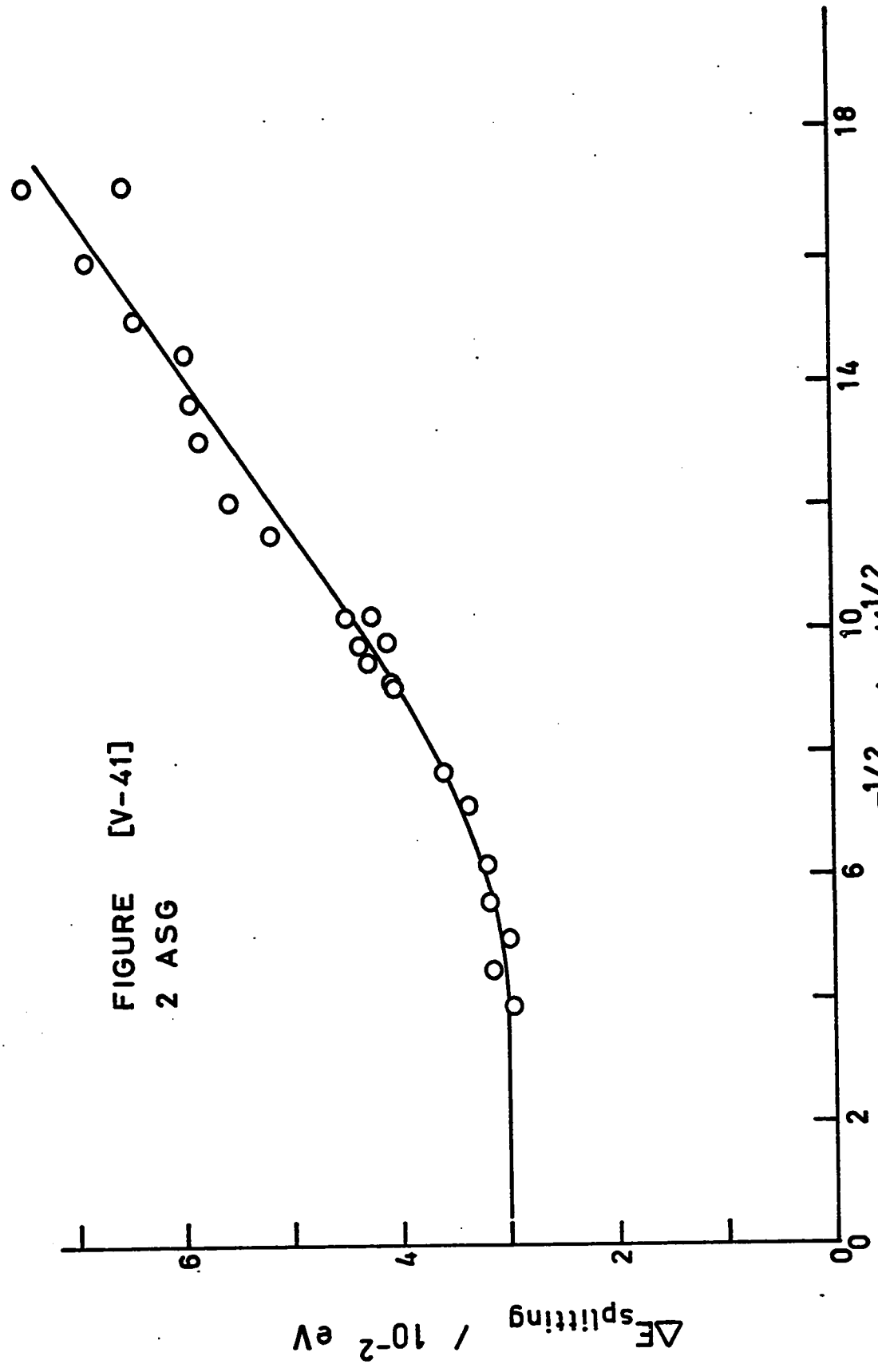

FIGURE [V-41]
2 ASG

A-BAND ABSORPTION KBr:Tl^+

3 SYMMETRIC GAUSSIAN BANDS

RUN 29 - 296.0 K

FIGURE [V-42]

Δ - experimental points

The solid lines are the calculated resolved bands and their sum.

FIGURE [V-43]

Plot of I(experimental) - I(calculated) for each experimental point.

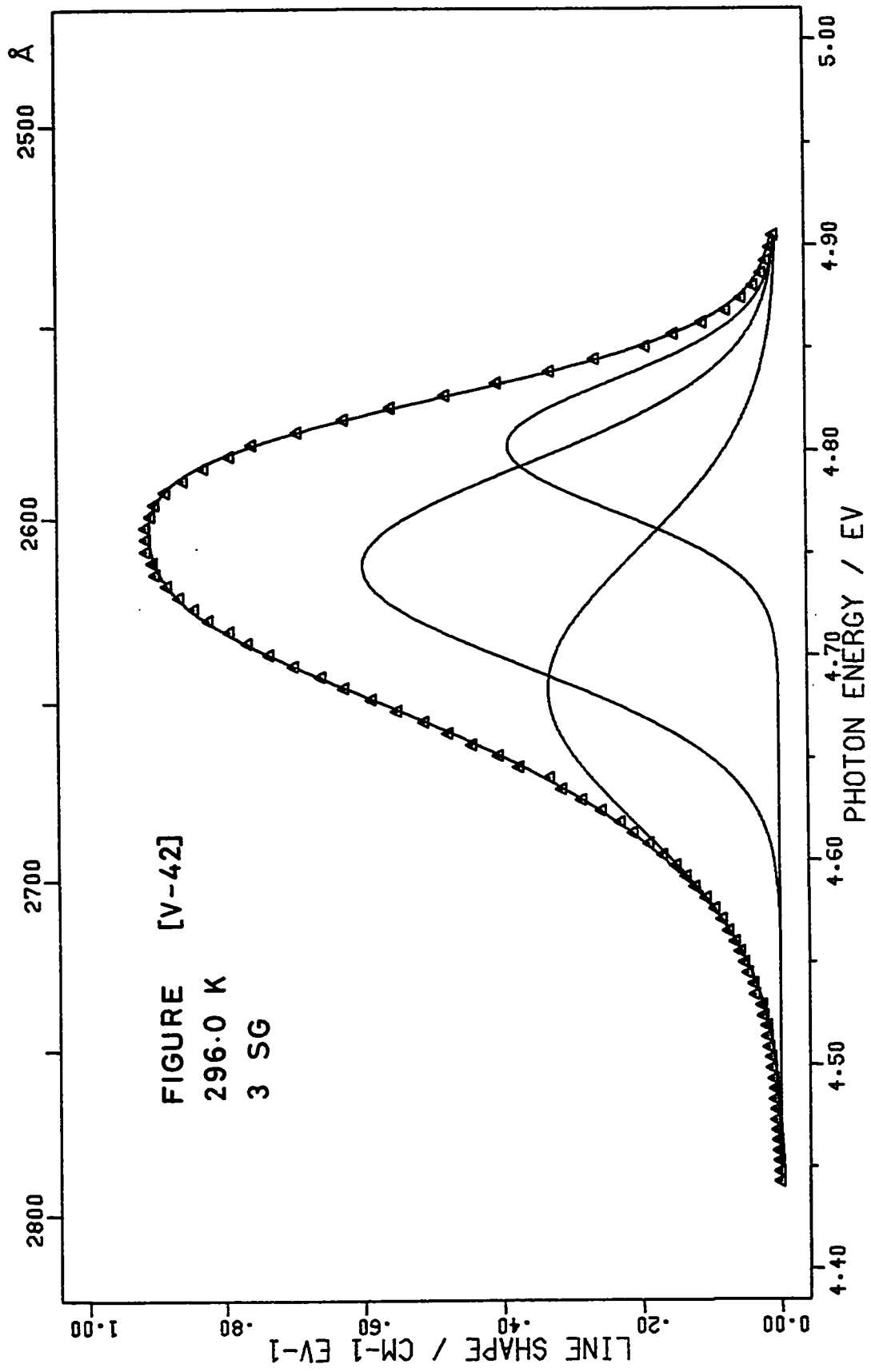
FIGURE [V-42]
296.0 K
3 SG
LINE SHAPE / CM-1 EV-1
PHOTON ENERGY / EV
Å
0.00
.20
.40
.60
.80
1.00
4.40
4.50
4.60
4.70
4.80
4.90
5.00
2800
2700
2600
2500

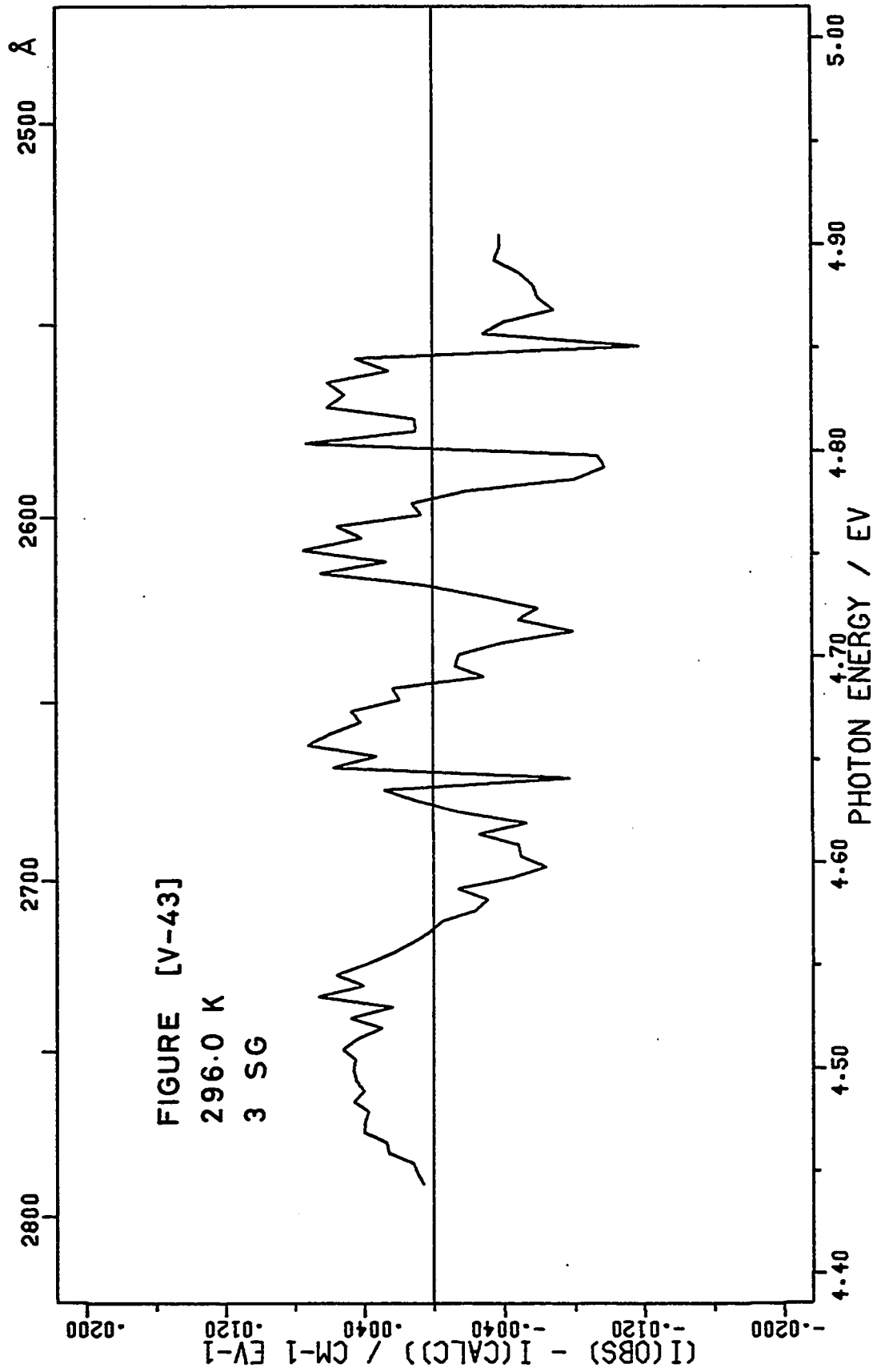
FIGURE [V-43]
296.0 K
3 SG
(I(OBS) - I(CALC)) / CM-1 EV-1
-.0200
-.0120
-.0040
.0040
.0120
.0200
PHOTON ENERGY / EV
4.40
4.50
4.60
4.70
4.80
4.90
5.00
Å
2800
2700
2600
2500

A-BAND ABSORPTION KBr:Tl^+

3 SYMMETRIC GAUSSIAN BANDS

RUN 30 - 83.0 K

FIGURE [V-44]

Δ - experimental points

The solid lines are the calculated resolved bands and their sum.

FIGURE [V-45]

Plot of I(experimental) - I(calculated) for each experimental point.

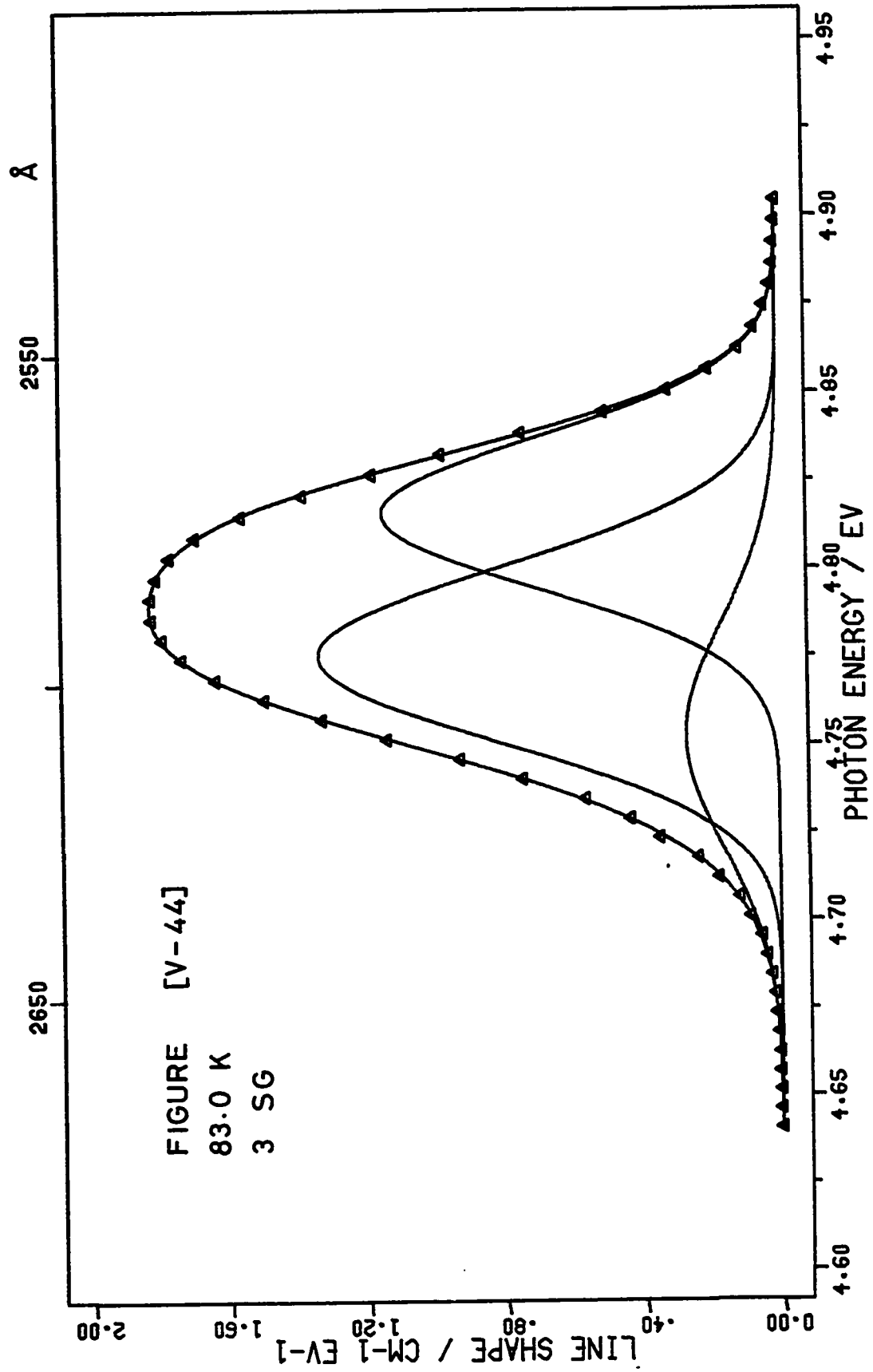
FIGURE [V-44]
83.0 K
3 SG
2650
2550
Å
LINE SHAPE / CM-1 EV-1
0.00
.40
.80
1.20
1.60
2.00
4.60
4.65
4.70
4.75
4.80
4.85
4.90
4.95
PHOTON ENERGY / EV

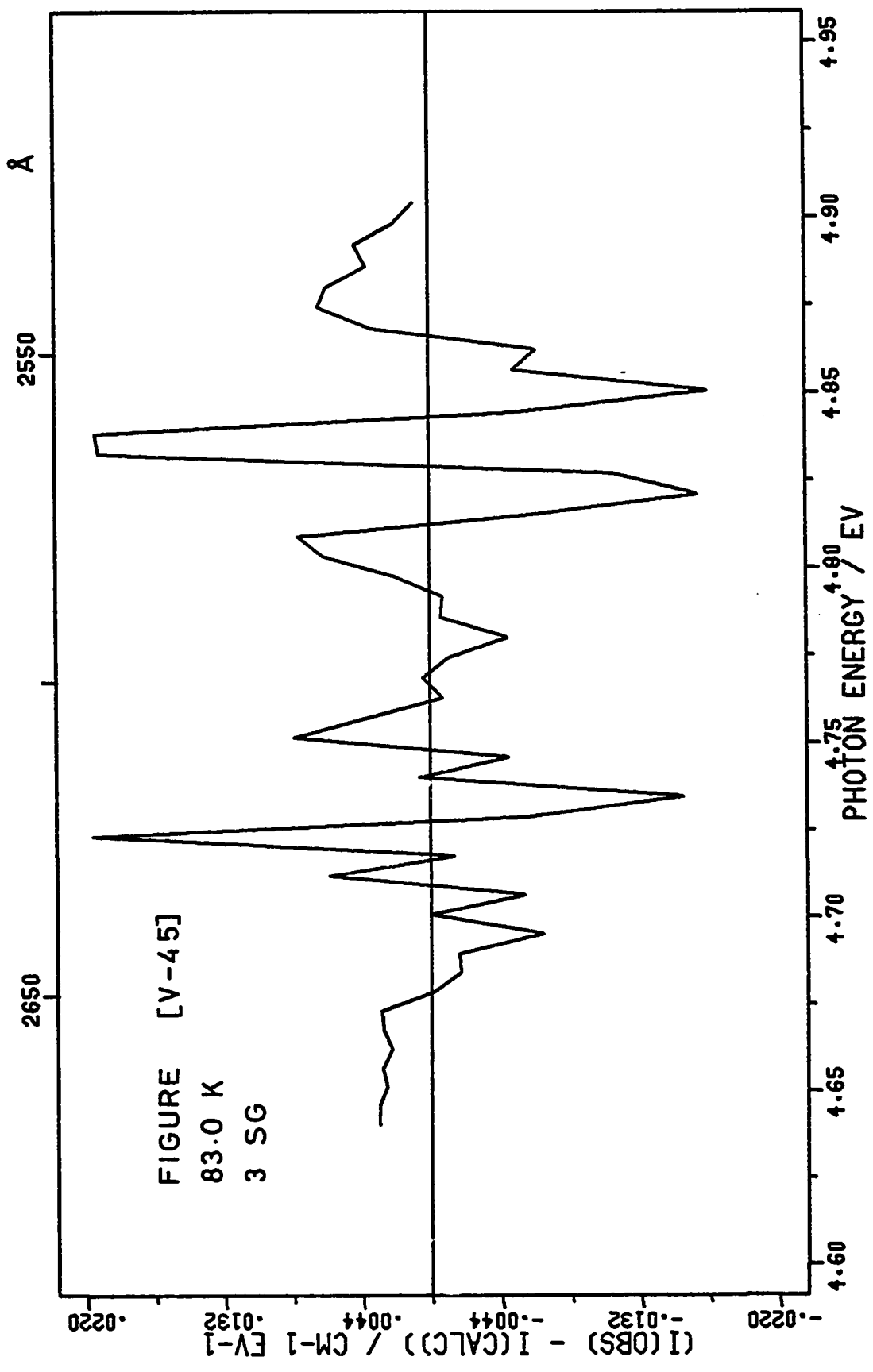
FIGURE [V-45]
83.0 K
3 SG
Å
2650
2550
4.60
4.65
4.70
4.75
4.80
4.85
4.90
4.95
PHOTON ENERGY / EV
(I(OBS) - I(CALC)) / CM-1 EV-1
-.0220
-.0132
-.0044
.0044
.0132
.0220

FIGURE [V-46]

A-BAND ABSORPTION KBr:Tl^{+}

3 SYMMETRIC GAUSSIAN BANDS

H_{obs} against $T^{\frac{1}{2}}$

■ - experimental parameter values Band 1

○ - experimental parameter values Band 2

△ - experimental parameter values Band 3

	H_0/eV	$\nu/10^{12}$ sec^{-1}
Band 1	0.038	3.1
Band 2	0.05	2.2
Band 3	0.072	2.5

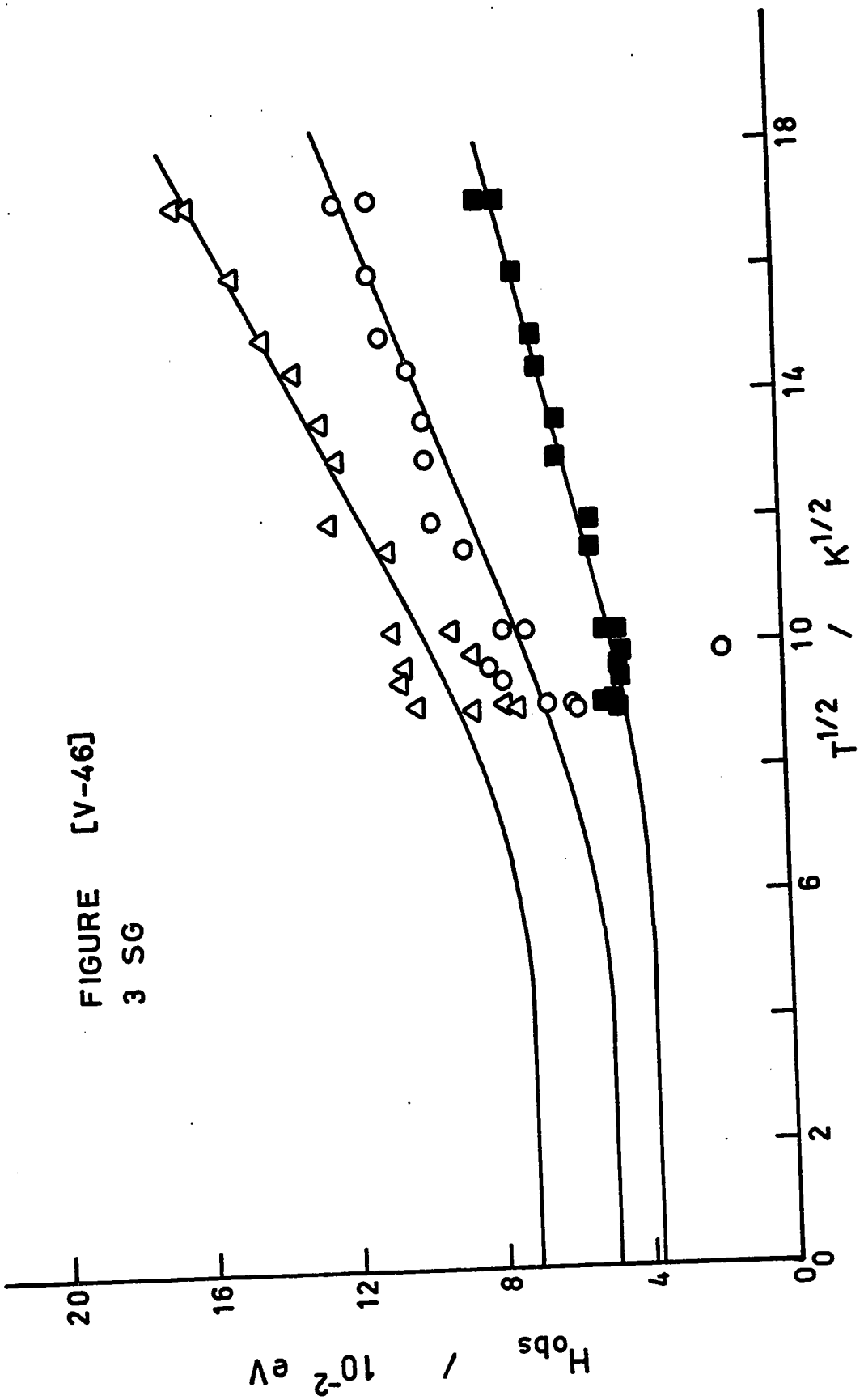

FIGURE [V-46]
3 SG

FIGURE [V-47]

A-BAND ABSORPTION KBr:Tl^{+}

3 SYMMETRIC GAUSSIAN BANDS

E_m against T

■ - experimental parameter values Band 1

○ - experimental parameter values Band 2

△ - experimental parameter values Band 3

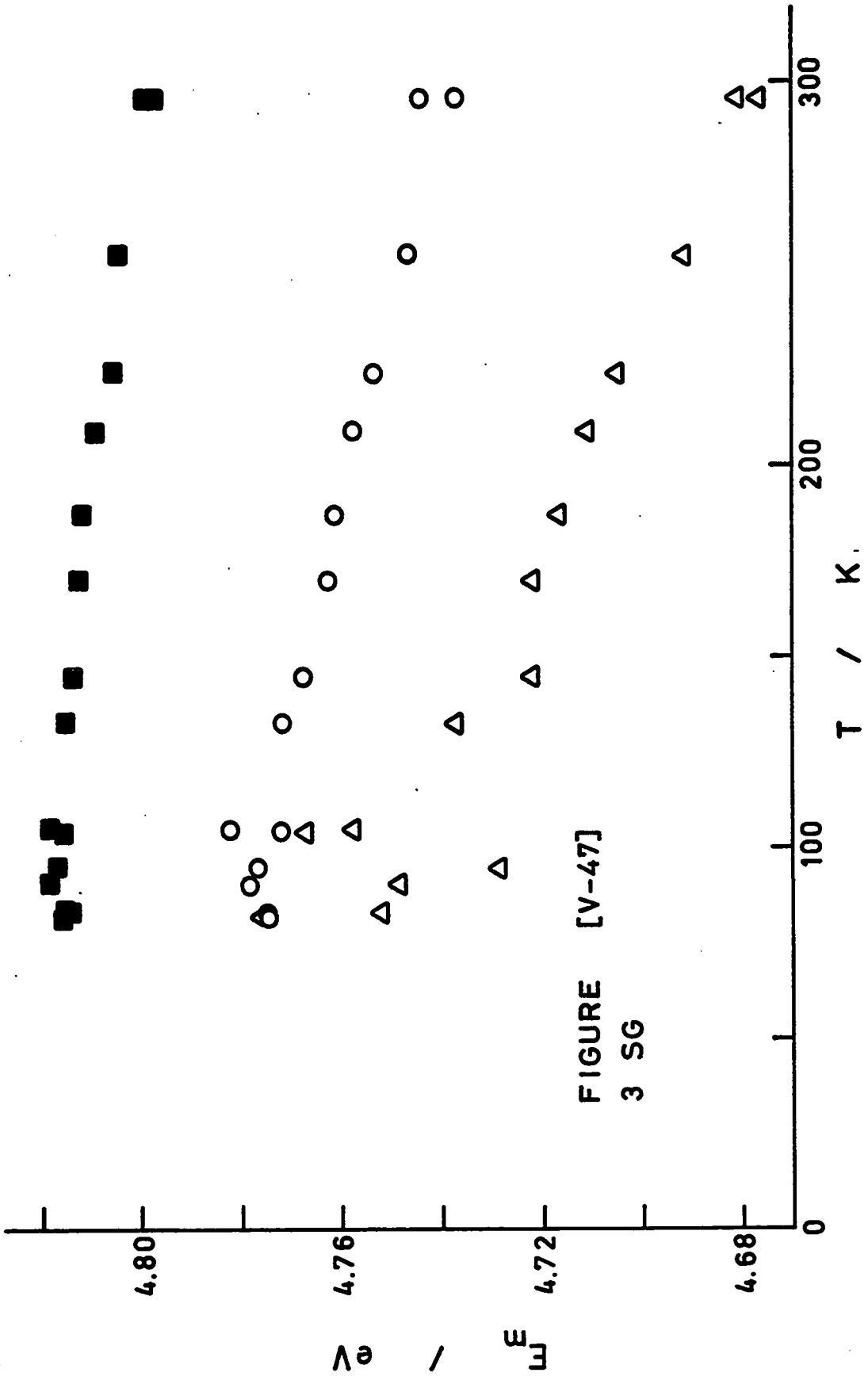

FIGURE [V-47]
3 SG

FIGURE [V-48]

A-BAND ABSORPTION KBr:Tl^+

3 SYMMETRIC GAUSSIAN BANDS

I_m against T

■ - experimental parameter values Band 1

○ - experimental parameter values Band 2

△ - experimental parameter values Band 3

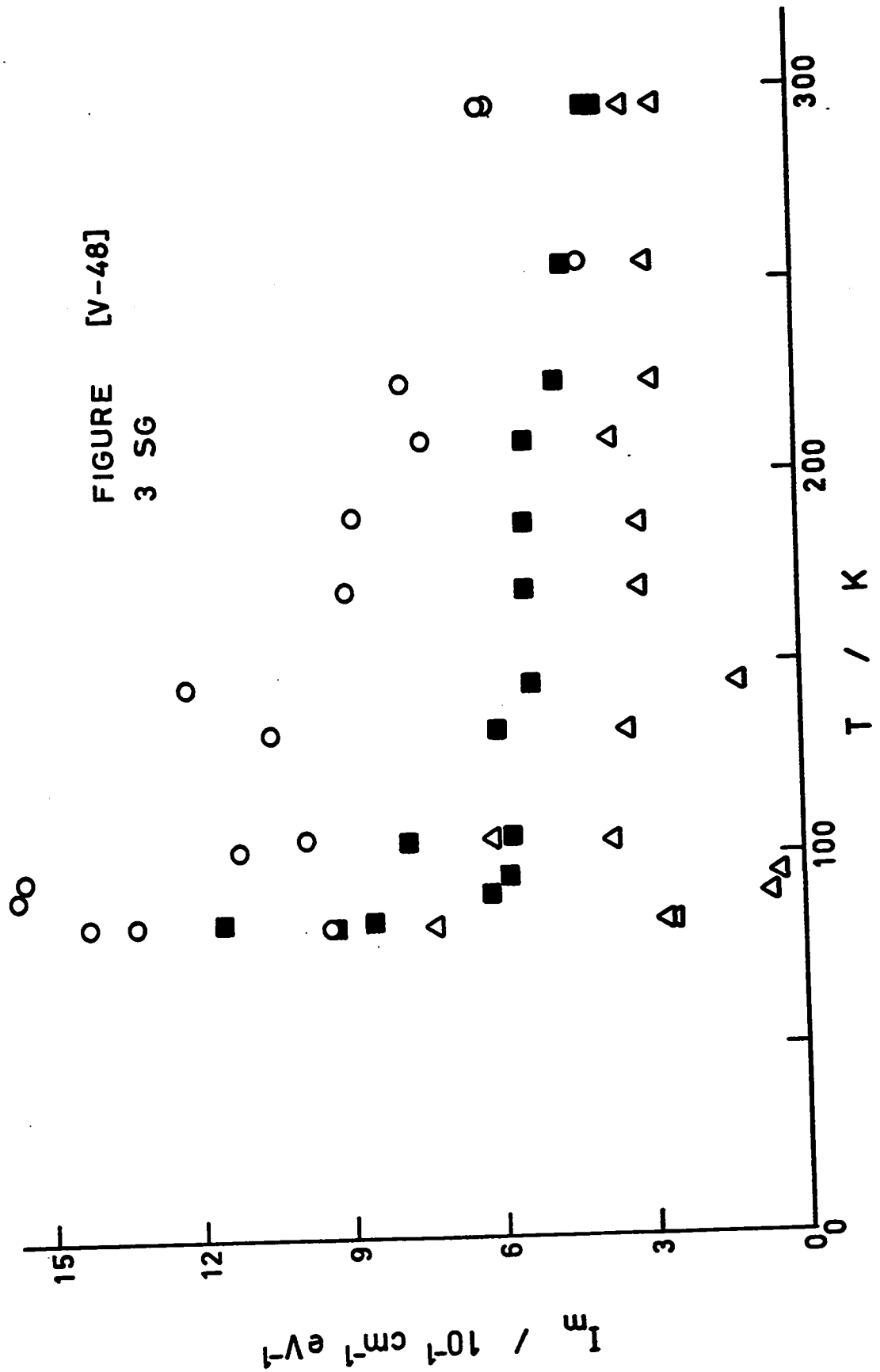
FIGURE [V-48]
3 SG
I_ε / 10^{-1} cm^{-1} eV^{-1}
15
12
9
6
3
0
0
100
200
300
T / K

FIGURE [V-49]

A-BAND ABSORPTION KBr:Tl^+

3 SYMMETRIC GAUSSIAN BANDS

$\Delta E_{splitting}$ against T

■ - E_{12} [E_m(Band 1) - E_m(Band 2)]

○ - E_{23} [E_m(Band 2) - E_m(Band 3)]

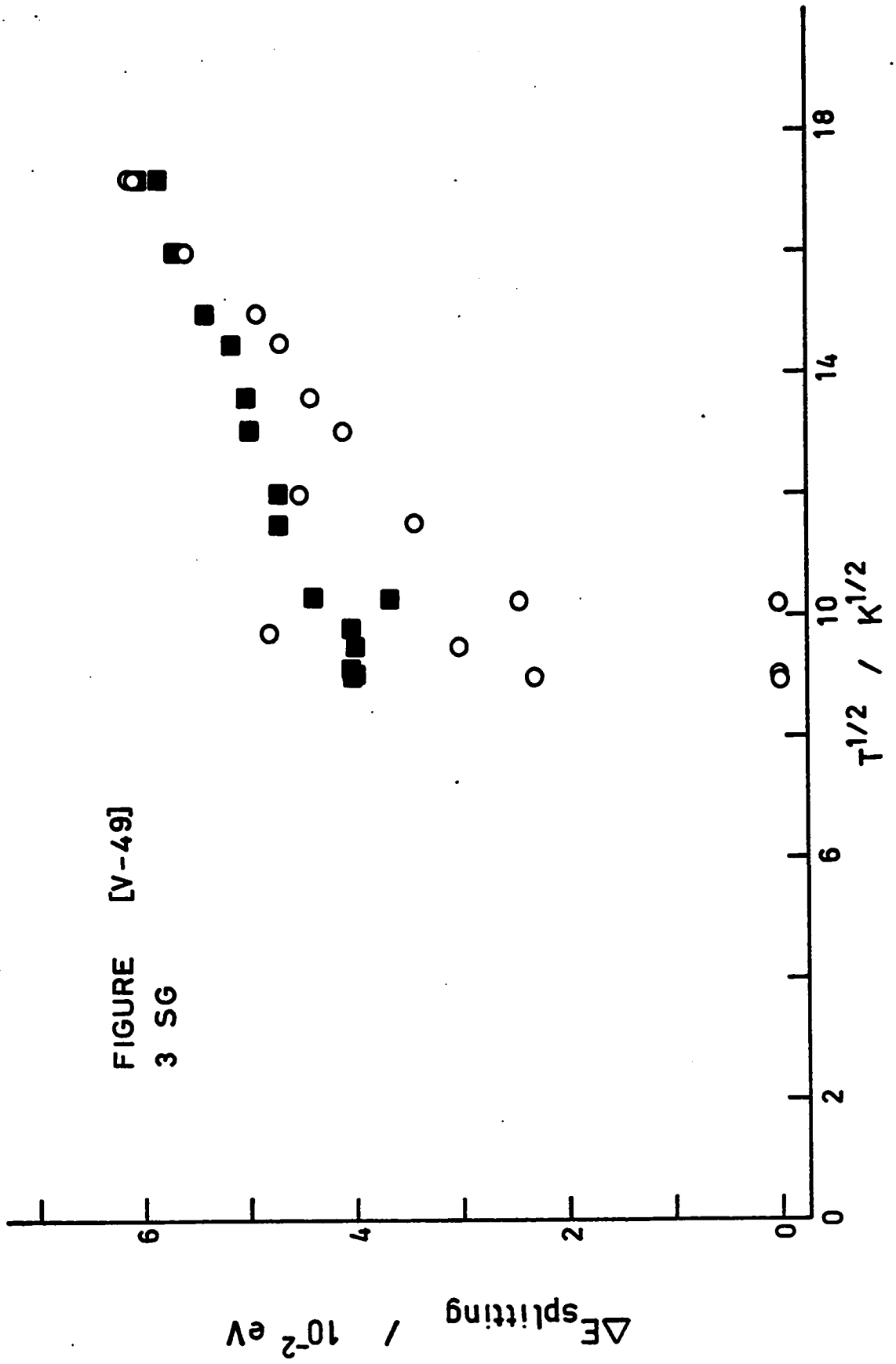

FIGURE [V-49]
3 SG

FIGURE [V-50]

A-BAND ABSORPTION KBr:Tl^+

STANDARD DEVIATION OF FIT

against

TEMPERATURE

○ - one symmetric gaussian band

● - two symmetric gaussian bands

■ - three symmetric gaussian bands

▲ - one asymmetric gaussian band

△ - two asymmetric gaussian bands

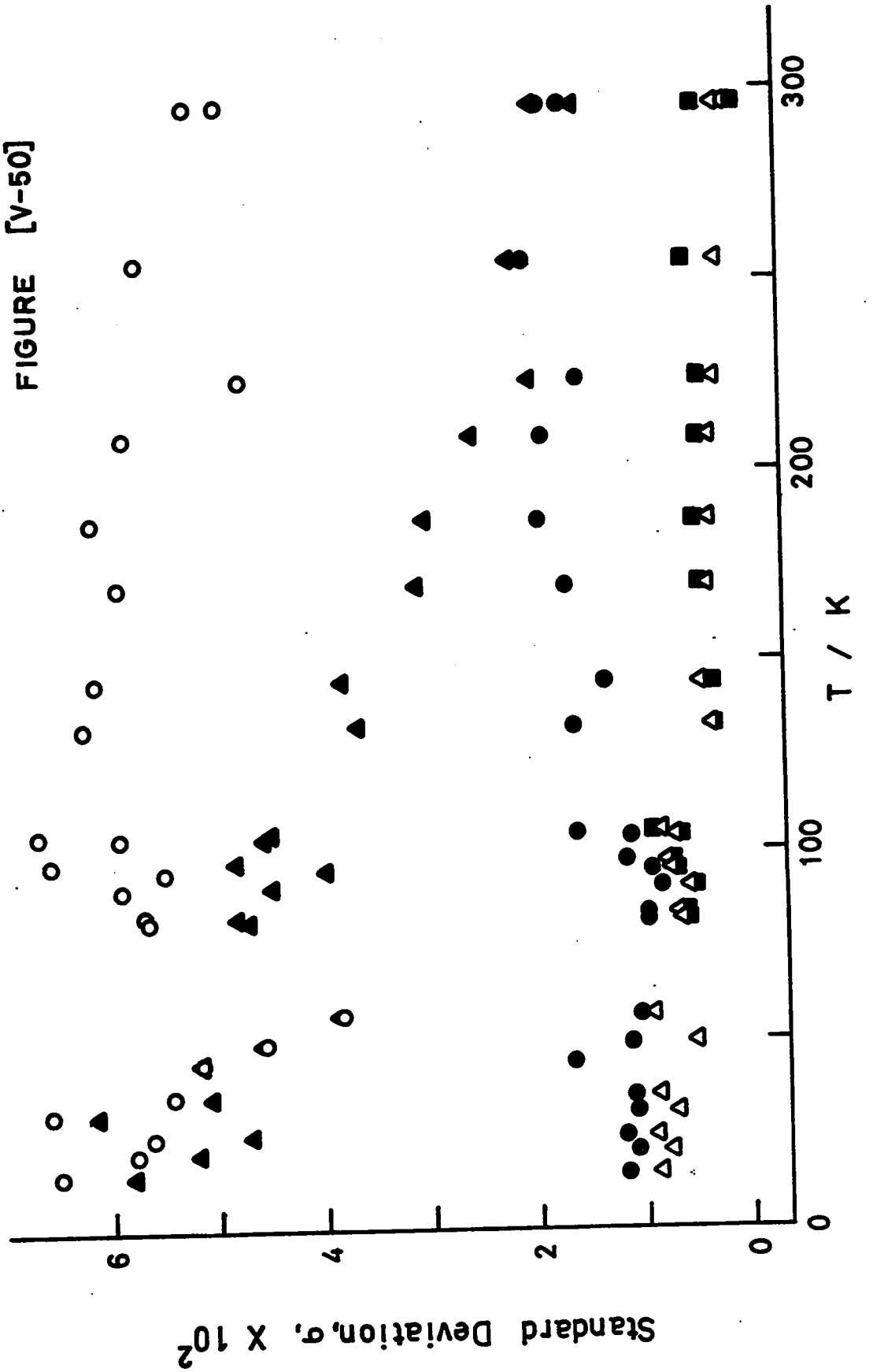
FIGURE [V-50]
Standard Deviation, σ, X 10²
0
2
4
6
0
100
200
300
T / K

3. Emission

3-1 Introduction

The emission of KBr:Tl^+ was produced by excitation in the short wavelength (high energy) tail of the A-absorption band by the 2537 Å line of a mercury arc.

Continuous excitation of the crystal ensured that relaxation in the excited state occurred before the emitted light was measured. As a result, the maximum intensity of the emission is at lower energy than the absorption maximum.

The emission line shape, I, is plotted against energy at five representative temperatures in the range 15.5 K to 296.0 K in Figure [V-51]. At room temperature, the emission is broad and not clearly resolved. At 83.0 K, the spectrum consists of two almost completely resolved bands of comparable intensity. At 15.5 K, the spectrum is dominated by the high energy component although two small bands are apparent. The relative intensity of the two major bands is very temperature sensitive.

3-2 Characterization of Emission Line Shape

The emission line shape was analyzed as the sum of two symmetric gaussian bands with the addition of a third band at low temperatures to take into account the small third band which appeared at liquid helium temperature. Three parameters, H_{obs}, E_m, and I_m were required for each gaussian band. Initial estimates for the parameters were readily available by inspection of the experimental data. Best fit values of the parameters are summarized in Table [V-6]. The maximum errors in the parameters are given in the table.

TABLE [V-6]

EMISSION KBr:Tl^+ A-BAND EXCITATION - THREE SYMMETRIC GAUSSIAN BANDS

Run No.	T/K	Band 1			Band 2			Band 3		
		E_m/eV	I_m	H_{obs}/eV	E_m/eV	I_m	H_{obs}/eV	E_m/eV	I_m	H_{obs}/eV
1	296.0	3.957	2.72	0.527	3.406	5.15	0.543			
2	83.0	3.983	7.02	0.281	3.378	8.44	0.300			
3	92.0	3.979	3.64	0.299	3.378	14.59	0.313			
4	83.0	3.983	6.65	0.279	3.378	8.01	0.304			
5	88.2	3.980	3.83	0.297	3.378	13.29	0.309			
6	93.0	3.977	2.54	0.318	3.378	14.62	0.304			
7	98.2	3.970	1.35	0.327	3.378	15.07	0.329			
8	107.2	3.960	0.96	0.353	3.380	16.87	0.340			
9	113.4	3.941	0.85	0.392	3.381	16.28	0.345			
10	133.8	3.943	1.13	0.389	3.385	13.69	0.374			
11	170.2	3.947	1.86	0.420	3.388	10.20	0.413			
12	170.2	3.926	1.83	0.480	3.380	10.26	0.412			

Run No.	T/K	Band 1			Band 2			Band 3		
		E_m/eV	I_m	H_{obs}/eV	E_m/eV	I_m	H_{obs}/eV	E_m/eV	I_m	H_{obs}/eV
13	209.0	3.939	2.34	0.492	3.385	8.49	0.448			
14	252.2	3.942	2.44	0.519	3.392	5.69	0.485			
15	296.0	3.948	2.45	0.552	3.394	4.48	0.545			
130	84.0	3.985	6.34	0.285	3.380	8.91	0.302			
131	84.0	3.994	8.83	0.287	3.382	11.21	0.308			
132	15.5	4.006	11.33	0.209	3.397	0.56	0.196	3.145	0.43	0.141
133	19.3	4.007	10.84	0.209	3.401	0.57	0.193	3.150	0.44	0.132
134	24.8	4.004	10.66	0.210	3.397	0.62	0.203	3.149	0.44	0.137
135	31.4	4.005	11.48	0.213	3.402	0.67	0.201	3.156	0.39	0.150
136	31.0	4.006	10.58	0.213	3.401	0.61	0.198	3.156	0.39	0.140
136	25.0	4.006	10.59	0.214	3.400	0.62	0.195	3.159	0.37	0.151
137	28.5	4.004	10.78	0.217	3.399	0.64	0.204	3.157	0.32	0.149
138	42.5	4.003	10.00	0.221	3.396	0.92	0.215	3.164	0.33	0.138
139	49.5	4.000	9.54	0.231	3.395	1.31	0.232	3.162	0.31	0.164

Run No.	T/K	Band 1			Band 2			Band 3		
		E_m/eV	I_m	H_{obs}/eV	E_m/eV	I_m	H_{obs}/eV	E_m/eV	I_m	H_{obs}/eV
140	49.0	3.999	10.07	0.230	3.396	1.30	0.232	3.162	0.30	0.148
141	57.0	3.999	9.61	0.244	3.390	1.35	0.247	3.159	0.28	0.129
142	64.1	3.996	10.00	0.255	3.388	1.64	0.266	3.155	0.25	0.130
143	73.0	3.994	8.66	0.267	3.385	2.71	0.282	3.145	0.21	0.108
144	77.8	3.987	8.66	0.275	3.376	4.80	0.299			
145	87.3	3.983	5.53	0.289	3.380	10.93	0.309			
σ_p		0.001	0.02	0.001	0.002	0.02	0.002	0.011	0.03	0.037

Experimental data at 296.0 K, 83.0 K, and 15.5 K are shown in Figures [V-52,V-54,V-56]. The corresponding error plots are given in Figures [V-53,V-55,V-57].

The temperature variation of the parameters is shown in Figures [V-58,V-59,V-60].

(a) H_{obs} against $T^{1/2}$ (Figure [V-58])

The half-widths of the high energy bands vary linearly with $T^{1/2}$ at high temperature and approach limiting values as T approaches 0 K. The variation in the half-width of the lowest energy band is characterized only at low temperature.

(b) E_m against T (Figure [V-59])

For the two major bands, E_m decreases as the temperature decreases to ~120 K and then increases as T approaches 0 K. The lowest energy band follows a similar trend in the region studied.

(c) I_m against T (Figure [V-60])

At low temperatures, the highest energy band, Band 1, is the more intense. As the temperature increases, the intensity in this band decreases while the lower energy band, Band 2, grows. At ~110 K, Band 1 reaches its minimum intensity and Band 2 its maximum. Above this temperature, Band 1 grows slightly and Band 2 becomes smaller until at room temperature the two bands are approaching the same intensity. The third band is small and decreases in intensity as the temperature increases.

The separation energies E_{12}, [E_m(Band 1)-E_m(Band 2)], and E_{23}, [E_m(Band 2)-E_m(Band 3)], plotted against $T^{1/2}$ are shown in Figure [V-61]. E_{12} shown two constant ranges with a shift at ~110 K. E_{23} increases as the temperature decreases.

FIGURE [V-51]

EMISSION KBr:Tl^+

A-BAND EXCITATION

— — — — 296.0 K

— — — — — 107.2 K

———————— 83.0 K

— — — — — — 57.0 K

— — — — — — — — 15.5 K

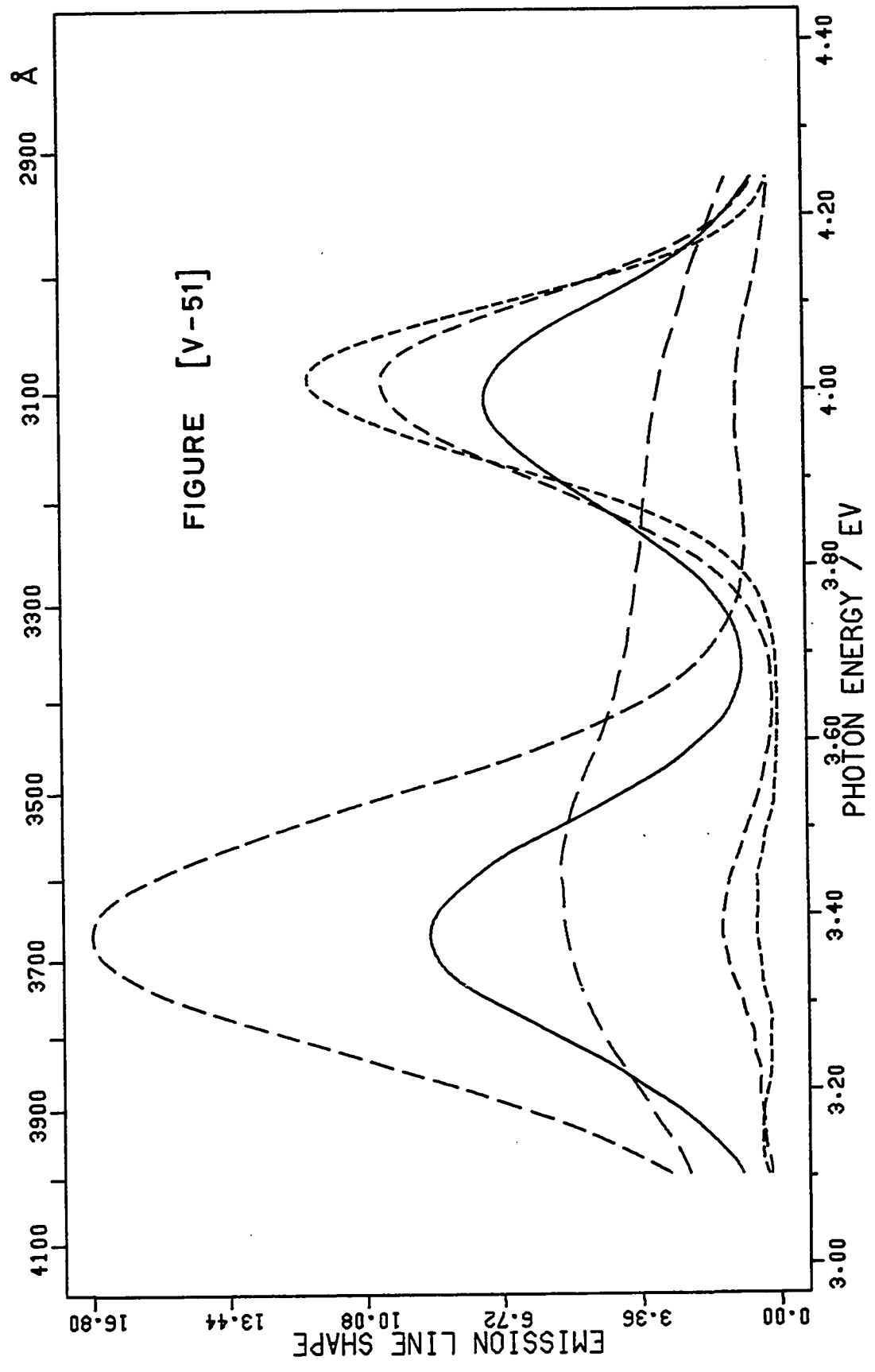
FIGURE [V-51]
EMISSION LINE SHAPE
0.00
3.36
6.72
10.08
13.44
16.80
Å
2900
3100
3300
3500
3700
3900
4100
PHOTON ENERGY / EV
3.00
3.20
3.40
3.60
3.80
4.00
4.20
4.40

EMISSION KBr:Tl^+

A-BAND EXCITATION

2 SYMMETRIC GAUSSIAN BANDS

RUN 1 - 296.0 K

FIGURE [V-52]

Δ - experimental points

The solid lines are the calculated resolved bands and their sum.

FIGURE [V-53]

Plot of I(experimental) - I(calculated) for each experimental point.

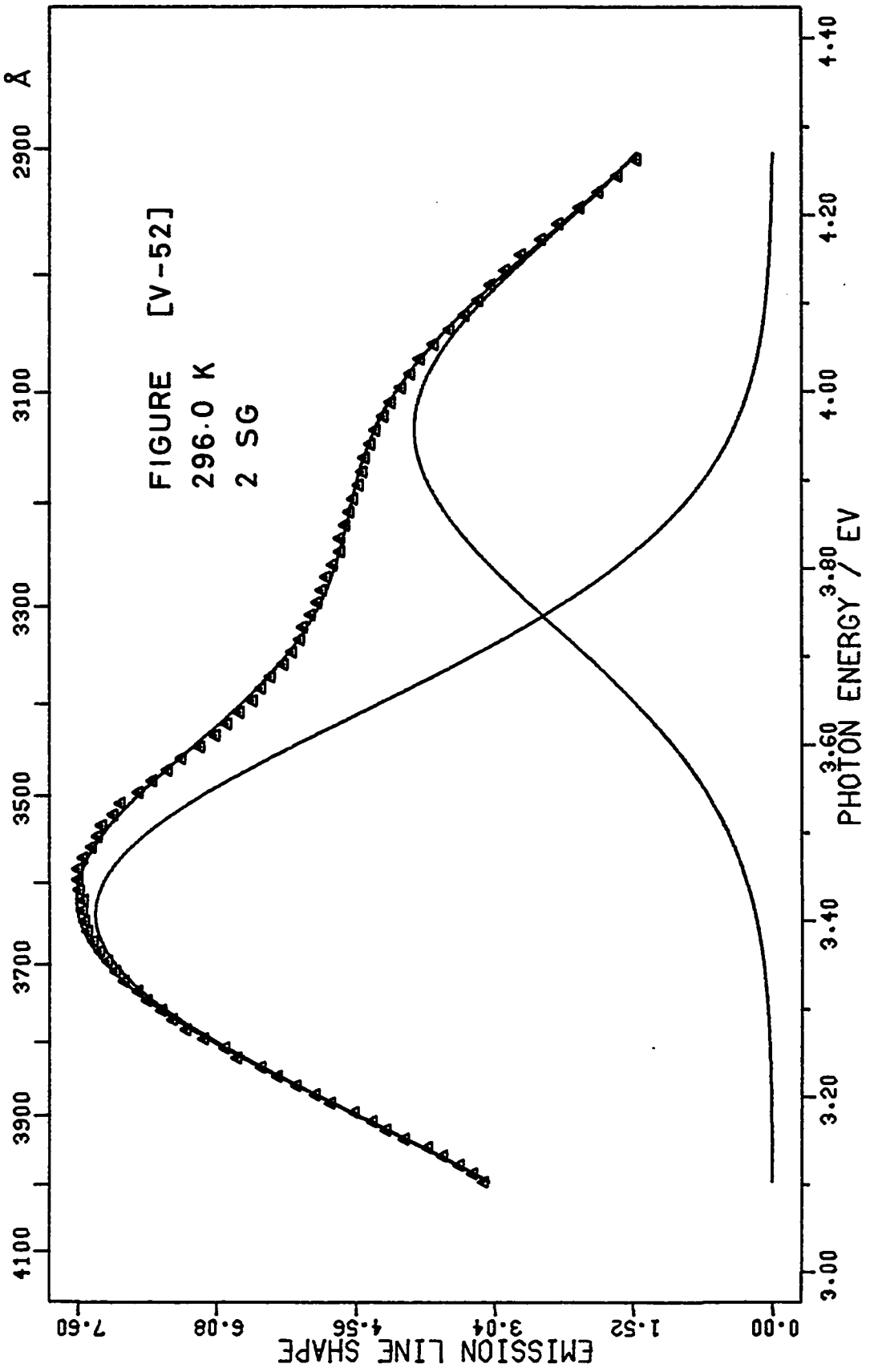
FIGURE [V-52]
296.0 K
2 SG
EMISSION LINE SHAPE
0.00
1.52
3.04
4.56
6.08
7.60
PHOTON ENERGY / EV
3.00
3.20
3.40
3.60
3.80
4.00
4.20
4.40
Å
4100
3900
3700
3500
3300
3100
2900

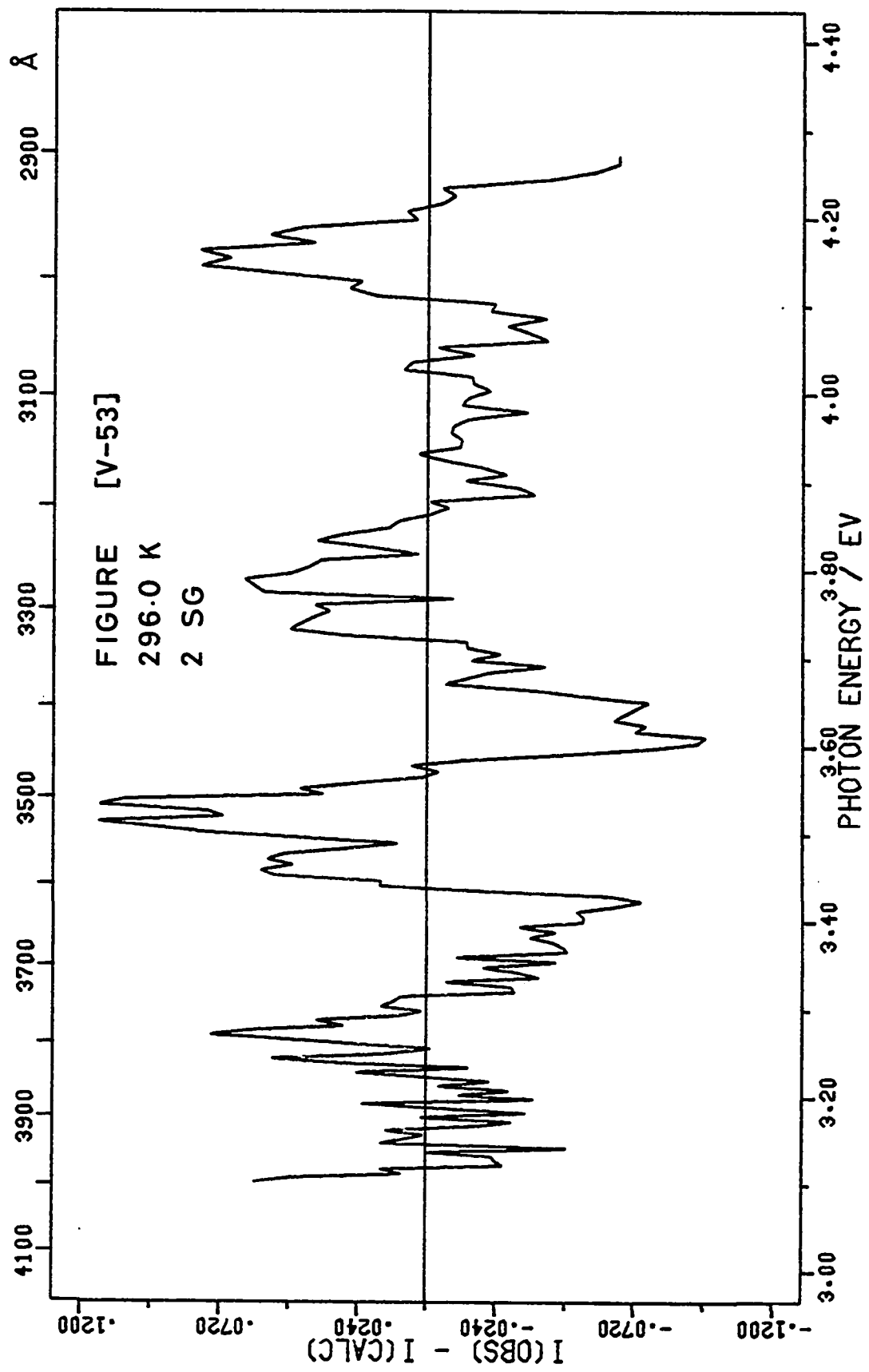
FIGURE [V-53]
296.0 K
2 SG
Å
2900
3100
3300
3500
3700
3900
4100
PHOTON ENERGY / EV
3.00
3.20
3.40
3.60
3.80
4.00
4.20
4.40
I (OBS) - I (CALC)
.1200
.0720
.0240
-.0240
-.0720
-.1200

EMISSION KBr:Tl^+

A-BAND EXCITATION

2 SYMMETRIC GAUSSIAN BANDS

RUN 2 - 83.0 K

FIGURE [V-54]

Δ - experimental points

The solid lines are the calculated resolved bands and their sum.

FIGURE [V-55]

Plot of I(experimental) - I(calculated) for each experimental point.

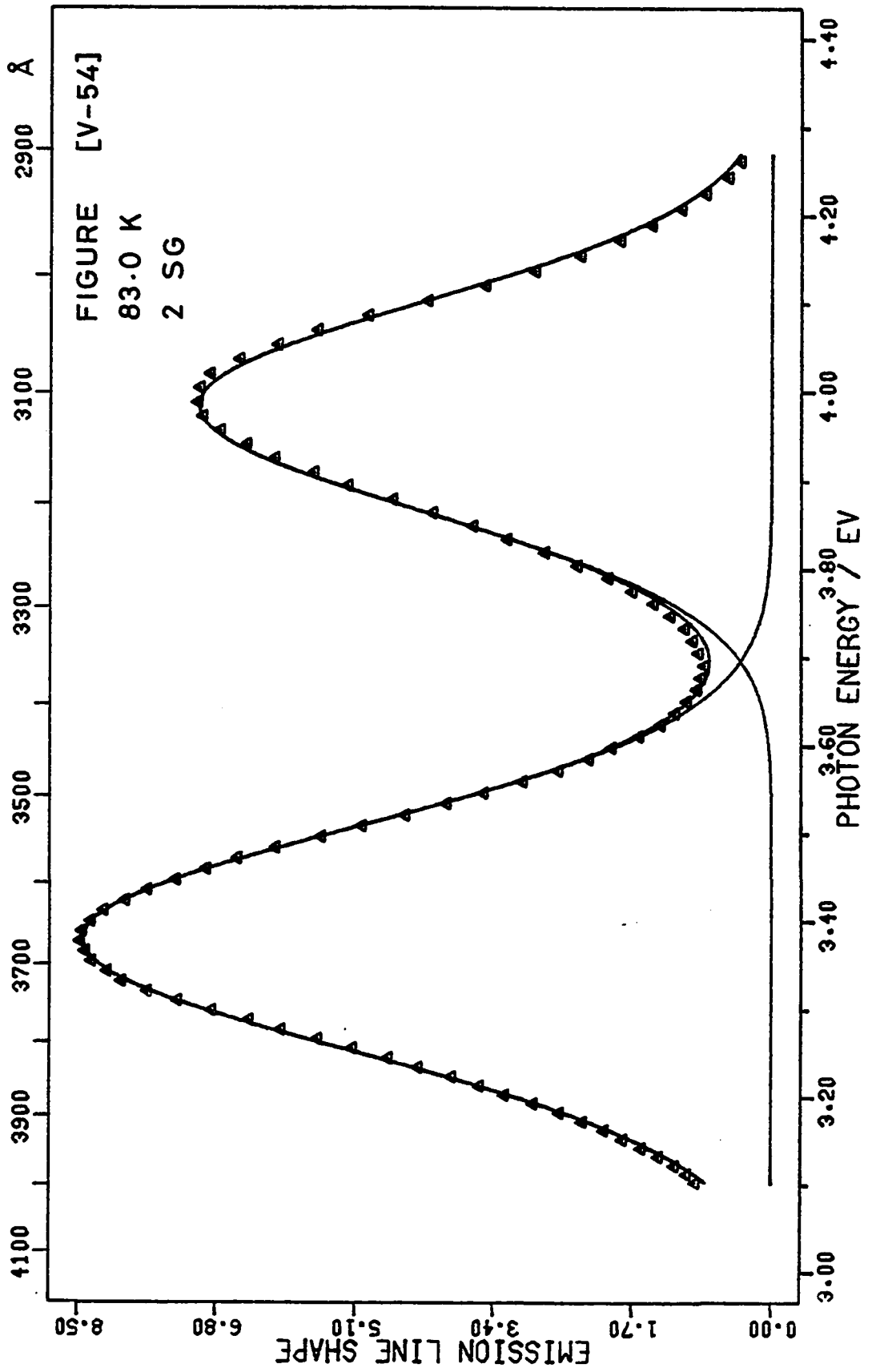
FIGURE [V-54]
83.0 K
2 SG
Å
2900
3100
3300
3500
3700
3900
4100
PHOTON ENERGY / EV
3.00
3.20
3.40
3.60
3.80
4.00
4.20
4.40
EMISSION LINE SHAPE
0.00
1.70
3.40
5.10
6.80
8.50

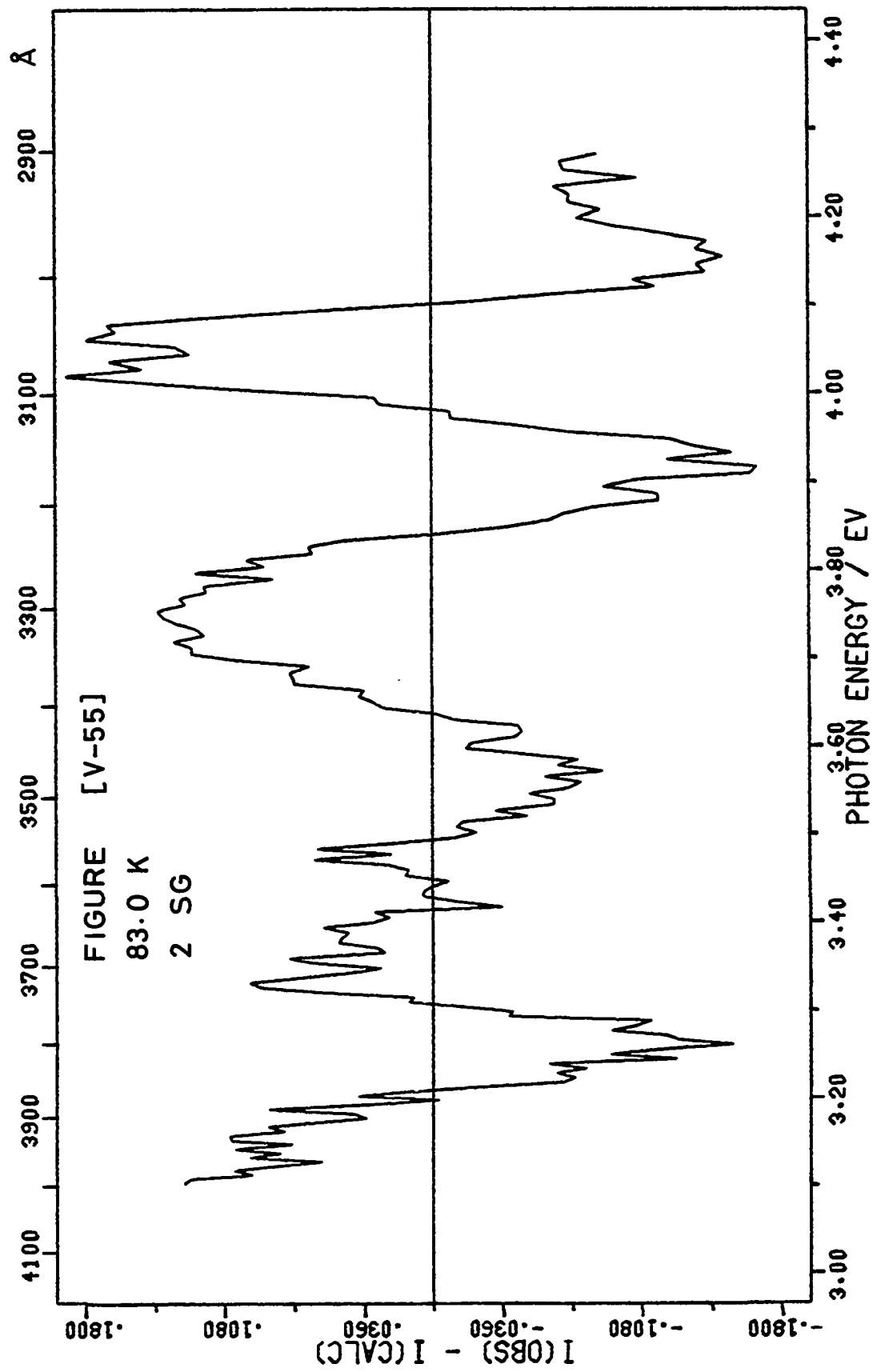
FIGURE [V-55]
83.0 K
2 SG
Å
2900
3100
3300
3500
3700
3900
4100
3.00
3.20
3.40
3.60
3.80
4.00
4.20
4.40
PHOTON ENERGY / EV
I(OBS) - I(CALC)
.1800
.1080
.0360
-.0360
-.1080
-.1800

EMISSION KBr:Tl^+

A-BAND EXCITATION

3 SYMMETRIC GAUSSIAN BANDS

RUN 132 - 15.5 K

FIGURE [V-56]

Δ - experimental points

The solid lines are the calculated resolved bands and their sum.

FIGURE [V-57]

Plot of I(experimental) - I(calculated) for each experimental point.

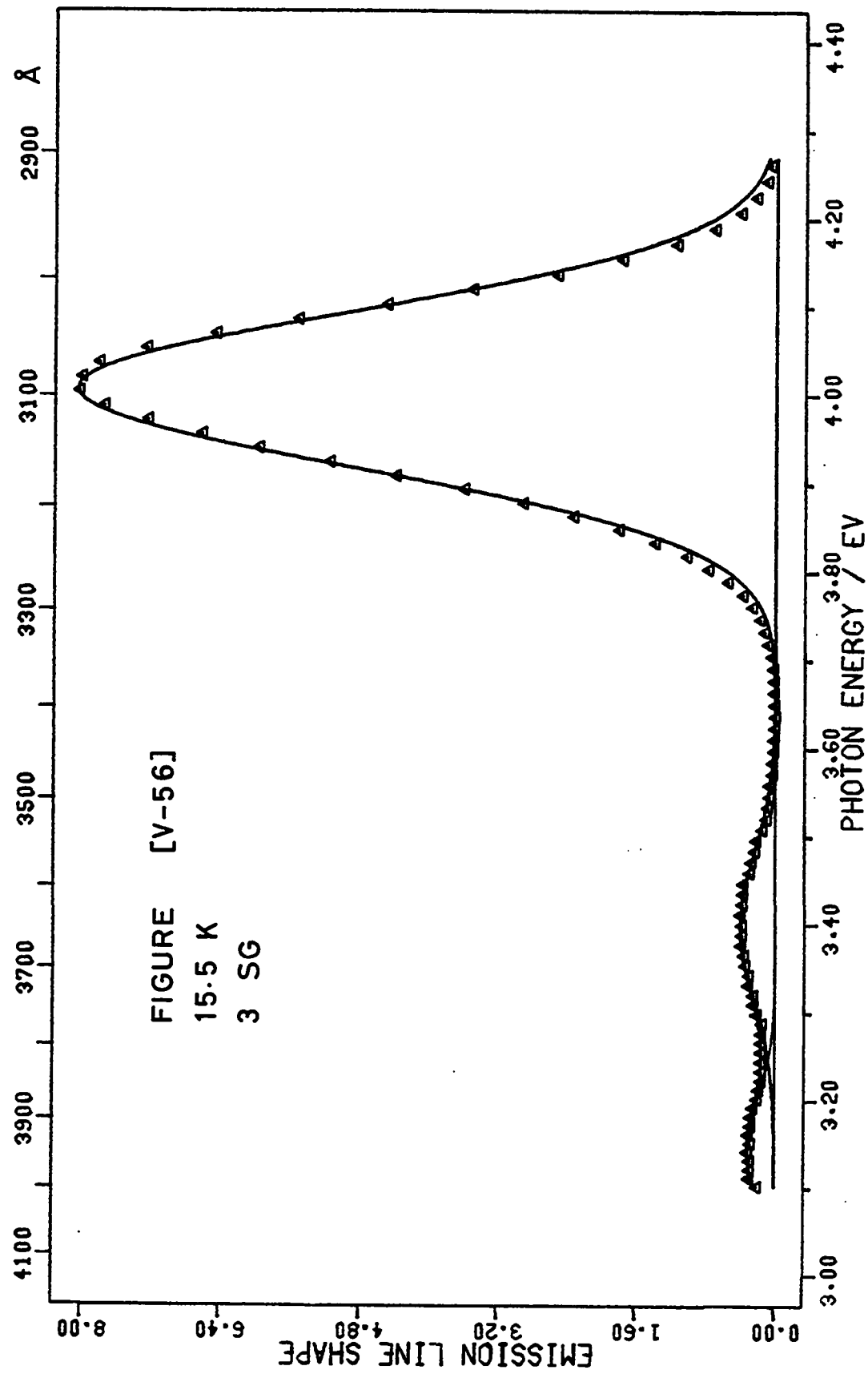
FIGURE [V-56]
15.5 K
3 SG
EMISSION LINE SHAPE
0.00
1.60
3.20
4.80
6.40
8.00
PHOTON ENERGY / EV
3.00
3.20
3.40
3.60
3.80
4.00
4.20
4.40
Å
4100
3900
3700
3500
3300
3100
2900

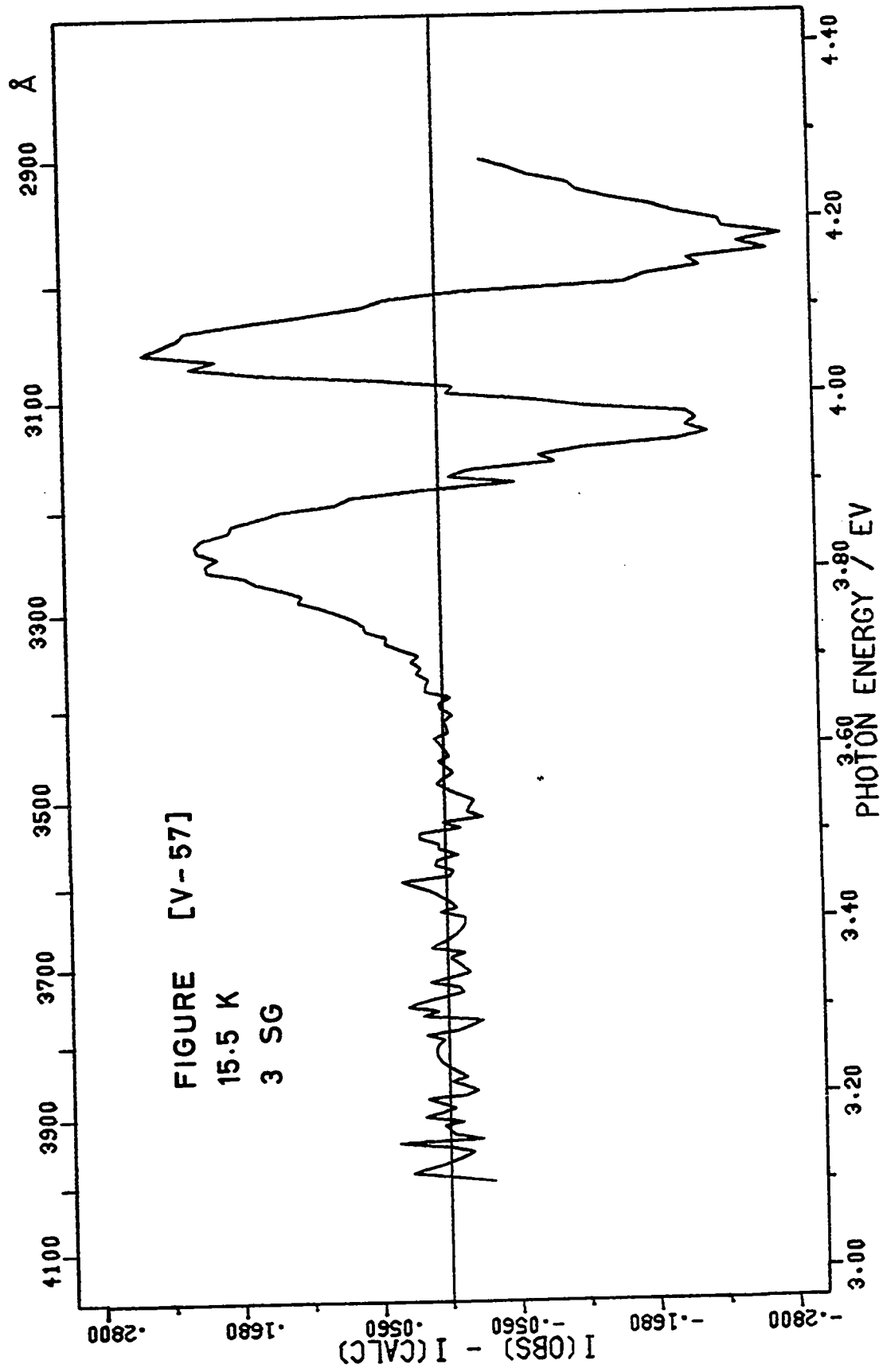
FIGURE [V-57]
15.5 K
3 SG
I (OBS) - I (CALC)
PHOTON ENERGY / EV
Å
4100
3900
3700
3500
3300
3100
2900
3.00
3.20
3.40
3.60
3.80
4.00
4.20
4.40
-.2800
-.1680
-.0560
.0560
.1680
.2800

FIGURE [V-58]

EMISSION $KBr:Tl^+$

A-BAND EXCITATION

3 SYMMETRIC GAUSSIAN BANDS

H_{obs} against $T^{\frac{1}{2}}$

■ - experimental parameter values Band 1

O - experimental parameter values Band 2

Δ - experimental parameter values Band 3

Band 1	Band 2
$H_0 = 0.194$ eV	$H_0 = 0.184$ eV
$\nu = 1.5 \times 10^{12}$ sec^{-1}	$\nu = 1.41 \times 10^{12}$ sec^{-1}

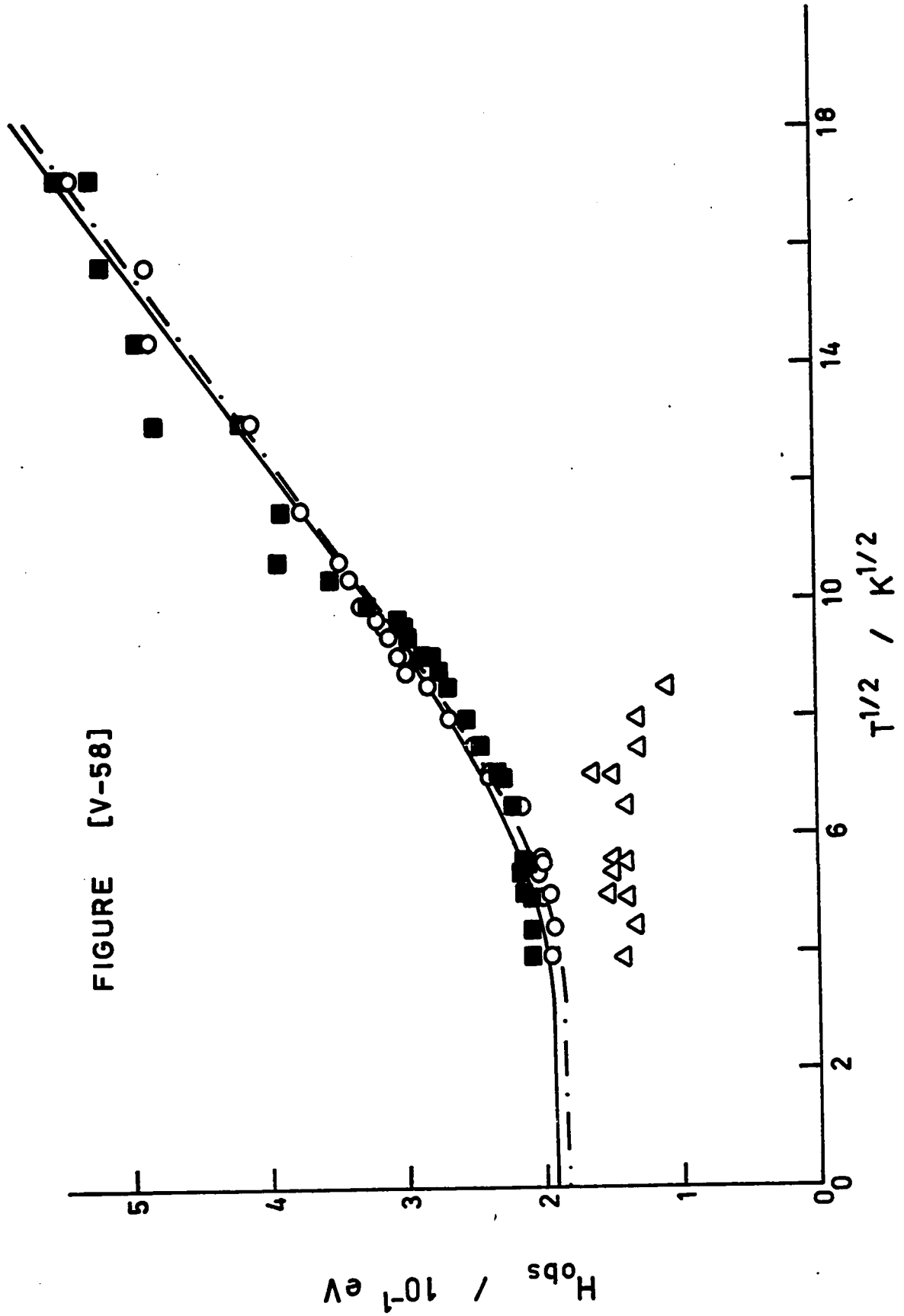

FIGURE [V-58]

FIGURE [V-59]

EMISSION KBr:Tl^+

A-BAND EXCITATION

3 SYMMETRIC GAUSSIAN BANDS

E_m against T

■ - experimental parameter values Band 1

○ - experimental parameter values Band 2

△ - experimental parameter values Band 3

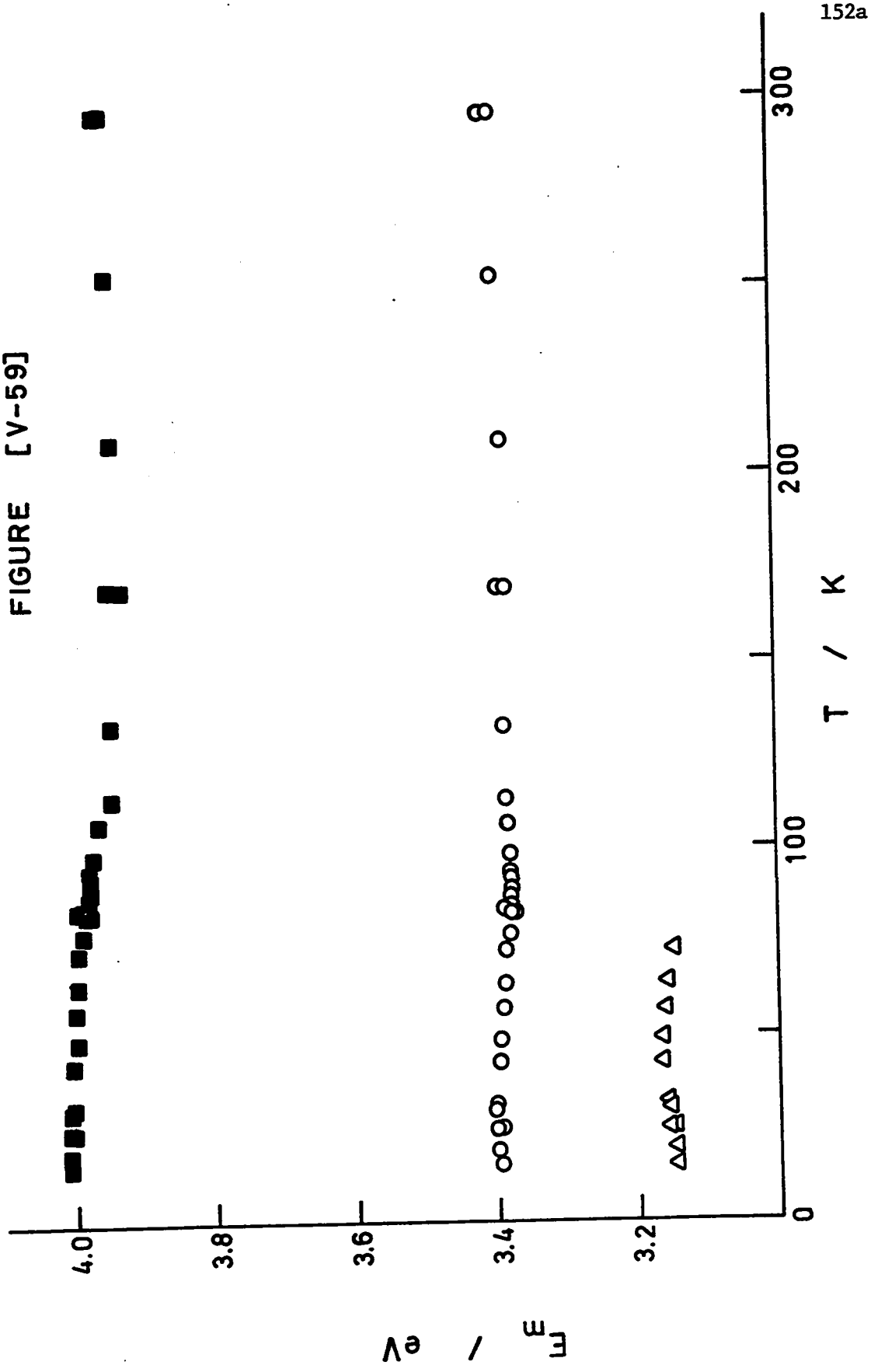

FIGURE [V-59]

FIGURE [V-60]

EMISSION KBr:Tl^+

A-BAND EXCITATION

3 SYMMETRIC GAUSSIAN BANDS

I_m against T

■ - experimental parameter values Band 1

○ - experimental parameter values Band 2

△ - experimental parameter values Band 3

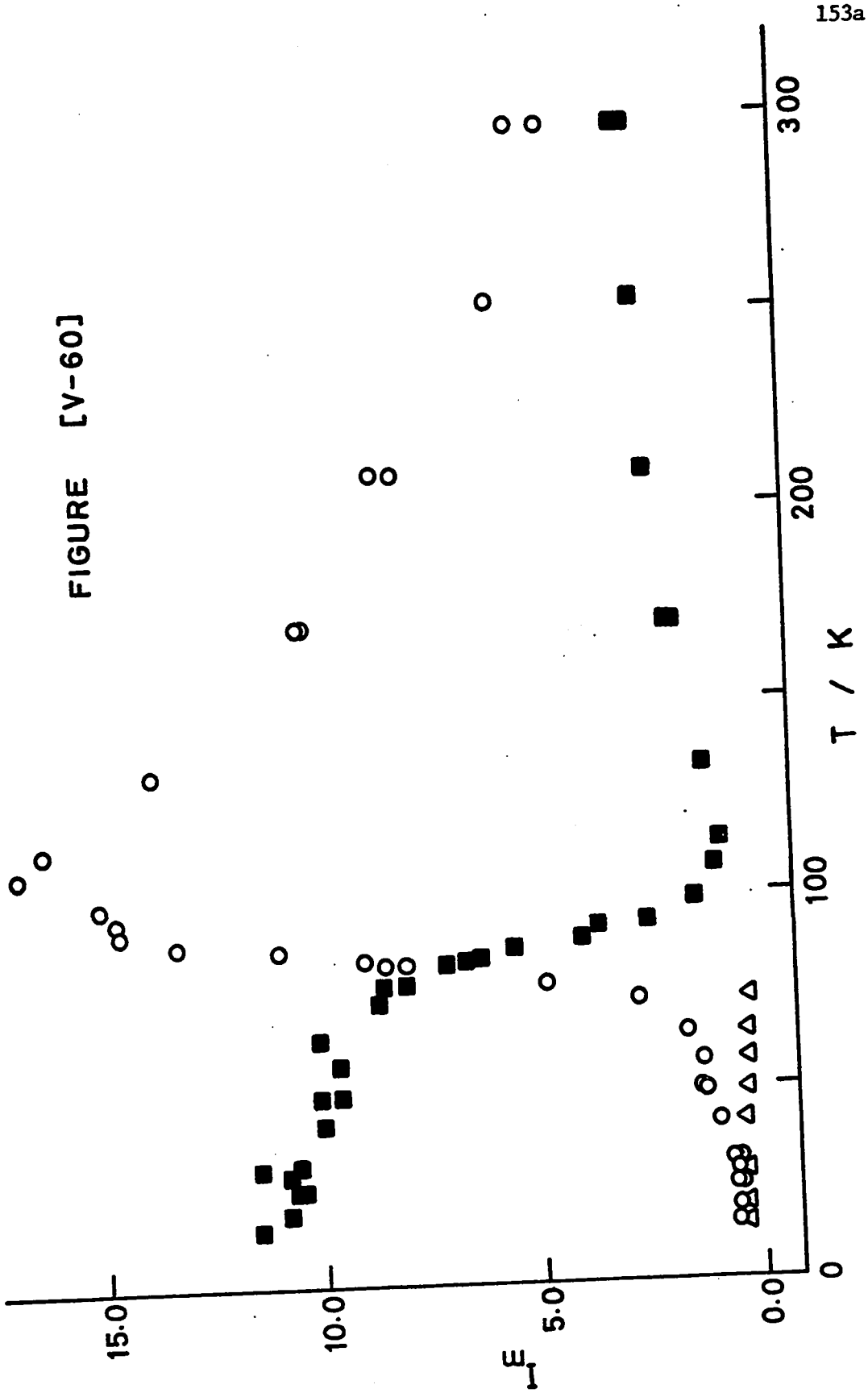

FIGURE [V-60]

FIGURE [V-61]

EMISSION $KBr:Tl^+$

A-BAND EXCITATION

3 SYMMETRIC GAUSSIAN BANDS

$\Delta E_{splitting}$ against T

■ - E_{12} [E_m(Band 1) - E_m(Band 2)]

○ - E_{23} [E_m(Band 2) - E_m(Band 3)]

FIGURE [V-61]

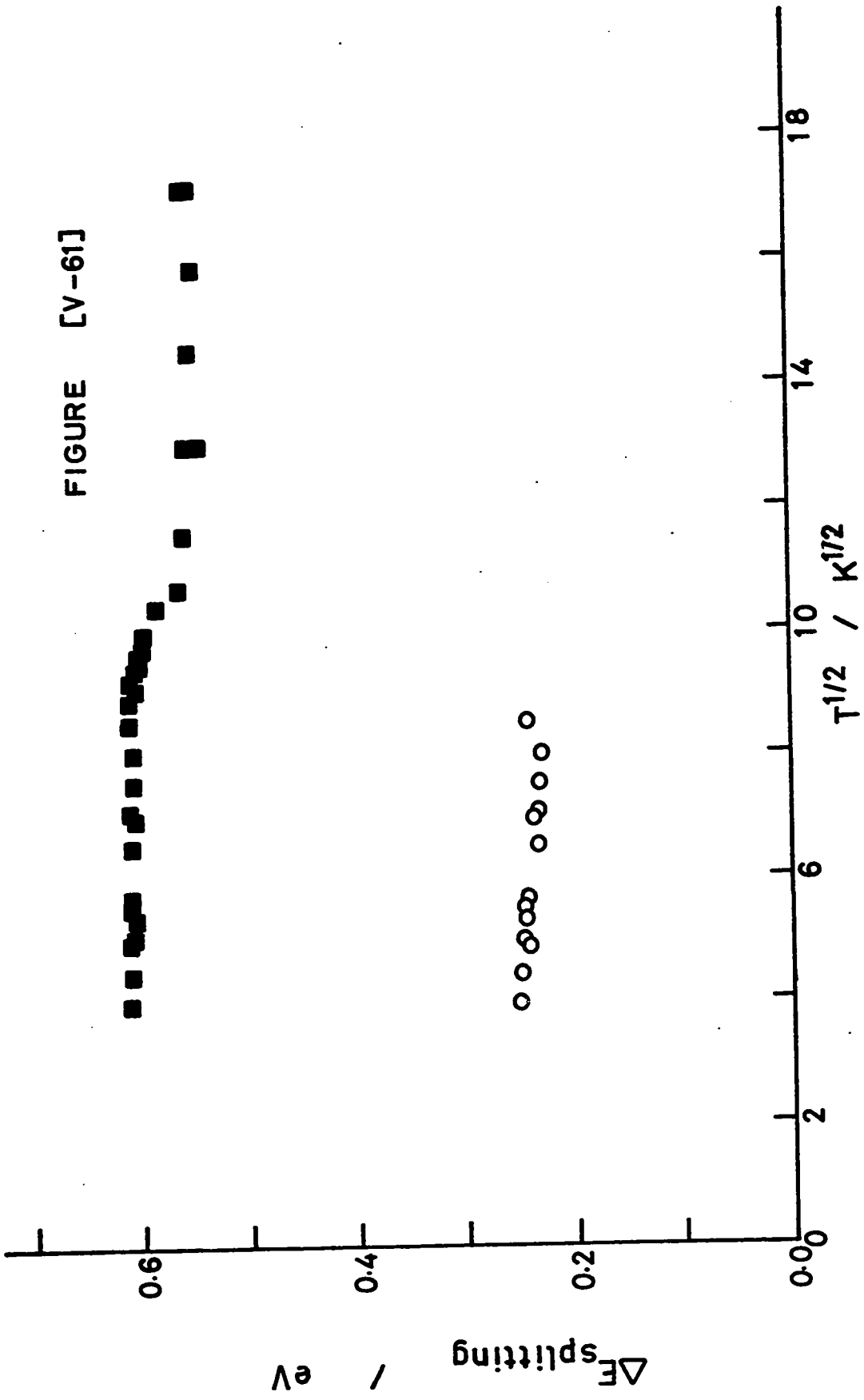

CHAPTER VI

DISCUSSION

1. Absorption

1-1 Introduction

The configuration coordinate approximation assumes that the adiabatic potentials for the ground and excited states can be expanded as a function of a single coordinate and that only terms up to and including the square of this coordinate are significant. If the force constants in the ground and excited states are the same (linear coupling), the absorption line shape can be derived quantum mechanically (see Equations [II-56] and [II-60]). At low temperatures for large values of the coupling constant, a, the line shape is very nearly gaussian. At high temperatures, the line shape is accurately gaussian. For the semi-classical approximation in linear coupling, the line shape is accurately gaussian at all temperatures (see Equation [II-76]). The position of the band maximum is independent of temperature and the temperature dependence of the half-width obeys the relationship

$$H_{obs} = H_o[\coth(\hbar\omega_a/2kT)]^{\frac{1}{2}} \qquad [II-78]$$

If the force constants in the ground and excited states are not the same (quadratic coupling), the semi-classical approximation gives a line shape which is asymmetric gaussian (see Equation [II-87]). E_m is dependent on temperature and the temperature dependence of the half-width is given approximately by equation [II-78].

In order to determine the most satisfactory model for the A-band absorption of KBr:Tl^+, the experimental results were analyzed as either symmetric or asymmetric gaussian bands (see Equations [IV-1] and [IV-2]). In addition, the temperature dependences of the derived parameters were investigated to determine whether or not they conform to the theoretical predictions.

1-2 Single Band Analysis

Representative results for the analysis of the line shape as a single symmetric gaussian band are given in Figures [V-2] to [V-7]. The fit is very unsatisfactory even at low temperatures where the band appears most symmetric. The error plots show that the deviations are large and systematic.

Results for the analysis as a single asymmetric gaussian band are given in Figures [V-11] to [V-16]. Although the fit is better, particularly at high temperatures, the analysis is still unsatisfactory since the deviations exhibit large systematic changes. For either analysis, the intensity of the band increases smoothly as the temperature decreases (see Figures [V-10] and [V-19]). For an asymmetric gaussian, the skew parameter, b, can be defined as

$$b = \log\left(\frac{E_1-E_m}{E_m-E_2}\right) \qquad \text{[VI-1]}$$

where E_1 and E_2 are the energies corresponding to I at $\frac{1}{2}I_m$ and E_m is the position of maximum intensity, I_m. b, Figure [V-20], is negative and increases smoothly with decreasing temperature indicating that the band is becoming more symmetric. At very low temperatures, b is positive showing that the band is now asymmetric to the high energy side.

Theoretically, for a symmetric gaussian, E_m is independent of T,

$$E_m = E_{ab} \qquad [VI-2]$$

and for an asymmetric gaussian, the temperature dependence of E_m is given by

$$E_m = E_{ab} - (r-1)kT^* - \frac{(r-1)^3}{r^2}\frac{(kT^*)^2}{\frac{1}{2}K_a q_o^2} \qquad [VI-3]$$

where

$$r = K_b/K_a \qquad [VI-4]$$

and the other quantities are as defined in Chapter II. Unless r is very large, the third term on the right hand side of equation [VI-3] should be negligible and E_m becomes a linear function of kT^*.

The theoretical expressions for the temperature dependence of E_m were derived for conditions of constant volume. However the experiments were done at constant pressure and the values of E_m must be corrected for thermal expansion before a comparison with theory can be made. Corrections of this type have been made by Jacobs and Krishna Menon [66] for the F centre in KBr. However, the calculation involves the use of bulk values of the thermal expansivity and compressibility and there is some doubt as to the validity of using macroscopic properties to describe the local values around the Tl^+ ion. Rough corrections to E_m for the single symmetric gaussian, Figure [V-9], indicate that E_m is constant.

Similar corrections to E_m for the single asymmetric gaussian, Figure [V-18], result in a negative value for r. This means that one of the force constants must be negative, a result not meaningful in this situation.

Thermal expansion corrections to the half-width are not necessary, so that the experimentally derived values of H_{obs} can be expected to follow the theoretical expressions accurately. Plots of H_{obs} against $T^{1/2}$ are given in Figures [V-8] and [V-17]. The solid line in both cases represents the best fit of the data to equation [II-78]. The values of H_o and $\nu(\Xi\omega/2\pi)$ are given in Table [VI-1]. In both cases, the experimental data curves too sharply for the coth function. To ensure that the difficulties in fitting were not caused by the least squares routine used, the data were analyzed on a generalized least squares program having the option of weighting both x and y variables [88]. With no weighting, the results were identical with those previously obtained. Using full weighting, the parameters obtained were essentially the same but the standard deviation indicated that the weighting factors were too small. The weights in H_{obs} were obtained from the least squares resolution of the original data and those in T were estimated from the observed experimental fluctuations in temperature during a run. Thus the weights were reasonably well known and it was concluded that the model did not fit the data. The introduction of an arbitrary additive constant to equation [II-78] gave an empirical model which did fit the data well. However no physical significance can be attached to a negative intercept in the high temperature limit of equation [II-78]. It should be noted that there is an inherent inconsistency in fitting the data for the asymmetric gaussian to equation [II-78] since this

TABLE [VI-1]

PARAMETERS DERIVED FROM THE TEMPERATURE DEPENDENCE OF H_{obs}

Model	Band	H_o/eV	$\nu/10^{12}$ sec^{-1}	S
1 SG		0.0572	1.61	13.5
1 ASG		0.0577	1.68	12.6
2 SG	1	0.044	3.80	1.5
	2*	0.035	0.689	27.8
2 ASG	1	0.040	3.38	1.5
	2	0.039	1.09	14.1
3 SG	1	0.038	3.10	1.6
	2*	0.050	2.23	5.4
	3	0.072	2.51	9.1

* - parameters uncertain

TABLE [VI-2]

PARAMETERS DERIVED FROM THE TEMPERATURE DEPENDENCE OF m_2

Model	Band	$\|r\|$	$K_a q_o^2/10^{-2}$ eV	$\nu/10^{12}$ sec^{-1}
1 ASG		3.22	1.46	1.85
2 ASG	1	1.72	1.20	4.10
	2	3.58	0.638	1.75

relationship is strictly valid only for linear coupling. A more significant quantity is the second moment, m_2, given by

$$m_2 = \frac{H_{obs}}{2\sinh(b)}^2 \left\{ \exp\left[\frac{2b^2}{1n2}\right] - \exp\left[\frac{3b^2}{21n2}\right] \right\} \qquad [VI-5]$$

In the limit of small b,

$$m_2 = H_{obs}^2 / (81n2)$$

which is the same as the expression derived for an accurately gaussian distribution. The temperature dependence of m_2 is

$$m_2 = r^2 K_a q_o^2 (kT^*) + \tfrac{1}{2}(r-1)^2 (kT^*)^2 \qquad [VI-6]$$

which is equivalent to equation [II-90]. A plot of m_2 against T is given in Figure [VI-1]. The solid line is the calculated best fit to equation [VI-6]. The values of the parameters, r, (Kq_o^2), and $\nu(\equiv\omega/2\pi)$, are given in Table [VI-2]. The value of r is very large and the value of (Kq_o^2) is very small. This is a reflection of overemphasizing the $\coth^2$ term in order to fit the data.

Despite the reasonably adequate representation of the temperature dependences of the derived parameters by the theoretical expressions, it is clearly evident from a comparison of the observed and calculated line shape that neither a single symmetric gaussian nor a single asymmetric gaussian can accurately characterize the experimental data. In particular, the flatness of the experimental data at the peak as compared to either calculated curves, suggests strongly that the band is multiple.

FIGURE [VI-1]

A-BAND ABSORPTION KBr:Tl^+

1 ASYMMETRIC GAUSSIAN BAND

m_2 against T

O - experimental parameter values

The solid line is calculated from equation [VI-6].

$|r| = 3.22$

$Kq_o^2 = 0.0146$ eV

$\nu = 1.85 \times 10^{12}$ sec^{-1}

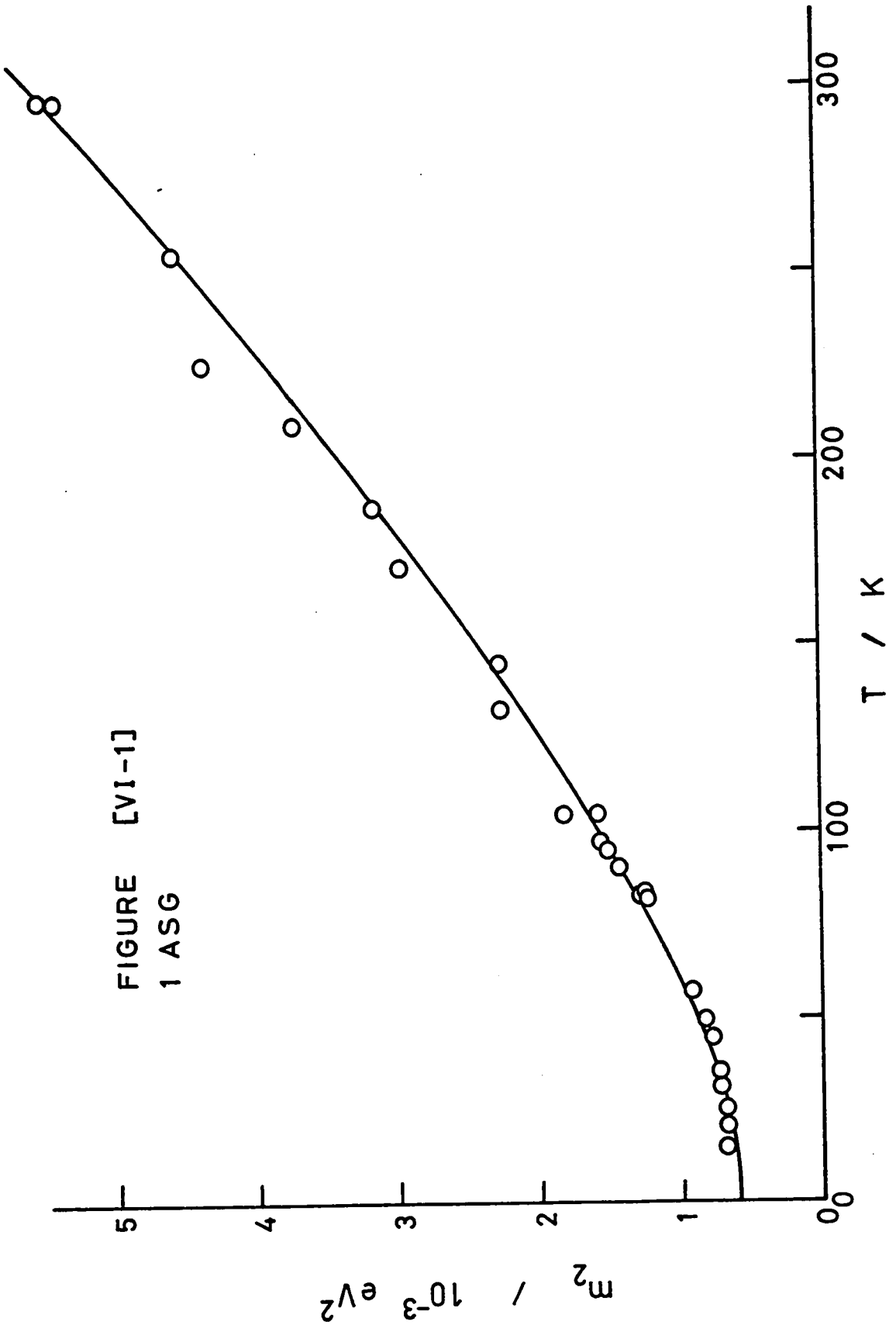

FIGURE [VI-1]
1 ASG

1-3 Two Band Analysis

The fit of the absorption line shape as two symmetric gaussian curves at representative temperatures is given in Figures [V-21] to [V-26]. Although the deviations are considerably smaller than those for either of the single band models especially at low temperatures (see Figure [V-50]), there is still a systematic fluctuation. At high temperatures the resolution is not significantly better than that for a single asymmetric gaussian curve.

The use of two asymmetric gaussian bands gives the results shown in Figures [V-31] to [V-36]. For this model, the deviations appear to be almost completely random over the complete range of temperatures studied.

The temperature dependence of I_m for both two symmetric gaussian and two asymmetric gaussian bands, Figures [V-29] and [V-39], show rather erratic behavior at low temperatures but it is difficult to attach any significance to this fact. The skew parameter, b, Figure [V-40], also shows considerable scatter. However, it is evident that the low energy component is the more asymmetric. As the temperature decreases, b tends to become more positive for both bands.

For two symmetric gaussian bands, the temperature dependence of E_m, Figure [V-28], shows very peculiar behavior. At high temperatures, E_m varies linearly with T but as the temperature decreases, E_m reaches a maximum and then decreases again. When thermal expansion corrections are made, E_m for the low energy band is approximately constant as predicted by theory although there is still a small hump around 70 K. For the high energy band, the thermal expansion correction results in a linear relationship between E_m and T where E_m increases with increasing T.

For the low energy band of two asymmetric gaussians, Figure [V-38], E_m decreases linearly with increasing T. For the high energy band, E_m is constant to ~150 K and then decreases with increasing T. Corrections for thermal expansion give $r(\equiv K_b/K_a)$ values of -3.2 for the high energy band and 0.2 for the low energy band.

The temperature dependences of H_{obs} for two symmetric gaussian bands, Figure [V-27], are unusual in that at low temperatures the half width for the high energy band (Band 1) increases from the value at ~70 K. The solid line represents the best fit to equation [II-78]. The parameters are given in Table [VI-1]. However, the fit is unsatisfactory. For the low energy band (Band 2) the solid line is the best fit achieved although the iteration procedure used failed to alter H_o and consequently the values of the parameters are suspect.

For two asymmetric gaussian bands, the temperature dependences of H_{obs}, Figure [V-37], are satisfactorily fitted by the coth function (see Equation [II-78]) although the data for the low energy band (Band 2) shows substantial scatter. The analysis of the second moments (see Equation [VI-6]) is shown in Figure [VI-2]. The parameters are given in Table [VI-2] and are not in the ranges expected.

It should be pointed out that the derived frequency, whichever analysis is used, is that of the ground state, ν_a. Even if more than one excited state is involved in the absorption process the frequency obtained from fitting the temperature dependence of the parameters to the theoretical expressions should be the same for all bands. This is not the case.

FIGURE [VI-2]

A-BAND ABSORPTION KBr:Tl^+

2 ASYMMETRIC GAUSSIAN BANDS

m_2 against T

■ - experimental parameter values Band 1

O - experimental parameter values Band 2

The solid lines were calculated from equation [VI-6].

Band 1		Band 2	
$\|r\|$	= 1.72	$\|r\|$	= 3.58
Kq_o^2	= 0.0120 eV	Kq_o^2	= 0.00638 eV
ν	= 4.10×10^{12} sec^{-1}	ν	= 1.75×10^{12} sec^{-1}

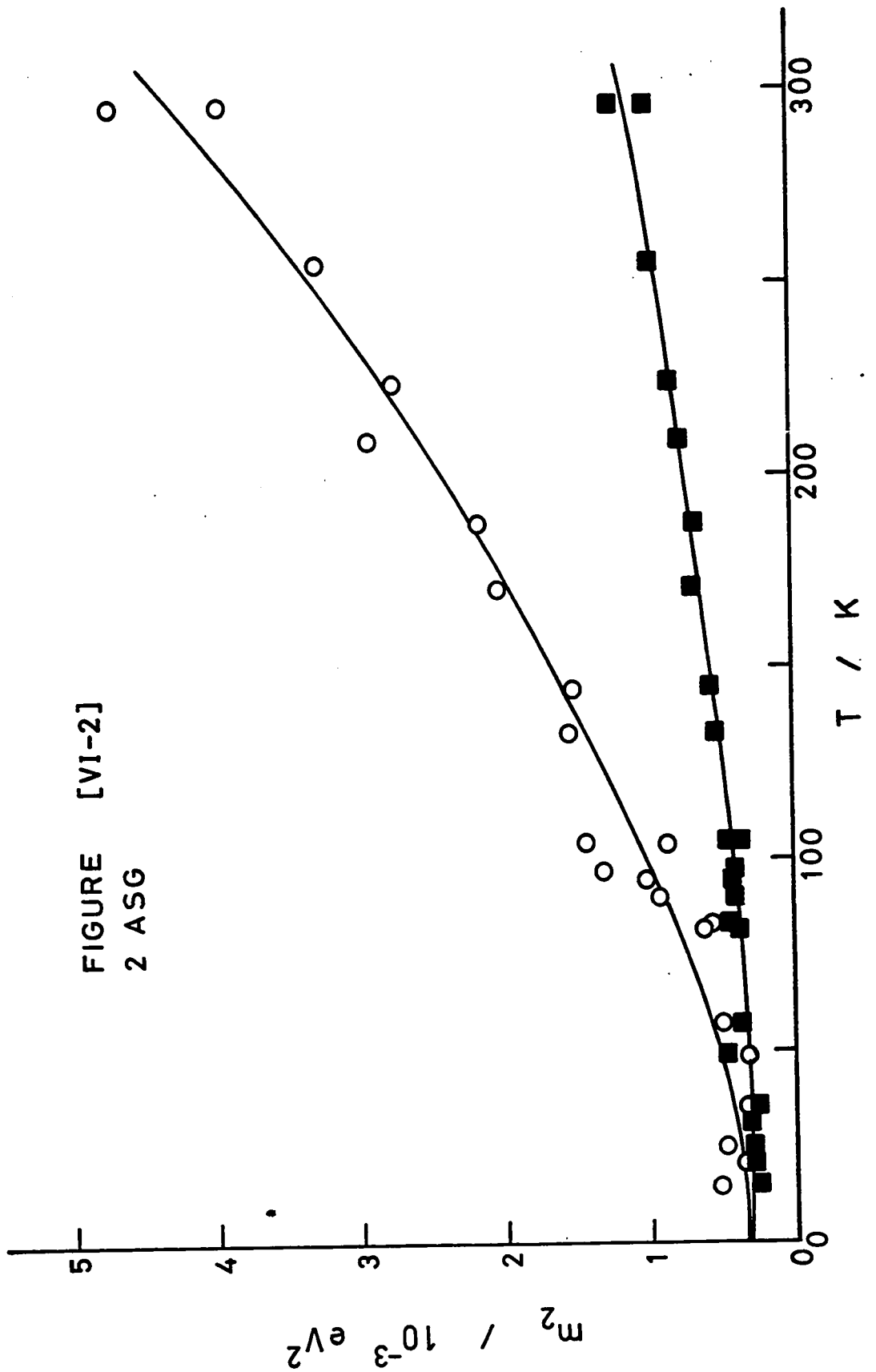

FIGURE [VI-2]
2 ASG

1-4 Three Band Analysis

The resolution of the absorption line shape into three symmetric gaussian bands was investigated and representative results are shown in Figures [V-41] to [V-46]. It was possible to resolve the shape as three bands only above liquid nitrogen temperature. The scatter in the derived parameters suggests that the analysis is dubious below 120 K. Also the standard deviation of the fit (see Figure [V-50]) is not significantly better than that for two asymmetric gaussian bands. From a purely statistical point of view, the use of an extra parameter should reduce the standard deviation [89]. In actual fact, at most temperatures, the standard deviation was higher.

Esser and Levy [90] were successful in resolving the A-band absorption in KCl:Tl^+ into three symmetric gaussian bands above 200 K but into only two symmetric gaussian bands below this temperature. Braner and Halperin [40] investigated the validity of resolving the A-band absorption in KCl:Tl^+ as two or three symmetric gaussian bands over the temperature range 4-700 K and concluded that resolution into three bands was not justified.

Despite reservations concerning the validity of the three band resolution, the temperature dependence of the parameters was investigated. All three parameters, I_m Figure [V-48], E_m Figure [V-47] and H_{obs} Figure [V-46], show smooth relationships with temperature at high temperatures. Thermal expansion corrections make the values of E_m for the two lowest energy bands approximately constant. However, after correction, the highest energy band shows an increase in E_m with increasing T. The half-widths were fitted to equation [II-78]. The lack of data below 80 K makes the values of H_o unreliable (see Table

[VI-1]). In fact, for the middle band, the computer program failed to alter H_o during iteration.

1-5 Conclusions

The best empirical fit to the experimental data is given by the sum of two asymmetric gaussian bands. However the parameters obtained by fitting the temperature dependences of H_{obs} or m_2 to the theoretical expressions do not lend themselves to interpretation on the basis of the configuration coordinate model. In particular, the frequencies obtained for the ground state from the two bands are very different. This is inconsistent with the model. It can be concluded that the assumptions inherent in the configuration coordinate model, particularly that the excited state adiabatic potential can be represented as an harmonic oscillator, are not valid. Moreover, the Huang-Rhys parameter, S, calculated from

$$H_o = 8\ln 2(\hbar\omega)^2 S \qquad [VI-7]$$

(see Table [VI-1]) shows that the average vibrational quantum number in the excited state is not large. Hence the assumption that the transition is to a sufficiently high vibrational state so that the excited state can be treated classically is violated. Consequently a different model is required.

1-6 Jahn-Teller Effect

The A-band absorption in $KBr:Tl^+$ is ascribed to the transition $^1A_{1g} \rightarrow {}^3T_{1u}$ (see Figure [II-1]). The transition is spin forbidden but becomes allowed through spin orbit mixing with the $^1T_{1u}$ state. The A-band corresponds to a transition from a non-degenerate ground state

to a triply degenerate excited state. Jahn and Teller [91] pointed out that polyatomic molecules in degenerate electronic states are unstable and the molecule will deform so as to reduce its symmetry and thereby remove the electronic degeneracy. Therefore, it is reasonable to suppose that the T_{1u} state will be split and that the A-band absorption of $KBr:Tl^+$ will consist of more than one component.

Toyozawa and Inoue [21] have shown that for a point imperfection in a system of cubic symmetry, e.g. Tl^+ in KBr, the T_{1u} state will interact with vibrational modes of A_{1g}, E_g, and T_{2g} symmetry. Interaction with the A_{1g} and E_g modes will not split the state but the absorption will be broadened. They therefore examined the effect of the T_{2g} modes on the structure of the A and C bands. Their analysis predicts a triplet structure for the C band and a doublet structure for the A-band.

The electron lattice interaction part of the total Hamiltonian can be written as

$$\hat{H}_{el} = \hat{H}_{JT} + \hat{H}_{Q} \qquad \text{[VI-8]}$$

where $\hat{H}_{JT}$ is the Hamiltonian for the Jahn-Teller interaction with the T_{2g} modes and $\hat{H}_{Q}$ is the quadratic interaction with the lattice. $\hat{H}_{el}$ is expressed in terms of interaction coordinates which are derived from the normal modes of vibration of the crystal lattice. There are a total of six interaction coordinates corresponding to the vibration interaction modes; A_{1g} - (Q_1), E_g - (Q_2,Q_3), and T_{2g} - (Q_4,Q_5,Q_6).

$$\hat{H}_{Q} = \left(\sum_{j=1}^{6} Q_j^2 \right) \underset{\sim}{1} \qquad \text{[VI-9]}$$

where $\underset{\sim}{1}$ is the unit matrix and the force constants have been included in the Q_j's.

The Jahn-Teller interaction Hamiltonian has been shown to be [21]

$$\hat{H}_{JT}(T_{2g}) = c_2\underset{\sim}{T}Q + (\alpha_2\underset{\sim}{1} + \beta_2\underset{\sim}{T}^2)Q^2 \qquad \text{[VI-10]}$$

where

$$Q = (Q_4^2 + Q_5^2 + Q_6^2)^{1/2} \qquad \text{[VI-11]}$$

$$T = \begin{bmatrix} 0 & n & m \\ n & 0 & \ell \\ m & \ell & 0 \end{bmatrix} \qquad \text{[VI-12]}$$

and ℓ, m, n are the direction cosines of Q.

$$c_2 = -\tfrac{1}{2}\frac{R-2}{R+1}\,c \qquad \text{[VI-13]}$$

$$\alpha_2 = -\frac{R}{R+1}\frac{c^2}{\Delta_{BA}} \qquad \text{[VI-14]}$$

$$\beta_2 = \frac{3}{4}\frac{R}{R+1}\frac{c^2}{\Delta_{BA}} - \frac{9}{4}\frac{R}{(R+1)^2}\frac{c^2}{\Delta_{CA}} \qquad \text{[VI-15]}$$

where c is the coupling constant between the T_{1u} state and the T_{2g} modes, R is the dipole strength ratio of the C to A bands and Δ_{BA} and Δ_{CA} are the energy differences between the B and A electronic states and the C and A electronic states respectively. It should be noted that the wave function for the excited state corresponding to the A-band absorption can be written as

$$|A\rangle = \mu|^1T_{1u}\rangle + \nu|^3T_{1u}\rangle \qquad \text{[VI-16]}$$

Then

$$R = (\nu/\mu)^2 \qquad \text{[VI-17]}$$

Denoting the eigenvalues of T by t_1, t_2 and t_3 and using the semi-classical approximation $kT \rightarrow kT^*$, the normalized line shape may be written as [21]

$$g(y,\theta) = \frac{1}{3}(\pi\theta)^{-3/2} \sum_{i=1}^{3} \int d\lambda \frac{d\Omega}{d\lambda} \int_o^\infty dq\, q^2 \exp[-q^2/\theta] \quad X$$

$$\delta[-t_i(\lambda)q + \{t_i^2(\lambda) - 4/3\}q^2 - y] \qquad \text{[VI-18]}$$

where

$$\lambda = 2\ell mn \qquad \text{[VI-19]}$$

$$q = \frac{3}{2}\frac{|c|}{\Delta_{BA}}\frac{R}{R-2}\left[1 - \frac{3}{R+1}\frac{\Delta_{BA}}{\Delta_{CA}}\right] \quad Q \equiv Q/(q') \qquad \text{[VI-20]}$$

$$\theta = kT^*/(q')^2 \qquad \text{[VI-21]}$$

$$y = \frac{E-\varepsilon_o}{\Delta/3} = \frac{2(E-\varepsilon_o)}{|c|q'}\frac{(R+1)}{(R+2)} \qquad \text{[VI-22]}$$

and ε_o is the difference between the ground state and the unsplit excited state. The limits of integration over λ are $-2/3\sqrt{3}$ to $+2/3\sqrt{3}$.

In deriving equation [VI-18], two terms have been omitted from $\hat{H}_{el}$; the quadratic interaction Hamiltonian, $\hat{H}_Q$, and a term in Q^2 from $\hat{H}_{JT}$ which becomes smaller as R increases.

For small values of λ, $d\Omega/d\lambda$ can be written as

$$\frac{d\Omega}{d\lambda} \approx 4\pi\delta(\lambda) \qquad \text{[VI-23]}$$

Then equation [VI-18] becomes

$$g(y,\theta) = \frac{1}{3}(\pi\theta)^{-3/2}\, 4\pi g_s \qquad \text{[VI-24]}$$

where

$$g_s = \sum_{i=1}^{3} g_i(y,\theta)$$

and

$$g_i(y,\theta) = \int_0^\infty dq\ q^2 \exp[-q^2/\theta]\ \delta[-t_i(0)q + \{t_i^2(0) - 4/3\}q^2 - y] \quad [VI-25]$$

Since $t_1(0)=-1$, $t_2(0)=0$, and $t_3(0)=1$, the integrals are readily evaluated.

To be physically significant, q must be real and positive. This restriction means that the value of y must be less than 0.75. Figure [VI-3] is a plot of the components, g_i, and their sum, g_s, for $\theta=0.20$. Two of the components, g_3 and g_2, overlap extensively. Consequently they are unresolved and the overall shape shows only two components.

Toyozawa and Inoue state that the temperature dependence of the A-band splitting is given to ±5% over a wide range of temperatures by

$$\Delta E_{splitting} = 0.77 \frac{(R-2)}{(R+1)} |c| (kT)^{1/2} \quad [VI-26]$$

In the semi-classical approximation, $kT \rightarrow kT^*$ and the temperature dependence of the peak separation should be given by

$$\Delta E_{splitting} = \Delta E_o [\coth(\hbar\omega_a/2kT)]^{1/2} \quad [VI-27]$$

Plots of $\Delta E_{splitting}$ against $T^{1/2}$ for the resolution of the A-band absorption as two symmetric gaussian bands and as two asymmetric gaussian bands are given in Figures [V-30] and [V-41]. The solid lines give the best fit of the data to equation [VI-27]. The values of the derived parameters are given in Table [VI-3].

FIGURE [VI-3]

A-BAND ABSORPTION KBr:Tl^+

THEORETICAL LINE SHAPE

$g_i(y,\theta)$ against y

$\theta = 0.2$

$g_i(y,\theta)$ was calculated from equation [VI-25]

$$g_s = \sum_{i=1}^{3} g_i(y,\theta)$$

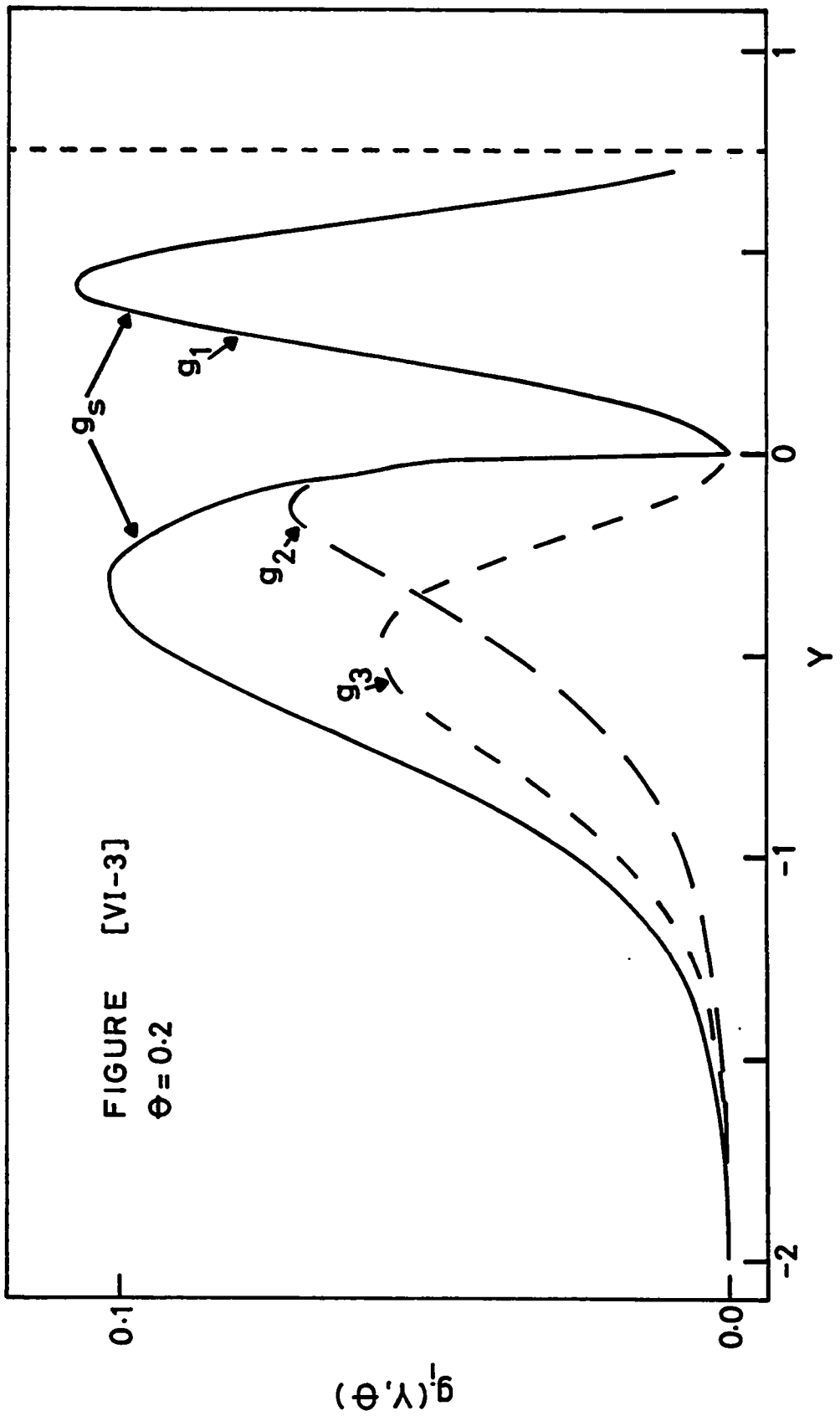

FIGURE [VI-3]
$\Theta = 0.2$

TABLE [VI-3]

PARAMETERS DERIVED FROM $\Delta E_{splitting}$

Model	E_o/eV	$\nu/10^{12}$ sec^{-1}
2 SG	0.031	2.53
2 ASG	0.030	2.19

Using experimentally determined values for R, Δ_{BA} and Δ_{CA}, the coupling constant, c, and the factor q' can be evaluated. Then θ and y can be related to experimental temperatures and energies thereby enabling a comparison of the theoretical line shape with experimental results. The relevant quantities for $KBr:Tl^+$ are given in Table [VI-4].

TABLE [VI-4]

ABSORPTION LINE SHAPE PARAMETERS

$$R = 4.4$$

$$\Delta_{CA} = 1.13 \text{ eV}$$

$$\Delta_{BA} = 0.80 \text{ eV}$$

$$c = 1.32 \text{ eV}^{1/2}$$

$$\theta = 7.55 \text{ kT}^*$$

$$y = (E-\varepsilon_o)/0.10$$

Plots of $g(y,\theta)$ against y for θ=0.20, 0.10, and 0.06 are given in Figures [VI-4], [VI-5] and [VI-6]. Superimposed on $g(y,\theta)$ are the experimental data at temperatures corresponding to these values of θ. The ordinate has not been adjusted for either set of data so the relative magnitudes are not necessarily meaningful.

FIGURE [VI-4]

A-BAND ABSORPTION KBr:Tl^+

COMPARISON OF THEORETICAL AND EXPERIMENTAL LINE SHAPES

$\theta = 0.2$ $T = 296.0$ K

● - experimental data

——— - theoretical line shape

The ordinate has not been scaled for either set of data.

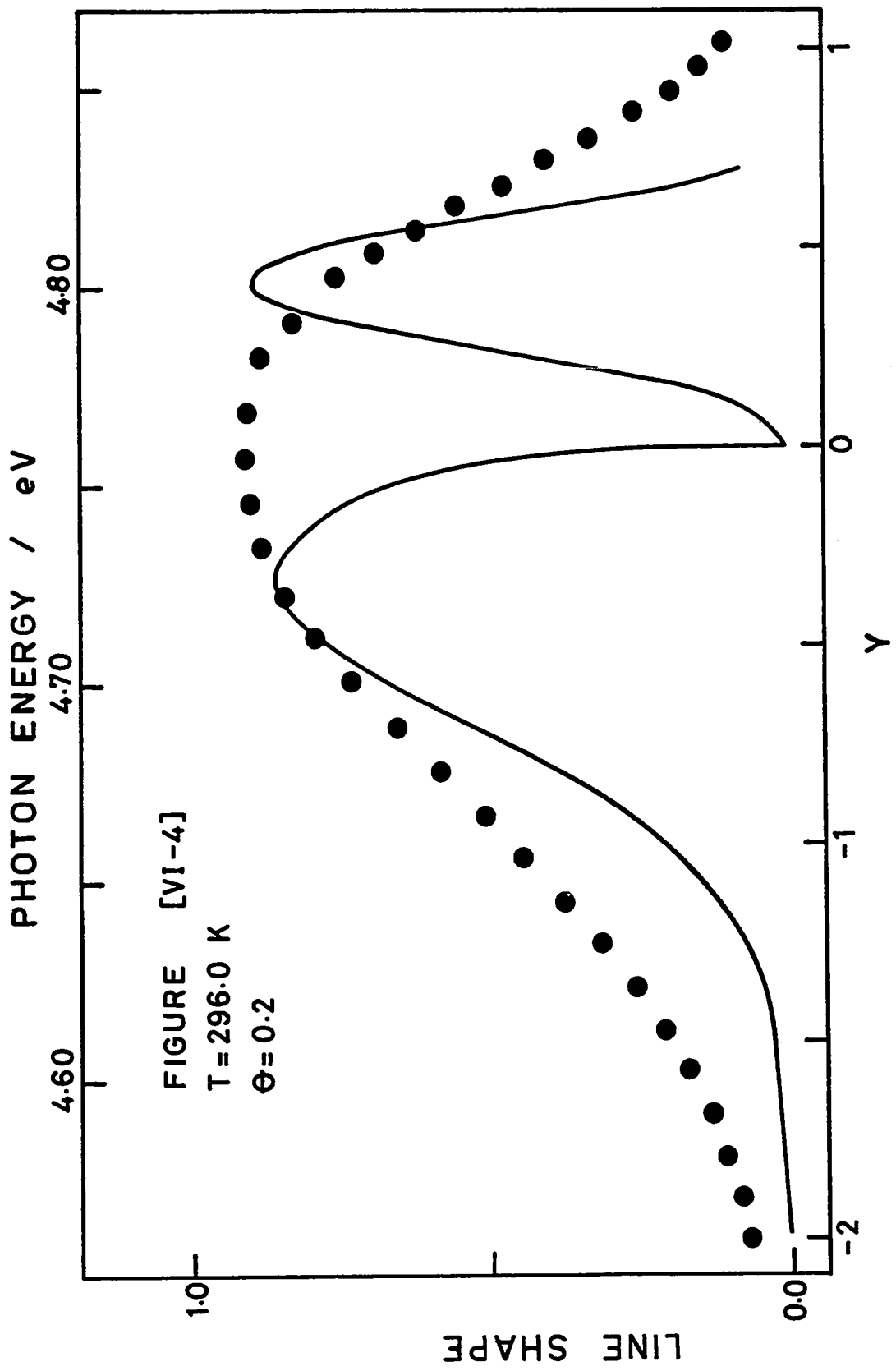
PHOTON ENERGY / eV
4.60
4.70
4.80
LINE SHAPE
0.0
1.0
Y
-2
-1
0
1
FIGURE [VI-4]
T=296.0 K
Θ=0.2

FIGURE [VI-5]

A-BAND ABSORPTION KBr:Tl^+

COMPARISON OF THEORETICAL AND EXPERIMENTAL LINE SHAPES

$\theta = 0.1$ $T = 144.5$ K

● - experimental data

——— - theoretical line shape

The ordinate has not been scaled for either set of data.

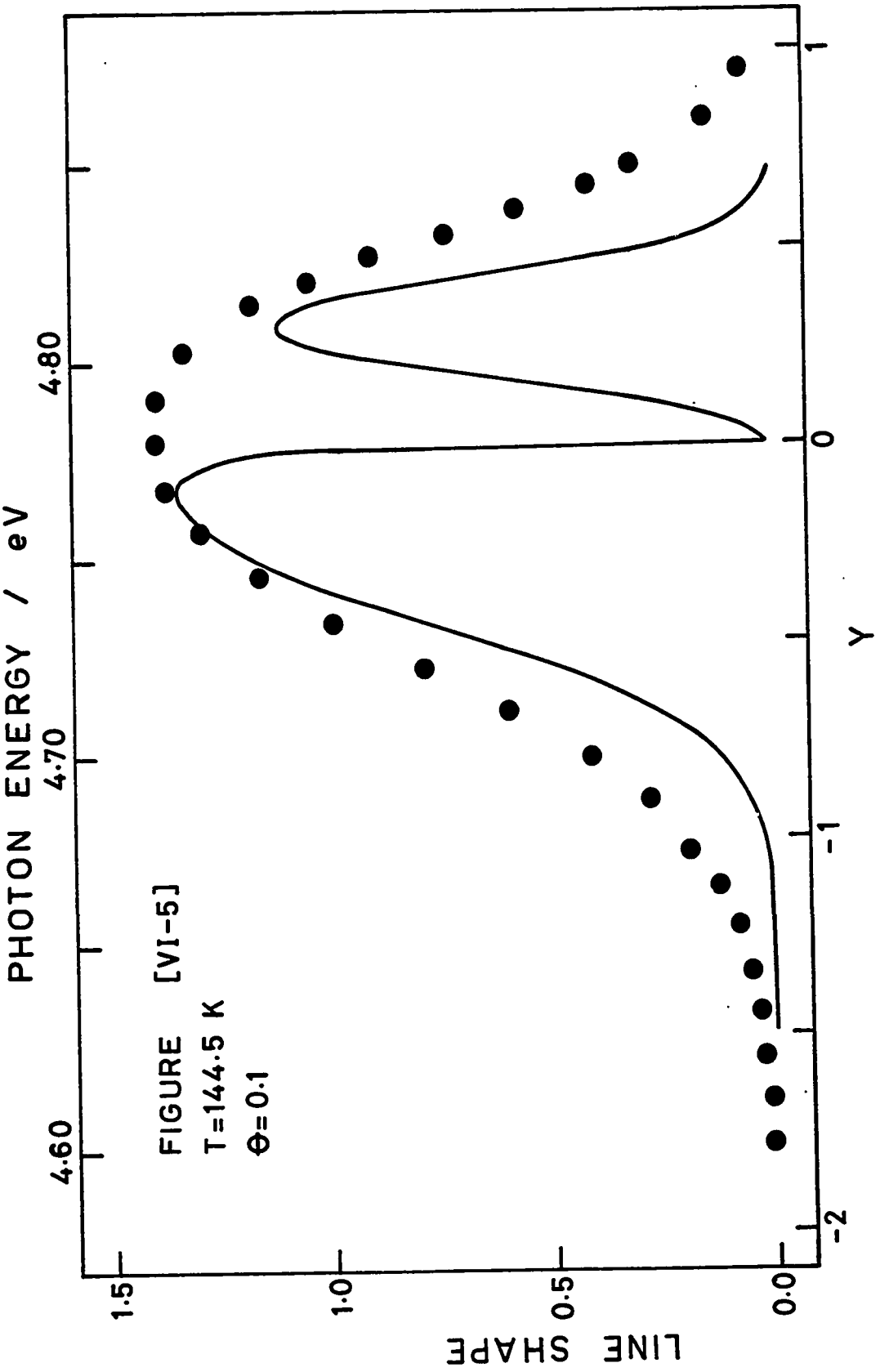
PHOTON ENERGY / eV
4.60
4.70
4.80
LINE SHAPE
0.0
0.5
1.0
1.5
Y
-2
-1
0
1
FIGURE [VI-5]
T=144.5 K
Θ=0.1

FIGURE [VI-6]

A-BAND ABSORPTION KBr:Tl^+

COMPARISON OF THEORETICAL AND EXPERIMENTAL LINE SHAPES

θ = 0.06 T = 83.0 K

● - experimental data

——— - theoretical line shape

The ordinate has not been scaled for either set of data.

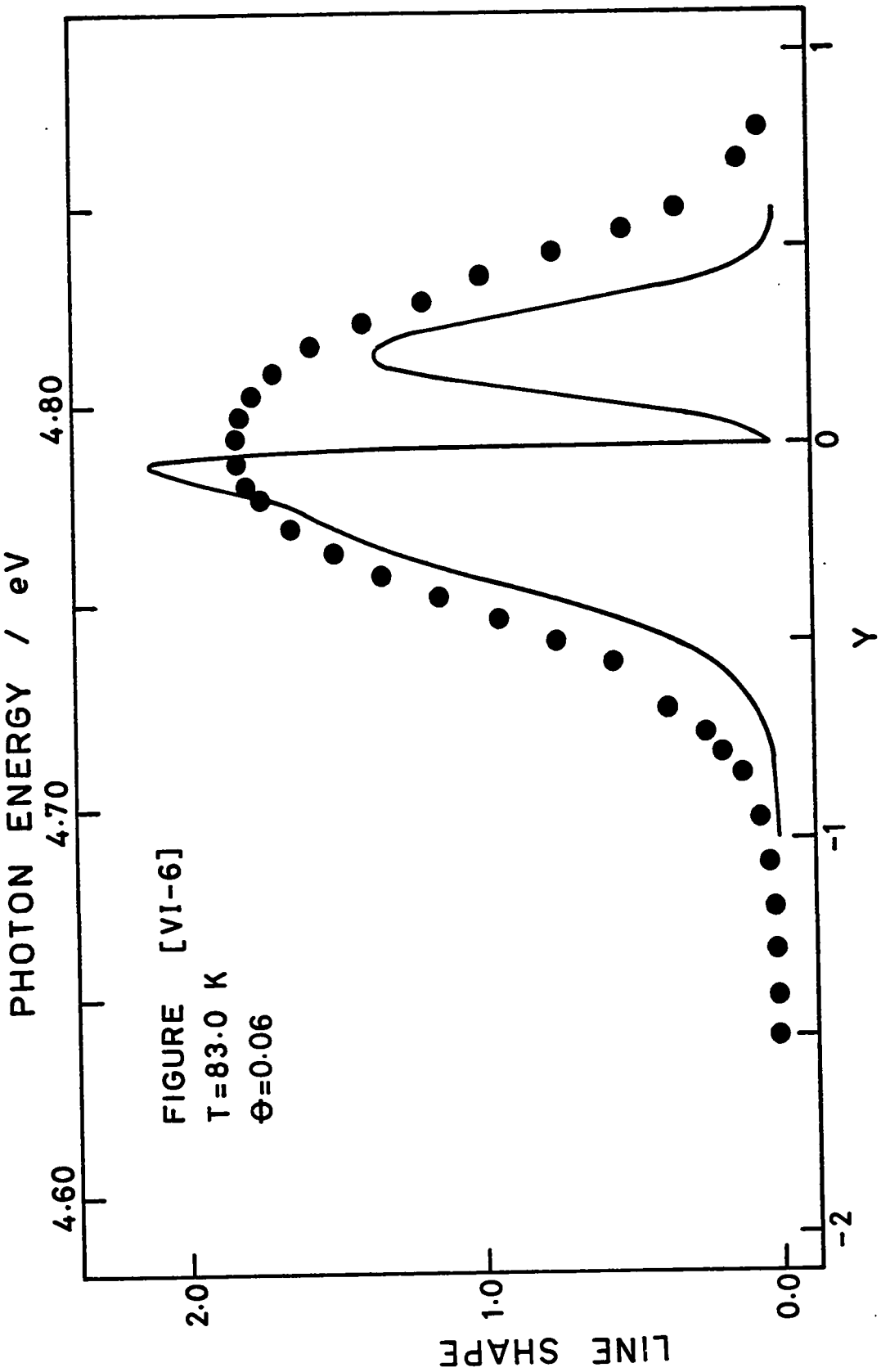
PHOTON ENERGY / eV
4.60
4.70
4.80
LINE SHAPE
0.0
1.0
2.0
Y
-2
-1
0
1
FIGURE [VI-6]
T=83.0 K
Θ=0.06

One of the most striking features of the experimental results (see Figure [V-1]) is that the high energy edge of the absorption band is virtually temperature independent. This is also reflected by the theory which predicts a high energy cut off corresponding to y=0.75. Also the experimental line shape becomes increasingly asymmetric on the low energy side as T increases. This feature is also predicted by the theory.

The overall agreement between the theory and experiment is good although the calculated band is narrower. However, the well defined splitting predicted by the theory is not seen experimentally. Although the splitting is predicted for all values of θ, the separation is small for small values of θ [92]. For KBr:Tl^+ for the temperature range 15 K<T<295 K, the range of θ is $0.034<\theta<0.20$ and the predicted splitting is therefore small. In addition several approximations were made in deriving equation [VI-24]. The inclusion of non-zero values of λ in the allowed range tempers the depth of the well between the bands. The term omitted from $\hat{H}_{JT}$ replaces the coefficient of q^2 in the delta function (see Equation [VI-18]) by

$$t_i^2(\lambda) - 4/3 - \mu$$

where

$$\mu = (q')^2 \frac{3R}{(R+1)^2} \frac{c^2}{\Delta_{CA}} \qquad \text{[VI-28]}$$

For KBr:Tl^+, the value of μ is 0.092. This term is therefore small compared with 4/3 and would not contribute significantly to the band shape.

The most severe approximation is the neglect of the effect of $\hat{H}_Q$ on the line shape. For the special case of coupling to a mode of A_{1g} symmetry only (e.g. a symmetric breathing mode)

$$\hat{H}_Q = Q_1^2 \underset{\sim}{1} \qquad [VI-29]$$

and

$$E_a(A_{1g}) = r(Q_1 - Q_o)^2 \qquad [VI-30]$$

where r accounts for the difference in curvature of the adiabatic potentials in the ground and excited states, ($r=K_{a1}/K_{b1}$), and Q_o is the displacement of the ground state minimum from that of the excited state. Then for linear coupling (r=1), the difference between the adiabatic potentials for one of the excited states and the ground state is

$$E_{bi} - E_a = \varepsilon_{ab} + \frac{\Delta}{3}[-t_i(\lambda)q + \{t_i^2(\lambda) - 4/3 - \mu\}q^2] + aq_1 \qquad [VI-31]$$

where

$$a = 2Q_o q'$$

and

$$\varepsilon_{ab} = \varepsilon_o - Q_o^2$$

Neglecting μ in comparison with 4/3

$$I(h\nu) = \frac{-4\Delta}{9a\pi\theta^2} \sum_{i=1}^{3} \int dy\ g_i(y,\theta)\ \exp[-(h\nu-\varepsilon_{ab} - \{\Delta/3\}y)^2/a^2\theta] \qquad [VI-32]$$

Thus the effect of $\hat{H}_Q$ is to convolute the line shape calculated from $\hat{H}_{JT}$ with a gaussian which leads to a broadening of each component. From the plots of $g(y,\theta)$ it can be seen that broadening of the components will cause the split in the A-band to vanish leaving a smooth asymmetric envelope.

Thus the application of the Jahn-Teller theorem to the A-band absorption in KBr:Tl^+ gives a theoretical line shape which is in good agreement with experimental results.

2. Emission

The emission of KBr:Tl^+ was produced by continuous excitation in the high energy tail of the A absorption band with the 2537 Å (4.89 eV) line of a mercury arc lamp.

The emission at five representative temperatures is shown in Figure [V-51]. The spectrum consists basically of two bands at 4.01 eV and 3.40 eV, although at low temperatures a tiny third band is seen at 3.14 eV. The most striking feature of the emission is the temperature dependence of the intensities of the two major bands (see Figure [V-60]). At low temperatures the spectrum is dominated by the band at 4.01 eV (Band 1). As the temperature increases, the intensity of Band 1 decreases while that of Band 2 (3.40 eV) increases. At ~110 K, the intensity of Band 1 has reached a minimum and the intensity of Band 2 is a maximum. As the temperature increases further, Band 1 begins to increase in intensity and Band 2 decreases in intensity until at room temperature I_m(Band 2)/I_m(Band 1) is ~2. The intensity of the small band at 3.14 eV is essentially independent of temperature from 15.5 K - 73.0 K, the temperature range over which it can be resolved.

Results for the analysis of the emission as symmetric gaussian bands are given in Figures [V-52] to [V-57]. The bands are very nearly gaussian in shape.

The temperature dependences of the half-widths are shown in Figure [V-58]. The values of H_{obs} for the two major bands are similar. The parameters derived from fitting the data to equation [II-78] are given in Table [VI-5]. Although the data over the complete range of temperatures for Band 1 were fitted, the experimental data shows a discontinuity at ~100 K. If only the data between 15.5 K and 83.0 K are fitted, the

deviations are much smaller. However, the values of the derived parameters are significantly different (see Table [VI-5]).

TABLE [VI-5]

PARAMETERS DERIVED FROM THE TEMPERATURE DEPENDENCE OF H_{obs}

Band	H_o/eV	$\nu/10^{12}$ sec^{-1}
1	0.194	1.52
2	0.185	1.41
1*	0.206	2.26

* - low temperature region

The origin of the two emission bands has been the subject of much discussion in the literature [18,41,51]. However, since an adequate explanation for the observed absorption requires a consideration of Jahn-Teller interaction in the excited state, it is probable that a Jahn-Teller interaction is also involved in the emission process. The situation is complicated by the fact that life time studies in KCl:Tl^+ [93,94] show that the high energy emission band has a slow and fast component which is evidence that the emission arises from two transitions one of which is forbidden. The only state that could be associated with the slow component is the $^3A_{1u}$. Ranfagni [52] has shown that the $^3A_{1u}$ adiabatic potential energy surfaces exhibit the same type of minima in the same positions as do the $^3T_{1u}$ surfaces in the j-j and Russell-Saunders coupling limits. Thus there is little doubt that in KCl:Tl^+ the high energy emission band consists of two components and that the transitions originate from almost degenerate states; one from the A state and the

other from the $^3A_{1u}$ state. Although there is no firm evidence for the existence of a slow component in KBr:Tl^+, our experimental results do not preclude such a possibility since the sum of two gaussian components having the same E_m will also be gaussian.

The situation regarding the low energy emission band is subject to more controversy [41,42,52,95]. However, the most likely explanation is the existence of a second kind of minimum on the adiabatic potential energy surface of the excited state of the A-band.

The interaction of the excited state of the A-band with vibrational modes of E_g symmetry has been investigated in a manner similar to that used by Fukuda [41] and Ranfagni [52]. The A state may be written as

$$|A\rangle = \mu|^1T_{1u}\rangle + \nu|^3T_{1u}\rangle \qquad \text{[VI-6]}$$

where μ and ν are the mixing coefficients for the singlet and triplet states. Its energy relative to the ground state can be written as

$$E_A = W_o + F - G + E \qquad \text{[VI-33]}$$

W_o is the energy difference between the s^2 and sp configurations ignoring electron-electron interactions, spin-orbit coupling and electron lattice coupling; F is the coulomb integral and G is the exchange integral. E includes the energy due to spin orbit coupling and electron lattice interaction and is obtained by diagonalizing the matrix for the interactions. In the E_g subspace, for the z component, $|A_z\rangle$, of the A state, the matrix is

$$\hat{H}_{e-e} + \hat{H}_{e-l} + \hat{H}_{s-o} - F\,\underset{\sim}{1} =$$

$$\begin{vmatrix} \frac{-b}{\sqrt{3}} Q_3 - G - \tfrac{1}{2}\xi & -ibQ_2 & \frac{1}{\sqrt{2}}\xi \\ ibQ_2 & \frac{-b}{\sqrt{3}} Q_3 - G + \tfrac{1}{2}\xi & 0 \\ \frac{1}{\sqrt{2}}\xi & 0 & \frac{2b}{\sqrt{3}} Q_3 + G \end{vmatrix} + (Q_2^2 + Q_3^2)\,\underset{\sim}{1} \qquad \text{[VI-34]}$$

where Q_2, Q_3 are the interaction coordinates, ξ is the spin-orbit coupling constant and b is the coupling constant between the A state and the E_g modes. Using the notation

$$\begin{aligned} A &= 12\xi/b^2 \\ g &= G/\xi \\ y &= E/\xi \\ x_{2,3} &= (-b/2\sqrt{3}\xi)Q_{2,3} \\ \bar{y} &= y - A(x_2^2 + x_3^2) \end{aligned} \qquad \text{[VI-36]}$$

the energy of the z component of the A state is given by the lowest root of

$$\bar{y}^3 + g\bar{y}^2 - \bar{y}(12x_2^2 + 12x_3^2 - 8x_3g + 3/4 + g^2) +$$

$$16x_3^3 - 48x_2^2x_3 + 1/4 + g(12x_2^2 - 20x_3^2 - 1/4) +$$

$$8x_3g^2 - g^3 = 0 \qquad \text{[VI-37]}$$

Profiles of $(y+g)\equiv(E+G)/\xi$, as a function of x_3 for $x_2=0$ are given in Figures [VI-7] and [VI-8]. The Russell-Saunders coupling limit corresponds to $g=\infty$ and the j-j coupling limit corresponds to $g=0$. Figure [VI-7] gives the profile for different values of g with A=2.4. As g increases, the minimum T_z^* becomes more shallow and when g=1 a minimum

FIGURE [VI-7]

EMISSION KBr:Tl^+

A-BAND EXCITATION

PROFILE PLOT OF (y+g) AS A FUNCTION OF x_3

A = 2.4 x_2 = 0.0

▲ g = 0.0

● g = 0.2

■ g = 0.4

⬢ g = 0.6

◆ g = 0.8

○ g = 1.0

□ g = ∞

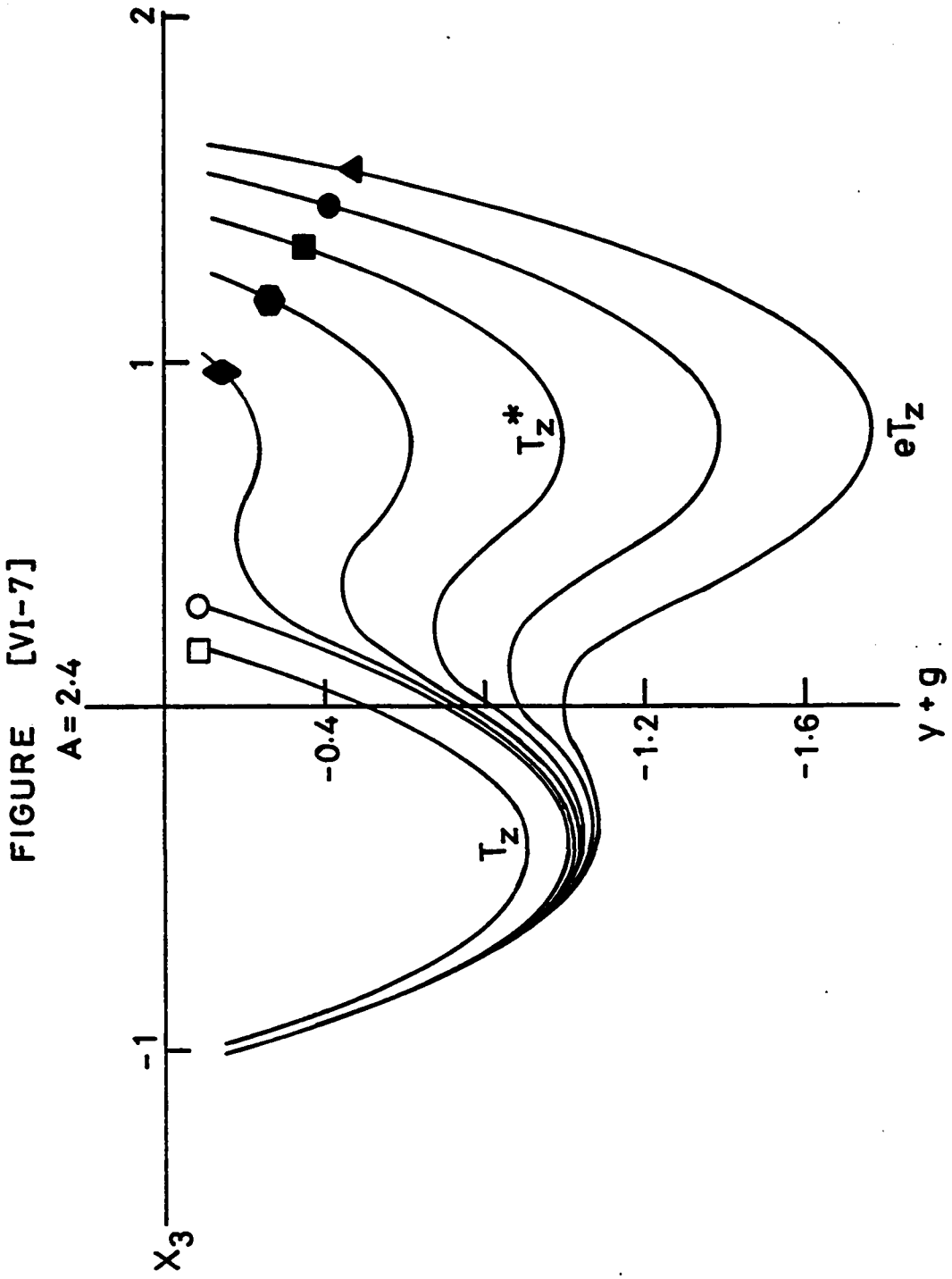

FIGURE [VI-7]

FIGURE [VI-8]

EMISSION KBr:Tl^+

A-BAND EXCITATION

PROFILE PLOT OF $(y+g)$ AS A FUNCTION OF x_3

$g = 0.4$ $x_2 = 0.0$

△ A = 2.0

▲ A = 2.2

○ A = 2.4

● A = 2.6

□ A = 3.0

■ A = 3.5

FIGURE [VI-8]

EMISSION KBr:Tl^+

A-BAND EXCITATION

PROFILE PLOT OF $(\dot{y}+g)$ AS A FUNCTION OF x_3

$g = 0.4$ $x_2 = 0.0$

△ A = 2.0

▲ A = 2.2

○ A = 2.4

● A = 2.6

□ A = 3.0

■ A = 3.5

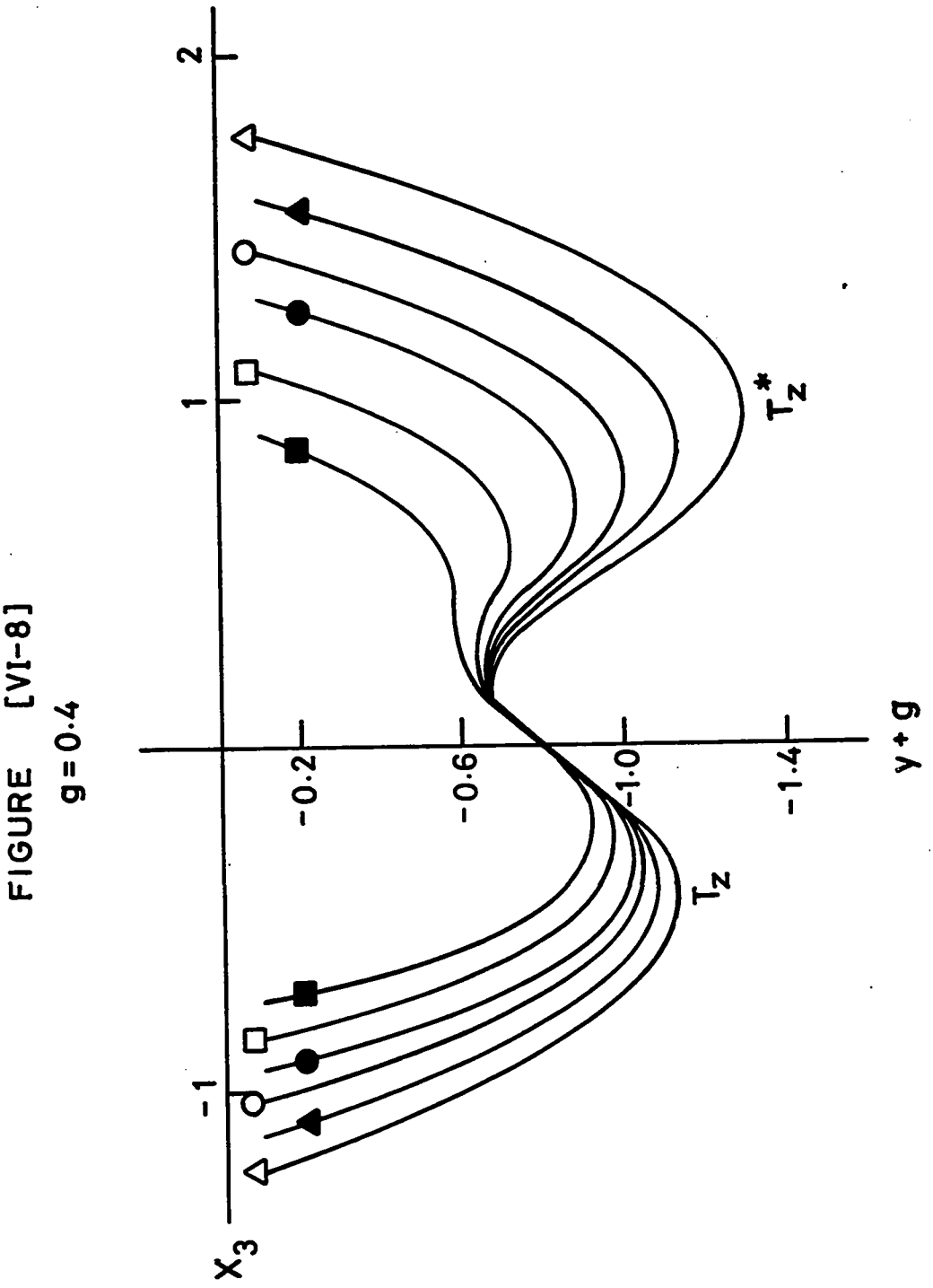

FIGURE [VI-8]
g=0.4

no longer is present. The apparent minima at negative values of x_3 are actually saddle points. Figure [VI-8] gives the profile for different values of A with g=0.4. Once again as A increases the minimum T_z^* becomes more shallow and eventually disappears. Thus there is a limited range for both g and A for which this minimum exists.

Figure [VI-9] is a contour map of the energy, (y+g), for A=2.4, g=0.0 (j-j coupling limit). The map shows that three minima exist and that they are equivalent. The minimum in Figure [VI-7] corresponds to eT_z and the saddle point corresponds to fT_z. Figure [VI-10] is a contour map of the energy, (y+g), for A=2.4, g=0.4. Under these conditions, two kinds of minima T_z^* and X are present. Only for intermediate values of the coupling constant will this situation exist. It should be noted that the X minima are deeper than the T_z^* minimum.

Reported values for G, ξ and b^2 [33,96,97] indicate that for KBr:Tl^+, A=2.4 and g=0.4. Thus, Figure [VI-10] represents the system under discussion. Although the qualitative features of the adiabatic potential energy surfaces are the same over a moderate range of A and g, the quantitative features are very sensitive to a particular choice of these parameters. In particular, the relative depths of the X and T_z^* minima are altered greatly for small changes in the parameters.

The minimum energy required to escape from T_z^* into X is 0.31ξ (0.19 eV). This corresponds to a vibrational quantum number, β, of ~30. The reverse process requires an energy of 0.59 eV or a value for β of ~96. The average vibrational quantum number can be calculated from

$$\bar{\beta} = (\exp[h\nu/kT] - 1)^{-1} \qquad [VI-37]$$

FIGURE [VI-9]

EMISSION $KBr:Tl^+$

A-BAND EXCITATION

CONTOUR PLOT

of

ADIABATIC POTENTIAL ENERGY SURFACE

A = 2.4 g = 0

△ y = 0.0

▲ y = -0.35

○ y = -0.7

● y = -1.0

⬢ y = -1.05

□ y = -1.2

■ y = -1.45

◊ y = -1.65

FIGURE [VI-9]
A=2.4
g=0

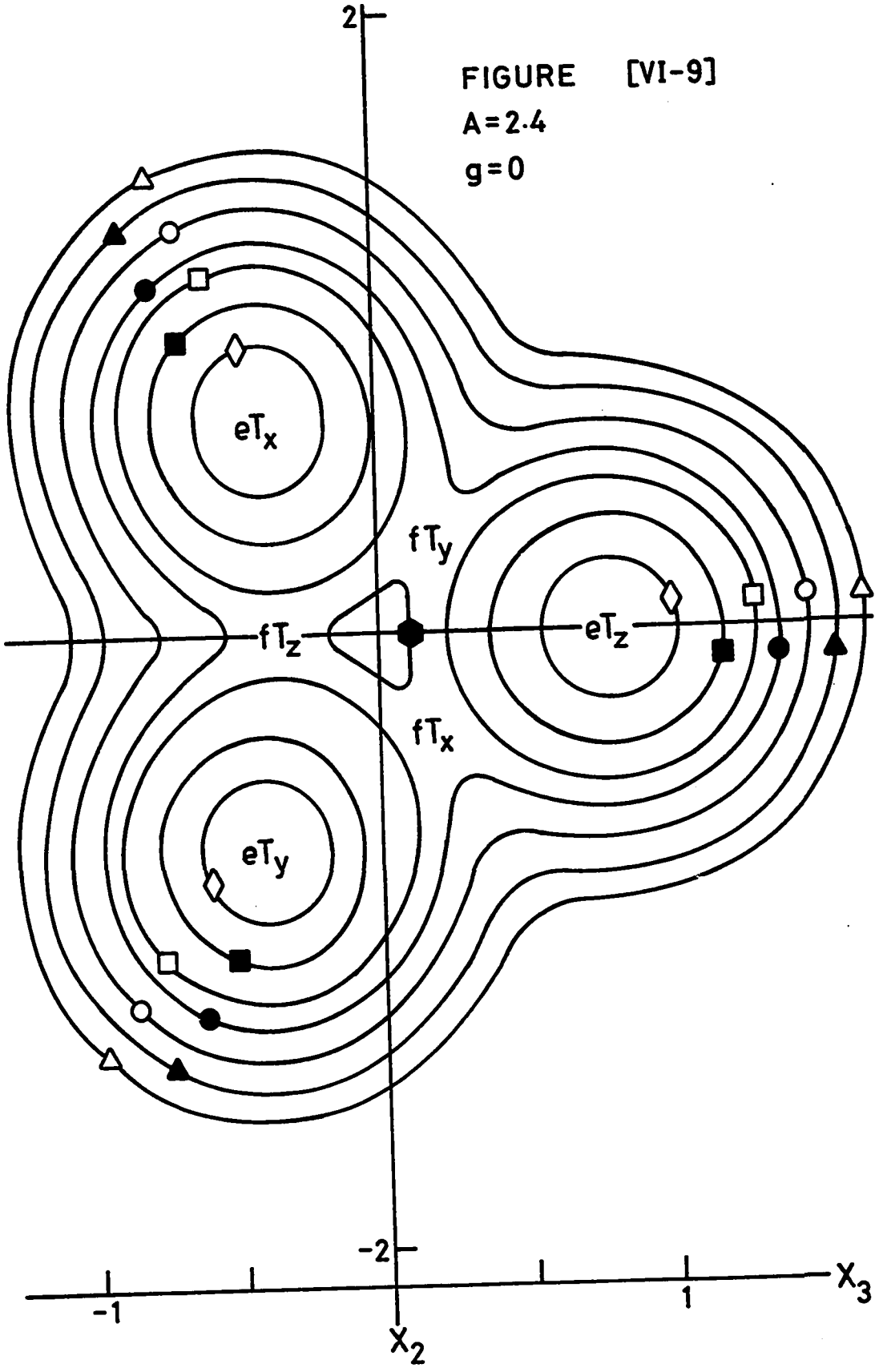

FIGURE [VI-10]

EMISSION KBr:Tl^+

A-BAND EXCITATION

CONTOUR PLOT

of

ADIABATIC POTENTIAL ENERGY SURFACE

A = 2.4 g = 0.4

△ y + g = 0.0

▲ y + g = -0.35

⬢ y + g = -0.5

○ y + g = -0.7

● y + g = -0.9

□ y + g = -1.2

■ y + g = -1.45

◊ y + g = -1.65

FIGURE [VI-10]
A=2·4
g=0·4

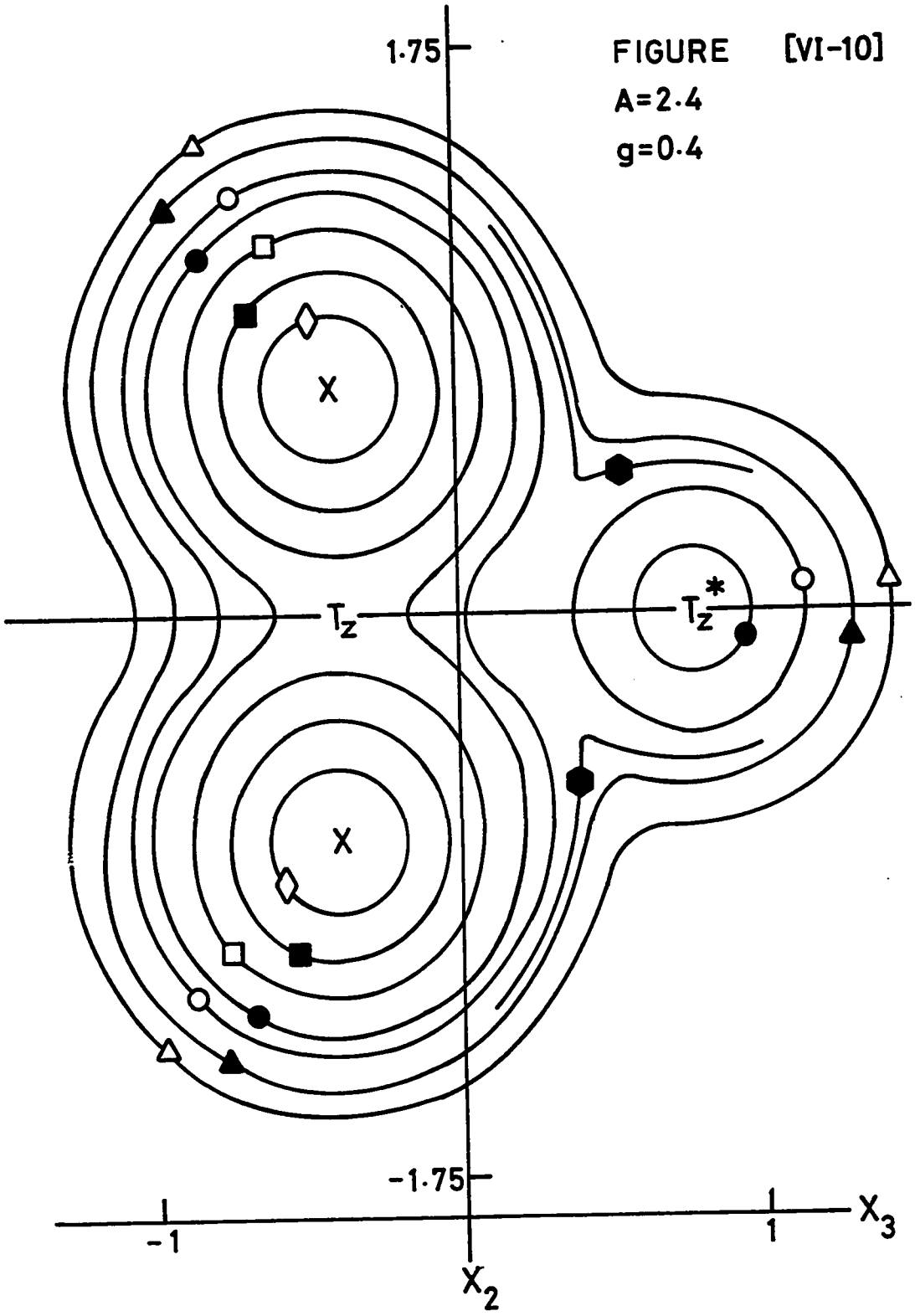

Using a frequency value of 1.5×10^{-12} sec^{-1}, $\bar{\beta}$=0.31 at 50 K. Consequently any electron which is in either T_z^* or X will remain there at low temperatures. As the temperature increases, the probability that an electron will acquire enough energy to overcome the barrier between the wells increases. At some temperature, a significant number of electrons will escape from T_z^* and be captured by X. Because the energy barrier for the reverse process is very much higher, the electrons will remain there. Consequently, the intensity of emission from the T_z^* minimum, A_T, will decrease and that from the X minima, A_X, will increase rapidly near this temperature. At higher temperatures, a thermal equilibrium will be established between the two wells. Since electrons will now move more readily between the two wells, the intensity of the A_X emission must decrease and that of the A_T increase. This is just the pattern which is observed experimentally. For electrons initially in the X minima, once they have gained sufficient energy to escape from the well, they will establish thermal equilibrium resulting in a gradual increase in the A_T emission and a gradual decrease in the A_X emission. Since at low temperatures the high energy emission band dominates, the electrons must be localized in either the T_z^* minimum or the X minima. The temperature dependence of the relative intensity of the two emission bands suggests that the high energy emission is associated with a transition from the T_z^* minimum and that the initial relaxation of the excited state is into this well.

The contour map, Figure [VI-10], shows the regions in which the potential wells are parabolic. The T_z^* and X wells are harmonic to ~0.12 eV and ~0.19 eV above their respective minima. The average energy of an electron at room temperature was calculated to be 0.025 eV. The

frequency of the ground state, ν_a, obtained from the temperature dependence of $\Delta E_{splitting}$ was $2.19 \times 10^{+12}$ sec^{-1}. This is almost the same as the frequency derived for the high energy emission from the temperature dependence of H_{obs} at low temperatures and reasonably close to those derived for both the high and low energy emission bands over the whole range of temperatures. Also the Huang-Rhys factor was calculated to be ~90. Consequently the quantum mechanical theory of the line shape in linear coupling can be expected to hold for the emission. Specifically, the line shapes should be accurately gaussian at high temperatures and almost gaussian at low temperatures. This was observed to a good approximation.

Qualitatively, the emission can be adequately explained by the existence of two different types of minima on the adiabatic potential energy surface of the excited state of the A-band. A more quantitative description would require a detailed study of life-times.

CHAPTER VII

SUMMARY

The optical absorption and emission of the A-band of single crystal potassium bromide containing thallous ion impurity was studied in the temperature range 15 K - 296 K. This absorption is ascribed to the spin orbit allowed transition $^1S_o(^1A_{1g}) \rightarrow {}^3P_1(^3T_{1u})$.

Crystals were prepared from reagent grade potassium bromide which was further purified by extraction of an aqueous solution with a solution of 8-hydroxyquinoline (oxine) in chloroform and subsequent recrystallization. The impurity ion (0.03 mole % Tl^+) was added either before or after the treatment of the KBr melt with HBr and Br_2. The first method resulted in a much lower concentration of Tl^+ in the final crystal. The crystals were grown in an atmosphere of N_2 and HBr by slowly lowering the melt through a sharp temperature gradient. Samples of suitable dimensions were cleaved from the resulting single crystal.

The samples were mounted in variable temperature cryostats which could be used with either liquid nitrogen or liquid helium as refrigerant. The temperatures were measured with a gold/0.03 atomic % iron vs. chromel thermocouple. By suitably balancing the cooling supplied by the refrigerant against the continuous heat from a heater wound on the controlled temperature block the temperature could be maintained constant to within ±0.6 K. The cryostats could be used for either absorption or emission measurements.

The absorption measurements were made using a Cary model 14R spectrophotometer in double beam mode. The measured values of optical density were automatically recorded as a function of wavelength on a strip chart recorder.

The spectrophotometer was modified so that the emission excited by a given wavelength could be analyzed using the Cary double monochromator. The emission intensities were recorded as before. The measured values were corrected for the spectral sensitivity of the optical system.

Before any systematic investigation of the absorption and emission band shapes was undertaken, the raw experimental data were corrected for any background and experimental line shapes were calculated by dividing the optical density values for absorption by their corresponding photon energies and by dividing the measured intensities of emission by the cube of the photon energies.

The absorption line shape was analyzed as either a gaussian or a log normal (asymmetric gaussian) distribution at each temperature. The best empirical fit to the experimental data was found to be given by the sum of two asymmetric gaussian bands. The temperature dependences of the parameters were investigated in terms of the predictions of the configuration coordinate model. It was concluded that the absorption could not be interpreted on the basis of this model. The effect of the Jahn-Teller interaction between the T_{2g} vibrational modes of the lattice and the excited state of the A-band was investigated. It was found that many of the features of the A-band absorption could be explained using this model. In particular, the existence of two component bands and their temperature sensitive asymmetry was predicted.

Also, the good agreement of the temperature dependence of the energy separation of the two components with the theoretical prediction supports this interpretation.

The emission produced by excitation in the A-absorption band was characterized by two symmetric gaussian bands. The results were explained on the basis of a Jahn-Teller interaction between the E_g vibrational modes of the lattice and the excited state of the A-band. For intermediate values of the spin orbit coupling constant, the model predicts that two different kinds of minima are present on the adiabatic potential energy surface. Thus the temperature dependence of the relative intensities of the two major experimentally observed bands could be explained.

REFERENCES

[1] R. Hilsch, Z. Physik, 44, 860 (1927).

[2] R. Hilsch and R.W. Pohl, Z. Physik, 48, 384 (1929); 57, 145 (1929); 59, 812 (1930).

[3] H. Lorenz, Z. Physik, 46, 558 (1928).

[4] M. Forro, Z. Physik, 56, 534 (1929); 58, 613 (1930).

[5] W. Koch, Z. Physik, 57, 638 (1929); 59, 378 (1930).

[6] F. Seitz, J. Chem. Phys., 6, 150 (1938).

[7] F.E. Williams, J. Chem. Phys., 19, 457 (1951).

[8] F.E. Williams and M.H. Hebb, Phys. Rev., 84, 1181 (1951).

[9] F.E. Williams, J. Chem. Phys., 57, 780 (1953).

[10] F.E. Williams and P.D. Johnson, Phys. Rev., 113, 97 (1959).

[11] C.C. Klick, Phys. Rev., 85, 154 (1952).

[12] G.A. Russell and C.C. Klick, Phys. Rev., 101, 1473 (1956).

[13] D.A. Patterson and C.C. Klick, Phys. Rev., 105, 401 (1957).

[14] C.C. Klick and J.H. Schulman in "Solid State Physics", edited by F. Seitz and D. Turnbull (Academic Press Inc., New York, 1957), 5, 97.

[15] P.H. Yuster and C.J. Delbecq, J. Chem. Phys., 21, 892 (1953).

[16] C.C. Klick, D.A. Patterson and R.S. Knox, Phys. Rev., 133, A1717 (1964).

[17] K. Edgerton and K. Teegarden, Phys. Rev., 136, A1091, (1964).

[18] H. Kamimura and S. Sugano, J. Phys. Soc. Japan, 14, 1612 (1959).

[19] A. Fukuda, Sci. Light, 13, 64 (1964).

[20] S. Sugano, J. Chem. Phys., 36, 122 (1962).

[21] Y. Toyozawa and M. Inoue, J. Phys. Soc. Japan, 21, 1663 (1966).

[22] K. Cho, J. Phys. Soc. Japan, 25, 1372 (1968).

[23] A. Honma, J. Phys. Soc. Japan, 24, 1082 (1968).

[24] F.E. Williams in "Luminescence of Inorganic Solids", edited by P. Goldberg (Academic Press, New York, 1966), Chapter 1.

[25] K. Teegarden in "Luminescence of Inorganic Solids", edited by P. Goldberg (Academic Press, New York, 1966), Chapter 2.

[26] W.B. Fowler in "Physics of Color Centers", edited by W.B. Fowler (Academic Press, New York, 1968), Chapter 2.

[27] D.A. Patterson, Phys. Rev., 112, 296 (1958).

[28] C.C. Klick and W.D. Compton, J. Phys. Chem. Solids, 7, 170 (1958).

[29] J. Ewles and R.V. Joshi, Proc. Roy. Soc. (London), A254, 358 (1960).

[30] D.A. Patterson, Phys. Rev., 119, 962 (1960).

[31] W. Wagner, Z. Physik, 181, 143 (1964).

[32] R. Edgerton and K. Teegarden, Phys. Rev., 129, 169 (1963).

[33] D. Bimberg, W. Dultz, K. Fussgaenger and W. Gebhardt, Z. Physik, 224, 364 (1969).

[34] D. Bimberg, W. Dultz and W. Gebhardt, Phys. Status Solidi, 31, 661 (1969).

[35] K. Fussgaenger, Phys. Status Solidi, 34, 157 (1969).

[36] A. Fukuda, J. Phys. Soc. Japan, 27, 96 (1969).

[37] P.L. Mattern, K. Lengweiler, P.W. Levy and P.D. Esser, Phys. Rev. Letters, 24, 1287 (1970).

[38] A.M. Lemos, M.C. Stauber and J.F. Marion, Phys. Rev. B, 2, 4161 (1970).

[39] A. Halperin and A.A. Braner, J. Luminescence, 4, 21 (1971).

[40] A.A. Braner and A. Halperin, Phys. Rev. B, 4, 543 (1971).

[41] A. Ranfagni, G.P. Pazzi, P. Fabeni, G. Viliani and M.P. Fontana, Phys. Rev. Letters, 28, 1035 (1972).

[42] R. Illingworth, Phys. Rev., 136, A508 (1964).

[43] A. Fukuda, S. Makishima, T. Mabuchi and R. Onaka, J. Phys. Chem. Solids, 28, 1763 (1967).

[44] W. Dultz and W. Gebhardt, Solid State Communications, 7, 1153 (1969).

[45] U. Giorgianni, V. Grasso and P. Perillo, Phys. Rev. B, 4, 3731 (1971).

[46] V. Grasso and G. Saitta, Phys. Rev. Letters, 22, 522 (1969).

[47] R. Edgerton, Phys. Rev., 138, A85 (1965).

[48] R. Edgerton and K. Teegarden, Phys. Rev., 136, A1091 (1964).

[49] T. Shimada and M. Ishiguro, Phys. Rev., 187, 1089 (1969).

[50] M.F. Trinkler, Opt. Spectrosc., 18, 495 (1965).

[51] A. Fukuda, Phys. Rev. B, 1, 4161 (1970).

[52] A. Ranfagni, Phys. Rev. Letters, 28, 743 (1972).

[53] N.F. Mott and R.W. Gurney, "Electronic Processes in Ionic Crystals", 2nd ed. (Dover Publications Inc., 1964) Chapter I.

[54] E.U. Condon and G.H. Shortley, "The Theory of Atomic Spectra" (Cambridge University Press, London and New York, 1935).

[55] D.L. Dexter in "Solid State Physics", edited by F. Seitz and D. Turnbull (Academic Press Inc., New York, 1958), 6, 355.

[56] E. Merzbacher, "Quantum Mechanics" (John Wiley and Sons Inc., New York, London, 1958), p. 439.

[57] E.U. Condon and G.H. Shortley, "The Theory of Atomic Spectra" (Cambridge University Press, London and New York, 1935) p. 175.

[58] M. Lax, J. Chem. Phys., 20, 1752 (1952).

[59] K. Huang and A. Rhys, Proc. Roy. Soc. (London), A204, 406 (1950).

[60] E.T. Copson, "Theory of Functions of a Complex Variable", (Oxford University Press, London, 1935) p. 270.

[61] M. Abramowitz and I.A. Stegun, "Handbook of Mathematical Functions" (Dover Publications Inc., New York, 1965) formula 9.6.7, p. 375.

[62] J.J. Markham, Rev. Mod. Phys., 31, 956 (1959).

[63] T.H. Keil, Phys. Rev., 140, A601 (1965).

[64] M. Abramowitz and I.A. Stegun, "Handbook of Mathematical Functions" (Dover Publications Inc., New York, 1965) formula 9.7.1, p. 377.

[65] S. Sugano, Y. Tanabe and H. Kamimura, "Multiplets of Transition-Metal Ions in Crystals" (Academic Press, New York and London, 1970) p. 233.

[66] P.W.M. Jacobs and A.K. Menon, J. Chem. Phys., 55, 5357 (1971).

[67] Operating Instructions for 'Versa-Stat' (Cryogenics Associates, Inc., Indianapolis, 1967).

[68] R. Berman, J.C.F. Brock and D.J. Huntley, Cryogenics, 4, 233 (1964).

[69] Cary Recording Spectrophotometer Model 14R (Cary Instruments, Monrovia, California) Drawing No. 1475430.

[70] Applications Report AR 14-2 (1964) (Cary Instruments, Monrovia, California) p. 6.

[71] R.E. Dodd, "Chemical Spectroscopy" (Elsevier Publishing Company, Amsterdam, 1962) p. 63.

[72] F.A. Jenkins and H.E. White, "Fundamentals of Optics", 3rd edition (McGraw Hill Book Co. Ltd., New York, 1957).

[73] "Handbook of Chemistry and Physics", 48th edition (The Chemical Rubber Co., Cleveland, 1968) p. 213.

[74] Sample courtesy of C.C. Klick, U.S. Naval Research Laboratory, Washington, D.C.

[75] R.F. Cook (Cary Instruments) - private communication.

[76] Applications Report AR 14-2 (1964) (Cary Instruments, Monrovia, California) p. 14.

[77] C.A. Parker, "Photoluminescence of Solutions", (Elsevier Publishing Company, Amsterdam, 1968) pp. 252-258.

[78] R. Stair, W.E. Schneider and J.K. Jackson, Applied Optics, 2, 1151 (1963).

[79] Instructions for using the NBS 1000 Watt Quartz Iodine Lamp Standards of Spectral Irradiance (The Eppley Laboratory, Inc., Newport, R.I.).

[80] Instructions for Filter Assembly (Cary Instruments, Monrovia, California).

[81] R.B. Cook and R. Jankow, J. Chem. Ed., 49, 405 (1972).

[82] W. Gebhardt and H. Kuhnert, Phys. Status Solidi, 14, 157 (1966).

[83] R.H. Pennington, "Introductory Computer Methods and Numerical Analysis" (The Macmillan Company, New York, 1968) p. 404.

[84] R.E. Biggers, J.T. Bell, E.C. Long and O.W. Russ, Oak Ridge National Laboratory, Oak Ridge, Tennessee, ORNL-3834 (1971).

[85] R.D.B. Fraser and E. Suzuki in "Spectral Analysis: Methods and Techniques", edited by J.A. Blackburn (Marcel Dekker, Inc., New York, 1970) p. 176.

[86] BMDX85, "Biomedical Computer Programs X-series Supplement", edited by W.J. Dixon (University of California Press, Berkeley, 1969).

[87] R.D.B. Fraser and E. Suzuki in "Spectral Analysis: Methods and Techniques", edited by J.A. Blackburn (Marcel Dekker- Inc., New York, 1970) p. 183.

[88] Dr. J. Ross Macdonald (Texas Instruments Inc.) - private communication.

[89] P.R. Bevington, "Data Reduction and Error Analysis for the Physical Sciences" (McGraw Hill Inc., New York, 1969) Chapter 10.

[90] P.D. Esser and P.W. Levy in "Proceedings of an International Symposium on Color Centres in Alkali Halides", Rome, Italy, September 1968, p. 87.

[91] H.A. Jahn and E. Teller, Proc. Roy. Soc. (London), A161, 220 (1937).

[92] Y. Toyozawa and M. Inoue, J. Phys. Soc. Japan, 21, 1663 (1966) Figure 11.

[93] M. Spiller, V. Gerhardt and W. Gebhardt, J. Luminescence, 1, 2, 651 (1970).

[94] M. Tomura, H. Nishimura and Y. Kawashina, J. Phys. Soc. Japan, 21, 213 (1965).

[95] J.M. Donahue and K. Teegarden, J. Phys. Chem. Solids, 29, 2141 (1968).

[96] R. Chaney, P.W.M. Jacobs and T. Tsuboi, in course of publication.

[97] V. Grasso, P. Perillo and G. Vermiglo, Il Nuovo Cimento, 13B, 42 (1973).